University of Louisville

ThinkIR: The University of Louisville's Institutional Repository

8-2019

Improving flow-induced hemolysis prediction models.

Mohammad Mohaghegh Faghih
University of Louisville

IMPROVING FLOW-INDUCED HEMOLYSIS PREDICTION MODELS

By

Mohammad Mohaghegh Faghih

A Dissertation

Submitted to the Faculty of the

J.B. Speed School of Engineering of the University of Louisville

in Partial Fulfillment of the Requirements

for the Degree of

Doctor of Philosophy in
Mechanical Engineering

Department of Mechanical Engineering
University of Louisville
Louisville, KY 40292

August, 2019

IMPROVING FLOW-INDUCED HEMOLYSIS PREDICTION MODELS

By

Mohammad Mohaghegh Faghih

A Dissertation Approved on

March 29, 2019

by the Following Dissertation Committee:

_____

Director: Dr. M. Keith Sharp

_____

Dr. George Pantalos

_____

Dr. Stuart Williams

_____

Dr. Srinivasan C. Rasipuram

DEDICATION

I dedicate this dissertation

to my dear wife who has been a tremendous source of love, inspiration and support throughout my PhD career, to my beloved son, Mohammad Sadegh, who has brought happiness to our life during the busiest time of my study, and last but not least, to my parents for their generous love and endless encouragement.

ACKNOWLEDGMENT

ABSTRACT

IMPROVING FLOW-INDUCED HEMOLYSIS PREDICTION MODELS

Mohammad Mohaghegh Faghih

March 29, 2019

Partial or complete failure of red blood cell membrane, also known as hemolysis, is a persistent issue with almost all blood contacting devices. Many experimental and theoretical contributions over the last few decades have increased insight into the mechanisms of mechanical hemolysis in both laminar and turbulent flow regimes, with the ultimate goal of developing a comprehensive, mechanistic and universal hemolysis prediction model. My research is broadly divided into two sections: theoretical/analytical/Computational Fluid Dynamics (CFD) analyses and experimental tests.

The first part of my research revolved entirely around analyzing the simplest and most popular hemolysis model, commonly called as the power-law model. This model was developed only for laminar pure shear flow within a limited range of exposure time. Subsequently, modified versions of this model have been developed to be used for more complex flows. Many of these modified models assume that hemolysis scales with a resultant, scalar stress representing all components of the fluid stress tensor. The most common representative stress used in the power-law model is a von-Mises-like stress. However, using membrane tension models for pure shear and pure extension in both laminar and turbulent flows, for some simple example cases, we have shown that scalar stress alone is inadequate for scaling hemolysis.

Alternatively, the rate of viscous energy dissipation rate has also been proposed as the parameter to scale hemolysis with. Applying the same order-of-magnitude estimate as

mentioned above, we have found that dissipation rate even behaves worse than the resultant scalar stress for hemolysis prediction. It is therefore concluded that energy dissipation rate alone is also not sufficient to universally scale blood damage across complex flows. These show that a realistic model of hemolysis must take into account different responses of the viscoelastic cell membrane to different stress type.

Various discretized version of the power-law model has also been introduced for post-processing of the CFD results. The power law can be either discretized in space, Eulerian treatment, or in time, Lagrangian treatment. Our study on the Eulerian approach revealed that the current equations used in the literature has a missing term, and thus incorrect. We also examined the mathematical stability of the discretized power-law model, and found that it may introduce significant error in red cell damage prediction for certain pathlines with specific stress history.

Experimental results on deformation of red cell in pure shear flow is present for a relatively wide range of shear rates. However, red cell deformation/elongation in pure laminar extensional flow is scarce, with only one publication reporting their results on red cell deformation for only up to stress level of 10 Pa. For the experimental part of my research, we conducted experiments to observe the difference in deformation of red cell in pure shear and pure extensional flows, for stresses beyond what has already been reported in the literature.

This dissertation is composed of three chapters. Chapter I is the literature survey and introductory materials. Chapter II contains the discussion and results for the theoretical/analytical/CFD part of the research. Finally, discussion and results for the experimental tests are presented in Chapter III.

Keywords: Red Cell Membrane Damage; Hemolysis Prediction Model; Cardiovascular Assist Devices; Laminar and Turbulent Flows; Extensional Flow; Lagrangian and Eulerian Discretization.

TABLE OF CONTENTS

LIST OF FIGURES

LIST OF TABLES

CHAPTER I: LITERATURE REVIEW[1]

1.1 Introduction

1.1.1 Types of hemolysis

Hemolysis is characterized by damage, whether transient or permanent, that causes release of hemoglobin from red cells. Mechanical, thermal, chemical, and biological factors can all cause blood damage in blood-contacting devices [2-4]. While each of these damage factors may be important in particular individuals and applications, mechanically-induced hemolysis has proven to be a persistent challenge across a wide range of devices. Accordingly, this article focuses on mechanical hemolysis, in particular on experiments that have quantified hemolysis for different fluid stress conditions, and on the development of mechanistic models that seek to interpret these results. Such models are essential to achieving the ultimate goal of creating reliable hemolysis prediction algorithms applicable to a wide range of flow fields for use in designing new blood-contacting devices.

Red blood cells (RBCs) passing through the cardiovascular system and through prosthetic devices experience combinations of different types of stresses for a range of exposure times. Under normal conditions in the natural circulation, these stresses are for the most part below the critical values for hemolytic damage to RBCs. However, irregular blood flow around the complex geometries in cardiovascular devices and in abnormal conditions in the natural circulation may create combinations of high stress and long duration of stress in regurgitant jets, rapidly converging flows, and turbulent and vortical flows. Such flows may cause complete or partial rupture of membranes that allows

---

[1] Most of the material in this chapter is adopted from our published work in Faghih and Sharp [1].

immediate release of hemoglobin. Alternatively, accumulated damage to the cell membrane may result in premature elimination of red cells from the circulation by the spleen and kidney (sublytic damage) [5, 6]. Model development in both areas will be discussed.

1.1.2 Hemolysis in cardiovascular devices

Hemolysis has been observed since the earliest application of intra-cardiac prosthetic material into the body [7-10]. Although improved knowledge about the dynamics of blood flow, enhanced engineering design of cardiovascular devices and the introduction of more bio-compatible materials have reduced the rate of severe hemolysis [11-13], mild hemolysis and sub-hemolytic damage remain clinical concerns for modern mechanical circulatory support (MCS) devices, including cardiopulmonary bypass (CPB), extracorporeal membrane oxygenation (ECMO), percutaneous cardiopulmonary system (PCPS), and left ventricular assist devices (LVAD) [12, 14-17].

1.2 Red blood cells

Mechanistic hemolysis prediction logically involves the red cell and its membrane. Therefore, properties of red cells are briefly reviewed. Dimensional and other information about human RBCs is listed in Table 1 [18, 19]. Red cells, also called erythrocytes, are the most numerous type of cells in the blood, comprising nearly half of the blood volume. Consequently, mechanical and rheological behavior of the blood is usually dominated by RBCs. Owing to their biconcave shape (Fig. 1.1), RBCs have 44% greater surface area than that required to enclose a sphere of the same volume, thus providing more surface area for gas exchange [20] and allowing the cells to squeeze through capillaries and other passages smaller than their unstressed dimensions [21].

RBCs lack a cell nucleus as well as most other common intracellular elements, which helps maximize space for hemoglobin, a protein molecule responsible for carrying oxygen. The total amount of hemoglobin in blood (intracellular plus extracellular) is typically 12-13.5g/dl. However, the normal level of extracellular hemoglobin, called plasma free hemoglobin (*PfHb*), is very small (0.008 g/dl). *PfHb* of more than 0.03-0.05

g/dl is considered clinically dangerous, and may cause physiological complications, particularly hemolytic anemia and renal impairment, or even multiple organ failure [22, 23].

Table 1. 1 Typical values for RBC propertie*s* [19, 24]

Property of RBC	Unit	Value
Diameter	µm	7.82±0.62
Thickness	µm	
at Thickest Point		2.58±0.27
at Center		0.81±0.35
Membrane Surface Area	μm^2	135±16
Volume	μm^3	94±14
Membrane Thickness	nm	5-10
Hematocrit (adult male)	%	47±5
Normal Life	Days	104±14
Shear Stress on RBC	$Dyne/cm^2$	
Vein		1-10
Artery		10-200
Artery at Stenosis		200-500
Centrifugal Pump		200-1000
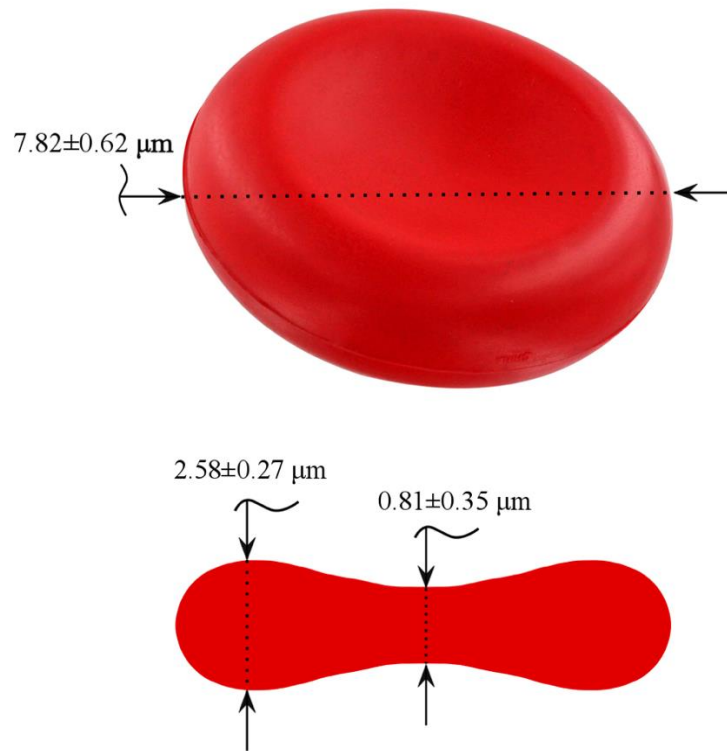
Fig. 1. 1 Shape and statistical dimensions of the RBC

1.2.1 Red cell membrane structure

The RBC membrane, which is composed of an outer lipid bilayer, an underlying spectrin network and transmembrane proteins, is a very flexible viscoelastic material (Fig. 1.2). It is generally held that the lipid bilayer acts as the viscous component while RBC elasticity is primarily attributed to the spectrin network [25]. The lipid bilayer is composed of lipid molecules with hydrophilic heads and hydrophobic tails. The tails interdigitate to form the bilayer, but the molecules are free to move tangentially, allowing the membrane to behave like a two-dimensional fluid. The cytoskeleton, a filamentous hexagonal protein network, has a significant role in RBC shape, flexibility, deformability and lipid organization [26]. Spectrin, which is the dominant component in the cytoskeleton, is a long and flexible protein [27]. Spectrin tetramers can stretch to approximately 200 nm in length when fully extended, and can contract to a length as short as 70 nm [28].

4
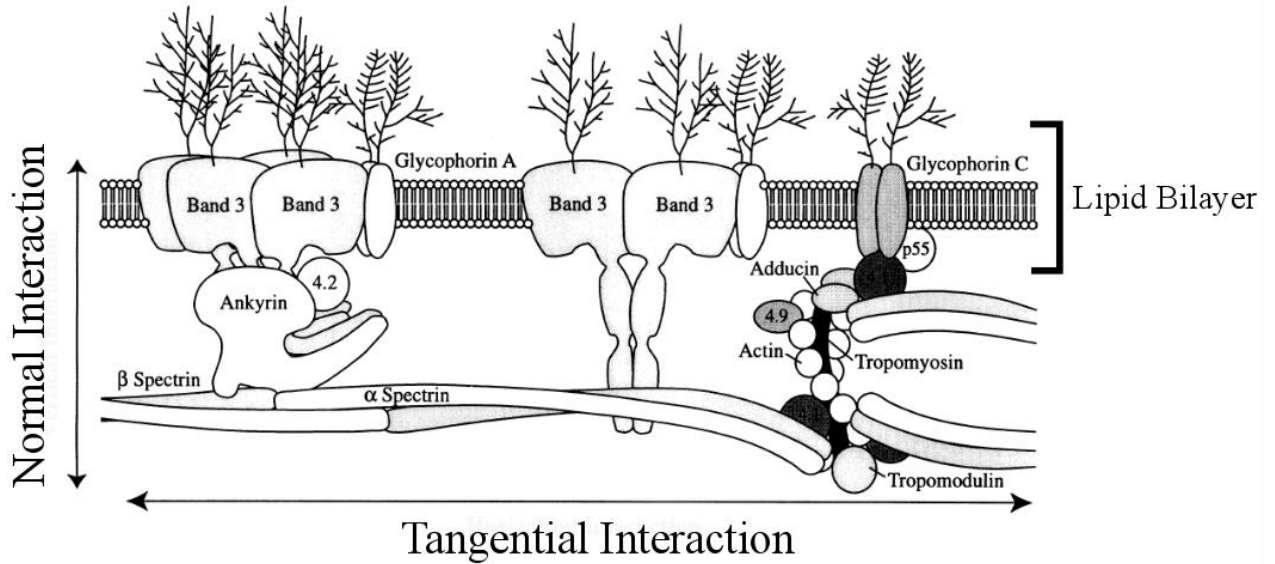
Fig. 1. 2 Schematic diagram of the RBC membrane structure (adopted from Lux and Palek [29])

Conceptually there are two types of interactions between components of the cell membrane: tangential and normal (Fig. 1.2). The tangential interactions include those among the spectrin skeleton components themselves and are responsible for the structural integrity of the RBC, whereas the normal interactions stabilize the membrane by linking the cytoskeleton to the bilayer [30]. It has become well established that disruptions in tangential and normal interactions can result in elliptocytes (abnormally oval-shaped RBCs) and spherocytes (abnormally sphere-shaped RBCs), respectively. For more information about the tangential and normal interactions and connections among different proteins in the RBC membrane, which also affect the cell's final shape and behavior, readers are encouraged to refer to Burton and Bruce [31].

Deformability of the red cell has been measured by several experimental methods, including micropipette aspiration, optical tweezer stretching, flow visualization, and recently atomic force microscopy (AFM) [32, 33]. The contribution of the bilipid layer to several properties of the membrane can be traced to the hydrophobicity of the phospholipid tails, which have a surface tension relative to water of $\gamma \approx 50\ mN/m$. Biaxial stretching of the layer exposes the tails to water on both sides (plasma and cytoplasm are aqueous), which by simplified models leads to an area expansion modulus of $\kappa \approx (4-6)\gamma = 200 - 300\ mN/m$ [34]. Experimental measurements of the area modulus, which include stretching of the spectrin network, are higher. The area modulus is the important property

for quasi-steady cell deformation near the hemolytic limit. Bending of the layer compresses heads on one side and exposes tails on the other, giving $B \approx \frac{\kappa h^2}{24} = (2 - 3) \times 10^{-19}\ Nm$. This value is higher than experimental measurements, which may be explained by the bumpiness of the unstressed layer, which allows some bending deformation without expanding the distance between heads [34]. When an edge of the layer is exposed, such as around a pore, the hydrophilic heads form a U from one side to the other to protect the tails. This is analogous to bending a single layer around 180 degrees, giving edge tension $\Lambda \approx \frac{B}{h} = 40 - 60\ pN$, which is close to the range measured for several types of bilipid layers [35]. Flow-induced forces exerted on the layer must be larger than Λ to grow a pore. The lipid bilayer being largely fluid in nature, the shear modulus arises primarily from the spectrin network. The membrane viscosity has contributions from both the bilipid and spectrin layers. The membrane relaxation time, which is given by the ratio of the shear modulus and the membrane viscosity, is important for unsteady deformation.

Many models have been developed to simulate the structural properties of the membrane [36-38]. Hemoglobin content of the cells can be released into the blood plasma either due to complete rupture of the cell membrane or through temporary pores created in the membrane when the cell is deformed. Because the size of hemoglobin is about 5 nm, the pores must be this size or larger for hemoglobin to exit the cell [39]. Since hemolysis is fundamentally a structural failure phenomenon within the RBC membrane, taking into account the mechanical properties of the membrane and its response to different flow dynamics seems central to providing an accurate hemolysis prediction model.

1.2.2 Human RBC vs. other species

Although human blood samples are necessary for final hemolysis testing, animal samples, especially ovine, bovine and porcine, are alternatives for other purposes because of their ease of accessibility and low cost [40]. Rheological properties and sensitivity to hemolysis vary among species, which can be expected in light of different morphological properties, including diameter and excess surface area that is the larger surface area the red cell has compared to a sphere of the same volume (Table 2) [41-43]. For instance, diameter of red cells in bovine (which is a very common type of species used hemolysis experiments)

is around half of that for human, with its surface area being almost an order of magnitude smaller than the human red cell.

Further, deformability of red blood cell membrane, which is an important factor in response of red cell to different stresses as well as in mass transport across the membrane, are different among different species [44].

Table 1. 2 Typical values for size of RBC among different species

Species	Diameter (µm)	Area (µm^2)	Volume (µm^3)
Human[*]	7.82	135	95
Porcine[**]	5.81	64.5 [†]	61
Bovine[***]	5.05	20.36	43

* Fung [19]
** Namdee, et al. [45]
*** Adili, et al. [42] and Roland, et al. [46]
[†] This value was mathematically approximated based on Houchin, et al. [47]

1.2.3 Platelet activation and RBC damage

While this paper focuses on red cells, fluid stresses also cause platelet activation, both directly and indirectly. Red cells contain adenosine diphosphate (ADP) that is released during RBC deformation and damage. Once in the plasma, ADP can activate platelets [48, 49]. RBCs also play a role in platelet-initiated coagulation, which depends on hematocrit, red cell deformability and shear rate [50, 51]. Stress levels that are not considered harmful to RBCs can activate platelets and ultimately cause thrombosis [16, 52]. The formed thrombus can in turn change the flow dynamics within the cardiovascular pathways and contribute to RBC damage, for example by creating restrictions where fluid stresses are high.

Furthermore, von Willebrand factor (vWF) is a blood plasma glycoprotein that has been shown to mediate platelet adhesion, activation and aggregation under excessive fluid dynamical stresses occurring in the mechanical blood-contacting devices [53]. In fact, the plasma free hemoglobin due to mechanically induced hemolysis results in thromboembolic complications [54].

1.2.4 Index of hemolysis

To compare among investigations, it is useful to be aware that many different measures of hemolysis have been applied, all of which are based on plasma free

7

hemoglobin (*PfHb*) [55]. The traditional index of hemolysis (*TIH*) uses units of milligrams of *PfHb* released per deciliter of blood (mg/dl) and is given simply by

$$TIH = \Delta PfHb \tag{1}$$

where $\Delta PfHb$ is the increase in *PfHb* relative to pre-trial measurements. The so-called normalized index of hemolysis (*NIH*) is normalized by hematocrit (*H*), which is the dimensionless volume percentage of red cells in whole blood. NIH is expressed as

$$NIH = \Delta PfHb \times \frac{100 - Hct}{100} \tag{2}$$

NIH takes into account that the maximum amount of hemoglobin that can be released into the plasma is proportional to the concentration of red cells in the blood, but still has dimensions (mg/dl). The dimensionless modified index of hemolysis (*MIH*) is formed by normalizing NIH by the total blood hemoglobin Hb (intracellular and extracellular, in mg/dl)

$$MIH = \frac{\Delta PfHb}{Hb} \times \frac{100 - Hct}{100} \tag{3}$$

Additional red cell damage functions will be introduced in section 6.

Although a high level of *PfHb* is an indication that hemolysis has occurred, a normal level of *PfHb* does not guarantee that the RBCs are healthy. A more comprehensive index of hemolysis would characterize hemolytic damage as well as accumulation of sublytic damage. Sublytic damage may depend on threshold stresses, strains and/or exposure times that are lower than those for hemolysis. Whether an accurate model of sublytic damage is otherwise similar to that for membrane rupture remains to be validated.

1.3 Fluid stresses in blood flow

The types of fluid stress exerted on red cells includes all possible categories (Fig. 1.3). The Reynolds number in the normal cardiovascular system varies from less than 1 in small capillaries, to around 4,000 in the aorta. In the former case, viscous forces are dominant, while in the latter case, inertial forces dictate the flow dynamics [56]. Blood flow in the cardiovascular system is mostly laminar, however, disease states and cardiovascular devices can induce transitional or turbulent flow [57]. True turbulence can

occur in large arteries, and disturbances with turbulence-like characteristics have been documented at branches, in narrowed arteries, across stenotic heart valves and in regurgitant aortic valves, as well as in blood pumps and other mechanical cardiovascular devices. Turbulent stresses in Fig. 1.3 are categorized in the Reynolds average sense as viscous (due to the mean velocity) and Reynolds (due to the fluctuating convective terms), though other characterizations, particularly based on energy conservation, have been applied to blood flow. Extensional stresses may also occur at bifurcations and areas where there is a rapid change in cross section (contraction). These stresses will be defined in the following subsections.
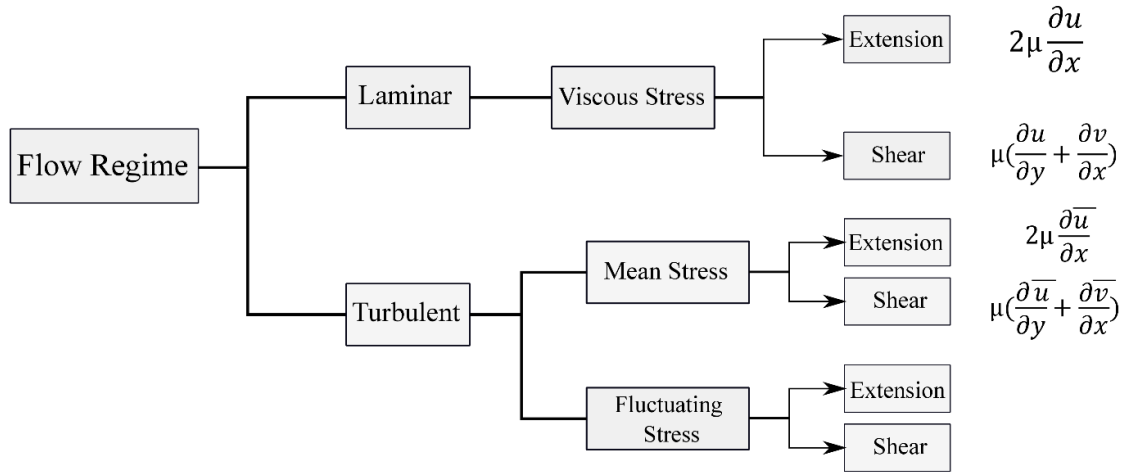
Fig. 1. 3 Different types of stresses encountered by the RBC in blood flow. 2D stresses shown (overbar denotes time average, there are several ways of quantifying fluctuating stresses)

1.3.1 Viscous stresses

The viscous stress tensor is symmetric, with the diagonal components representing normal stresses, which tend to compress or extend the fluid element, while its off-diagonal components represent the shear stress acting on the fluid element [58]

$$
\sigma = \begin{pmatrix} 2\mu\dfrac{\partial u}{\partial x} & \mu\left(\dfrac{\partial v}{\partial x}+\dfrac{\partial u}{\partial y}\right) & \mu\left(\dfrac{\partial w}{\partial x}+\dfrac{\partial u}{\partial z}\right) \\ " & 2\mu\dfrac{\partial v}{\partial y} & \mu\left(\dfrac{\partial w}{\partial y}+\dfrac{\partial v}{\partial z}\right) \\ " & " & \mu\dfrac{\partial w}{\partial z} \end{pmatrix} = \begin{pmatrix} \sigma_{xx} & \tau_{xy} & \tau_{xz} \\ \tau_{yx} & \sigma_{yy} & \tau_{yz} \\ \tau_{zx} & \tau_{zy} & \sigma_{zz} \end{pmatrix} \qquad (4)
$$

where μ is the viscosity of the fluid, u, v and w are velocities in x, y and z directions, respectively, and σ and τ are the normal and shear (viscous) stresses, respectively. The viscous stress tensor exists for both laminar and turbulent flows, with the difference that mean values are used for the turbulent flow regime.

1.3.1.1 Principal stresses

Like stresses in solid material, the viscous fluid stress tensor can be transformed to its principal orientations. The transformed principal stresses represent the viscous momentum flux due to velocity gradients in the directions of the principal axes. The reason for devoting the mathematical effort is the hope that, following the example of solid mechanics, these fluid principal stress values may correlate with red cell membrane stresses and membrane failure. Considering a two-dimensional viscous stress tensor, whose values are based on the measurement coordinates x and y:

$$\sigma = \begin{pmatrix} \sigma_{xx} & \tau_{xy} \\ \tau_{yx} & \sigma_{yy} \end{pmatrix} \tag{5}$$

by rotating the measurement axes by the angle

$$\theta_P = \frac{1}{2} tan^{-1} \left(\frac{2\tau_{xy}}{\sigma_{xx} - \sigma_{yy}} \right) \tag{6}$$

one can derive the principal viscous normal stresses using the relations already known from solid mechanics [59]

$$\sigma_{max,1,2} = \frac{\sigma_{xx} + \sigma_{yy}}{2} \pm \sqrt{\left[\frac{\sigma_{xx} - \sigma_{yy}}{2} \right]^2 + \tau_{xy}^2} \tag{7}$$

The last term on the right side of the above equation is the principal viscous shear stress

$$\tau_{max} = \sqrt{\left[\frac{\sigma_{xx} - \sigma_{yy}}{2} \right]^2 + \tau_{xy}^2} \tag{8}$$

the orientation of which is perpendicular to that of principal viscous normal stress.

For a 3-D flow with stress tensor as shown in Eq. (4), the three principal stresses can be expressed as

$$\sigma_1 = \frac{I_1}{3} + \frac{2}{3}\left(\sqrt{I_1^2 + 3I_2}\right)\cos\phi \tag{9}$$

$$\sigma_2 = \frac{I_1}{3} + \frac{2}{3}\left(\sqrt{I_1^2 - 3I_2}\right)\cos\left(\phi - \frac{2}{3}\pi\right) \tag{10}$$

$$\sigma_3 = \frac{I_1}{3} + \frac{2}{3}\left(\sqrt{I_1^2 - 3I_2}\right)\cos\left(\phi - \frac{4}{3}\pi\right) \tag{11}$$

where

$$\phi = \frac{1}{3}\cos^{-1}\left(\frac{2I_1^3 - 9I_1I_2 + 27I_3}{2(I_1^2 - 3I_2)^{\frac{3}{2}}}\right) \tag{12}$$

and the stress invariants are

$$I_1 = \sigma_{xx} + \sigma_{yy} + \sigma_{zz} \tag{13}$$

$$I_2 = \sigma_{xx}\sigma_{yy} + \sigma_{xx}\sigma_{zz} + \sigma_{yy}\sigma_{zz} - \tau_{xy}^2 - \tau_{xz}^2 - \tau_{yz}^2 \tag{14}$$

$$I_3 = \sigma_{xx}\sigma_{yy}\sigma_{zz} - \sigma_{xx}\tau_{yz}^2 - \sigma_{yy}\tau_{xz}^2 - \sigma_{zz}\tau_{xy}^2 + 2\tau_{xy}\tau_{xz}\tau_{yz} \tag{15}$$

The three direction cosines of each principal stress are, then, obtained by solving the following system of equations

$$(\sigma_{xx} - \sigma_i)n_1 + \tau_{xy}n_2 + \tau_{xz}n_3 = 0$$
$$\tau_{yx}n_1 + (\sigma_{yy} - \sigma_i)n_2 + \tau_{yz}n_3 = 0 \tag{16}$$
$$\tau_{zx}n_1 + \tau_{zy}n_2 + (\sigma_{zz} - \sigma_i)n_3 = 0$$

where σ_i is the principal stress and n_1, n_2 and n_3 are the direction cosines of each corresponding principal stress.

The usefulness of the principal stress transformation to characterize fluid stresses for hemolysis prediction is uncertain, and may depend on the type of flow exerted on the cells. For extensional flow, cells are deformed into approximately prolate ellipsoids along the first principal axis, and for compressive flow are deformed into oblate ellipsoids. But for high shear flow, cells are more or less aligned with the flow direction, rather than the first principal axis, which is 45 degrees to the flow. These differences in cell response in simple flows could mean that hemolysis prediction in complex flows may require additional information beyond the principal stresses.

1.3.1.2 Resultant scalar stress

An even more drastic simplification of the stress state has been applied. Many authors have used a resultant scalar stress, similar to the von Mises stress in solid mechanics, to represent the combined state of stress. In particular, the following scalar stress (though with some inconsistency, see [60]) has often been used in the popular power-law hemolysis prediction model, which was developed from data for shear stress only [17, 61, 62].

$$\sigma = \frac{1}{\sqrt{3}}\left(\sqrt{\sigma_{xx}^2 + \sigma_{yy}^2 + \sigma_{zz}^2 - \left(\sigma_{xx}\sigma_{yy} + \sigma_{xx}\sigma_{zz} + \sigma_{yy}\sigma_{zz}\right) + 3\left(\tau_{xy}^2 + \tau_{xz}^2 + \tau_{yz}^2\right)}\right) \qquad (17)$$

This resultant scalar stress gives normal stresses one third the weight of shear stresses. The appropriateness of this weighting remains to be validated.

1.3.2 Turbulent stresses

1.3.2.1 Reynolds stress

The Reynolds-averaged Navier-Stokes (RANS) equation is the time-averaged equation of motion for a fluid flow, which assumes that each velocity and the pressure in a turbulent flow may be decomposed into mean and fluctuating components. After applying the Reynolds decomposition, the Navier-Stokes equations for a compressible fluid can be written in tensor form as

$$\rho \frac{D\bar{u}_\iota}{Dt} = -\frac{\partial \bar{P}}{\partial x_i} + \frac{\partial}{\partial x_j}\underbrace{\left(\mu \frac{\partial \bar{u}_\iota}{\partial x_j} - \rho \overline{u'_\iota u'_J}\right)}_{Total\ stress} \tag{18}$$

where $\frac{D}{Dt}$ is the material derivative, ρ is the fluid density, $\bar{P}$ is time-averaged hydrostatic pressure acting on the fluid element, $\bar{\boldsymbol{u}}$ is the time-averaged fluid velocity and $\boldsymbol{u}'$ is the velocity fluctuation. The first term in the parenthesis is the (time-averaged) viscous stress tensor, while the second term is the well-known Reynolds stress tensor, due to the velocity fluctuations. The total stress can be written as

$$\boldsymbol{\sigma}_t = \bar{\boldsymbol{\sigma}} + \boldsymbol{\sigma}' \tag{19}$$

where $\bar{\sigma}$ and σ' are viscous and Reynolds stresses, respectively. The Reynolds stress tensor has the following matrix form

$$\boldsymbol{\sigma}' = -\rho \begin{pmatrix} \overline{u'^2} & \overline{u'v'} & \overline{u'w'} \\ " & \overline{v'^2} & \overline{v'w'} \\ " & " & \overline{w'^2} \end{pmatrix} \tag{20}$$

Note that both diagonal (normal) and off-diagonal (shear) components are included in Eq. (20). It has been shown that, under some flow conditions, normal components of Reynolds stress may become greater than the Reynolds shear stress at some particular locations in the flow cross section [63-66]. For example, the maximum Reynolds shear stress immediately downstream of an artificial aortic valve was estimated to be half of the maximum Reynolds normal stress [67, 68]. However, it still remains unresolved how the ratio of Reynolds normal and shear stresses affects blood damage. To answer this question, experiments must be carried out and, subsequently, mathematical models can be developed to capture the detailed response of RBC membrane to the different forms of Reynolds stresses.

Similar to the viscous stress tensor, the Reynolds stress at any point within the flow geometry is a second order tensor and is not invariant to coordinate transformation. The experimentally measured Reynolds stresses are usually reported based on the measurement axes, which may be misleading [69, 70]. It may be useful to determine the eigenvalues of the Reynolds stress tensor (i.e. principal stresses) at any point of measurement, which

13

quantify the maximum Reynolds normal and shear stresses and their directions [65, 71, 72]. Considering only a 2-dimensional flow field, the Reynolds stress can be written as

$$\boldsymbol{\sigma'} = -\rho \begin{pmatrix} \overline{u'^2} & \overline{u'v'} \\ \overline{u'v'} & \overline{v'^2} \end{pmatrix} \tag{21}$$

Then, the maximum Reynolds normal and shear stresses are [59]

$$\boldsymbol{\sigma'}_{max,1,2} = \frac{\rho\overline{u'^2} + \rho\overline{v'^2}}{2} \pm \underbrace{\sqrt{\left[\frac{\rho\overline{u'^2} - \rho\overline{v'^2}}{2}\right]^2 + (\rho\overline{u'v'})^2}}_{\tau'_{max}} \tag{22}$$

$$\tau'_{max} = \sqrt{\left[\frac{\rho\overline{u'^2} - \rho\overline{v'^2}}{2}\right]^2 + (\rho\overline{u'v'})^2} \tag{23}$$

and the angle that the measurement coordinate must be rotated to give the maximum Reynolds normal stresses is

$$\theta'_P = \frac{1}{2} tan^{-1}\left(\frac{2\rho\overline{u'v'}}{\rho\overline{u'^2} - \rho\overline{v'^2}}\right) \tag{24}$$

The same expressions for 3-D principal stresses as discussed for the viscous stress tensor (Eqs. (9)-(11)) can also be developed for the turbulent stress tensor.

Therefore, the representative scalar stress including both viscous and Reynolds stresses may be written as [73]

$$\sigma_t = \frac{1}{\sqrt{3}}\left(\sqrt{\sigma_{xx,t}^2 + \sigma_{yy,t}^2 + \sigma_{zz,t}^2 - (\sigma_{xx,t}\sigma_{yy,t} + \sigma_{xx,t}\sigma_{zz,t} + \sigma_{yy,t}\sigma_{zz,t}) + 3(\tau_{xy,t}^2 + \tau_{xz,t}^2 + \tau_{yz,t}^2)}\right) \tag{25}$$

where Eq. (25) is the same as Eq. (17), except that $\sigma_{xx,t}$ and $\tau_{xy,t}$ are the total normal and total shear stresses, respectively, which comprise both viscous and Reynolds components (Eq. (19)).

1.3.2.2 Kolmogorov and Taylor scales

Inherent to turbulence is the presence of swirling eddies of different time and length scales. During the energy cascade, energy is transferred from larger eddies, with higher kinetic (inertial) energy, to smaller eddies. This continues to eddies of the smallest (Kolmogorov) size, in which viscous dissipation takes place. The Kolmogorov scale, η_k, is given by

$$\eta_k = \upsilon^3/\varepsilon \tag{26}$$

where ε is the kinetic energy dissipation rate and υ is kinematic viscosity. This scale was developed for a continuum fluid, thus its applicability to the flow of particles (red cells) with size that is significant compared to η_k has been questioned. With arguments relating the energy dissipation rate to energy supply rate, which must be equal in steady state, the Kolmogorov scale depends on the Reynolds number

$$\frac{\eta_k}{L} = Re^{-3/4} \tag{27}$$

where L is the large scale of the flow regime (such as the diameter of the artery). Therefore, η_k decreases with an increase in velocity in a given flow geometry. For instance, η_k has been reported to vary from 20 to 70 µm in a bi-leaflet mechanical heart valve (BMHV) [70]. It has been proposed that only eddies with length scales similar to that of RBC are capable of damaging the cell [74].

An alternative scale that to our knowledge has yet to be applied to blood flow is the Taylor microscale

$$\lambda_t^2 = \frac{u'^2}{\left(\dfrac{\partial u'}{\partial x}\right)^2} \tag{28}$$

where λ_t is a measure of the distance over which strain energy is dissipated. Because cell membrane strain, which is a precursor to membrane failure, has a logical connection to surrounding fluid strain, λ_t may be as relevant to hemolysis as η_k. In particular, λ_t equal

to or smaller than the red cell size means that strain energy may be focused and dissipated within a single cell, which might promote membrane damage. With similar assumptions in continuum flow, the Taylor microscale can also be related to the Reynolds number

$$\frac{\lambda_t}{L} = \sqrt{10}\ Re^{-1/2} \tag{29}$$

Given the clear mathematical differences between η_k and λ_t (a different coefficient and different exponent), the relationships of the two to hemolysis could be compared in experiments quantifying both turbulent velocity fluctuations and *PfHb*.

1.3.2.3 Viscous energy dissipation rate

The dissipation rate of kinetic energy, which represents by the energy flux converted into heat by viscous forces in both laminar and turbulent flows, has also been suggested as a quantity to scale blood damage [75, 76]. The instantaneous dissipation rate for a 3-D flow field is [77]

$$\varepsilon = \upsilon \left\{ \begin{array}{l} \left[\frac{\partial u}{\partial x}\right]^2 + \left[\frac{\partial u}{\partial y}\right]^2 + \left[\frac{\partial u}{\partial z}\right]^2 \\ + \left[\frac{\partial v}{\partial x}\right]^2 + \left[\frac{\partial v}{\partial y}\right]^2 + \left[\frac{\partial v}{\partial z}\right]^2 \\ + \left[\frac{\partial w}{\partial x}\right]^2 + \left[\frac{\partial w}{\partial y}\right]^2 + \left[\frac{\partial w}{\partial z}\right]^2 \end{array} \right\} + \upsilon \left\{ \begin{array}{l} \left[\frac{\partial u}{\partial x}\right]^2 + \left[\frac{\partial u}{\partial y}\frac{\partial v}{\partial x}\right] + \left[\frac{\partial u}{\partial z}\frac{\partial w}{\partial x}\right] \\ + \left[\frac{\partial u}{\partial y}\frac{\partial v}{\partial x}\right] + \left[\frac{\partial v}{\partial y}\right]^2 + \left[\frac{\partial v}{\partial z}\frac{\partial w}{\partial y}\right] \\ + \left[\frac{\partial u}{\partial z}\frac{\partial w}{\partial x}\right] + \left[\frac{\partial v}{\partial z}\frac{\partial w}{\partial y}\right] + \left[\frac{\partial w}{\partial z}\right]^2 \end{array} \right\} \tag{30}$$

Note that for the dissipation rate of turbulent fluctuations (ε'), the velocities in Eq. (30) must be replaced by velocity fluctuations. Furthermore, if we assume local homogeneity of the turbulent flow, the second bracket in Eq. (30) would be zero [78].

Equivalently, Eq. (30) can be re-written in terms of the normal and shear stresses as

$$\varepsilon = \frac{1}{\rho\mu}\left[\frac{1}{2}\left(\sigma_{xx}{}^2 + \sigma_{yy}{}^2 + \sigma_{zz}{}^2\right) + \left(\tau_{xy}{}^2 + \tau_{xz}{}^2 + \tau_{yz}{}^2\right)\right] \tag{31}$$

However, measuring all the components in Eq. (30) in an experiment is not an easy task. Therefore, some simplifications are usually adopted. For instance, based on

16

Kolmogorov's theory of local isotropy of small-scale structures in a turbulent flow, the mean viscous dissipation rate an isotropic homogenous turbulence can be simplified as [79]

$$\varepsilon' = 15 \, v \, \overline{\left(\frac{\partial u'}{\partial x}\right)^2} \tag{32}$$

Additionally, a useful approximation of Eq. (32) is based on [80]

$$\varepsilon' = 15 \, v \, \frac{u'^2_{rms}}{\lambda_t^2} \tag{33}$$

where u'_{rms} is the root mean square of the velocity fluctuations.

1.4 Red cell motion

1.4.1 Motion in viscous shear flow

Previous investigations of red cell behavior have concentrated largely on shear stress. This historic emphasis on shear stress led to considerable literature on bulk and single-cell flow of RBCs in shear flows [81-83]. Based on the level of the applied shear, RBCs exhibit several characteristic motions within the plasma. Under very small shear rate (< 1 s^{-1}), isolated RBCs maintain a biconcave disk shape and are observed to tumble (Fig. 1.4a). On the other hand, concentrated RBCs tend to aggregate, so long as the shear is not too large (< 50 s^{-1}), into rod-shaped structures called rouleaux, which dramatically increase the apparent viscosity of the red cell suspension. These aggregates are dynamically reversible such that the rouleaux break apart when shear increases, and reform when shear decreases.

It has been shown that among other factors, the ratio of internal (cytoplasmic) viscosity to external viscosity has an important effect on RBC deformation in shear flow [84]. As the shear rate increases, RBCs in low viscosity suspending media continue to tumble with increasing deformation into irregular shapes [81, 85]. At moderate shear rates, the cells are found to undergo a swinging motion with periodic change of inclination and shape deformation (Fig. 1.4b), with superimposed tank-treading motion (Fig. 1.4c). In highly viscous suspending media, cells take on an elongated shape with their long axis

more or less aligned with the flow direction, but with their downstream end angled toward higher velocity, and the membrane rotating about the cytoplasm, in a motion commonly referred to as tank-treading [86] (Fig. 1.4c). With further increase in the shear rate, the RBCs continue to elongate [87, 88]. This area-preserving elongation is reversible, i.e., RBCs demonstrate shape memory (up to a certain areal strain) [81, 89].

As introduced in section 1.2.1, beyond a threshold elongation, the RBC membrane area must increase to contain a constant volume of cytoplasm. Because the membrane is much more resistant to area dilation than to shear deformation, substantial increases in flow-induced stresses are required for this to occur. As the membrane area is stretched, the potential increases for leakage of the cell contents, for permanent damage to the membrane structure and for catastrophic membrane rupture. In some cases, the RBCs biological function is compromised, which consequently leads to the premature need to remove the cell from the circulation. This places an added demand on the erythropoietic system that it may or may not be capable of fulfilling.
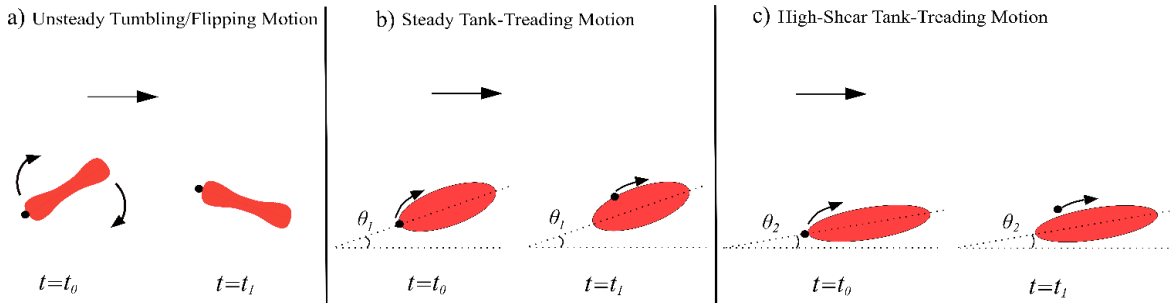
Fig. 1. 4 Cell motion in: (a) low shear stress and low viscosity medium, (b) moderate shear stress and high viscosity and c) high shear stress and high viscosity. The black dot indicates circulation of the membrane in the tank-treading case

Vesicles are composed of a viscous liquid encapsulated by a lipid bilayer membrane, which have been extensively used in both experimental studies and simulations as a simplified model to better understand RBC motion [90]. Their behavior is different from that of RBCs mainly due to lack of a spectrin network in vesicles, so their shape in the flow is mainly governed by the bending rigidity of their membrane [91]. Based on numerical studies of vesicles, it has been shown that by decreasing the ratio of intracellular to extracellular viscosity in a uniform shear flow, three modes of motion similar to that of RBCs occur, starting in low shear with unsteady tumbling, changing in moderate shear to

swinging, trembling and/or vacillating-breathing and ending in high shear with steady tank-treading [92]. Lacking the shear elasticity provided by the spectrin network, vesicles tank-tread when the shear is weak and the ratio of internal viscosity to external viscosity is near unity, whereas RBCs tumble under the same condition. This is because in the case of RBCs, the weak shear cannot overcome the cytoskeletal stiffness. However, when the shear is stronger, the shear stress can overcome the resistance to network deformation and tank-treading occurs [93].

In the more complex dynamics of Poiseuille flow that has a non-uniform shear rate [94-96], particles migrate away from the walls and towards the centerline due to the wall effect and the curvature in the velocity profile. Numerical analysis has predicted that vesicles in a non-inertial Poiseuille flow in a narrow capillary may develop three shapes: bullet-like, parachute-like and slipper-like, depending on the initial conditions of cell orientation in the flow, as well as the flow conditions and properties of the membrane (Fig. 1.5) [94, 97]. Experiments and simulations show that when the ratio of internal to external viscosities is about 5, the transition from parachute mode to slipper mode occurs with increasing shear rate [93]. The vesicle may also assume either parachute or bullet-like shapes depending on the confinement of the flow and the flow rate [25].
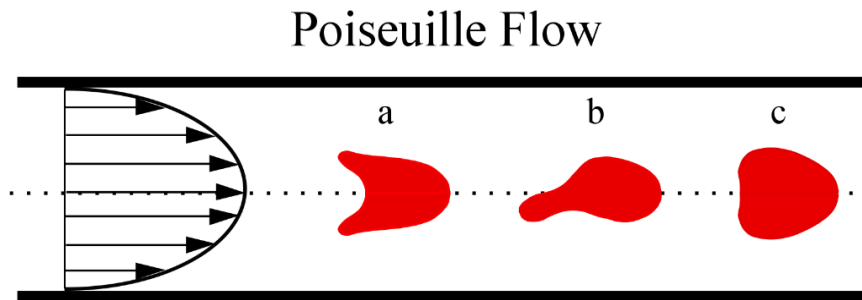
Fig. 1. 5 Different modes of RBC motion in Poiseuille capillary flow; (a) parachute mode, (b) slipper mode, and (c) bullet mode

1.4.2 Motion in viscous extensional flow

While shear stress has long been the focus for damage to RBCs, the extensional component of viscous stress has also been noted to play a significant role in inducing cell damage [98]. RBCs are initially highly deformable under extensional flow conditions, however as the extensional stress increases, deformation reaches a plateau that corresponds

to a shape beyond which areal strain of the membrane is required for further elongation [99, 100].

RBCs may experience extensional (elongational) stresses in contractions entering blood vessels and/or blood contacting devices [101]. Extension occurs when different parts of an RBC are subjected to different velocity magnitudes, for example, when there is a spatial acceleration in the flow due to changes in the cross-sectional area (converging flow) where the leading tip of the RBC is surrounded by higher velocity than that surrounding the trailing tip. Similarly, the RBC may also be oriented in a shear velocity profile in such a way that the leading and trailing ends experience different velocity, resulting in an extensional tension in the cell membrane (Fig. 1.6). In fact, a combination of shear and extensional stresses may often act on the cell. A cell in a simple shear flow may rotate (i.e., tumble or tank-tread), thereby partially mitigating the tension caused by shear stress. On the other hand, during a uniaxial extensional flow, the cell is stretched without rotation or other tension-mitigating mechanisms. This sustained extensional stress may stretch cells more readily and be more damaging to the membrane than shear. For this reason, it is important to also study the behavior of the RBCs within extensional flow.
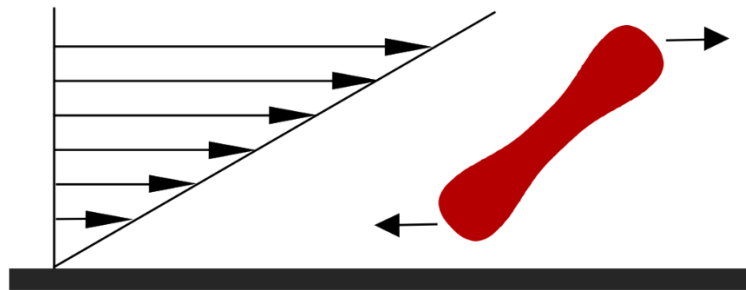
Fig. 1. 6 Extensional stress applied to the RBC in a steep velocity gradient

Researchers have used different devices, including opposed jets (Fig. 1.7) and hyperbolic micro-contractions (Fig. 1.8), to evaluate cell deformability and cell membrane behavior within extensional flow [99, 102-108]. One of the earliest studies on the behavior of RBCs in extensional flow used two concentrically opposed suction jets that created a stagnation point at which symmetrical extensional stresses were exerted on the cell (Fig. 1.7) [102]. At a bulk stress of 5.2 dyne/cm^2 in the high-viscosity suspending medium, the

20

ratio of the major axis to minor axis of the cell was observed to reach a value of 4.8, which McGraw claimed to be the maximum area-preserving threshold.
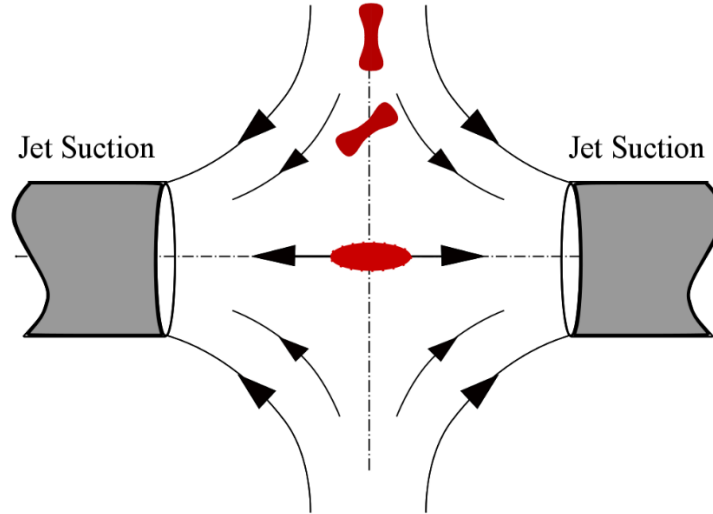
Fig. 1. 7 Extensional stress applied to the RBC by suction jets

The hyperbolic micro-contraction is popular because it provides a nearly constant strain rate at the centerline of the channel, and is capable of producing a quasi-homogenous extensional flow condition [108-110]. Within the stress range of 1-200 dyne/cm^2 in such a channel, extensional stress was shown to produce more cell deformation than shear stress of the same level [101].
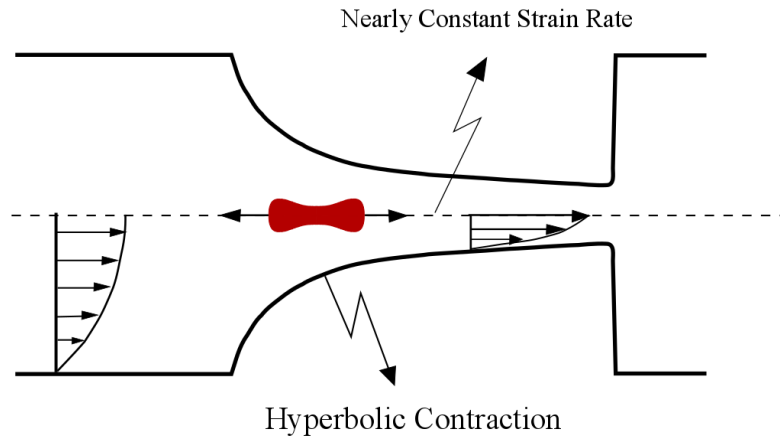
Fig. 1. 8 Extensional stress applied to the cell by hyperbolic micro-channel contraction

1.4.3 Motion in turbulent flow

The only experimental study of the response of red cells flowing in turbulent flow is that of Sutera and Mehrjardi [111]. RBCs exposed to turbulent shear stress ranging from 100 to 2500 dyne/cm^2, were chemically "frozen" by glutaraldehyde to observe deformation and fragmentation of the cells. Based on their observations, RBCs began to lose their bi-concave shape at 500 dyne/cm^2, with the first signs of fragmentation occurring at 2500 dyne/cm^2. They also found that by increasing the turbulent shear stress, the cells first underwent a recoverable deformation and then deformed irreversibly until they assumed a dumbbell-like shape, after which the cell finally ruptured into two crenated cells. Due to the method of fixing and subsequent image acquisition, cell orientation with respect to the flow and temporal history of motion could not be determined. Shakeri, et al. [64] also imaged red cell motions in turbulent flow up to Reynolds number of 3000 through a square channel of 0.8 mm×0.8 mm. It was concluded that Reynolds stress of up to 3000 was not sufficient to significantly deform cells in turbulent flow. To the best of the authors' knowledge, there exists no other experimental studies revealing the behavior of red cells in turbulent flow.

1.5 Previous hemolysis measurements in controlled flows

Threshold values for the initiation of hemolysis have been demonstrated across a range of stresses, flow regimes (laminar and turbulent), exposure times, experimental set-

ups, hematocrit, species and suspending medium viscosities. Early studies included interaction of red cells with a turbulent free jet [112], as well as locally laminar flows generated around an oscillating wire [113] and a pulsating gas bubble [114] (Table 3). Later, concentric cylinders, cone-and-plate, Couette flow and capillary flow were commonly used to study the effects of shear stress and exposure time on hemolysis. Each of these devices is associated with its own advantages, as well as uncertainties, limitations and inaccuracies [115]. For example, Couette flow can generate secondary flows (Taylor vortices) at high shear rates and, thus, is typically used for low shear rates [115]. However, Leverett et al. [116] used Couette flow to investigate the secondary flow effects that in combination with primary shear stress, might cause hemolysis.

Results initially seemed inconsistent, because studies reported significantly different threshold stress. Furthermore, in a study that used capillary tubes of different lengths, and thus different residence time, incipient blood damage was observed at a minimum wall shear stress of about 40-50 dyne/cm^2 for residence time of around 70 s [117]. The inconsistencies might be partly due to different experimental conditions, including blood from different species. However, the proposed theory that appeared to resolve these inconsistencies is that hemolysis is caused by surface and bulk-flow effects. In particular, at high shear stress, cell membrane rupture occurs mainly in the bulk flow, whereas under low shear stress, hemolysis is dominated by surface properties [111, 118].

1.5.1 Hemolysis threshold in laminar viscous shear flow

It is widely accepted that lysis of RBCs depends on shear stress and exposure time. For duration of less than 1 µs, RBCs can withstand shear stress of about 10^5 dyne/cm^2 [119]. When the exposure time is about 1 s, the threshold for laminar flow has been reported to be 20,000 dyne/cm^2. For exposure time in range of minutes (≥ 100 s), the threshold in laminar flow has been suggested as 1500 dyne/cm^2 [119].

Many authors have already attempted to estimate a threshold value of laminar shear stress for the onset of red cell damage using different apparatus (Table 3).

Table 1. 3 Experimental studies on threshold level of RBC hemolysis in laminar flow

| Reference | Blood type properties | | | Experimental set-up | Exposure Time (s) | Stress Threshold (dyne/cm^2) |
	Species	Hematocrit (%)	Viscosity (cP)			
Nevaril, et al. [120]	Human	-	-	Concentric Cylinder	120	3,000
Forstrom [112]	Goat	0.5	4.2	Jet Nozzle	-	42,000 (wall shear stress)
Rooney [114][*]	Canine/Human	Small Fraction	31	Pulsating Gas Bubble	10^{-3}	4,500
Williams, et al. [113][*]	Canine/Human	Small Fraction	31	Oscillating Wire	10^{-4}	5,600
Leverett, et al. [116]	Human	-	3.63	Concentric Cylinder	120	1,500
Paul, et al. [115]	Porcine	41	5	Concentric Cylinder	0.62	4,000
Lee, et al. [121]	Human	-	31	Concentric Cylinder	120	300, onset of cell membrane damage
Kameneva, et al. [122][**]	Bovine	24	6.3	Capillary Tube	1^{***}	3,000 (wall shear stress)
Zhao, et al. [123]	Bovine	5	30	Microfluidic Channel	2×10^{-3}	51,700
Boehning, et al. [124]	Porcine	40	5	Concentric Cylinder	0.873	6,000

* For the oscillating wires and bubbles the exposure time was taken to be the boundary layer length divided by the product of the maximum shear rate and the boundary layer thickness.
** Increase of 20mg/dl in plasma Hb was considered as the threshold value for Kameneva, et al. [122] study.
*** This is the cumulative exposure time estimated by Ozturk, et al. [125]

1.5.2 Hemolysis in viscous extensional flow

Shock waves were used to create inertia-based extensional flow to study the effect of membrane tension on membrane poration/lysis. It has been found that a momentary extensional surface tension (force per meter) of around 64 mN/m for exposure time of 3 ns created by the shock wave lithotripsy caused an areal strain of approximately 10^{-5} in the membrane. Although this level of strain is less than the critical level (order of magnitude of 10^{-2} [126]), it was sufficient to produce energetically reversible pores in the RBC membrane [3].

The importance of extensional stress in causing cell lysis was shown in a computational fluid dynamics analysis of laminar flow through a capillary tube with a contraction [98]. The investigators used the geometry and hemolysis threshold value from Keshaviah [127] to compare the effect of shear and extensional stresses on cell damage. Results showed that the shear stress as well as the gradient of the shear stress anywhere in the flow domain failed to reach the threshold value consistent with the level of hemolysis reported by Keshaviah [127], but the extensional stress at the entrance region reached or exceeded the stress threshold for hemolysis of 30,000 dyne/cm^2 for duration of the order of microseconds.

1.5.3 Hemolysis in turbulent flow

Although under normal conditions blood flow within most of the circulation is laminar, local turbulence that may occur *in vivo* (e.g., in the ascending aorta [128]) and in adverse flow conditions in medical devices has been suggested as a contributing factor in RBC trauma [57, 129]. Therefore, many studies have attempted to determine a threshold for RBC damage in turbulent blood flow (Table 4). One of the earliest studies on the effect of turbulence found the threshold of viscous stress for RBC lysis in free turbulent jets to be nearly 40,000 dyne/cm^2 for small exposure time (10^{-6} s) [112].

In an important, later study, RBCs exposed in Couette flow to 4 minutes of turbulent viscous shear stresses varying from 100 to 4,500 dyne/cm^2 were fixed by glutaraldehyde to observe cell response [111]. Cells fragmented in the bulk flow starting at 2,500 dyne/cm^2. The cell fragments had continuous membranes without holes. Cells stressed at 2,000 dyne/cm^2 were deformed into elongated spindle-like shapes, but if left unfixed, largely recovered their original shape after the applied stress was discontinued.

In an attempt to overcome weaknesses of previous experiments, Sallam and Hwang [129] designed a new set-up to fully survey the velocity field within a free submerged axisymmetric turbulent jet, and used laser Doppler anemometer to quantify the turbulence intensities in the flow field [129]. They used an aspirator to collect human blood samples for hemoglobin measurements at locations in the jet where the streamwise mean velocity, turbulence intensities, and Reynolds shear stresses were experimentally pre-determined. It was concluded that Reynolds shear stress of more than 4,000 dyne/cm^2 for duration of 10^{-5} s is needed to cause RBC lysis. To provide a better defined shear field and to compare the effect of laminar and turbulent flows of the same flow rate and wall shear stress on hemolysis rate, Kameneva, et al. [122] used a simple capillary geometry to demonstrate that turbulent stresses contribute strongly to blood trauma, generating exponential increases in hemolysis as Reynolds number increased. They postulated that local stretching/deformation of RBCs due to interaction with small scale turbulent eddies and/or fatigue loading due to cyclical stretching of cells by the fluctuating velocity field may cause the increased hemolysis. Flow through an orifice has also been used to investigate the effect of Reynolds shear stress on hemolysis [130]. Reynolds shear stress at the edge of the orifice

were found to be several hundred times greater than that of turbulent viscous shear stress and should not be neglected when predicting hemolysis for devices containing geometries with flow similar to an orifice. The hemolytic threshold for Reynolds shear stress in the orifice was reported to be 18,000 dyne/cm^{-2} with a corresponding exposure time of 10^{-6}-10^{-5} s.

Based on a theoretical analysis of the experimental values of Reynolds shear stress reported by Sallam and Hwang [129], Grigioni, et al. [131] stated that the threshold values in Sallam and Hwang's paper could be underestimated because they did not consider the peak shear stress through calculation of principal axes and principal stress. Using a relationship between velocity fluctuations in measurement axis and the principal axes as mentioned in Barbaro, et al. [132], they established a correlation between values of Reynolds shear stress measured by Sallam and Hwang [129] with the actual measurable values, and found that the maximum measurable value for Reynolds shear stress in Sallam and Hwang [129] should be 6,000 dyne/cm^2 (instead of 4,000 6,000 dyne/cm^2 reported by. Reynolds shear stress thresholds for initial hemolysis have more recently been reported to be 5,170 dyne/cm^2 for exposure time of 10^{-5} s in porcine blood [133] and 30,000 dyne/cm^2 in bovine blood [134].

In contrast to studies that regard the Reynolds stress as the main mechanism of turbulence-mediated hemolysis [135], others have suggested that turbulent viscous stress at scales similar to or smaller than the RBC size is more responsible for hemolysis [70, 133, 136]. To explore this question, Yen, et al. [133] used Particle Image Velocimetry (PIV) to compare the two terms in turbulent jet flow. At each point, PIV measurements were used to calculate the Reynolds shear stress, and to estimate the energy dissipation rate, from which the viscous shear stress was obtained. Then, they conducted experimental tests on fresh porcine red cells to experimentally calculate the incremental increase in hemolysis between two adjacent points in the flow field using the two-point sampling technique of Sallam and Hwang [129]. They finally concluded that the threshold value for incipient hemolysis due to turbulent viscous shear stress is one order of magnitude smaller than that due to Reynolds shear stress (600 dyne/cm^2 for the turbulent viscous shear stress vs. 5,170 dyne/cm^2 for Reynolds shear stress).

Additional comparisons between Reynolds and viscous stresses, both shear and extensional, are needed to test the universality of this conclusion. Identifying the conditions under which one predominates over the other may be important in understanding hemolysis in particular devices [72].

As an alternative to turbulent viscous and Reynolds stress, turbulent energy dissipation has been suggested as the more appropriate and physically meaningful criteria for RBC damage in turbulent flow [75, 136, 137].

Table 1. 4 Experimental studies on threshold level of RBC hemolysis in turbulent flow

| Reference | Blood type properties | | | Experimental Setup | Exposure Time (s) | Shear Stress (dyne/cm^2) | |
		Hematocrit (%)	Viscosity (cP)			Reynolds Stress	Viscous Stress
Blackshear, et al. [138]	Dog	-	-	Tube Flow	-	-	30,000
Forstrom [112]*	Human	Normal Whole Blood	4.2	Turbulent Jet	3×10^{-6}	-	50,000
Sutera and Mehrjardi [111]	Human	0.2	-	Concentric Cylinder	240	-	2,500
Sallam and Hwang [129]	-	-	-	Free Turbulent Jet	10^{-5}	4,000	-
Tamagawa, et al. [130]	Bovine	-	-	Orifice Flow	10^{-5}	18,000	-
Lu, et al. [74]	-	-	-	Turbulent Jet	10^{-3}	8,000	-
Kameneva, et al. [122]**	Bovine	24	2	Tube Flow	1^{***}	2,000	
Yen, et al. [133]	Porcine	-	-	Turbulent Jet	1.2×10^{-5}	3,400	600
Jhun, et al. [134]	Bovine			Turbulent Jet		30,000	

* For the jet experiments the exposure time was based on the time required for the stress on a cell to decay by one order of magnitude.
** Increase of 20mg/dl in plasma Hb was considered as the threshold value for Kameneva, et al. [122] study.
*** This is the cumulative exposure time estimated by Ozturk, et al. [125]

1.5.4 Models of the hemolysis threshold

One of the earliest attempts to provide a predictive model for mechanical hemolysis was a simple equation [138] involving threshold shear stress and exposure time

$$\tau_t \, E^{0.5} = const \tag{34}$$

where τ_t is a threshold shear stress (scalar). An additional term – a stress below which no hemolysis occurs – was added by Sharp and Mohammad [52]

$$(\tau_t - \tau_0) \, E^{0.5} = const \tag{35}$$

These equations do not quantify hemolysis, rather they only describe the threshold at which hemolysis begins. The threshold of Eq. (35) is compared to experimental results as well as to threshold values predicted by some of the most common hemolysis models in Fig. 1.9, i.e. the Heuser and Opitz [139], the Giersiepen, et al. [140], and the Richardson [141] models, which are presented in section 6, used 1% hemolysis to characterize the threshold. As can be seen in Fig. 1.9, viscous stress in turbulent flow and extensional stress in laminar flow have received little attention. It is also evident that the hemolysis prediction models could be improved with a fluid stress threshold below which no hemolysis occurs, like that of the Sharp and Mohammad [52] threshold model.
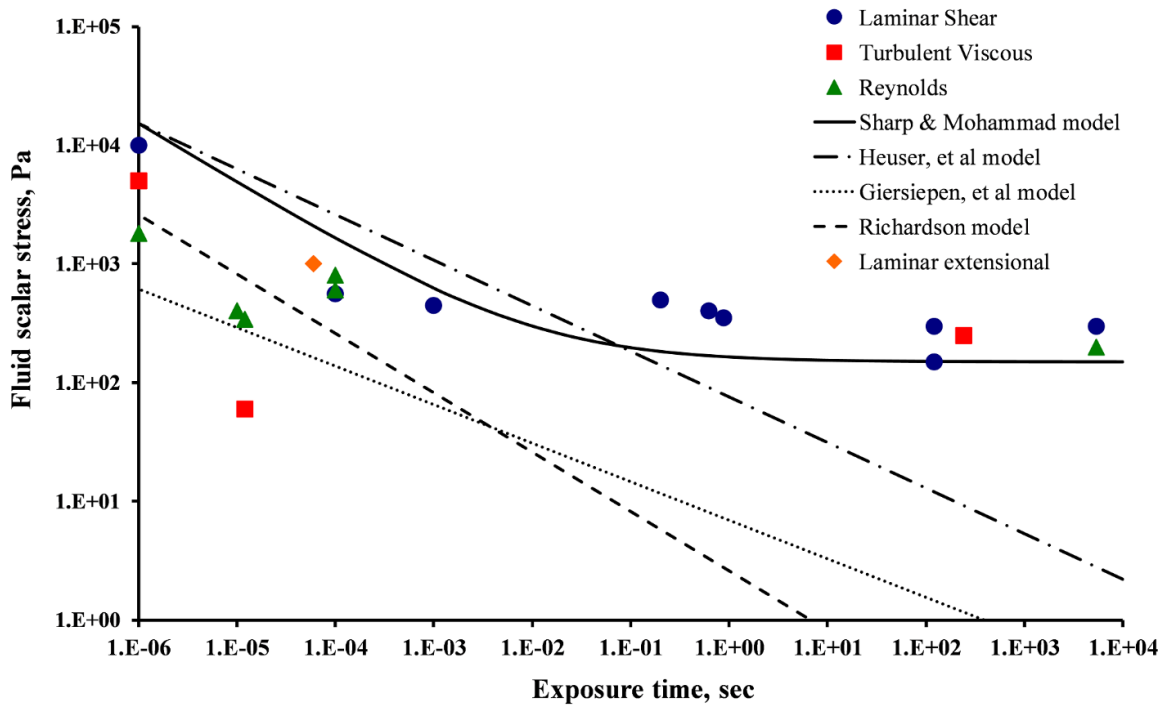
Fig. 1. 9 Threshold values reported by experimental studies and theoretical hemolysis prediction models

1.6 Hemolysis prediction models

Hemolysis is challenging to model, because it is a complex, multi-factorial process that occurs at different temporal and spatial scales [142]. A number of approaches have been attempted, which will be discussed in sections 1.6.2-4. But first, the components necessary to represent the mechanics of hemolysis are listed in section 1.6.1.

1.6.1 Components of a mechanistic hemolysis prediction model

The following steps can be categorized to provide a comprehensive and mechanistic hemolysis prediction model.

1. First, the *velocity field* for the flow domain must be calculated/measured with sufficient temporal and spatial resolution to accurately describe the stress history exerted on the cells likely to be lysed. This process may be iterative to focus the greatest accuracy on the hemolytic regions of the flow. For turbulent flow, the question of sufficient accuracy takes on layers of additional meaning, since viscous and Reynolds stresses, eddy size, time scales and spectral distribution of energy may be important. (An implicit assumption of this step is that continuum flow fields are sufficient as a basis for characterizing the processes heading to hemolysis. If fluid/cell and cell/cell interactions significantly modify the balance of stresses on the cell, then an additional step may be needed to model the relationship of continuum flow field stresses to those local to the cells).

2. Second, the fluid stress must be related to the *membrane stress*. Scaling laws, rather than fully-resolved simulations of concentrated suspensions of deformable cells, would seem to be necessary for efficient algorithms for clinical use. The use of a scalar resultant fluid stress is an attractive means to simplify the model, but its application to complex flows is questionable (see section 3.1.2). The scaling laws may need to take into account cell shape, the semi-permeable and viscoelastic properties of the RBC membrane and the plasma and cytoplasm properties (e.g., extracellular and intracellular viscosity, *Hb* concentration, etc.). Furthermore, for some applications, the model may need to be capable of predicting sub-hemolytic damage.

3. Third, based on the calculated membrane stress, a *constitutive law for the cell membrane* must be applied to model the formation of pores and/or catastrophic failure of the membrane. Large and long-lasting holes in cells with nearly complete loss of hemoglobin, such as occurs due to osmotic stress, may be uncommon. Rather, cells may cleave by pinching off in the middle of dumbbell shapes [111], or shed blebs from high stress areas [143], with small loss of hemoglobin. A number of models have involved determination of strain and prediction of failure at a threshold strain, without explicit modeling of the type of failure.

4. Fourth, the amount of *hemoglobin release* must be determined. This part of the model may need to include a spectrum of membrane disruption from reversible poration to complete failure, with associated differences in transport of hemoglobin to the plasma. At lower stress levels, hemoglobin can be transported through pores in the membrane by diffusion (due to a transmembrane concentration gradient) and/or by advection (due to a pressure gradient). For larger holes, the internal and external flow regions are joined, creating a fundamentally distinct modeling problem. While Vitale, et al. [144] included diffusion in their model, advection has yet to be incorporated into a hemolysis prediction model.

In the last several decades, computational fluid dynamics (CFD) has been extensively utilized for analysis and estimation of blood damage in blood-contacting devices. By providing the velocity field within the blood-handling device, CFD conveniently accomplishes the first of the four steps outlined above. A range of approaches have been applied to address the last three steps, including fluid stress-based, membrane-strain-based and computational biomechanics methods addressed in subsequent sections. For a complete review of hemolysis prediction models specifically for CFD applications, readers are referred to the recent review article by Yu, et al. [145].

1.6.2 Fluid stress-based models

Fluid stress-based models skip steps 2 and 3, to empirically correlate hemolysis directly to fluid stress. The advantage is simplicity and computational speed. However, due to the variability in cell response to different types of fluid stresses (see section 4), it seems unlikely that this approach can lead to predictions that are universally accurate across all types of flows. A power-law model [117] was proposed for low shear stress flows (≤ 300 dyne/cm^2), in which the damage was related to shear rate and tube length (thus, the residence time)

$$D_{LB} = K_i \, \dot{\gamma}^n \tag{36}$$

where D_{LB} is the dimensionless damage index (ratio of *PfHb* concentration after the test to that before the test), $\dot{\gamma}$ is the wall shear rate (s^{-1}), K_{LB} is the rate constant (dependent on tube length) and n is the constant related to the slope of the curve.

In the most widely-used power-law model [139, 140], the hemoglobin release is related to the levels of shear stress (scalar) and exposure time by the following regression equation

$$D = \frac{\Delta PfHb}{Hb} \times 100 = C\,E^{\alpha}\,\tau^{\beta}. \qquad (37)$$

where D is the damage function, τ is the shear stress (N/m^2), and C, α and β are experimentally determined constants (Table 5). The damage function is related to the traditional index of hemolysis (Eq. (1))

$$D = \frac{\Delta PfHb}{Hb} \times 100 = \frac{TIH}{Hb} \times 100 \qquad (38)$$

Table 1. 5 Values of empirical constants in power-law model

Researcher	Species	C	α	β	Shear stress range, dyne/cm^2	Exposure time, s
Heuser and Opitz [139]	Porcine	1.800×10^{-4}	0.7650	1.991	$\tau < 7{,}000$	$3.0\times10^{-3} < E < 6.0\times10^{-1}$
Giersiepen, et al. [140]	Human	3.620×10^{-5}	0.7850	2.416	$\tau < 2{,}550$	$E < 7\times10^{-1}$
Zhang, et al. [146]	Ovine	1.228×10^{-5}	0.6606	1.9918	$500 < \tau < 3{,}200$	$3.9\times10^{-2} < E < 1.48$
Ding, et al. [40]	Ovine	1.228×10^{-5}	0.6606	1.9918	$250 < \tau < 3{,}200$	$4.0\times10^{-2} < E < 1.50$
Ding, et al. [40]	Porcine	6.701×10^{-4}	0.2778	1.0981	"	"
Ding, et al. [40]	Human	3.458×10^{-6}	0.2777	2.0639	"	"
Ding, et al. [40]	Bovine	9.772×10^{-5}	0.2076	1.4445	"	"

Note that based on the Figs. 1.11 and 1.12 in the original paper, the correct value of C for the Heuser and Opitz [139] model is 1.8×10^{-4}, as correctly cited by Song, et al. [147] and Faghih and Sharp [148]. However, some authors used 1.8×10^{-6} either due to confusion between percent and non-percent ratio of $\frac{\Delta PfHb}{Hb}$ or a better curve-fit with their data.

Extensions that have been applied to Eq. (37) include using a scalar stress in place of the shear stress in 2D and 3D laminar flows, and using a similar scalar representing turbulent stresses. While many authors have suggested Reynolds stress as an empirical predictor of cell damage [140, 149, 150], others have argued against it, noting that Reynolds stress is not a true viscous stress, but rather originates from convective acceleration due to the fluctuating part of the local velocity [136]. Based on an energy balance approach, Jones reasoned that the resultant turbulent viscous stress, which is

proportional to the square root of energy dissipation, could be a more meaningful criterion for hemolysis prediction.

Damage accumulation has been interpreted from Eq. (37) by differentiation in time alone [151-154]

$$\Delta D_i = \alpha \, C \, E_i^{\alpha-1} \, \tau_i^{\beta} \, \Delta t_i \tag{39}$$

where ΔD_i is the incremental damage, E_i is the exposure time from the beginning of the stress event and Δt_i is the time step at iteration i, and τ_i is the shear stress during the time step. The questionable validity of Eq. (39) is evident by considering different stress histories leading up to a particular time step. Whether the previous stresses were small or large, Eq. (39) gives the same contribution to the total blood damage for that time step.

The time derivative of Eq. (37) is

$$\frac{d}{dt}(D) = \alpha \, C \, E^{\alpha-1} \, \tau^{\beta} \frac{dE}{dt} + \beta \, C \, E^{\alpha} \tau^{\beta-1} \frac{d\tau}{dt} \tag{40}$$

There is an inconsistency in using the total derivative. When decreasing stress ($d\square/dt < 0$) is acting on the cell, the total derivative (Eq. (40)) predicts negative blood damage, i.e., hemoglobin in the plasma returning to red cells, which is not plausible [151]. Therefore, the derivative of exposure time only (Eq. (39)) is recommended.

The age of RBCs flowing through cardiovascular devices also plays a part in the sensitivity of the cell to the applied shear stress. This factor motivated Yeleswarapu, et al. [155] to formulate a theoretical hemolysis model including aging

$$\widetilde{D}(t) = \widetilde{D}_0 + \frac{1}{\sigma_0^r} \int_{t_0}^{t} \frac{\tau(\xi)^r}{\left[1 - \widetilde{D}(\xi)\right]^k} \, d\xi \tag{41}$$

where σ_0, r and k are non-negative characteristic constants, $\tau(\xi)$ and $\widetilde{D}(\xi)$ are shear stress and damage histories, respectively, while $\widetilde{D}_0$ is the initial damage at $t = t_0$. $\widetilde{D}$ for a single cell is considered to be zero initially and increases as the cell enters the circulation and experiences different forces. Therefore, the damage is assumed to start to accumulate from

the beginning until it reaches a pre-defined threshold value at which hemolysis is assumed to occur.

The methods discussed so far bridge the gap between fluid stresses and *Hb* release from red cells with a variety of simplifications, but all more or less follow the paths of individual cells through the flow regime and use the fluid stress history along these paths to determine how much hemolysis occurs, i.e., the methods are Lagrangian [156-158]. This method adds a significant postprocessing step to calculate pathlines and to verify sufficient density of pathlines in hemolytic regions of the flow to achieve acceptable resolution of hemolysis. An alternative that is simpler, but decidedly more empirical, is to correlate the fluid stress field directly to hemolysis values [159-162]. For example, the Eulerian method of Garon and Farinas uses a source term

$$\zeta = C^{1/\alpha} \tau^{\beta/\alpha} \tag{42}$$

that is derived from the material derivative of a linearized damage function based on the power-law

$$D_L = D^{1/\alpha} = C^{1/\alpha} E \tau^{\beta/\alpha} \tag{43}$$

To understand the conditions for which this source term applies, the material derivative for a general function f

$$\frac{D}{Dt}(f) = \left(\left. \frac{\partial}{\partial t} \right|_{\vec{x}=fixed} + \vec{v} \cdot \nabla|_{t=fixed} \right) f \tag{44}$$

becomes for the linearized damage function for steady flow (and inserting Eq. (42))

$$\frac{D}{Dt}(D_L) = \left[\frac{\partial D_L}{\partial t} + \vec{v} \cdot \left(\frac{\partial D_L}{\partial E} \frac{dE}{d\vec{s}} \frac{d\vec{s}}{d\vec{x}} + \frac{\partial D_L}{\partial \tau} \frac{d\tau}{d\vec{s}} \frac{d\vec{s}}{d\vec{x}} \right) \right] = C^{\frac{1}{\alpha}} \left[0 + \vec{v} \cdot \left(\tau^{\frac{\alpha}{\beta}} \frac{n_i \hat{\imath}_i}{\overline{U}_s} + E \frac{\beta}{\alpha} \tau^{\frac{\beta}{\alpha}-1} \frac{\partial \tau}{\partial \vec{x}} \right) \right] \tag{45}$$

where $\bar{U}_s$ is the mean velocity during time E along the streamline s passing through the fixed point. Again ignoring spatial variations in shear stress, the source term becomes

$$\zeta = \frac{D}{Dt}(D_L) = C^{1/\alpha}\tau^{\beta/\alpha}\frac{U}{\bar{U}_s} \tag{46}$$

where U is the local magnitude of velocity. Comparing Eq. (46) and Eq. (42), it is evident that the source term of Eq. (42) is valid only for flows in which $\bar{U}_s = U$. This is the case for uniaxial flows with constant velocity along streamlines, such as Poiseuille and Couette flows. However, for more complex flows, $\bar{U}_s$ must be determined along streamlines, which adds a Lagrangian step to the Eulerian method.

An additional issue has been identified with the Eulerian method and, in particular, the linearized damage function. The average of the original damage function is intended to be returned by applying an exponent to the volume integral of the source term

$$\bar{D} = \left(\frac{1}{\hat{u}A}\int \zeta dV\right)^\alpha \tag{47}$$

where $\hat{u}$ and A are the average velocity and the area of the exit cross section, respectively, and V is the volume. To be valid, this average damage function should be equal to that of the original Lagrangian method, which is found by a velocity weighted integral over the exit cross section

$$\bar{D} = \frac{1}{\hat{u}A}\int uDdA \tag{48}$$

Equating hemolysis predicted by Eqs. (47) and (48) (and using Eq. (46)) gives

$$\frac{\int uDdA}{(\int uD^{\frac{1}{\alpha}}dA)^\alpha} = (\hat{u}A)^{1-\alpha} \tag{49}$$

This equation is satisfied only if $\alpha = 1$ or $D = CE^\alpha\tau^\beta$ is constant. However, $\alpha \neq 1$ for any of the power-law models (Table 5). D is constant for Couette flow, but not for Poiseuille flow nor for more complex flows. The root of this inconsistency is that exponents

34

are not distributive across integrals, i.e. $\left(\int f^{\frac{1}{\alpha}} dx\right)^{\alpha} \neq \int f\, dx$ or as shown by Eq. (49), $\left(\int uD^{\frac{1}{\alpha}} dA\right)^{\alpha} = \int uDdA$ only for some rather limiting conditions.

In general, neither the Lagrangian nor Eulerian approaches have shown satisfactory results for hemolysis prediction in blood-contacting devices [163, 164].

1.6.3 Membrane strain-based models

In spite of the extensions that have been developed to broaden the applications of the power-law model (Eq. (37)), validation is limited to the original experimental data and their associated ranges of simple shear stress and exposure time. Perhaps more important is that the power-law model does not incorporate physical and mechanical properties of the RBCs, nor mechanisms of the transmission of fluid stresses to the membrane. As pointed out by Ezzeldin, et al. [142], the simpler fluid stress-based models lack a strong connection with the mechanics of membrane failure, which may limit their performance in the complex, unsteady flows that often occur in cardiovascular devices. For this reason, a number of investigators have turned to membrane strain-based models as potential avenues for improving hemolysis prediction.

1.6.3.1 Deformation index

Strain-based models fit between the extremes of purely empirical correlation of hemolysis with fluid flow parameters (such as the power-law model [151]) and molecular-scale modeling of red cell membrane failure to predict hemolysis. Strain-based models utilize observations that the RBC membrane can withstand no more than 5–10% increase in area before being ruptured [165, 166]. With a model relating fluid stress conditions to membrane strain, this threshold of strain has been used to predict hemolysis (thus the name "strain-based" models). The relationship between fluid stress and membrane strain commonly adopts a simplified model of whole-cell deformation along pathlines through the flow. A deformation index may be used as a proxy for local or uniform membrane strain. One such index is the simple ratio of major and minor radii a/b of an assumed prolate ellipsoidal cell (Fig. 1.3). Another option, called the deformation index (*DI*), is expressed as

$$DI = \frac{a - b}{a + b} \tag{50}$$

A third index is sphericity, which is defined as

$$Sph = \frac{\pi^{1/3}(6V_p)^{2/3}}{A_p} \tag{51}$$

where V_p and A_p are the volume and surface area of the cell. For a cell beginning with mean surface area and volume of 135 µm^2 and 94 µm^3, respectively, the initially biconcave disk can be deformed without areal strain of the membrane to a prolate ellipsoid with $a/b =$ 4.8895 ($2a = 8.1254$ µm and $2b = 1.6618$ µm), $DI = 0.6604$, and $Sph = 0.7406$. Beyond this level of cell elongation, areal strain must occur, as shown in Fig. 1.11. To better compare the indices, they are normalized in Fig. 1.11 by their unstrained values $(a/b)_0$, DI_0 and Sph_0. It is apparent that Sph is less sensitive to strain than the other two, but nonetheless, is directly (inversely) proportional to membrane area.

a=Cell major radius
b=Cell minor radius

a /b= 1	*a /b= 2*	*a /b = 3*
DI=0	*DI=0.33*	*DI=0.5*
Sph=1	*Sph=0.9287*	*Sph=0.8461*
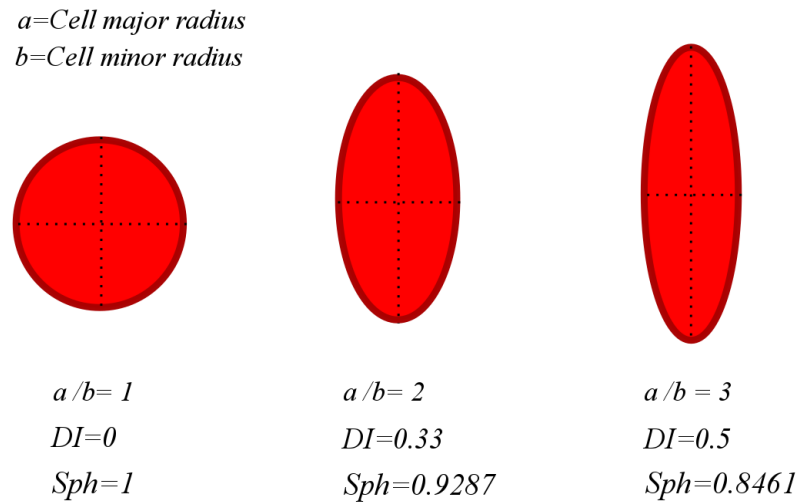
Fig. 1. 10 Definition of deformation index
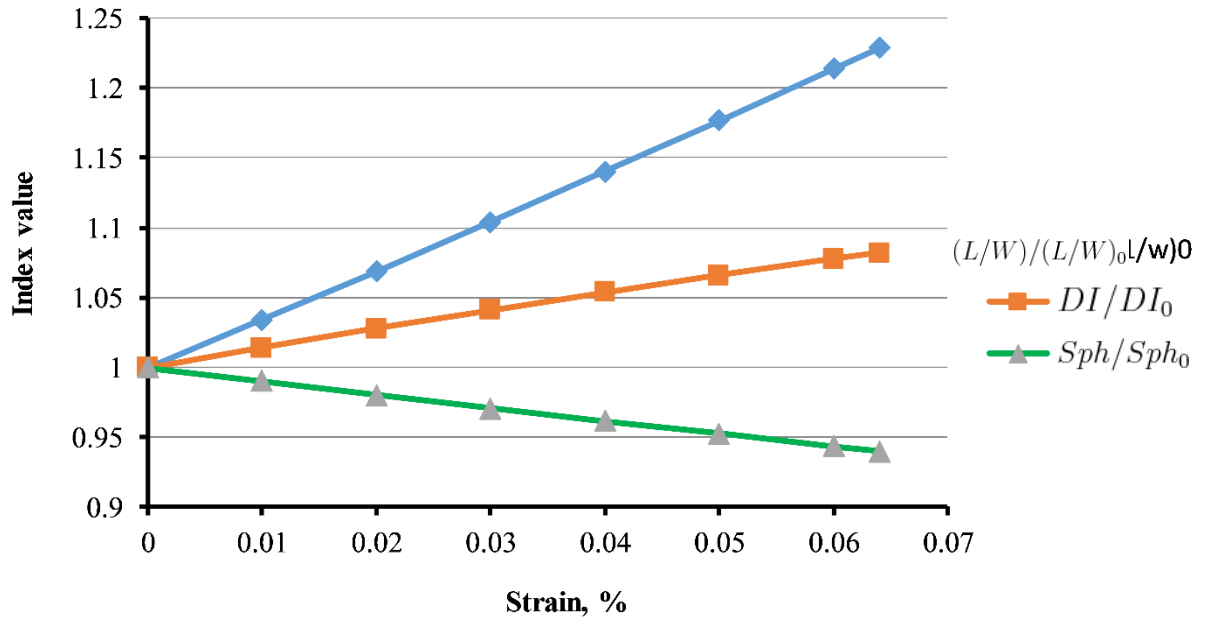
Fig. 1. 11 Three deformation indices versus membrane strain

Relationships between these deformation indices and hemolysis are yet to be fully established. Validation experiments are needed to relate the indices to hemoglobin release (sublytic membrane damage is a further question).

Three uncertainties should be considered when using the above-mentioned deformation indices. First, the indices are calculated based on shape symmetry about the long axis, which is clearly not valid for all flows. Additionally, the deformation indices do not take into account the initial shape and size of the cell. For instance, an RBC with greater membrane surface area to volume ratio may have the same value of deformation index at a lower state of strain. Considering the range of surface area and volume among cells in a particular patient or population of cells (such as the means and standard deviations in Table 1) leads to a distribution of strain and of resulting hemolysis, even for the same flow conditions.

Still, the use of a simple deformation index is attractive, because calibration experiments involving two-dimensional, projected images of cells allow straightforward quantification of the index. More complex experimental setups are required to measure angles and lengths in the third dimension. In such experiments, optical access to individual cells within the flow regime has so far required testing at low hematocrit. Because the low

concentration of cells largely eliminates cell/cell interactions, the behavior of individual RBCs may be different from those experiencing collisions under physiologic hematocrit. Although hematocrit has been shown to have a negligible effect on hemolysis in a concentric cylinder viscometer under pure shear stress [116], low hematocrit may not fully capture the bulk flow behavior of RBCs in the more complex fluid dynamics in cardiovascular devices.

In a study on the deformation of RBCs flowing through a microchannel [123], it was observed that under laminar shear stress as high as 50,000 dyne/cm^2 for duration of around 23 ms, the deformation index of cells reached a plateau at *DI= 0.54*, and the cells surprisingly exhibited no cell lysis/rupture, and returned to their original shape after removal of the stress. These experiments used a very low hematocrit in order to capture images of individual cells, as well as a suspending medium viscosity more than 10 times that of normal plasma to achieve a high shear stress at reasonable flow rate. This tactic has been used by others for the same reasons, as well as to maintain laminar flow [100, 113, 114, 121]. However, it has been demonstrated that cell deformation is a function of suspending medium viscosity [167], thus it may impact the combination of fluid stress and exposure time at which lysis occurs.

1.6.3.2 Membrane strain-based models

Membrane strain-based models, defined strictly, utilize the first three steps in section 6.1, but also typically include the fourth step, as well. This category of models, therefore, includes those that simplify cell deformation and treat hemoglobin release empirically, and others that use a cell-scale or molecule-scale computational models for deformation and hemoglobin diffusion.

Using Rand's model of the cell membrane [168] as well as membrane shell theory, Richardson [141, 169] modeled the RBC as an isolated spheroid with flexible membrane in a uniform shear field to obtain the stresses on the cell surface, with the goal of developing a model for hemolysis in high shear-rate experiments. He showed that membrane strain of the cell in a uniform shear flow is composed of three terms: a term linear in time, a periodic

term and an exponentially decreasing term. It was then concluded the time it takes for hemolysis to occur is dictated by the linear term and is equal to

$$t_R = \frac{C_R}{\mu \dot{\gamma}^2} \tag{52}$$

where C_R is an experimental constant equal to 6.7×10^4 dyn/cm^2 based on Rand's critical strain value.

Modeling the red cell as a deformable liquid droplet and assuming that instantaneous *Hb* leakage through the RBC membrane depends on instantaneous RBC shape distortion, Arora, et al. [170] proposed a tensor-based hemolysis model to estimate the time and space-dependent straining by individual RBC under steady shear stress. They used a constitutive equation for the deformation of the droplet by balancing the interfacial tension with the fluid stresses on both side of the interface [171, 172]. Then, a deformation function is used as the stress term in the power-law model format (Eq. (37))

$$D = C \, t^{\alpha} \left(\mu \, \frac{2 f_1(DI)}{f_2(1 - (DI)^2)} \right)^{\beta} \tag{53}$$

where D is the damage function, as previously described by Eq. (37), DI is the deformation index previously expressed by Eq. (50), f_1 and f_2 are parameters related to physical properties of the liquid droplet model of the RBC. This model adds mechanistic fidelity, but hemolysis was scaled to the power-law model, thus it shares the limitations of that empirical model.

Chen and Sharp [100] developed a scaling model to relate membrane stress to the von-Mises-like scalar stress in the fluid, and used a viscoelastic model for the RBC membrane that fails at a critical strain [168]

$$\frac{S}{S_c} = T \left[\frac{1}{S_c h Y_2} + \frac{1}{S_c h Y_1} \left(1 - e^{\left(-\frac{Y_1}{\eta_1} t \right)} \right) + \frac{1}{S_c h \, \eta_2} t \right] \tag{54}$$

where S is the membrane strain, S_c is the critical strain (taken as 0.064 [168]), T is the biaxial tension in the RBC membrane, h is the membrane thickness and Y and η are

parameters related to elastic and viscous properties of the modeled RBC, respectively. Importantly, this work included new experimental data that documented red cell deformation in pure shear flow, but due to limitations of the equipment, tests could not be run all the way to membrane failure. Thus, the model includes extension of the experimental results to the hemolysis threshold. This model was compared with two power-law models, namely the Heuser and Opitz [139] and Giersiepen, et al. [140] models, in the flow through needles of different entrance geometry, i.e. standard, beveled and rounded [173]. Chen and Sharp's strain-based model provided good trends for hemolysis in the three different needles with subtle variations in entrance geometry compared to the power-law-based models, which produced opposite trends. This comparison of needle geometries is emblematic of the types of problems bioengineers would like to solve in the course of optimizing the flow within a blood-contacting device. To develop a reliable and accurate hemolysis prediction algorithm, more work like this is needed in comparing the performance of models in such problems, which also means that more experimental validation data is needed for cases that involve incremental changes in device geometry and flow conditions.

Arwatz and Smits [21] modified the theoretical model proposed by Rand [168] by using a viscoelastic strain-based model with two time-constants. The first time-constant is related to the short time-scale during which the deformed RBC releases part of its hemoglobin (change in membrane permeability/poration). The second time-constant, that is larger than the first time constant, represents the decay of elastic behavior of membrane. The resulting formulation is

$$\frac{D}{100} = \frac{A_{AR}\tau}{G}\left[2 - \left(e^{-\frac{t}{T_1}} + e^{-\frac{t}{T_2}}\right) + \frac{t}{T_2}\right] \tag{55}$$

G is the membrane shear modulus, T_1 and T_2 are the first and second time constants, and A_{AR} is an empirical constant.

Vitale, et al. [144] added an important factor, namely, membrane poration, into their model. Their multiscale biophysical model involved all four steps: 1) calculating the flow field, 2) determining membrane stress from the calculated flow field; 3) finding areal

strain and modeling membrane poration due to deformation; 4) calculating *Hb* mass transfer through the pores due to transmembrane *Hb* concentration difference. For the third step, they used the tensor-based model of Arora, et al. [170] to define cell deformation and morphology along its trajectory. Then, energy changes on the membrane governed by two forces, namely hydrophobic attraction of lipid tails and headgroup repulsion, were considered to determine nucleation of pores in the membrane. For the last step, the rate of mass transport *J* of *Hb* out of the cell through the pores

$$J = K_c(Hb_{in} - Hb_{ex}) \tag{56}$$

where Hb_{in} and Hb_{ex} are internal and external hemoglobin, respectively, was modeled with an empirical mass-transfer coefficient K_c correlated to shear rate

$$K_c = h_c \dot{\gamma}^{k_c} \tag{57}$$

where h_c and k_c are empirical coefficients. Advective *Hb* transport induced by transmembrane pressure difference was not included. The damage function was approximated by:

$$D(t) \approx 1 - \exp\left[-\int_0^t R(\alpha_s(t), K_c)\, dt\right] \tag{58}$$

where *R* is a parameter representing transmembrane *Hb* transport that depends on K_c and the size of the pores, which depends on membrane areal strain α_s. In deriving the above relation, it was assumed that damage is zero at *t=0*.

In a more recent study [142], the model by Arora, et al. [170] was extended by using coarse-grained molecular models of the erythrocyte membrane and spectrin cytoskeleton [174]. In contrast to the model by Arora, et al. [170], which used the instantaneous strain tensor of the membrane to obtain the RBC deformation, the model developed by Ezzeldin, et al. [142] employed the eigenvalues of the instantaneous moment of the inertia tensor of the membrane to calculate the average macroscopic deformation of the cell. Based on that, the average deformation (a scalar) was calculated and used in Eq. (50) to estimate hemolysis. The model was applied to simple shear flow and compared to

the results of previous models. They found that in one-dimensional flow, fluid stress-based models predict hemolysis reasonably well, while in multi-dimensional flows, they may either over-estimate or under-estimate hemolysis, depending on the frequency of cell loading and other conditions. For instance, in multi-dimensional flow, the strain-based model of Arora, et al. [170] predicts lower damage compared to the spectrin-based model of Ezzeldin, et al. [142]. To validate these numerical findings, they conducted a simple experiment of flow in an aortic graft which is equipped with a bileaflet mechanical valve and found a good agreement between the experimental and numerical results.

Modeling of local membrane strain was added by Sohrabi and Liu [175]. Based on the support of the bilipid membrane by the spectrin network, pores were limited in size to that of a stretched spectrin molecule. Hemoglobin was transported through the pores by diffusion, including steric hinderance and increased hydrodynamic drag due to the size of the hemoglobin molecule being a significant fraction of the pore size. The resulting mass transport coefficient was in the same range as that of Vitale, et al. [144], but is less empirical.

For higher stresses, unstable growth of pores may lead to catastrophic membrane rupture. Poorkhalil, et al. [176] developed a semi-empirical hemolysis model adding this phenomenon. Their model included Fickian diffusion of *Hb* through pores at lower levels of shear stress and a second term accounting for release of all intracellular hemoglobin beyond a threshold shear stress. By differentiating these two hemoglobin release mechanisms, they achieved better agreement with existing experimental hemolysis data. Experiments using a Couette device were also conducted on both human and porcine blood samples to validate the model and a good agreement was found between the experimentally measured damage function and the one predicted by their model.

1.6.4 Energy dissipation rate-based models

An alternative to the application of the scalar stress as a parameter to quantify red cell membrane damage is the viscous energy dissipation rate, $\square$. Bluestein and Mockros [75] previously showed that the rate of red cell damage ($\dot{D}_B$ is defined as *PfHb* per cm^3 of red cells per unit time) can be scaled as

$$\dot{D}_B = k_d \varepsilon^{\alpha_d} \tag{59}$$

for flow in round tubes, orifice plates and a venturi tube and in uniform shear in a viscometer with combined Couette and cone/plate geometry. However, empirical constants k_d and α_d varied among the flow types, with nonuniform energy dissipation producing more hemolysis, implying that the local rate of energy dissipation should be considered if energy dissipation is to become a universal hemolysis prediction parameter.

More recently, Morshed, et al. [76] argued that the energy dissipation in blood plasma dominates the energy dissipation in the cell membrane and its intracellular content. Based on this assumption, strain occurs only in the blood plasma, and the shear stress exerted on the cell membrane (τ_p) is

$$\tau_p = \frac{\upsilon_B}{\eta_k{}^2} \sqrt{\frac{\mu_B \mu_p}{(1-H)}} \tag{60}$$

μ_B and μ_p are the viscosities of whole blood and plasma, respectively and H is the hematocrit fraction.

1.7 A fresh approach: greater accuracy through more mechanistic models

While cellular and molecular-level simulations have the potential to provide accurate predictions of flow and of cellular responses, including membrane deformation and failure and hemoglobin release, it remains a formidable challenge to resolve all the necessary scales to solve the problem in real cardiovascular devices. With this in mind, this section will discuss opportunities for improving models that are within the current capacity of modern computers, in particular, modifications that may be required to address differences in the responses of cells to different components of the fluid stress tensor and to turbulent versus laminar flow.

1.7.1 Dimensional analysis

A potentially important avenue for improving the accuracy of hemolysis models is reevaluating the mapping between fluid stresses and membrane stresses across different

types of cell motion (step 2 in section 1.6.1). Once membrane stresses are known, the next challenge is to model the mechanical response of the cell membrane up to and including failure that results in loss of hemoglobin from the cell.

The independent variables that may influence this response include external fluid density ρ_{ex}, internal fluid (cytoplasm) density ρ_{in}, external fluid viscosity μ_{ex}, internal fluid viscosity μ_{in}, red cell shape at rest (array $\boldsymbol{D_0}$ of several dimensions, represented by the major diameter a_0 in Fig. 1.12 left), membrane mechanical properties (array $\boldsymbol{\psi}$, represented by membrane surface viscosity η_m and membrane edge tension Λ in Fig. 1.12 left), the initial internal Hb_{in0} and external Hb_{ex0} hemoglobin, and the external fluid stress tensor $\boldsymbol{\sigma}_{ex}$ applied to the cell (Fig. 1.12 left) (The strain rate tensor is a suitable alternative that eliminates the external fluid viscosity, which is already included separately.).
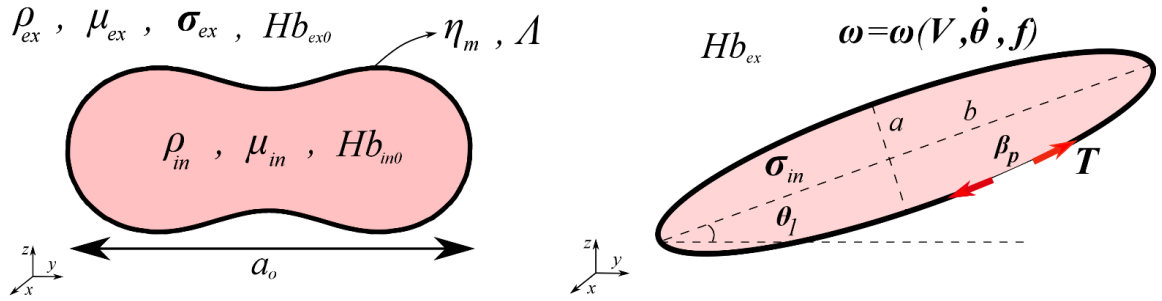
Fig. 1. 12 Schematic of unstressed cell (left) and stressed (right) cell with independent variables on the left and dependent variables on the right

The dependent variables that result from flow-induced stress include the distorted cell shape ($\boldsymbol{D_s}$), cell orientation in the flow (array $\boldsymbol{\theta}$, represented by the angle θ_1 in the yz plane in Fig. 1.12 right), cell motion parameters ($\boldsymbol{\omega}$), membrane tension ($\boldsymbol{T}$), cytoplasmic stress tensor ($\boldsymbol{\sigma}_{in}$), pore properties (number and sizes, represented by $\boldsymbol{\beta_p}$ in Fig. 1.12 right) and the external Hb_{ex} hemoglobin for the stressed condition (Fig. 1.12 right). Note that internal hemoglobin Hb_{in} has not been included, since by conservation of mass, total hemoglobin remains the same $Hb = Hb_{in} + Hb_{ex} = Hb_{in0} + Hb_{ex0}$. Hence the relationship of the variables in dimensional form is

$$
\begin{aligned}
&\left(\boldsymbol{T}, \boldsymbol{\theta}, \boldsymbol{\omega}, \boldsymbol{D_s}, \boldsymbol{\beta_p}, \boldsymbol{\sigma}_{in}, Hb_{ex}\right) \\
&\quad = f\left(\rho_{ex}, \rho_{in}, \mu_{ex}, \mu_{in}, \boldsymbol{D_0}, \boldsymbol{\psi}, \boldsymbol{\sigma}_{ex}, Hb_{ex0}, Hb_{in0}\right)
\end{aligned}
\tag{61}
$$

By expanding some of the arrays, the relationship becomes

$$\left\{ T, \boldsymbol{\theta}, \underbrace{(\boldsymbol{V}, \dot{\boldsymbol{\theta}}, \boldsymbol{f})}_{\omega}, \underbrace{(a, b, c)}_{D_s}, \boldsymbol{\beta_p}, \sigma_{in}, Hb_{ex} \right\} = f \left\{ \rho_{ex}, \rho_{in}, \mu_{ex}, \mu_{in}, \boldsymbol{D_0}, \underbrace{(\eta_m, \Lambda)}_{\psi}, \boldsymbol{\sigma_{ex}}, Hb_{ex0}, Hb_{in0} \right\} \quad (62)$$

where $\boldsymbol{V}$ is the cell linear (translational) velocity vector, $\dot{\boldsymbol{\theta}}$ is the cell rotational velocity vector, $\boldsymbol{f}$ is the tank-treading frequency vector, and a, b and c are the dimensions of an assumed ellipsoidal cell in its deformed state. Note that the membrane bending (B) and area expansion (κ) moduli are dependent on the membrane thickness (h, which is considered a constant here for simplicity) and membrane edge tension Λ, thus neither are included as independent variables [34] (see section 2.1). Also note that membrane shear modulus, which is an important parameter in characterizing cell motion in shear flow (the ratio of shear elastic modulus μ_s and bending stiffness B form the Koeppl-von Karman number $\gamma = 4\mu_s a_0^2/B$, which is a determinant of the transition from tumbling to tank-treading in shear flow [177], and in the capillary number $Ca = \sigma_{ex}a_0/\mu_s$, which has been shown to scale membrane tension in shear flow [178], is neglected here within the ellipsoidal shape assumption for the models employed in this study.

Counting the vectors and $\boldsymbol{\beta_p}$ as single variables, there are 20 dimensional independent and dependent variables. By the Buckingham Pi theorem with three fundamental units, the number of dimensionless ratios can be reduced to 17. Candidate dimensionless groups are listed in Table 7, along with existing dimensionless numbers in many cases. The number of dimensionless ratios is reduced by one more (to 16), because all three hemoglobin variables are combined into one ratio , $\boldsymbol{\Pi_{10}}$, that compares the change in external hemoglobin (caused by hemolysis) to the total hemoglobin. This ratio can be applied to whole blood, and becomes MIH (Eq. (3)) by adjusting by the hematocrit $\frac{100-Hct}{100}$. The first vector of ratios $\boldsymbol{\Pi_1}$ weigh the components of membrane surface tension versus viscous forces in the extracellular fluid. The orientation angles $\boldsymbol{\Pi_2}$ are already dimensionless. $\boldsymbol{\Pi_3}$ represents primary and secondary flow cell Reynolds numbers, which might be reduced to a scalar by using the resultant velocity. $\boldsymbol{\Pi_4}$ and $\boldsymbol{\Pi_5}$ are Roshko numbers comparing whole-cell rotational and membrane tank-treading forces to external fluid viscous forces. Deformed cells are nondimensionalize by the unstressed major radius, $\boldsymbol{\Pi_6}$,

Π_7 and Π_8. An example of Π_9 is the Litster number, which compares the pore radius β_p to the critical pore radius Λ/T above which the pore grows unstably and below which it shrinks. Other components may be added to characterize the number of pores and distribution of sizes. Π_{11} is the Reynolds number for cytoplasmic flow based on internal fluid stresses, which compares convective to viscous forces.

For the independent variables, Π_{12} is the Reynolds number for external flow based on external fluid stresses, which again compares convective to viscous forces. Because of the small size of the red cell, the Reynolds number may always be small for flows in cardiovascular devices, but fluctuating stresses will indicate the effects of turbulence. Π_{13} is the ratio of internal to external fluid viscosities, which has been shown to be important in regulating the type of cell motion, particularly in shear flow (tumbling tends to occur when the cytoplasm is more viscous than the surrounding fluid, and tank-treading occurs when the surrounding fluid is more viscous). Π_{14} is a ratio of membrane line tension to membrane viscosity, but because the membrane area expansion modulus is proportional to line tension, it also characterizes this expansion modulus with respect to membrane viscosity. As such, it is a factor in determining how rapidly the membrane is stretched and in the growth of pores. Π_{15} compares membrane surface viscosity and external fluid viscous forces, thus it affects the deformation of cells in viscous flow (which is the predominant flow at the cellular level in cardiovascular devices, as opposed to the inertial flow in shock wave lithotripsy, see section 5.2). Finally, Π_{16} is a ratio of internal to external fluid densities, which is important in sedimentation and in inertial flows.

Table 1. 6 Dimensionless groups for modelling mechanical hemolysis

Dependent variables	Physical interpretation	Existing dimensionless number
$\Pi_1 = \dfrac{\rho_{ex} a_0 \boldsymbol{T}}{\mu_{ex}^2}$	membrane tension froce / external fluid force	
$\Pi_2 = \boldsymbol{\theta}$	cell orientation angle	
$\Pi_3 = \dfrac{\rho_{ex} a_0 \mathbf{V}}{\mu_{ex}}$	cell velocity convective froce / external fluid viscous force	Cell Reynolds number
$\Pi_4 = \dfrac{\rho_{ex} a_0^2 \dot{\boldsymbol{\theta}}}{\mu_{ex}}$	cell rotation convective froce / external fluid viscous force	Cell rotation Roshko number
$\Pi_5 = \dfrac{\rho_{ex} a_0^2 \boldsymbol{f_i}}{\mu_{ex}}$	cell tank − treading convective froce / external fluid viscous force	Cell tank-treading Roshko number
$\Pi_6 = \frac{a}{a_0}, \Pi_7 = \frac{b}{a_0}, \Pi_8 = \frac{c}{a_0}$	cell shape ratio	
$\Pi_9 = \dfrac{\boldsymbol{\beta_p T}}{\boldsymbol{\psi}}$	pore radius / critical pore radius	Litster number[*]
$\Pi_{10} = \dfrac{Hb_{ex} - Hb_{ex0}}{Hb_{in0} + Hb_{ex0}}$	released hemoglobin / total hemoglobin	Modified index of hemolysis is similar $MIH = \frac{\Delta PfHb}{Hb} \times \frac{100-H}{100}$
$\Pi_{11} = \dfrac{\rho_{in} a_0^2 \boldsymbol{\sigma_{in}}}{\mu_{in}^2}$	internal convective froce / internal fluid viscous force	Internal fluid stress Reynolds number
Independent variables		**Possible dimensionless number**
$\Pi_{12} = \dfrac{\rho_{ex} a_0^2 \boldsymbol{\sigma_{ex}}}{\mu_{ex}^2}$	external convective froce / external fluid viscous force	External fluid stress Reynolds number
$\Pi_{13} = \dfrac{\mu_{in}}{\mu_{ex}}$	internal viscosity / external viscosity	
$\Pi_{14} = \dfrac{\boldsymbol{\Lambda}}{h\eta_m}$	membrane line tension / membrane viscosity	
$\Pi_{15} = \dfrac{\eta_m}{a_0 \mu_{ex}}$	membrane viscosity / external fluid viscosity	
$\Pi_{16} = \dfrac{\rho_{in}}{\rho_{ex}}$	internal density / external density	

* The pore radius normalized by the critical pore radius at which membrane tension equals pore edge tension

The variables in Table 7 represent a first attempt to characterize hemolysis generally for any kind of cell motion under any flow condition. A benefit of dimensional analysis is in establishing a context within which specific solutions can be understood as a part of the whole. For instance, modeling of stable poration of the membrane applies only in the low Litster number regime and is just a part of an overall solution for all Litster numbers, which also includes catastrophic failure of membranes at high Litster number.

Another example is the restriction of solutions to viscous (and not inertial) flow, which reduces complexity by allowing Π_{16} to be neglected.

Another benefit is in reducing the matrix of experimental or computational cases that must be tested to completely explore the effects of independent variables. For demonstration purposes, consider a simplified flow with one component of the external fluid stress tensor, or a scalar stress that represents multiple components. Also for simplicity, let the cell shape and membrane property arrays be represented by one value each. Thus, the dimensional Eq. (62) has nine independent variables. With ten values of each variable to test the effect of each, the set of experimental or computational cases to blindly quantify the relationships of these variables to the dependent variables would be 10^9. Using dimensional analysis, however, the set of nondimensional independent variables is immediately reduced to four (Table 7 with only one membrane property variable, i.e., the ratio of membrane variables Π_{14} vanishes). Further, let us say that through the insight gained by performing the dimensional analysis, we also recognize that the flow is viscous so that Π_{16} can be ignored. By doing so, the number of cases is reduced further to 10^3. In the latter case, if three cases could be tested per day, the matrix could be completed in about one year. However, the dimensional set of independent variables would take over 2.7 million years! Clearly, dimensional analysis reduced the necessary effort.

1.7.2 Improved modeling of membrane tension

Continuum-based models of hemolysis have so far been unsuccessful in providing useful hemolysis prediction results that are universal across a wide range of flows. For turbulent flow, which is especially problematic, correlations have been attempted with turbulent viscous stress, Reynolds stress and energy dissipation, as discussed in section 1.3.2 and 1.3.3. Here, an attempt will be made to go beyond correlations between hemolysis and scalar representations of fluid stress, and to evaluate the scaling of red cell membrane tension with fluid stress in a range of simplified flows. These relationships, which represent step 2 of section 1.6.1, are the current, and arguably the greatest, bottleneck toward more accurate continuum-based hemolysis prediction. The following subsections will present scaling models that connect fluid stress to membrane tension in simple laminar and

48

turbulent flows. By more clearly defining this problem, there is hope that progress will be made toward universal hemolysis prediction.

1.7.2.1 Modeling membrane tension in laminar extensional flow

Using dimensional analysis and applying a force balance on a prolate ellipsoidal cell (Fig. 1.13), the membrane tension around the circumference of the middle of the cell is [100]

$$T = K \frac{4}{5} b (\sigma - \sigma_c) \qquad (63)$$

where T is the membrane tension (force per unit length), b is the characteristic length of the RBC (minor axis of the 2-D projected RBC), σ is the extensional stress, σ_c is the critical stress (1,500 dyne/cm^2) and K is an empirical constant. Assuming the absence of circulation of the membrane (tank-treading or tumbling), the membrane tension is constant.
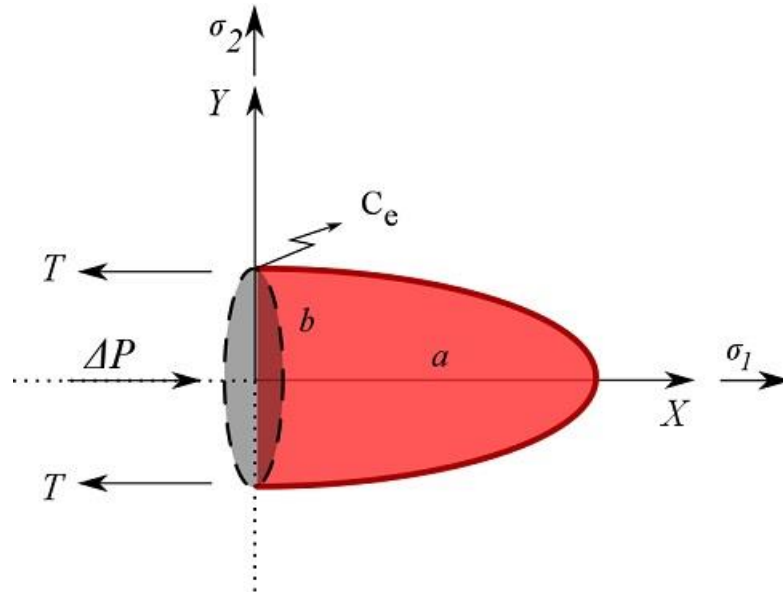
Fig. 1. 13 Schematic diagram of the ellipsoidal RBC model under extensional stress

1.7.2.2 Modeling membrane tension in laminar shear flow

In laminar shear flow with sufficient ratio of suspending media viscosity versus cytoplasmic viscosity, an approximately ellipsoidal cell tank-treads with its downstream end elevated with respect to the shear field (Fig. 1.14). Using this assumed shape and with orientations matched to experiments, and with assumed internal and external velocity fields

[86], Tran-Son-Tay, et al. [179] calculated the stress tensors acting on the outer and inner surfaces of the membrane, τ^o and τ^i, respectively. Then, with assumed tank-treading motion of the cell membrane [86] and ignoring bending stress, a force balance provided, at any point on the membrane, two in-plane extensional tensions T_α and T_φ, and an in-plane shear tension S_m (Fig. 1.15). The maximum extensional tension occurs on the central strip C_0, where shear within the membrane is also zero.
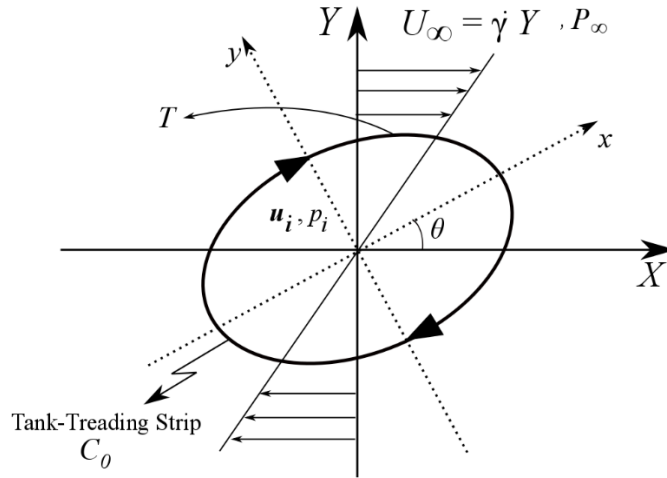
Fig. 1. 14 An ellipsoidal model of RBC tank-treading in a pure shear flow with corresponding external shear rate, velocity and pressure, having internal velocity and pressure denoted as u_i and p_i

Embedded in this analytical solution is the internal cytoplasmic pressure (p_i) that is solved using a Kelvin-Vogt viscoelastic model for the RBC membrane. Because the mathematics of the solution is extensive, readers are referred to the original article for details [179].
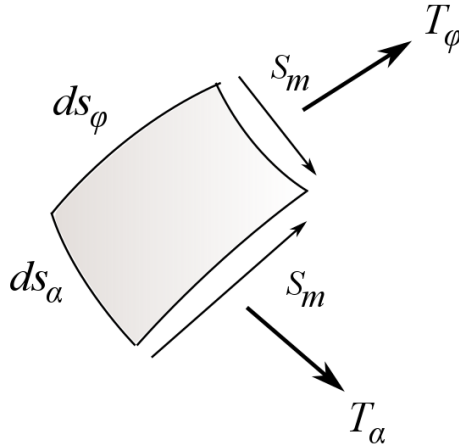
Fig. 1. 15 One in-plane shear stress and two in-plane extensional stresses acting on a massless elemental cell membrane

1.7.2.3 Modeling membrane tension in turbulent flow

Because of the chaotic nature of turbulence, there is not a consensus on the fluid stress that is applied to the red cell, even in simple turbulent flows. Therefore, this section will discuss models for the relevant fluid stress, as well as those for the membrane tension that results.

First, Quinlan and Dooley [63] recognized that the distribution of turbulent energy across the spectrum from microscopic to macroscopic length scales may impact the characteristic fluid stress that can be used to scale hemolysis. They used order of magnitude estimates to approximate the shear stress 1) on a cell with a uniform, oscillating velocity field surrounding it, and 2) on a cell sheared inside a rotating turbulent eddy. In both cases, the flow near the cell was considered laminar due to the small spatial scale, even though the global Reynolds number is turbulent. Because the stress for the first case was about an order of magnitude smaller than for the second case across the spectrum of frequencies relevant to the experimental data to which they were applied [180], and the same data will be used here, this case will not be further analyzed. From the second case, they concluded that Reynolds stress is at least an order of magnitude higher than the shear stress experienced by the cell.

Expanding their previous model, Dooley and Quinlan [181] used the immersed boundary method to investigate the interaction of an isolated, tank-treading, 2D circular cell with flexible and deformable membrane with idealized 2D turbulent eddies of varying

51

size from 4 to 40µm. They used an elastic circle as a 2-D model of the red cell and adopted the constitutive equation by Hochmuth and Waugh [182] to model the cell membrane tension. They found peak membrane tension nearly identical to the 3D model of Tran-Son-Tay, et al. [179], which validates its use for comparisons here. They concluded that the RBC damage is independent of the Kolmogorov scale, suggesting that the Kolmogorov scale may not be the most important factor for hemolysis prediction in turbulent flow. They also raised the question of whether the hypothesis of local homogenous and isotropic turbulent motion in Kolmogorov theory is valid under the typical cardiovascular blood flow that is associated with significant inhomogeneity and anisotropy.

Second, Antiga and Steinman [183] developed scaling for the shear experienced by cells in adjacent 100 □m diameter co-rotating eddies separated by a distance estimated from the packing density of aligned prolate ellipsoidal cells at a physiological hematocrit of 45%. Applying the model to the data of Liu, et al. [180], a viscous shear stress of around 160 dyn/cm^2 was estimated to be applied on the cell, which is larger than the 60 dyn/cm^2 found by Dooley and Quinlan [181] for a cell inside a Kolmogorov-size eddy, and smaller than the 520 dyn/cm^2 Reynolds stress.

In a computational analysis, total surface area (or total volume) of all the turbulent eddies of critical size (up to 10µm) was correlated to hemolysis measured in Couette and capillary tube viscometers [184]. Results suggested that Kolmogorov scale smaller than the RBC size promotes cell damage.

1.8 Conclusion

Although there has been considerable research on mechanical hemolysis in the past 50 years, there is still much to be discovered. Cells travelling in either physiological pathways or mechanical devices experience a wide range of stresses (Fig. 1.3). A truly universal hemolysis prediction model must provide accurate results across the entire range. To accomplish such a model, more attention is needed on the response of the RBC membrane to the different types of stress.

For laminar shear stress, a number of measurements of hemolysis at physiological hematocrits have been made that provide validation data for hemolysis prediction. Real-

time microscopic observations of cell motion have also been accomplished, but not for physiologic hematocrit and internal/external viscosity ratio, nor for shear and exposure time that produce membrane lysis. Therefore, in spite of the relative wealth of information for this flow type compared to others, important fundamental information is lacking.

For laminar extensional flow, no experimental hemolysis results exist (in terms of increase in *PfHb* in pure extensional flow), and images of red cell have only been captured for limited hematocrit and fluid extensional stress [99, 110]. Cell motion under these conditions is very different from shear flow, leading to the expectation that hemolysis scales differently, as well. Though initial cell deformation is simple stretching, deformation at hemolytic levels of extensional stress remains to be experimentally documented.

For turbulent flow, distinctions between the effects of shear and extensional fluid stresses have not been explored experimentally. Observation of cells in real time has only been accomplished at low Reynolds number [64]. Post-stress images of cells from high-shear flow suggest deformation to a dumbbell shape, as well as fragmentation with rapid closure of membrane voids [111]. Hypotheses have been forwarded for the stresses that are exerted on cells that arise from the fluctuating component of velocity, as well as for the resulting cell motion and deformation, but none have been validated. Experiments carefully comparing fluctuating stresses of shear and extensional types have not been performed. Important information might be gained from such experiments, since hemolysis results differ in uniform shear, orifice flow, venturi flow and pipe flow at the same energy dissipation rate, suggesting that cells respond differently to turbulent shear and extensional stresses [75].

It would be highly beneficial to membrane-strain-based methods to experimentally document membrane response to both laminar shear and extensional stress beyond membrane-area-conserving deformation. These data would be invaluable for mechanistic hemolysis scaling models and micro-scale computational models. Hemolysis measurements in laminar extensional stress are needed for all types of hemolysis prediction methods. Such information may lead to better alternatives to scalar stress and energy dissipation for continuum-based models.

For turbulent flow, microscopic observations of cell motion and deformation are needed to validate computational models and to facilitate fluid-stress-to-membrane-stress scaling for continuum models. Such data, as well as hemolysis measurements, are needed for controlled levels of turbulent mean shear and extensional stresses, and for fluctuating shear and extensional stresses, so that universality of hemolysis prediction can be evaluated.

While this review has focused on the earlier steps leading to cell deformation, modeling of poration, rupture and hemoglobin release are essential components of hemolysis prediction. These processes may depend on the type of flow. For tank-treading in shear flow, cell membrane strain is periodic and viscous dissipation occurs continuously in the cytoplasm. Transient poration may occur as the membrane passes through the area of highest membrane tension [175]. Blebs may be pulled from the upstream and downstream ends of the cells [143]. Fatigue may also be a factor in membrane failure. In contrast for extensional flow, membrane tension is not periodic, and the cytoplasm does not circulate. Unstable rents that progress to catastrophic membrane failure may be more likely. Dumbbell shapes that pinch off in the middle, which are suggested by observations in turbulent shear flow [111] and may occur for other flows as well, would obviously cause less hemoglobin release.

The mechanisms by which hemoglobin is transferred out of the cell also need more thorough investigation. Hemoglobin may be driven from the cell by either a concentration difference or a pressure difference across the cell membrane. Recent micro-scale models have employed empirical mass transport based on concentration difference [144] or diffusive transport only [175]. Pressure-driven advection, which typically causes greater transport for large molecules with low diffusivity, may be important and may vary according to the type of fluid stress applied to the cell. Considering the difficulty of measuring the pressure inside a moving cell and the flow of hemoglobin through the membrane, computational models may be an effective means of comparing these transport mechanisms.

CHAPTER II: ANALYTICAL APPROACH

2.1 Introduction

As mentioned in previous chapter, the power-law hemolysis model is the most popular model that uses a representative scalar stress and exposure time to predict damage to red cells, across all flow conditions. The theoretical/analytical/CFD works in my research entirely revolve around different aspects of the power-law model. Particularly, section 2.2 discusses the inaccurate use of the scalar stress by some authors and introduces the corrected form. In section 2.3, the answer to the question of whether the von-Mises-like scalar stress can be a good estimator of blood damage is covered. In section 2.4, exactly the same order-of-magnitude analysis as in section 2.3 is performed, but this time on the appropriateness and accuracy of using dissipation-rate to scale hemolysis.

In section 2.5, a numerical instability is presented which appears when the power law is discretized. Finally, section 2.6 discusses issues with the Eulerian discretization of the power-law model.

2.2 Inconsistent application of the scalar stress[2]

2.2.1 Introduction

The focus of this section is not on the power law itself, but on the inconsistency of its application to flows involving more than one (shear) component of fluid stress. As was mentioned, the model was developed from data for steady, simple laminar shear, for a limited range of shear rate and exposure time. Lacking suitable data for more complex flows, the model has been extended by inserting a scalar, resultant stress σ for shear stress

---

[2] Most of the material in this section is adopted from our published work in Faghih and Keith Sharp [185].

(see section 1.3.1). While questions remain regarding whether red cells deform similarly such that their membranes fail for all possible combinations of stress tensor components that provide a given resultant stress, the concept has a ready analog in the von Mises stress, which has a long history of application in predicting yield of solid materials under static conditions. To the extent that a reduction of the fluid stress tensor to a scalar index may be useful, the purpose of this article is to clarify the appropriate form of resultant stress for extending the popular power-law hemolysis prediction algorithms to complex flows.

2.2.2 A von Mises-like fluid stress consistent with the power-law model

The von Mises stress, which is directly related to deviatoric strain energy, is given by [59]

$$\sigma_{vM} = \left[\frac{3}{2}\sigma'_{ij} : \sigma'_{ij}\right]^{\frac{1}{2}} \tag{64}$$

where $\sigma'_{ij} = \sigma_{ij} - \frac{1}{3}\delta_{ij}\sigma_{kk}$ is the deviatoric stress and σ_{ij} is the full stress. The last term represents the pressure, in which δ_{ij} is the Kronecker delta. i, j, k are tensor indices, each representing all three orthogonal coordinate axes in a three-dimensional flow. Normal stresses correspond to $i = j$ and shear stresses to $i \neq j$. Expanded forms of Eq. (64) for Cartesian coordinates x, y, z include

$$\sigma_{vM} = \left\{\frac{1}{2}\left[(\sigma_{xx} - \sigma_{yy})^2 + (\sigma_{yy} - \sigma_{zz})^2 + (\sigma_{zz} - \sigma_{xx})^2\right] \right. \\ \left. + 3\left[\sigma_{xy}^2 + \sigma_{yz}^2 + \sigma_{zx}^2\right]\right\}^{1/2} \tag{65}$$

and

$$\sigma_{vM} = \left\{\left[\sigma_{xx}^2 + \sigma_{yy}^2 + \sigma_{zz}^2\right] - \left[\sigma_{xx}\sigma_{yy} + \sigma_{yy}\sigma_{zz} + \sigma_{zz}\sigma_{xx}\right] + 3\left[\sigma_{xy}^2 + \sigma_{yz}^2 + \sigma_{zx}^2\right]\right\}^{1/2} \tag{66}$$

The constant in Eq. (64) 2 is somewhat arbitrarily chosen such that the von Mises stress equals the normal stress for purely extensional flow, e.g., $\sigma_{vM} = \sigma_{xx}$ when all other stress components are zero. This can be seen most easily in Eq. (66). Note, however, that a simple shear flow with shear stress τ, for which the symmetric stress tensor is $\sigma_{xy} =$

$\sigma_{yx} = \tau$ and all other components are zero, does not yield such a simple result. Rather the von Mises stress is the square root of three times the shear stress $\sigma_{vM} = \sqrt{3}\sigma_{xy}$.

Hemolysis modeling has historically focused on shear stress rather than normal stress. The reason may be simply related to the ease with which flows with constant shear can be created, for instance between counter-rotating concentric cylinders or between cone and plate, compared to extensional flow. Whatever the reason, existing data are predominantly for shear flows. The power-law model, the focus of this article, is no exception. The appropriate scalar stress σ for extending the power-law model must, therefore, reduce to the shear stress for simple shear flow $\sigma = \sigma_{xy} = \sigma_{yx} = \tau$. This can be accomplished with a change in the constant such that $\sigma = \sigma_{vM}/\sqrt{3}$, so that the scalar stress is given by

$$\sigma = \left[\frac{1}{2}\sigma'_{ij} : \sigma'_{ij}\right]^{1/2} \tag{67}$$

Expanded for Cartesian coordinates, the scalar stress becomes

$$\sigma = \left\{\frac{1}{6}\left[\left(\sigma_{xx} - \sigma_{yy}\right)^2 + \left(\sigma_{yy} - \sigma_{zz}\right)^2 + (\sigma_{zz} - \sigma_{xx})^2\right] + \left[\sigma_{xy}^2 + \sigma_{yz}^2 + \sigma_{zx}^2\right]\right\}^{1/2} \tag{68}$$

and

$$\sigma = \left\{\frac{1}{3}\left[\sigma_{xx}^2 + \sigma_{yy}^2 + \sigma_{zz}^2\right] - \frac{1}{3}\left[\sigma_{xx}\sigma_{yy} + \sigma_{yy}\sigma_{zz} + \sigma_{zz}\sigma_{xx}\right] + \left[\sigma_{xy}^2 + \sigma_{yz}^2 + \sigma_{zx}^2\right]\right\}^{1/2} \tag{69}$$

From both Eqs (68) and (69), it is easy to see that $\sigma = \sigma_{xy} = \sigma_{yx}$ when all other stress components vanish.

2.2.3 The Bludszuweit scalar stress

Let us compare this scalar stress to Bludszuweit's formula [61, 186]

$$\sigma = \left[\frac{1}{6}\sum(\sigma_{ii} - \sigma_{jj})^2 + \sum\sigma_{ij}^2\right]^{1/2} \tag{70}$$

This formula uses the convention that the summations do not include terms for which $i = j$ Now $\sigma_{ii} - \sigma_{jj} = \sigma_{jj} - \sigma_{ii}$, and $\sigma_{ij} = \sigma_{ji}$ because the stress tensor is symmetric, so the expanded formula becomes

$$\sigma = \left\{\frac{1}{3}\left[(\sigma_{xx} - \sigma_{yy})^2 + (\sigma_{yy} - \sigma_{zz})^2 + (\sigma_{zz} - \sigma_{xx})^2\right] + 2\left[\sigma_{xy}^2 + \sigma_{yz}^2 + \sigma_{zx}^2\right]\right\}^{1/2} \tag{71}$$

or

$$\sigma = \left\{\frac{2}{3}\left[\sigma_{xx}^2 + \sigma_{yy}^2 + \sigma_{zz}^2\right] - \frac{2}{3}\left[\sigma_{xx}\sigma_{yy} + \sigma_{yy}\sigma_{zz} + \sigma_{zz}\sigma_{xx}\right] + 2\left[\sigma_{xy}^2 + \sigma_{yz}^2 + \sigma_{zx}^2\right]\right\}^{1/2} \tag{72}$$

There is nothing fundamentally wrong with this formula. The scalar stress is merely a representative scale for the state of stress that is hypothesized to correlate with membrane failure in red cells. However, one thing upon which we must insist is that it be consistent with the power-law model in the limit of σ devolving into pure shear. Comparing Eqs (71) and (72) to Eqs (68) and (69), it is evident that Bludszuweit's formula gives $\sigma = \sqrt{2}\,\tau$ in pure shear flow for which $\sigma_{xy} = \sigma_{yx} = \tau$ and all other stress components are zero. The hemolysis predictions using σ in the power-law model are, therefore, $2^{\beta/2}$ times larger than those using τ. For this reason Eqs (70), (71) and (72) are not proper for use with the power-law model.

It seems that Bludszuweit intended the correct scaling. The mistake appears to arise in Bludszuweit's thesis [186] in assumptions leading to equation 4.7, which does not take into account that $\sigma_{zr} = \tau$, in addition to $\sigma_{rz} = \tau$ in Poiseuille flow in a pipe with r and z as the radial and axial coordinates. The corrected equation 4.7 is

$$W_s = \frac{1}{12G}[12\sigma^2] \tag{73}$$

where W_s is strain energy and G is the shear modulus, which yields a different equation 4.8 for scalar stress, as well. The corrected equation is

$$\sigma = \left[\frac{1}{12}\sum(\sigma_{ii} - \sigma_{jj})^2 + \frac{1}{2}\sum \sigma_{ij}^2\right]^{1/2} \tag{74}$$

which is smaller by a factor of $1/\sqrt{2}$ than the original equation 4.8. Note also that the summations are unnecessary, because summation is implicit in the tensor notation, so this equation can be simplified to

$$\sigma = \left[\frac{1}{12}(\sigma_{ii} - \sigma_{jj})^2 + \frac{1}{2}\sigma_{ij}^2\right]^{1/2} \tag{75}$$

and it is important to also specify that the $i \neq j$ rule is applied.

2.2.4 Inconsistent application of scalar stress

Those who used the corrected scalar stress include Apel, et al. [187], Yano, et al. [157], Arvand, et al. [188], Zhang, et al. [162], Chua, et al. [189], Alemu and Bluestein [62], de Tullio, et al. [190], Segalova, et al. [191] , Ezzeldin, et al. [142] and Ishii, et al. [73]. Those who used the original incorrect form of the scalar stress with the power-law model include Mitoh, et al. [156], Throckmorton, et al. [192], Wu, et al. [158], Dongdong, et al. [193], Kennington, et al. [194], Fraser, et al. [17], Taskin, et al. [163] and Soares, et al. [195]. Studies for which it is unclear which form of scalar stress was used because the equation is not given include De Wachter and Verdonck [196], Untaroiu, et al. [197] and Giridharan, et al. [198]. Nakamura, et al. [199] used the incorrect scalar stress, but only to test its correlation with membrane strain in a numerical model of flow-induced cell deformation. While Chen and Sharp [100] and Chen, et al. [173] developed a strain-based model, rather than using the power-law model, their model used the corrected scalar stress. Arora, et al. [170] calibrated their strain-based model to the power law using the corrected scalar stress. Garon and Farinas [160] used the von Mises stress in the power-law model, rather than the scalar stress.

The scalar stress representation of the fluid stress tensor has also been used for platelet activation as it relates to thrombogenesis, e.g. [200-202]. Two of these articles focus on techniques for Lagrangian particle tracking for estimating platelet activation, but also mention that the same principles apply to hemolysis [201, 202]. These three references all use the scalar stress coefficient that is correct for power-law hemolysis. While predicting platelet activation requires separate validation experiments that could legitimately be fit to a different form of scalar stress, it is fortunate for the community of investigators studying both types of blood damage that the precedent from earlier hemolysis research has been followed.

The effect of the incorrect coefficient on the conclusions of the studies depends on the details of the flow, the version of the power-law model used and how it is applied, as well as on how the results are compared. However, one example involving the predominance of a single event of uniform stress provides the opportunity to estimate the effect without processing the full flow field. In the passage through the gap between a spinning rotor and a stationary housing (the Hemolyzer-H device), in which the stress is primarily a single event of constant shear [163], a straightforward application of the power-law models with corrected scalar stress provides estimated hemolysis that is $2^{\beta/2} = 2.31$, 1.994 and 1.994 times lower for the Giersiepen, et al. [140], ($\beta = 2.416$), Heuser and Opitz [139] ($\beta = 1.991$) and Zhang, et al. [146] ($\beta = 1.9918$) models, respectively. To the extent that these factors scale those based on the more complex stress histories along streamlines through the device, conclusions would change regarding which model and which method of application is closest to the experimental results. However, this study highlights another potential inconsistency among studies using the original form of the scalar stress. Taskin, et al. [163] validated their CFD-derived scalar stress versus the analytical value of shear stress in the annular gap, and obtained good agreement. Using Eq. (70), a match should not exist unless perhaps the stress component symmetric with the shear stress was ignored, as Bludszuweit [186] apparently did. If one of each of the components of the symmetric pairs of shear stresses were ignored in three-dimensional flow, then the shear components of the scalar stress would scale correctly but the normal components would still be over-represented by a factor of $\sqrt{2}$. Other studies using the incorrect scalar stress may or may not have neglected some stress components. Further, the convention of omitting from Eq.

(70) components for which $i = j$ is typically not confirmed in the papers. These uncertainties leave questions regarding the conclusions in articles utilizing Eq. (70).

2.2.5 Conclusions

The correspondence of the von Mises-like scalar stress to hemolysis is not a law based on physical principles, but rather is a hypothesis that at this time still remains to be tested. It is possible that a different scalar measure of the state of fluid stress may prove to provide better correlations. Alternatives include the maximum principle stress difference, which has been compared to the von Mises stress [161]. Another common alternative scale is the maximum shear stress, which has not yet been evaluated. Experiments show that erythrocytes deform more readily in extensional flow than in shear flow of the same stress magnitude [101], suggesting that the scalar stress should more strongly weight extensional stress [98].

Further challenges are presented in developing reliable predictions of hemolysis. For instance, sublytic damage accumulation eventually leading to hemolysis at lower levels of fluid stress is a popular concept [155]. How such sublytic damage correlates with the scalar stress versus the full stress tensor is an important, related question. In addition, a recent model [176] supports the idea that membrane failure comprises diffusive transport through temporary pores in an otherwise intact membrane at low stress [144] and large-scale rupture at high stress (as assumed by many early models), which adds another layer of complexity to this challenging problem.

Regardless of the additional complexities, identifying a resultant stress, or a simplified combination of stresses that adequately represents the more complex stress tensor for hemolysis prediction remains an attractive and potentially useful goal for further research. However, to unambiguously validate such a scalar stress, new experiments in shear and extensional flows, and in controlled combinations of these in varying proportions, are needed to quantify the effects of different types of stress on red cell damage.

2.3 Scalar stress as a predictor of hemolysis[3]

2.3.1 Introduction

An unresolved question is whether membrane tension scales similarly with fluid stresses of different types. Three independent components each of shear and extensional stresses occur in laminar flow. Although physiological blood flow is mainly laminar, flow in cardiovascular devices may also be turbulent. Turbulent flows are associated with eddies of different length and time scales, each of which may have different impacts on particles suspended in the plasma. Therefore, to develop a comprehensive hemolysis model valid for all types of flow, interaction of red cells with swirling turbulent eddies of different sizes, or with the Reynolds stresses that characterize turbulent velocity fluctuations, must be examined and quantified.

2.3.1.1 Membrane tension in laminar shear flow

The model of Tran-Son-Tay, et al. [179] provides cell membrane tension for the tank-treading case. Based on the original of Keller and Skalak [86] this model uses an idealized viscoelastic ellipsoidal cell, tank-treading within a pure shear flow with an inclination angle equal to θ (Fig. 1.14).

Note that the membrane and cytoplasm velocity fields prescribed by Keller and Skalak (1982) do not provide local area conservation. However, membrane tension is calculated from surface tractions, rather than membrane deformation, which limits the error created by this assumption to 30% [179]. Disturbance of the fluid external to the membrane by the membrane motion is not taken into consideration, thus avoiding the complication of the full fluid-solid interaction problem.

The membrane is assumed to have zero thickness and mass, thus no momentum nor bending stresses exist in the membrane. Therefore, the state of stress for an arbitrary membrane element, as shown in Fig. 1.15, can be defined by two in-plane normal stresses, σ_{φ} tangent to the streamline and σ_{α} perpendicular to the streamline, and an in-plane shear stress, τ_m.

For more details about this model, please refer to section 1.7.2.2.

2.3.1.2 Membrane tension in laminar extensional flow

For the case of pure extensional flow, the model of membrane tension by Chen and Sharp [100] can be used. In this model, the cell is approximated as a viscoelastic prolate ellipsoid with axes aligned with the principal axes of the flow. Therefore, the three principal stresses σ_1, σ_2 and σ_3 correspond to the ellipsoidal axes *X*, *Y* and *Z*, respectively. The membrane tension is calculated around the circumference, C_e, where the maximum tension is located. For more details about this model, please refer to section 1.7.2.1.

Note that in the case of pure extensional flow, a point anywhere on the membrane experiences a constant tension over time, unlike pure shear flow, in which membrane tank-treading results in periodic tension

2.3.1.3 Fluid stresses applied to cells in turbulent flow

Turbulent flow is characterized by fluctuating eddies of different size and fluctuation frequencies, in addition to the mean flow. Therefore, quantities, such as velocity and pressure, can be decomposed into two parts, namely average and fluctuation. The mean velocities contribute a stress tensor analogous to the laminar flow case. In addition, this decomposition adds Reynolds stresses in the form of $\rho \overline{u_\iota' u_j'}$ to the Navier-Stokes equation. The Reynolds stress is also a tensor with three normal and six shear components. Hence, additional unknowns are present in the problem, which requires a closure model to relate the fluctuating velocities to the mean velocities.

It is still an open question as to which type of stress is most responsible for red cell membrane damage in turbulent blood flow, because the mechanisms of damage are not well established. Almost all the theories that have been developed so far for prediction of hemolysis in turbulent flow have stopped short of incorporating a relationship between fluid stress and the actual tension in the cell membrane.

First, Jones [136] argued that Reynolds stress cannot be a good estimator of hemolysis in turbulent flow, as it is not an actual physical load on the cell. This perspective suggests that membrane tension does not correlate with Reynolds stress, but rather depends on the turbulent viscous stress alone.

Quinlan and Dooley [63] forwarded a second theory conceptualizing the microscopic flow around a cell, modeled as a sphere, within an eddy (Fig. 2.3). Because the Reynolds number based on cell size is small, the flow at this level is essentially laminar. Using the experimental data of turbulent flow through a prosthetic heart valve from Liu, et al. [180], they estimated the shear stress experienced by the cell for two cases: accelerating flow characterized by the temporally fluctuating velocity, and quasi-steady shear scaled by the rotational velocity of the vortex. It was found that the estimated stresses in both cases (12 dyn/cm^2 and 56 dyn/cm^2, respectively) were at least an order of magnitude smaller than the measured Reynolds stress, 520 dyn/cm^2.
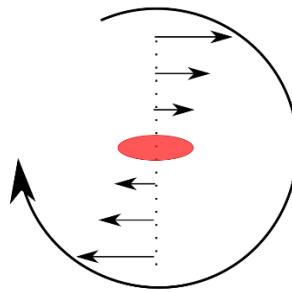
Fig. 2. 1 A red cell being sheared inside a turbulent eddy (not to scale)

Antiga and Steinman [183] used an alternative order of magnitude analysis to estimate shear stress on a cell passing between co-rotating vortices (Fig. 2.4). They chose vortices of 100 μm diameter, and used a typical hematocrit to estimate the plasma-filled gap between prolate ellipsoidal cells. Again using the experimental data of Liu, et al. [180], it was found that a shear stress of around 160 dyn/cm^2 would be applied to the cell.
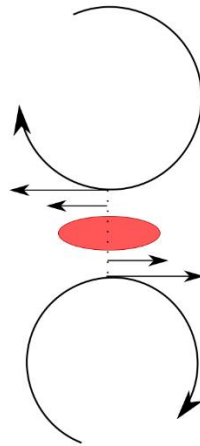
Fig. 2. 2 A red cell sandwiched between two co-rotating eddies (not to scale)

Counter-rotating eddies (Fig. 2.5) also occur in turbulent flow, but models for estimating the stress on cells between such eddies have not been reported.
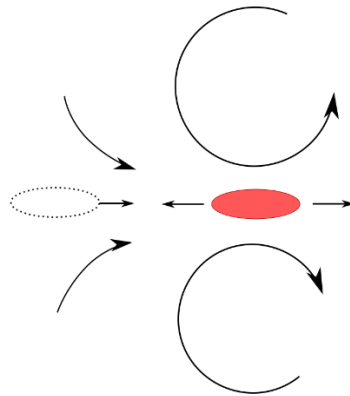
Fig. 2. 3 A red cell exposed to extension between two counter-rotating eddies (not to scale)

The history of stress applied to a red cell may be more complicated. It might be trapped inside a vortex until the eddy is dissipated into smaller eddies (i.e., the energy cascade) or be swallowed by another eddy of a similar or different size. Additionally, the RBC may be transferred to the space between two eddies that are either co-rotating or counter-rotating. Each condition imposes a different stress on the cell. Over long time scales, the cell may follow a chaotic path through a turbulent flow, which may require probabilistic methods to model.

Membrane tension has not been estimated in turbulent flows. In this paper, several simplified cases of fluid stress histories within turbulent flow are considered for the purpose of exploring the range of membrane responses that may result.

2.3.2 Methods

To test the plausibility of the scalar stress hypothesis, this paper will compare analytical estimates of membrane tensions in laminar shear flow and laminar extensional flow, as well as estimates derived from three concepts of cell motion in turbulent flow. The same scalar stress, 520 dyn/cm^2, will be used in each case. Differences in predicted membrane tension among the cases will imply that scalar stress is not a reliable index for quantifying hemolysis.

2.3.2.1 Membrane tension in laminar shear flow

For the case of pure shear stress, the model of membrane tension developed by Tran-Son-Tay, et al. [179] was used. Since we are only concerned with the membrane stress around the tank-treading strip C_0 that lies in the x-y plane (i.e. z=0), σ_α is always parallel to the z axis (Figs. 1.14 and 1.15). Due to symmetry, τ_m is zero along the strip C_0.

While the original Keller and Skalak [86] model assumed a uniform internal pressure, the Tran-Son-Tay, et al. [179] model yields a different internal pressure for each point on the membrane. In order to comply with the Keller and Skalak model, a constant average intracellular pressure is assumed in the Tran-Son-Tay et al. model. Pressure at the cell tip, point (a, 0) in Fig. 1.15, (i.e. location I in the Tran-Son-Tay et al. original paper) was used to calculate the membrane tension, since other pressure values show unstable behavior at high shear rates. Finally, the membrane tensions are given by

$$T_\alpha = \frac{1}{\sqrt{(a\ sin\varphi)^2 + (b\ cos\varphi)^2}} \{T_1{}^\alpha\ cos2\varphi + T_2{}^\alpha\ sin2\varphi + T_3{}^\alpha\} \qquad (76)$$

$$T_\varphi = \sqrt{(a\ sin\varphi)^2 + (b\ cos\varphi)^2}\ \{T^\varphi\} \qquad (77)$$

where $T_1{}^\alpha$, $T_2{}^\alpha$, $T_3{}^\alpha$ and T^φ are functions of the shear rate as defined in the Appendix A. The biaxial tension that causes membrane poration or failure is then

66

$$T = \sqrt{T_\alpha{}^2 + T_\varphi{}^2} \tag{78}$$

Note that φ is the angle in the x^*-y^* plane counterclockwise with $\varphi = 0$ being the x^* axis, where the x^*-y^* coordinates are those resulting from mapping the ellipsoid in x-y coordinates into a sphere. The corresponding angle in the x-y plane is denoted as ω and its relation with φ is

$$\tan(\omega) = \frac{\tan(\varphi)}{a/b} \tag{79}$$

Numeric values for the input parameters needed to calculate the membrane tension in a pure shear flow based on the Tran-Son-Tay, et al. [179] model are listed in Table 2.1. Tran-Son-Tay et al. (1987) used an elevated external viscosity that matched that of experiments used to measure tank-treading orientation and velocity. In this study, whole blood viscosity (0.0035 Pa s) was used. Even though low-viscosity plasma is the fluid actually in contact with the cell, within the bounds of a continuum model, inserting the effective viscosity of the suspension mimics the effect of the suspension on the shear exerted on the cell. The internal viscosity was set to 0.006 Pa s, as measured for hemoglobin at physiologic concentration and at body temperature [203-205].

Table 2. 1 Input values used to calculate membrane tension in pure shear flow with shear stress of 520 dyn/cm^2

Parameter	Symbol	Units	Value
Major radius of cell in x direction	a	*μm*	*7.93*
Minor radius of cell in y direction	b	*μm*	*1.19*
Minor radius of cell in z direction	c	*μm*	*2.42*
Angle of inclination	θ	*degrees*	*12.1*
External fluid viscosity	η_o	*Pa.s*	*0.0035*
Internal fluid viscosity	η_i	*Pa.s*	*0.006*
Membrane shear modulus of elasticity	μ_m	*N.m^{-1}*	6×10^{-6}
Membrane component of viscosity	η_m	*N.m^{-1}.s*	0.6×10^{-6}

Note that the resulting tensions T_φ, T_α and T are periodic in time at each point on the cell membrane as it tank-treads around the cell content. A sample plot of the periodic membrane tensions in pure shear flow is shown in Fig. 2.4.
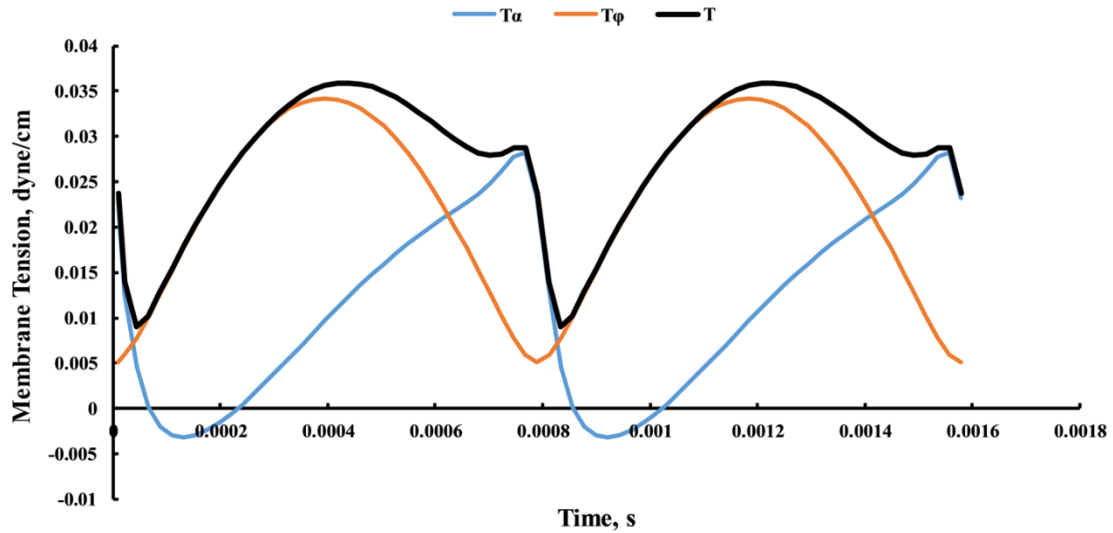
Fig. 2. 4 Periodic cell membrane tension in a tank-treading motion (based on values in Table 2 and for shear rate of 3000 s^{-1}

2.3.2.2 Membrane tension in laminar extensional flow

For the case of pure extensional flow, the model of membrane tension by Chen and Sharp [100] is used. The preferred Chen and Sharp model includes a critical stress below which no biaxial membrane tension occurs. However, due to the limited scalar stress used for this comparison, which was dictated by the available turbulent flow data [180], it was necessary to use the reduced model of Eq. (63) without a threshold to obtain positive membrane tension. $b = 1.7\,\mu m$ (from Chen and Sharp) was used for this model.

2.3.2.3 Membrane tension in turbulent flow

Three cases corresponding to different locations of the cell with respect to eddies (Figs. 2.1-2.3) are analyzed in the following subsections. The same experimental data by Liu, et al. [180] for turbulent flow downstream of a prosthetic heart valve employed by Quinlan and Dooley [63] and Antiga and Steinman [183] was used for each case. The energy spectral density curve normalized by the root mean square of the velocity fluctuations for the centerline 7.8 mm downstream of the valve at peak flow is shown in Fig. 11. At this point, the scalar Reynolds stress was 520 dyn/cm^2 (Quinlan and Dooley [63]. Due to experimental limitations, Liu et al. only reported data up to the turbulent frequency of 5 kHz. Therefore, for data above this frequency, extrapolation proposed by Quinlan and Dooley [63] (curve E3 in their article) was used to plot Fig. 2.5.
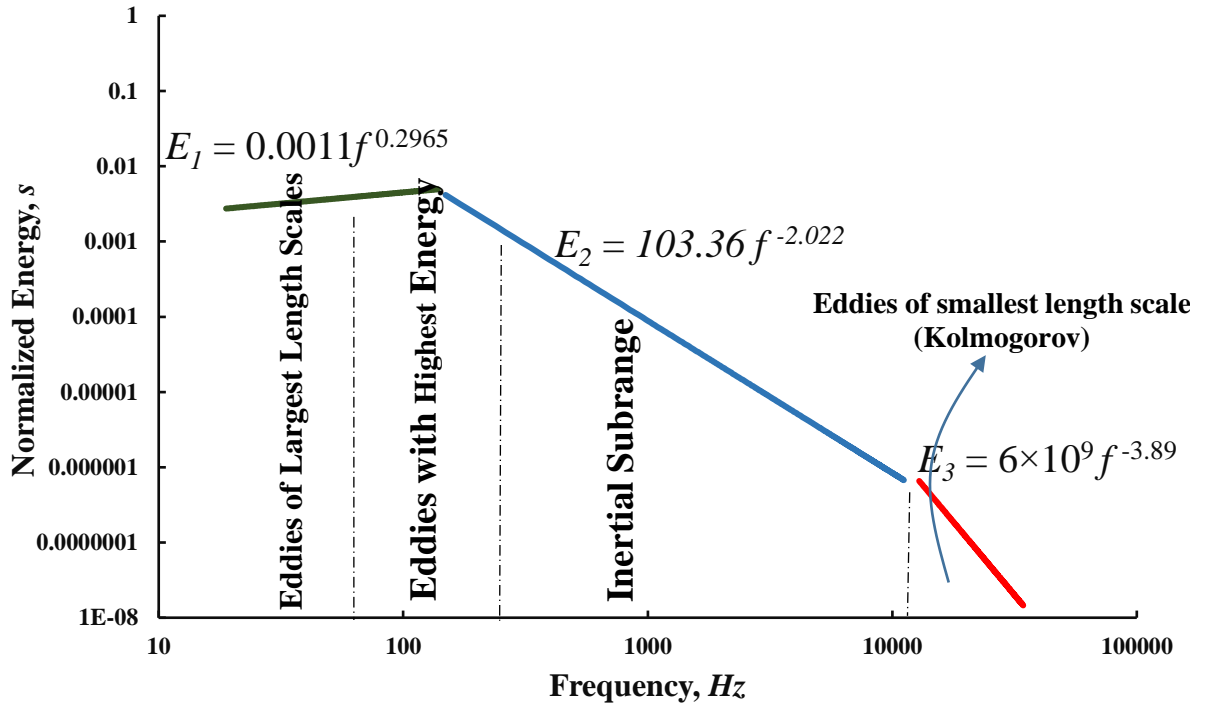
Fig. 2. 5 Normalized energy spectral density for flow downstream of a valve (data of Liu, et al. [180])

Liu, et al. [180] defined normalized energy spectral density such that the velocity fluctuation within the frequency band f_1 and f_2 is equal to

$$u' = u'_{rms} \sqrt{\int_{f_1}^{f_2} E(f)\, df} \tag{80}$$

where $E(f)$ and u'_{rms} are the normalized energy spectral density and the root mean square of velocity fluctuations, respectively. u'_{rms} was equal to 0.2 m/s (experimental data of Liu, et al. [180] as interpreted by Quinlan and Dooley [63]). The data up to 130 Hz can be fitted by the following power law equation

$$E_1(f) = 0.0011\, f^{0.2965} \tag{81}$$

The data within the range 130 Hz to 10 kHz can be approximated by

$$E_2(f) = 103.36\, f^{-2.022} \tag{82}$$

69

and above 10 kHz

$$E_3(f) = 6 \times 10^9 \, f^{-3.89} \tag{83}$$

While it is still an open discussion which turbulent eddy size is most damaging to the cell, Quinlan [57] argued that the energy content of an eddy, as well as the energy distribution across different length and time scales, must be considered for analysis of the potential cell damage in turbulent flow.

To demonstrate the effect of eddy size, results will be obtained for eddies with the greatest energy content and for Kolmogorov eddies. For the Liu, et al. [180] data, the eddies with the greatest energy content ranged in frequency range from 100 to 200 Hz. Based on Taylor's hypothesis, turbulent frequency of an eddy with a characteristic length l is equal to $\frac{U}{l}$ where U is the mean velocity of the bulk flow. With the mean velocity being around 1.7 m/s (data of Liu et al. as interpreted by Quinlan and Dooley [63]), the corresponding length scales for the frequency range of 100 to 200 Hz are 17 to 8.5 mm, respectively. Since these length scales are much larger than the RBC size, it is reasonable to assume that the cell may tank-tread within a laminar shear flow inside the eddy. Because this frequency range spans the curve fits of Eqs. (81) and (82), both are used in Eq. (83) to calculate the velocity fluctuation of the eddies

$$u' = 0.2 \sqrt{\left(\int_{100}^{130} 0.0011 \, f^{0.2965} \, df\right) + \left(\int_{130}^{200} 103.36 \, f^{-2.022} \, df\right)} = 0.2 \times 0.386 = 0.077 \, ms^{-1} \tag{84}$$

Using the average length scale of 12.75 mm, the shear rate inside the eddy is estimated as $\frac{u'}{l} = 6.039$ s^{-1}.

Eddy lifetime is also needed to characterize the exposure of cells to this shear. Using order of magnitude estimates, lifetime of an eddy can be approximated as l/u' [80] which is equal to the reciprocal of the estimated shear rate inside the eddy. Again, taking $l = 12.75$ mm, the eddy lifetime is 0.166 s.

Using the Kolmogorov length-scale of 46 μm, reported by Liu, et al. [180] and following the same procedure as above, the fluctuating velocity, shear rate inside the eddy and lifetime can be calculated as 0.015 m/s, 326 s⁻¹ and 3×10^{-3} s, respectively.

Membrane tension for shear flow inside an eddy

When a cell is inside an eddy, it is subjected to a spatial velocity gradient equal to $\frac{u'}{l}$. Since the flow inside an eddy (Fig. 2.1) on the scale of the cell is laminar, the Tran-Son-Tay, et al. [179] model can be used to estimate the membrane tension for the cell. In this case, the scalar stress is equal to the laminar shear stress $\eta_o \frac{u'}{l}$.

According to Tran-Son-Tay, et al. [179], the tank-treading frequency of the cell inside a pure shear flow is around 0.21 times the shear rate, i.e., 1.274 Hz for the high-energy eddies and 68.786 Hz for Kolmogorov eddies. Regardless of the eddy size, the cell membrane only completes 21% of a tank-treading rotation before the eddy is broken down into smaller eddies or dissipates. Subsequently, the cell may experience a number of different fluid dynamical environments within the turbulent flow. However, for the sake of comparison among cases, the results are plotted as if the cell is repeatedly sheared within identical eddies, such that it completes multiple tank-treading rotations.

Dooley & Quinlan (2009) calculated that a 2D circular model of a red cell took a dimensionless time $\dot{\gamma}t$ of 28.6 to approach steady-state tank treading. While this time for a more realistic 3D cell may be somewhat different, the Quinlan and Dooley [63] criterion gives estimates of time to approach steady state of 4.77 s and 0.0877 s for highest-energy and Kolmogorov eddies, respectively. These times are significantly longer than the eddy lifetimes of 0.166 s and 0.003 s, respectively. While cells entering the eddy with the orientation matching that of tank treading might more immediately achieve steady state, this criterion suggests that most cells experience predominantly transient motion. Again, for the sake of comparison, the steady state solution was used.

Membrane tension for shear flow between co-rotating eddies

For the second case, cells are considered to be sheared between two co-rotating eddies (Fig. 2.2). The eddies are assumed to have the same turbulent characteristics as

described above. The shear rate applied to the cell, however, depends on the distance between the vortices, and is approximated by $2\,u'/h$ where h is the distance between the two co-rotating eddies. Distance h is estimated as the cell's minor axis plus two times the distance between the cell and each eddy. The latter distance was estimated by Antiga and Steinman [183] based on the maximum packing density of prolate ellipsoids with 1.8 aspect ratio (major and minor axes equal to 8.24 and 4.5 μm, respectively), which gives a value of 0.74 μm. Therefore, h is approximately 5.98 μm. Finally, the shear rate between high energy eddies is estimated as 25,752 s^{-1} and between Kolmogorov eddies as 5,017 s^{-1}. The Tran-Son-Tay, et al. [179] model is again used to estimate cell membrane tension. Although the lifetimes of the eddies are again 0.166 s and 3×10^{-3} s for the high energy and Kolmogorov eddies, respectively, the cell is able to complete many tank-treading cycles because of the higher shear rate compared to the first case. Steady state is a good assumption for the high energy eddies, since the Quinlan and Dooley [63] time constant of 0.00111 s is much smaller than the eddy lifetime. The time constant of 0.0057 s for Kolmogorov eddies is of the same order as its lifetime, thus transient behavior may be important

Membrane tension for extensional flow between counter-rotating eddies

Both co-rotating and counter-rotating eddies occur in turbulent flow, thus the third case represents a cell swept between two counter-rotating eddies (Fig. 2.3). In this case, the cell experiences a laminar extensional strain rate equal to $2\,{\partial u}/{\partial x} \sim 4\,{u'}/{l}$. This results in an extensional strain of 24 s^{-1} for the high-energy eddies and 1,304 s^{-1} for the Kolmogorov eddies, respectively. Chen and Sharp [100] model of cell membrane tension is used for this case, since it is based on extensional flow. The cell is assumed not to tank-tread, which corresponds to cells that are pulled exactly in the middle between identical vortices. Therefore, the cell membrane tension is constant. The results are again plotted as if the cell repeatedly experiences the same condition.

2.3.2.4 Parametric sensitivity

The sensitivity of membrane tension to parameters in each model was evaluated with sensitivity defined as

$$Sen(T, z) = \frac{\partial logT}{\partial logz} \tag{85}$$

where T is membrane tension and z is the parameter. The derivative was approximated by increasing and decreasing the value of each parameter by 5% and averaging the resulting changes in membrane tension.

2.3.3 Results

Membrane tensions for cells in the two laminar and three turbulent flow cases, each with the same scalar stress of 520 dyn/cm^2, are compared in Figs. 2.6 and 2.7. For laminar extensional flow, this scalar stress causes a constant membrane tension of 3.748 dyn/cm on the membrane strip C_e.

For the laminar shear flow, a periodic membrane tension results on strip C_0 as it tank-treads around the intracellular content. The peak tension is two orders of magnitude lower than that of the laminar extension case.

For shear flow between co-rotating eddies, membrane tension is again periodic, with the maximum tension being an order of magnitude smaller than that of the laminar extensional case. The frequency of tank-treading in this case is an order of magnitude faster than the laminar shear case.

For extensional flow between counter-rotating eddies, membrane tension is constant and is the lowest among all the cases, about three orders of magnitude less than for laminar extension.

Since the frequency of tank-treading for a cell inside an eddy is two orders of magnitude slower than for laminar shear, this case is plotted separately in Fig. 2.7. The magnitude of membrane tension is less than for laminar shear, but more than for the turbulent extension case. The waveform shape is distinct from the other shear cases, with lower secondary peaks between the main peaks.
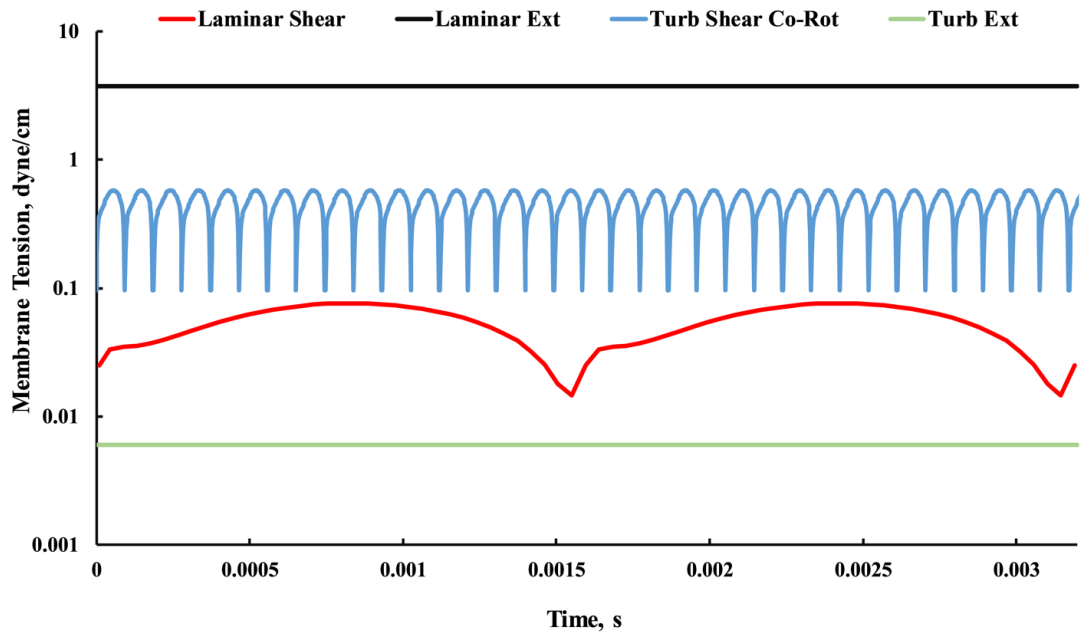
Fig. 2. 6 Cell membrane tension for different laminar and turbulent cases having the same scalar stress. The turbulent cases are for eddies of the highest energy content. (Laminar shear - laminar shear stress, Laminar ext - laminar extensional stress, Turb shear co-rot - turbulent shear stress between co-rotating vortices, Turb shear inside - turbulent shear stress inside a vortex, Turb ext - turbulent extensional stress between counter-rotating vortices)
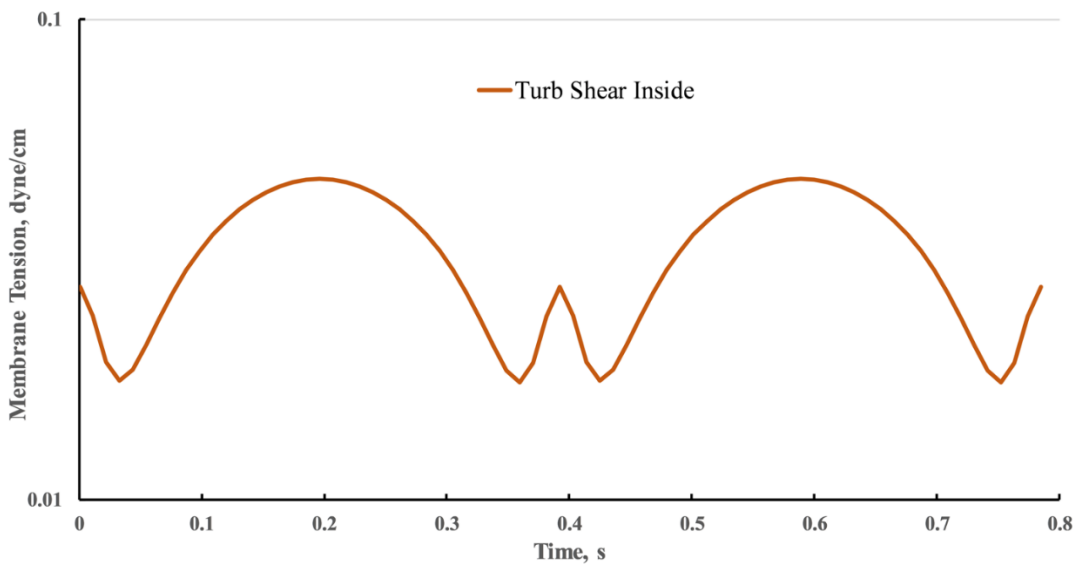
Fig. 2. 7 Cell membrane tension for the case of a tank-treading cell inside a turbulent eddy with scalar stress being equal to cases shown in Fig. 2.6 (See Fig. 2.6 caption for a key to the abbreviations)

74

Insight into the effect of eddy size can be gained from a comparison of Fig. 2.6 and 2.7 for eddies of the highest kinetic energy content to Fig. 2.8 with eddies of Kolmogorov size. In Fig. 2.8, which shows only the turbulent cases for Kolmogorov eddies, membrane tension for extension between counter-rotating eddies is about two orders of magnitude higher than for high energy eddies, and, remarkably, is the highest among the Kolmogorov cases. Membrane tension for shear between co-rotating eddies is lower and tank-treading frequency is lower, as well. For shear inside an eddy, tension and tank-treading frequency are both increased, but are still lower than for shear between co-rotating eddies.
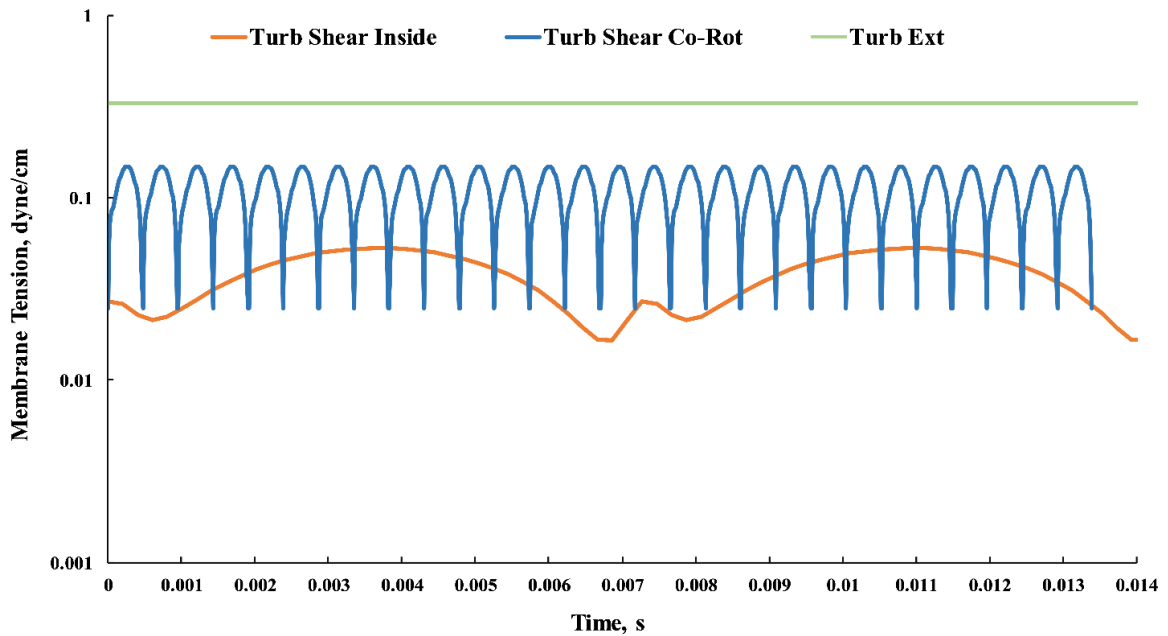
Fig. 2. 8 Cell membrane tension for eddies of Kolmogrov scale, with the same scalar stress as for high energy eddies (See Fig. 2.6 caption for a key to the abbreviations)

Exposure time to turbulent stress is strongly influenced by vortex lifetime. For a cell tank-treading inside an eddy, the cell membrane is not able to complete a tank-treading cycle (Table 2.2). With eddy lifetime scaling as the reciprocal of the shear rate inside the eddy, the number of cycles is independent of eddy size.

Table 2. 2 Summary of results for eddies of highest energy content and Kolmogorov scale (See Fig. 2.6 caption for a key to the abbreviations)

75

Type of Eddies	Turbulent Case	Exposure Time (i.e., Eddy Lifetime), s	Number of Tank-treading Cycles	Maximum Membrane Tension, dyn/cm
Highest energy content	Turb Shear Inside	0.166	0.21	4.7×10^{-2}
	Turb Shear Co-Rot	0.166	897	57.8×10^{-2}
	Turb Ext	0.166	Not applicable (constant strain rate)	0.6×10^{-2}
Smallest length scale (Kolmogorov eddies)	Turb Shear Inside	3×10^{-3}	0.21	5.3×10^{-2}
	Turb Shear Co-Rot	3×10^{-3}	3	14.8×10^{-2}
	Turb Ext	3×10^{-3}	Not applicable (constant strain rate)	32.9×10^{-2}

However, for a cell sheared between two co-rotating vortices, the cell tank-treads more rapidly, due to the higher shear rate in this case (Table 2.2). The number of cycles is much higher for the high-energy vortices than for Kolmogorov eddies.

Parametric sensitivity – Sensitivities, as quantified by Eq. (85), of membrane tension to parameters in each model are shown in Tables 2.3 and 2.4. Because the extensional flow model is linear with its three parameters, all sensitivity values are the same and membrane tension changes are proportional to those for each parameter (Table 2.3). The most sensitive parameters for the other models based on shear flow are a for laminar shear (for which a 5% change in a results in a 6.6% change in membrane tension), C_0 for turbulent shear inside an eddy (a 5% change in C_0 results in a 10.6% change in membrane tension) and a for turbulent shear between co-rotating eddies (a 5% change in a results in a 8.3% change in membrane tension).

Table 2. 3 Sensitivity of membrane tension in extensional flow cases

	K	b	$\square$
Laminar Ext	0.187	0.187	0.187
Turb Ext	3×10^{-3}	3×10^{-3}	3×10^{-3}

Table 2. 4 Sensitivity of membrane tension in shear flow cases

	a	b	c	C_0	θ	$\dot\gamma$	η_o	η_i	μ_m
Laminar Shear	5.1×10^{-3}	-3.5×10^{-3}	-5.0×10^{-3}	4.9×10^{-3}	1.4×10^{-3}	1.5×10^{-3}	1.5×10^{-3}	1.6×10^{-5}	2.3×10^{-3}
Turb Shear Inside	2.0×10^{-3}	-3.2×10^{-3}	-3.7×10^{-3}	4.9×10^{-3}	5.6×10^{-6}	6.1×10^{-6}	6.1×10^{-6}	0	1.8×10^{-3}
Turb Shear Co-Rot	4.8×10^{-2}	-8.9×10^{-3}	-1.7×10^{-2}	4.4×10^{-3}	2.3×10^{-2}	2.7×10^{-2}	2.4×10^{-2}	2.4×10^{-3}	2.1×10^{-3}

2.3.4 Discussion

In turbulent flow, red cells may interact with eddies of different length and time scales, resulting in different types of fluid stress and levels of membrane tension. In reality, it is unlikely that the cells experience pure shear or pure extensional stress, but more likely

a combination of both. However, there may be regions in the flow field where one type of stress dominates, diminishing the effect of the other type of stress. With this in mind, a more realistic, though still simplified, membrane tension history in turbulent flow is depicted in Fig. 2.9. (Maximum membrane tension only is plotted for each case.) In the sample history shown in Fig. 2.9, the cell begins by tank-treading within an eddy of the highest energy content, applying a pure shear on the cell membrane. After the eddy breaks down, the cell experiences extensional strain by flowing between two counter-rotating eddies of the same size as the previous one and then get trapped inside another high-energy eddy. After the eddy's break-down, the cell is sheared between two co-rotating eddies, experiencing its high shear stress and membrane tension. Note that each time the cell tank-treads inside an eddy, a different part of the membrane may experience high tension, because the eddy's lifetime is shorter than the tank-treading period. Further, each eddy or pair of eddies that the cell encounters may be of different sizes, which influences the level of fluid stress. Adjacent eddies of dissimilar size are likely, with shear stresses between two co-rotating eddies being intermediate to the two cases included here. Counter-rotating eddies of dissimilar size create a combination of shear and extensional stress.

Furthermore, to plot Fig. 2.9, it was assumed that the cell interacts with eddies of the same length and time scale. In reality, the cell might interact with eddies of different time and length scales, resulting in a stress history significantly different than shown in Fig. 2.9. As an example, the cell may be trapped between two counter-rotating Kolmogorov eddies, thus experiencing a much higher membrane tension (32.9×10^{-2} dyn/cm versus 0.6×10^{-2} dyn/cm) than for the counter-rotating eddies of highest energy content. For any pair of eddies, but particularly for small eddies, viscous dissipation would cause the fluid stresses between them to decrease with time, rather than remain constant as implied in Fig. 2.9.
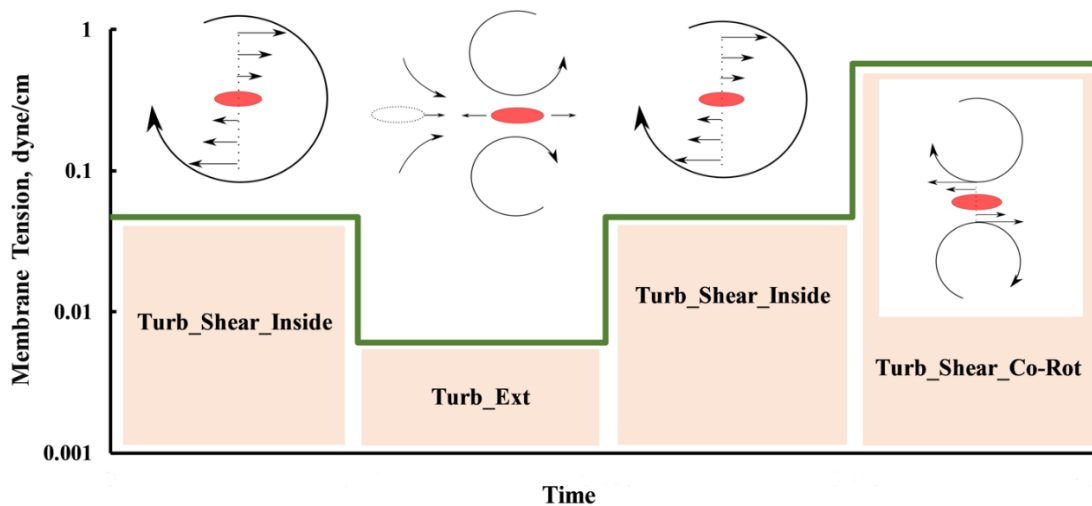
Fig. 2. 9 Maximum membrane tension for a cell interacting with turbulent eddies of highest energy content (See Fig. 2.6 caption for a key to the abbreviations)

As an additional complication, the data of Liu, et al. [180] was only obtained along the centerline of the wake behind the prosthetic valve, where turbulent viscous stresses are theoretically zero. Other parts of the flow include a combination of viscous and Reynolds stresses, which may require further analysis to fully characterize the relationship between fluid stress and membrane tension.

2.3.5 Conclusions

For decades, many investigators have based hemolysis prediction on the untested hypothesis that hemolysis is proportional to scalar stress. The models employed in this work suggest that this hypothesis is untrue. Specifically, membrane tension depends not only on the scalar stress, but also on the type of flow. Indeed, for the same level of scalar stress in different flow scenarios, estimated membrane tension varied by up to three orders of magnitude. Therefore, it appears unlikely that hemolysis, which fundamentally depends on membrane tension, can be accurately scaled by scalar stress alone.

A more highly resolved representation of the state of fluid stress may be required to achieve hemolysis prediction algorithms that are universally accurate across the range of complex flows. Whether all six independent components of the fluid stress must be taken into account remains to be discovered. Perhaps a reduced set, such as principal stresses (to

78

follow again the solid mechanics precedent), may suffice. In addition, the viscoelastic nature of the membrane suggests that stress history is equally important, which further complicates development of algorithms involving scaling arguments. The smaller the set of necessary parameters, the easier hemolysis prediction would tend to be. Energy dissipation rate is a single parameter that has shown promise in unifying hemolysis prediction in laminar and turbulent pipe flows (Morshed, et al 2014).

On the other hand, computational modeling has progressed toward cell-level simulations of hemolysis, in which membrane tension and its history can, in principle, be resolved for every cell throughout the flow field. While such resolution may be impractical well into the future for cardiovascular devices of realistic complexity, selective resolution along hemolytic pathlines might provide an avenue for useful predictions.

Neither the shear nor extensional flow models used here have been fully validated within the ranges of fluid stresses and exposure times that have been shown to produce hemolysis in cardiovascular devices. Fundamental experiments are needed to verify that red cells are deformed as represented by the models and that their membranes fail as predicted. Microrheoscopic imaging of cells in controlled flows could provide valuable data for advancing model development.

2.4 Dissipation rate as a predictor of hemolysis[4]

2.4.1 Introduction

Understanding the transfer of fluid stresses to the red cell membrane across different types of flows is arguably the greatest challenge for hemolysis prediction. In comparison, exposure time is relatively straightforward if the path of the cell through the flow can be approximated. Experiments to measure membrane tension in flowing cells and to validate that hemolysis is reliably scaled by candidate scalar stresses are lacking. An analytical approach was reported by section 2.3. We calculated erythrocyte membrane tension in five simplified laminar and turbulent flows. The results showed that, even though the scalar stress was equal for all the cases, the membrane tension varied by up to two

---

[4] Most of the material in this chapter is adopted from our published work in Faghih and Sharp [206].

79

orders of magnitude. Therefore, it is unlikely that scalar stress can fulfill the promise of universal hemolysis prediction.

An alternative to scalar stress is the rate of energy dissipation, ε. Bluestein and Mockros [75] found that hemolysis index (*IH;* defined as mg of hemoglobin per 100 ml of the blood pumped in the test) scaled as

$$IH = k\varepsilon^n \tag{86}$$

for flow in round tubes, orifice plates and a venturi tube, and in uniform shear in a viscometer with combined Couette and cone/plate geometry. However, empirical constants k and n varied among the flow types, with nonuniform energy dissipation producing greater hemolysis. This suggests that the local rate of energy dissipation should be considered if energy dissipation is to become a universal hemolysis prediction parameter.

More recently, Morshed, et al. [76] found a strong correlation between hemolysis and energy dissipation in the experiments of Kameneva, et al. [122], which spanned laminar and turbulent conditions in pipe flow. This result supports the findings in laminar and turbulent pipe flow of Bluestein and Mockros [75]. Morshed, et al. [76] further promoted energy dissipation rate as a potential universal scale for hemolysis. While this idea is not consistent with the results of Bluestein and Mockros [75], a perhaps more relevant question is whether energy dissipation rate is more universal than is scalar stress.

Having established that scalar stress does not yield similar erythrocyte membrane tension in simplified models of laminar and turbulent flow [148], this article uses similar techniques to evaluate the performance of energy dissipation rate. Specifically, membrane tension is estimated for six laminar and turbulent cases that have the same dissipation rate, namely pure laminar shear and extensional flows, and turbulent flows in which the red cell is sheared between co-rotating eddies, stretched between counter-rotating eddies and sheared inside a eddy with shear stress based on a continuum approach and on a cellular-level model by Morshed, et al. [76]. While flows in real clinical situations can be more complex, the rationale for studying simplified shear and extensional flows is that they represent the limits of the range of flows that can occur clinically, which include various

combinations of shear and extensional stresses. If membrane tension can be matched in the limits of flows that are the most different, then future work can proceed to determine whether the match is maintained for combinations of these stresses. If membrane tension is not matched in these limits, then there is little chance of universality of the chosen stress parameter for predicting hemolysis. Indeed, such simple flows are directly relevant to some locations in devices, for instance, the pure shear flow in long tubes and the predominantly extensional flow in the orifice of a closing valve.

2.4.2 Methods

The models for each type of flow are the same as those of in section 2.3, except that energy dissipation rate was the same among all the cases. The model of Morshed, et al. [76] was also added. The models used to estimate the membrane tension in extensional and shear flows are also outlined in section 2.3.

2.4.2.1 Energy dissipation rate and membrane tension

To calculate membrane tension for each case, relationships between the energy dissipation rate and the fluid strain rates are required. The energy dissipation rate for a 3-D flow field is [77]

$$\varepsilon = 2 v s_{ij} s_{ij} \tag{87}$$

where v is the kinematic viscosity, i and j are the coordinate axes that take on x, y and z, and s_{ij} is

$$s_{ij} = \begin{bmatrix} \dfrac{\partial u}{\partial x} & \dfrac{1}{2}\left(\dfrac{\partial u}{\partial y}+\dfrac{\partial v}{\partial x}\right) & \dfrac{1}{2}\left(\dfrac{\partial u}{\partial z}+\dfrac{\partial w}{\partial x}\right) \\ \dfrac{1}{2}\left(\dfrac{\partial u}{\partial y}+\dfrac{\partial v}{\partial x}\right) & \dfrac{\partial v}{\partial y} & \dfrac{1}{2}\left(\dfrac{\partial v}{\partial z}+\dfrac{\partial w}{\partial y}\right) \\ \dfrac{1}{2}\left(\dfrac{\partial u}{\partial z}+\dfrac{\partial w}{\partial x}\right) & \dfrac{1}{2}\left(\dfrac{\partial v}{\partial z}+\dfrac{\partial w}{\partial y}\right) & \dfrac{\partial w}{\partial z} \end{bmatrix} \tag{88}$$

where u, v and w are the velocity components in x, y and z directions, respectively. For the laminar flows in this paper, the 2D version of Eqs. (87) and (88) suffice

81

$$\varepsilon = v \left[2\left(\frac{\partial u}{\partial x}\right)^2 + \left(\frac{\partial u}{\partial y}\right)^2 + \left(\frac{\partial v}{\partial x}\right)^2 + 2\left(\frac{\partial v}{\partial y}\right)^2 + \left(\frac{\partial u}{\partial y}\frac{\partial v}{\partial x}\right) + \left(\frac{\partial u}{\partial y}\frac{\partial v}{\partial x}\right) \right] \tag{89}$$

Energy dissipation rate for laminar flow cases

For pure, incompressible 2D laminar extensional flow, for which $\left|\frac{\partial u}{\partial x}\right| = \left|\frac{\partial v}{\partial y}\right|$, energy dissipation rate (Eq. (89)) becomes

$$\varepsilon = 4v\left(\frac{\partial u}{\partial x}\right)^2 \tag{90}$$

Therefore, the extensional stress, which is an input for the Chen and Sharp [100] model, is

$$\sigma_{xx} = 2\eta\frac{\partial u}{\partial x} = 2\eta\sqrt{\varepsilon/4v} \tag{91}$$

For pure laminar shear, where only $\frac{\partial u}{\partial y}$ is nonzero, the energy dissipation rate (Eq. (89)) is

$$\varepsilon = v\left(\frac{\partial u}{\partial y}\right)^2 \tag{92}$$

Therefore, the shear rate input for the Tran-Son-Tay et al. [24] model is

$$\dot{\gamma} = \frac{\partial u}{\partial y} = \sqrt{\varepsilon/v} \tag{93}$$

Energy dissipation rate for turbulent flow cases

For turbulent flow, Eq. (87) can be used to calculate the energy dissipation rate of both mean flow $\bar{\varepsilon}$ and fluctuations ε', given velocities that are expressed by the sum of mean and fluctuating values $u_i = \bar{u}_i + u_i'$.

Furthermore, based on Kolmogorov's theory of local isotropy and homogeneity of small-scale structures in turbulent flow, the fluctuating component of energy dissipation rate may be written as [79, 80]

$$\bar{\varepsilon}' = 15\,\upsilon\,\overline{\left(\frac{\partial u'}{\partial x}\right)^2} \tag{94}$$

where the overbar denotes the time average.

Additionally, the energy dissipation rate within a certain frequency band can also be calculated from the turbulent energy spectrum for a specific flow [207, 208]

$$\bar{\varepsilon}' = 15\,\upsilon\int_{f_1}^{f_2}\left(\frac{2\pi}{\bar{u}}\right)^2 f^2 E(f)df \tag{95}$$

where f is frequency and $E(f)$ is turbulent energy density. This equation is introduced here because it is later used to adjust the Kolmogorov eddy size and frequency for the data of Liu, et al. [180].

The energy spectrum used in this work comes from measurements by Liu, et al. [180] for turbulent flow downstream of a prosthetic heart valve. The normalized energy spectral density curve $(E_n(f) = E(f)/u'_{RMS}{}^2$ with unit of seconds) for the centerline 7.8 mm downstream of the valve at peak flow is shown in Fig. 2.10. Due to the experimental limitations, Liu et al. only reported turbulence data up to the frequency of 5 kHz. Therefore, for data above this frequency, an extrapolation proposed by Quinlan and Dooley [63] (curve E3 in their article) was used to plot Fig. 2.10.
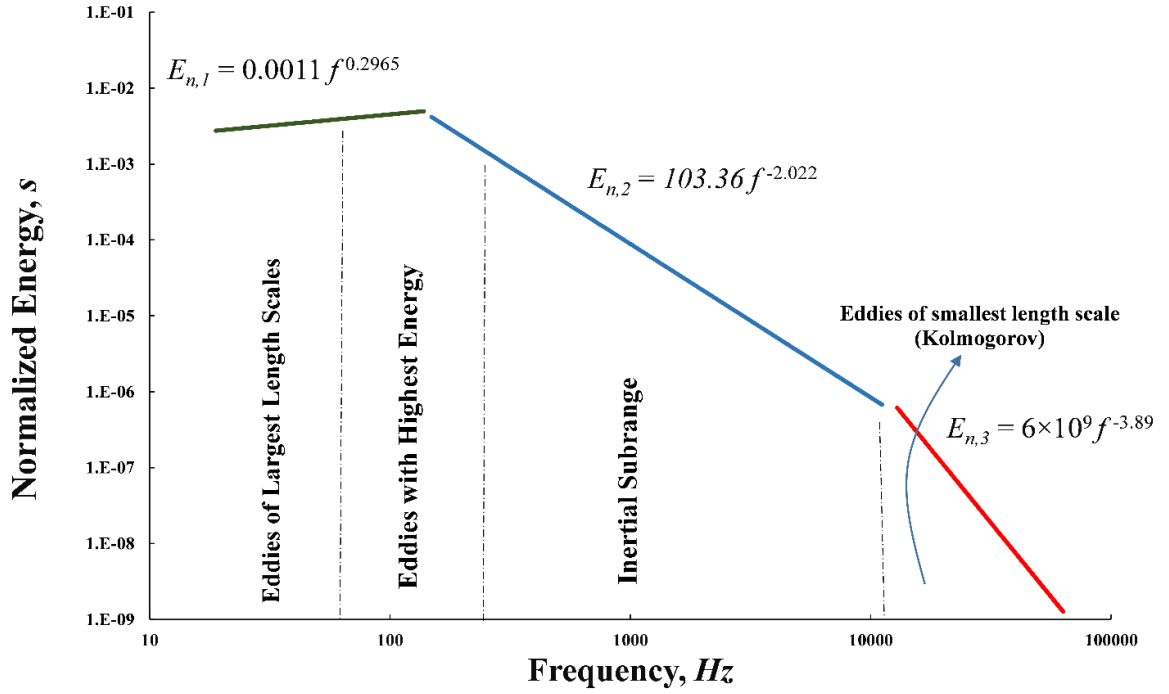
Fig. 2. 10 Normalized turbulence energy downstream of an artificial heart valve reported by Liu, et al. [180] and curve-fit of Quinlan and Dooley [63].

For the measurements up to 5 kHz (Liu, et al. [180], the mean velocity $\bar{u}$ and the root mean square of velocity fluctuations u'_{RMS} were equal to 1.69 m/s and 0.2 m/s, respectively, while the Kolmogorov length scale was 46 µm with corresponding frequency of 36.74 kHz. These scales were used subsequently by Quinlan and Dooley [63], Antiga and Steinman [183] and Faghih and Sharp [148]. The energy dissipation rate of this limited spectrum, calculated with Eq. 95 is 6.24 m^2/s^3. However, the 5 kHz limit is well below the dissipative frequencies (Fig. 2.10). When the estimated energy at higher frequencies is added (the $E_{n,3}$ curve of Quinlan and Dooley [63] in Fig. 2.10), energy dissipation (Eq. 95) increases and the Kolmogorov scale decreases. This upper frequency limit of Eq. (95) was extended to a frequency (63.2 kHz) that encompasses at least 99% of the total energy dissipation. Assuming that neither $\bar{u}$ nor u'_{rms} change significantly, the energy dissipation rate of this more complete spectrum becomes 54.4 m^2/s^3 and the revised Kolmogorov length scale is $\eta_k = \left(\frac{v^3}{\varepsilon'}\right)^{\frac{1}{4}} = 26.7$ µm. This revised energy dissipation rate is used as a baseline for all cases in this study.

84

Also, because on the centerline downstream of the valve all mean velocity gradients were zero, $\bar{\varepsilon} = 0$ and the fluctuating component represents the entire energy dissipation rate, $\varepsilon_{eff} = \sqrt{(\bar{\varepsilon}')^2 + (\bar{\varepsilon})^2} = \bar{\varepsilon}'$.

Note that the four turbulent cases discussed here are all based on eddies of dissipative scale in the same flow (Liu, et al. [180]. Therefore, they already share the same dissipation rate of 54.4 m²/s³. The velocity scale of these dissipative eddies is estimated by $u'_{d,RMS} = (\bar{\varepsilon}'\eta_k)^{\frac{1}{3}} = 0.11$ m/s.

For the first case of turbulent flow in Fig. 2.1, the continuum-based shear rate inside an eddy can be simply estimated as $\dfrac{u'_{d,RMS}}{\eta_k}$.

For the second case (Fig. 2.2), for a cell sheared between co-rotating eddies, the shear rate applied to the cell is approximated by $2u'_{d,RMS}/h$, where h is the distance between the two eddies. Distance h is estimated as the cell's minor axis plus two times the distance between the cell and each eddy. The latter distance was estimated by Antiga and Steinman [183] based on the maximum packing density of prolate ellipsoids with 1.8 aspect ratio (major and minor axes equal to 8.24 and 4.5 µm, respectively), which gives a value of 0.74 µm. Therefore, h is estimated as 5.98 µm.

For the third case (Fig. 2.3), in which a cell is stretched between counter-rotating eddies, the extensional strain rate experienced by cell can be estimated to be $2\dfrac{\partial u'}{\partial x} = 4\dfrac{u'_{d,RMS}}{\eta_k}$.

For the last case, energy dissipation is assumed to occur only in the plasma and not in cells (Morshed, et al. [76]), which gives a characteristic shear rate inside dissipative eddies of

$$\dot{\gamma} = \sqrt{\frac{\bar{\varepsilon}'\rho^*}{\upsilon\,(1 - Hct)}} \tag{96}$$

where ρ^* is the ratio of the density of the whole blood to that of the plasma, and Hct is the hematocrit (taken as 45% here).

Case Conditions

Inserting the energy dissipation rate of 54.4 m²/s³ and kinematic viscosity of 3.03×10⁻⁶ m²/s [180] into Eq. (90), the extension rate for the laminar extensional case becomes $2{,}118 \text{ s}^{-1}$. Similarly, the shear rate for the laminar shear case becomes $4{,}237 \text{ s}^{-1}$ by using Eq. (93). Now, using this shear rate and parameter values in Table 2.1, membrane tension in pure laminar shear case can be calculated.

For the first turbulent case, the shear rate is equal to $\frac{u'_{d,RMS}}{\eta_k} = \frac{0.11 \frac{m}{s}}{26.7 \ \mu m} = 4{,}120 \text{ s}^{-1}$. Next, with h being estimated as 5.98 μm, the shear rate between the co-rotating eddies becomes $2\frac{u'_{d,RMS}}{h} = 36{,}790 \text{ s}^{-1}$. For the third turbulent case, extensional strain becomes $4\frac{u'_{d,RMS}}{\eta_k} = 16{,}480 \text{ s}^{-1}$. Finally, using Eq. (96), the shear rate for the Morshed, et al. [76] model is $6{,}402 \text{ s}^{-1}$.

2.4.2.2 Parametric sensitivity

Sensitivity of the cell membrane tension to parameters in each of the models, namely the Chen and Sharp [100] and Tran-Son-Tay, et al. [179] models, was obtained using the sensitivity relation defined as in Eq. (85).

2.4.3 Results

Membrane tensions for the two laminar and four turbulent flow cases are plotted in Fig. 2.11. For the case of laminar extension, a constant membrane tension of 1.19 dyn/cm results on the membrane strip C_e shown in Fig. 1.13.

For laminar shear flow, a periodic membrane tension results on strip C_0 (Fig. 1.14) with a maximum membrane tension of 0.13 dyn/cm. The peak tension is one order of magnitude lower than that of the laminar extension case.

Maximum membrane tension for the case of a cell tank-treading inside an eddy is 0.13 dyn/cm. The wave shape, magnitude and tank-treading frequency are almost the same as the laminar shear case.

The peak membrane tension predicted by the Morshed et al. [22] model (0.18 dyn/cm) is within the same order of magnitude as those for laminar shear and for continuum shear inside an eddy, but its tank-treading frequency is higher than both those cases.

For turbulent shear flow between co-rotating eddies, membrane tension is again periodic, with the maximum tension being 0.8 dyn/cm, which is greater than the three previous shear cases. The tank-treading frequency for this case is also about an order of magnitude higher.

For turbulent extensional flow between counter-rotating eddies, membrane tension is constant and equal to 4.63 dyn/cm. This is the highest membrane tension among all the cases.
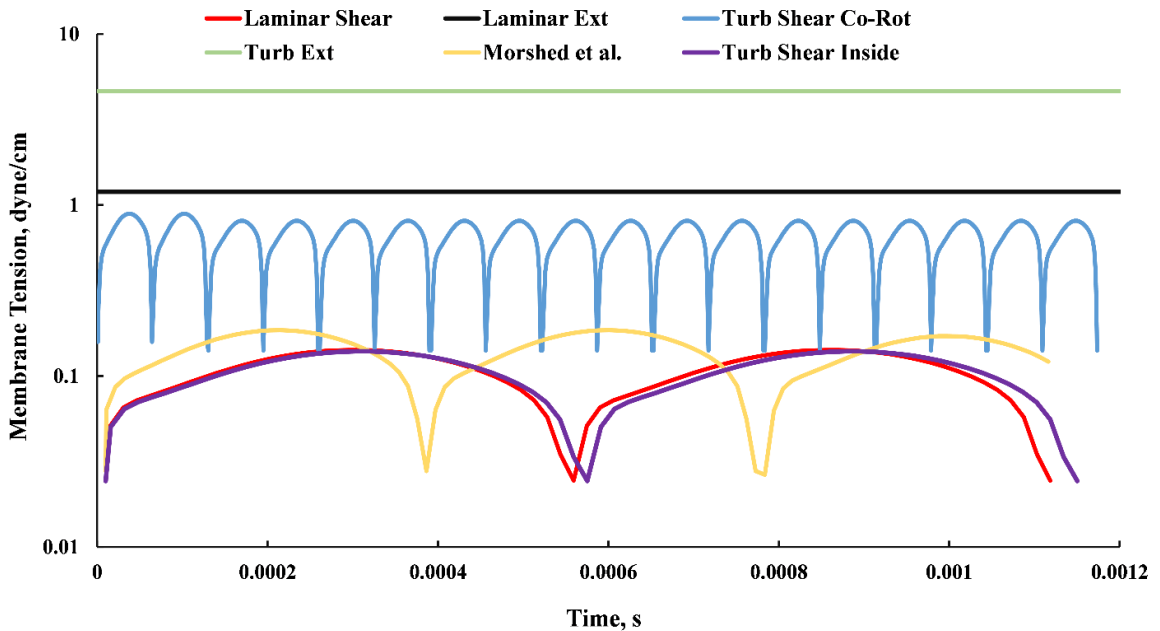
Fig. 2. 11 Cell membrane tension for different laminar and turbulent cases having the same turbulent energy dissipation rate. (Laminar shear - laminar shear stress, Laminar ext - laminar extensional stress, Turb shear co-rot - turbulent shear stress between co-rotating vortices, Turb shear inside - turbulent shear stress inside a vortex, Turb ext - turbulent extensional stress between counter-rotating vortices).

The root mean square (RMS) values of membrane tension for all the cases examined in this study are shown in Fig. 2.12. The values vary by a factor of 46, with extensional flow causing higher tension than shear flow.

87
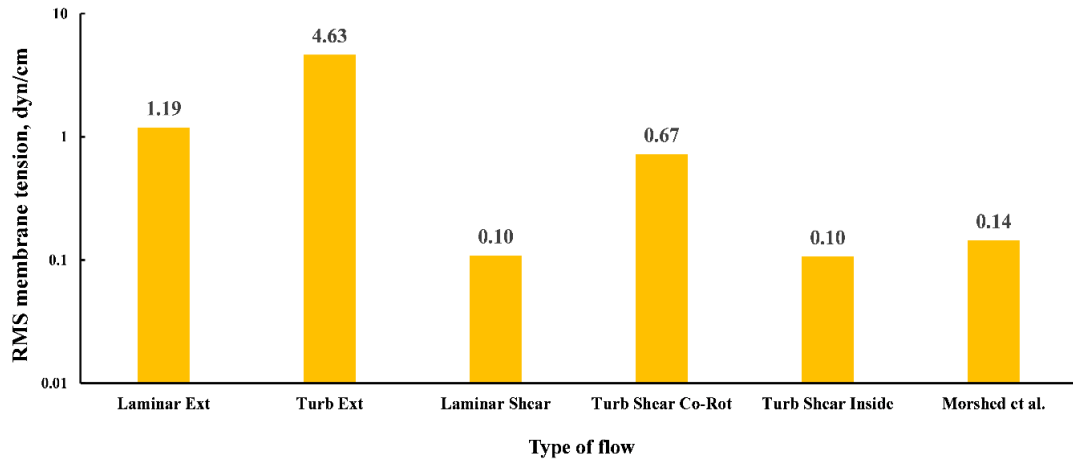
Fig. 2. 12 Comparison of RMS value of membrane tension obtained based on the same energy dissipation rate.

Duration of tension to the red cell is also important. For turbulent cases, exposure time can be estimated to be equal to the eddy turnover time, which would be equal to $\frac{\eta_k}{u'_{d,RMS}} = 0.24\ ms$ for the experimental data of Liu, et al. [180].

Parametric sensitivity – Sensitivities, as quantified by Eq. (85), of red cell membrane tension to the different parameters in each of models are listed in Tables 2.5 and 2.6. Because the extensional flow model is linear with its three parameters, all sensitivity values are the same, as expected (Table 2.5). Membrane tension changes are proportional to those for each parameter. The most sensitive parameters for the models based on shear flow are *a* for laminar shear (for which a 5% change in *a* results in a 8% change in membrane tension), *a* for turbulent shear inside an eddy (a 5% change in *a* results in a 8.2% change in membrane tension) and *a* for turbulent shear between co-rotating eddies (a 5% change in *a* results in a 9% change in membrane tension).

Table 2. 5 Sensitivity of membrane tension in extensional flow cases

	K	b	$\sigma_{x'x'}$
Laminar Ext	0.187	0.187	0.187
Turb Ext	3×10^{-3}	3×10^{-3}	3×10^{-3}

Table 2. 6 Sensitivity of membrane tension in shear flow cases

	a	b	c	C_0	θ	$\dot{\gamma}$	η	η_i	μ_m
Laminar Shear	1.1×10^{-2}	-4.0×10^{-3}	-7.4×10^{-3}	4.8×10^{-3}	4.4×10^{-3}	4.8×10^{-3}	4.7×10^{-3}	1.2×10^{-4}	2.3×10^{-3}
Turb Shear Inside	1.1×10^{-2}	-3.9×10^{-3}	-7.7×10^{-3}	4.9×10^{-3}	4.3×10^{-3}	4.7×10^{-3}	4.6×10^{-3}	5.2×10^{-5}	2.3×10^{-3}
Turb Shear Co-Rot	8.0×10^{-2}	-1.1×10^{-2}	-3.1×10^{-2}	4.6×10^{-3}	3.7×10^{-2}	4.2×10^{-2}	4.0×10^{-2}	2.2×10^{-3}	2.2×10^{-3}

2.4.4 Discussion

RMS values of the membrane tensions calculated with the same energy dissipation rate (Fig. 2.11) are compared to those based on the same scalar stress (results for scalar stress of 520 dyn/cm^2 from section 2.3 using the revised Kolmogorov length and frequency scales of section 2.3.2) in Fig. 2.13. The tensions for the same scalar stress vary by a factor of 29, while those for the same energy dissipation rate vary by a factor of 46.

Tensions are equal between the common energy dissipation rate and common scalar stress cases for both laminar extension and laminar shear. The effective scalar stress derived from the energy dissipation rate in terms of stress tensor components becomes

$$\sigma_e = \sqrt{\rho\eta\varepsilon} = \sqrt{\frac{1}{2}\left(\sigma_{xx}^2 + \sigma_{yy}^2 + \sigma_{zz}^2\right) + \left(\tau_{xy}^2 + \tau_{xz}^2 + \tau_{yz}^2\right)} \tag{97}$$

For comparison, the von-Mises-like scalar stress [60, 153] is

$$\sigma_s = \sqrt{\frac{1}{3}\left(\sigma_{xx}^2 + \sigma_{yy}^2 + \sigma_{zz}^2\right) - \frac{1}{3}\left(\sigma_{xx}\sigma_{yy} + \sigma_{xx}\sigma_{zz} + \sigma_{yy}\sigma_{zz}\right) + \left(\tau_{xy}^2 + \tau_{xz}^2 + \tau_{yz}^2\right)} \tag{98}$$

Comparing Eq. (97) to Eq. (98) reveals that the energy dissipation rate-based scalar stress lacks the normal stress cross-product terms, but weighs the squared normal stress components more heavily than does the von-Mises-like scalar stress. The result is that for 2D laminar extensional flow, in which $\sigma_{xx} = -\sigma_{yy}$ are the only nonzero stress components, $\sigma_e = \sigma_s$. The shear stress terms are equally weighted for the two scalar stresses. Thus for laminar shear flow, in which $\tau_{xy} = \tau_{yx}$ are the only nonzero stress components, again $\sigma_e = \sigma_s$. However, for both cases, tensions for laminar extension are an order of magnitude higher than for laminar shear. These identical trends for membrane tension for the two

scalar stresses therefore suggest that they are equally ineffective in producing a universal hemolysis scaling parameter for laminar flow.

The forms of Eqs. (97) and (98) suggest alternatives for developing an improved scaling parameter. For instance, Eq. (97) gives membrane tension for laminar extension that is 11.9 times higher than the RMS value for laminar shear (Fig. 2.12). These predicted membrane tensions could be made equal by adjusting the coefficient for the normal stress term by a factor equal to the ratio of the two membrane tensions in Fig. 2.12. The new coefficient would be $\frac{1}{2} \times 11.9^2 = 70.8$ rather than $\frac{1}{2}$. Reynolds stresses for turbulent flow might be similarly weighted to achieve an empirical balance of membrane tension.

It is evident that higher membrane tensions result from using a common energy dissipation rate than a common scalar stress for each of the turbulent flow cases (Fig. 2.13). The Morshed, et al. [76] model yields membrane tension that is slightly higher than the continuum-based estimate for shear inside an eddy. This is consistent with the assumption of this model that all dissipation occurs in the plasma and none in the erythrocytes.

Note that all the turbulent flow estimates are for the same location downstream of a valve [180], thus a single, unique hemolysis rate should prevail for a given sample of blood. Therefore, a single-valued scaling parameter would be appropriate for hemolysis prediction. The individual values of membrane tension for turbulent flow in Fig. 2.13 represent alternative predictions, which remain to be validated. Since cells may be exposed to all the different flow situations described by these cases, a weighted average may produce a suitable parameter. Greater weighting on cases with higher membrane tension and longer duration of tension may be appropriate. Some cases may have strong effects on hemolysis, while others have negligible impact. Among the turbulent cases in Fig. 2.13, turbulent extensional stress produces higher tension that is also constant rather than periodic. This suggests that extension may have an important, and perhaps even predominant, influence on hemolysis.
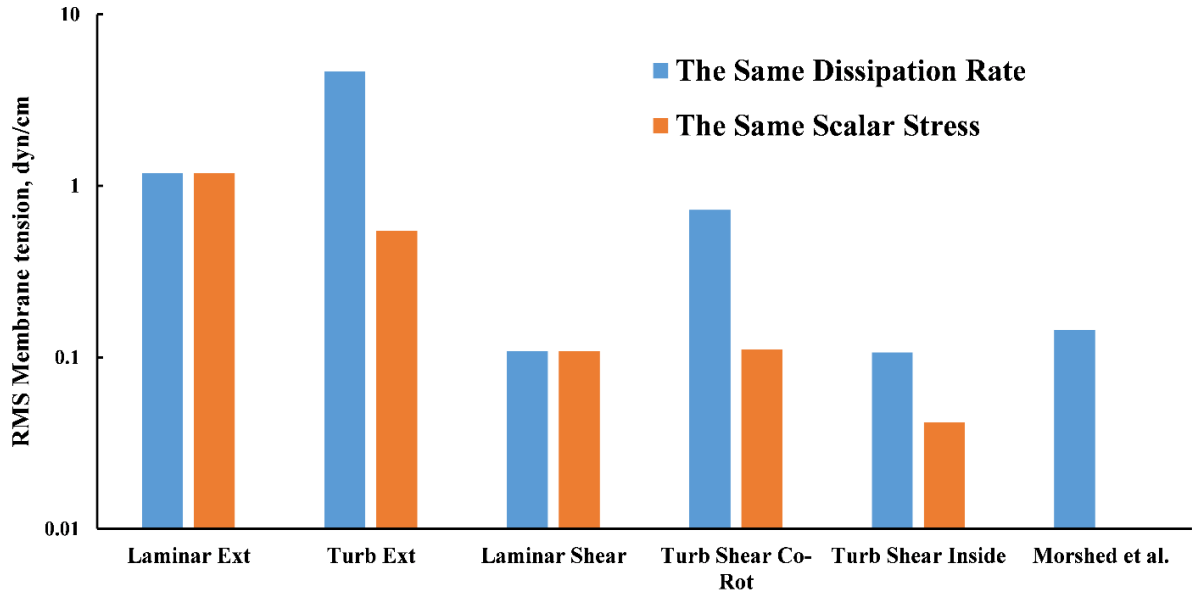
Fig. 2. 13 Comparison of RMS value of membrane tension obtained based on the same scalar stress vs. the same energy dissipation rate.

For turbulent shear inside an eddy, both for the continuum-based and Morshed, et al. [76] models, membrane tension for common energy dissipation is closer to the laminar shear value, suggesting an improvement in universal hemolysis prediction across laminar and turbulent shear flows. This closer agreement in membrane tension between laminar and turbulent shear flows supports the finding by Morshed et al. that the higher energy dissipation rate may explain the greater hemolysis measured by Kameneva, et al. [122] in turbulent pipe flow compared to laminar flow with the same wall shear stress.

However, for turbulent shear between co-rotating eddies and for turbulent extension between counter-rotating eddies, the energy dissipation-based estimates in Fig. 2.13 diverge farther from the laminar shear value than does the von-Mises-like estimate. These latter difference echoes the results of Bluestein and Mockros [75] that extensional turbulent flows with equal energy dissipation rates in orifices and venturi tubes produce greater rates of hemolysis than do shear flows in pipes and in Couette and cone/plate devices. The results of Bluestein and Mockros [75] show that the improvement in hemolysis prediction noted by Morshed, et al. [76] for shear flow does not extrapolate to turbulent extensional flows.

91

2.4.4.1 Limitations

Except for laminar shear, a common limitation is that validation data is lacking even for simple flows, let alone more complex flows. Hemolysis measurements in laminar extension and simple turbulent flows would be invaluable for assessing the models and choosing scaling parameters. Beyond these simple flows, questions arise regarding how combinations of fluid stresses affect hemolysis. While simple flow experiments would provide foundational information for forming models, experiments are also needed to discover how cells move and deform in more complex flows. Bulk hemolysis (due to the entirety of the flow field) is available for a number of devices, but such information is of little value for verifying which pathlines are, in fact, hemolytic and to what extent.

For the current study, experimental measurements of membrane tension are lacking, and would be difficult to obtain. For validation purposes, multi-scale (from membrane to flow regime scales) simulations of the fluid-solid interaction would be beneficial. Such simulations could show the local effect of the cell on the flow and its subsequent influence on cell deformation and motion. In particular, the simplified models employed in this study assume ellipsoidal cell shapes and no motion other than tank-treading. Nonlinearities in membrane response, which were not included in the Tran-Son-Tay, et al. [24] model, may need to be incorporated to differentiate between membrane area-conserving deformation at low stress and biaxial deformation leading to membrane rupture at high stress.

Another limitation is that to complete the calculation of hemolysis, duration of exposure to fluid stress must be considered. In laminar flow, exposure time is straightforward if the path of the cell through the flow is known. However, fundamental questions remain about the history of stress exerted on cells in turbulent flow. These questions begin with the suitability of an approach based on a continuum fluid, rather than particulate flow, which affects laminar and turbulent flow. Only recently have simulations been conducted with high concentrations of deformable cells in laminar flow, and of single cells during membrane failure. More work is needed to understand which of the models of cell response to turbulent flow presented in this paper are most appropriate for scaling, or indeed if more advanced models are necessary. The ubiquitous circular-vortex

characterization of turbulence used in this work and by previous authors may or may not be accurate enough for scaling of membrane tension.

Another related question is whether turbulence statistics embodied by the Reynolds average approach are adequate for scaling membrane tension and failure. Velocity fields are characterized by the Reynolds average concept only by the long-term average and local fluctuation spectra, yet a cell intrinsically responds to the instantaneous velocity field applied to it, including the history of the flow surrounding it before it reaches the point of interest. Further, Reynolds average statistics have thus far been computed based on measured flows that are devoid of red cells (a continuum fluid, as mentioned above). This problem of red cells affecting turbulent flow, and vice versa, has long been recognized, but measurements of velocity in concentrated suspensions of cells is challenging. Here again, direct numerical simulations may help to assess the authenticity of continuum Reynolds statistics for determining membrane tension.

2.4.5 Conclusions

Predictions of red cell membrane tension were compared among laminar shear and extension and four cases of turbulent flow for common energy dissipation rate. Results show that the estimates are closer between laminar shear and turbulent shear inside eddies than for similar estimates for common von-Mises-like scalar stress. However, disagreement remains between laminar extension and laminar shear, as well as for other types of turbulent flows. Therefore, while both energy dissipation rate and von-Mises-like scalar stress have been shown in previous literature to be correlated to hemolysis, the current results show that neither demonstrate promise as hemolysis scaling parameters that are universal across different types of flows. Future work should focus on alternative parameters.

2.5 On discretization of the power-law model

2.5.1 Introduction

Thanks to recent advancement in the field of computing technologies, it is now possible to simulate fluid flow even in complex geometries. Computational Fluid

Dynamics (CFD) for hemolysis prediction is usually carried out based on a single-phase homogenous Newtonian fluid. By using the continuum approximation, the power-law model can be applied in a post-processing step to the CFD velocity fields to predict hemolysis. Like other fluid mechanics phenomena, hemolysis within a geometry can be analyzed using either Lagrangian or Eulerian approaches. In the Lagrangian approach, the inlet is used as the releasing plane of sufficient number of sample particles. Pathlines of particles are tracked individually until they exit the domain at the outlet. In this approach, it is necessary to carry out temporal discretization for each pathline. Then, hemolysis is calculated for each discretization interval and the cumulative hemolysis is calculated at the exit for each pathline. Finally, after collecting cumulative hemolysis for all the pathlines, the total hemolysis is calculated as the velocity-weighted average of cumulative hemolysis of all the pathlines at the outlet [151].

In the Eulerian approach, the entire flow domain is spatially discretized into small volumes. Then, the linearized version of the power-law model is used as a source term in a transport equation for plasma-free hemoglobin [160]. In this section, the number of time steps needed to converge the discretized power-law model is investigated, assuming that the stress varies as a monotonic function of time. Then, a few examples, both analytical as well as CFD, are presented to justify our discussion.

2.5.2 Methods

The original power-law model has the form as Eq. (37)

$$D = \frac{\Delta PfHb}{Hb}\% = C\,\tau^\beta\,E^\alpha$$

where D is the damage function, $\Delta PfHb$ is the increase in plasma-free hemoglobin ($PfHb$), Hb is the total intracellular and extracellular hemoglobin, τ is the shear stress, E is the exposure time and α, β and C are empirical constant (Table 1.5). For more complex geometry in which other components of the stress tensor are non-zero, τ is replaced by a representative scalar stress, σ_s.

One of the most popular forms of the representative stress is a von-Mises-like stress, expressed as Eq. (17)

$$\sigma = \frac{1}{\sqrt{3}} \left(\sqrt{\sigma_{xx}^2 + \sigma_{yy}^2 + \sigma_{zz}^2 - \left(\sigma_{xx}\sigma_{yy} + \sigma_{xx}\sigma_{zz} + \sigma_{yy}\sigma_{zz}\right) + 3\left(\tau_{xy}^2 + \tau_{xz}^2 + \tau_{yz}^2\right)} \right)$$

Although application of the scalar stress in above equation for hemolysis prediction has been questioned [148], its use is sufficient to demonstrate the convergence behavior of the discretized damage function. Convergence will be tested for each set of empirical coefficients in Table 1.5.

2.5.2.1 Lagrangian temporal discretization

For the Lagrangian approach, the accumulated damage is found by integrating the rate of damage [152]

$$D_A = \int_0^T C\alpha\sigma_s^\beta(t)E^{\alpha-1}dt \tag{99}$$

where T is the total time for a cell to flow along a pathline. Here, it must be noted that, since all the analyses here are based on steady flow, pathlines and streamlines coincide, thus they can be used interchangeably.

In order to apply Eq. (3) to CFD results, the temporally-discretized damage function along a single pathline is then defined as [152, 163]

$$D_D = \sum_{i=1}^{n} C\alpha \, \sigma_{s,i}^\beta \, E_i^{\alpha-1}\Delta t_i \tag{100}$$

where n is the number of time steps, E_i is the exposure time from the beginning of the pathline up to the end of ith time step, Δt_i is the time step, and $\sigma_{s,i}$ is the average representative stress acting during that time step.

When n tends to infinity in Eq. (100), the result of Eq. (100) should converge to the analytical solution of Eq. (99). However, in terms of input parameters for post-processing

of the CFD results to predict blood damage, it is important to know how large n must be for Eq. (100) to give acceptable accuracy, for instance, less than 0.1% different from the hemolysis value calculated based on the definite integral of Eq. (99). We analyze this in the following sections by using a few examples, starting from a simple single-pathline case experiencing increasing and decreasing exponential stress, then 2-D gradual expansion and contraction Couette flows as well as 2-D sudden expansion, and ending with the 3-D Food and Drug Administration (FDA) benchmark nozzle. Where needed, the fluid viscosity and density were taken as 3.5 cp (3.5 mPa.s) and 1056 kg/m^3 to simulate blood properties. For the CFD simulations, the convergence criteria were set as residuals of 10^{-10} for the continuity and momentum equations.

The convergence of Lagrangian discretization of power-law hemolysis prediction with Heuser and Opitz [139] constants were examined for each case. Two types of criteria were used to check convergence for exponential stresses. First is based on the difference in damage function between the analytical solution and the discretized solution,

$$e_1 = \frac{D_A - D_D}{D_A} \times 100 \qquad (101)$$

where D_A and D_D are the damage obtained from the analytical solution and from discretized solution, respectively. The second is based on the difference in discretized damage between the current and previous number of time steps

$$e_2 = \frac{D_D^n - D_D^{n-1}}{D_D^n} \times 100 \qquad (102)$$

where D_D^n and D_D^{n-1} are the damage at current number of time steps and previous number of time steps, respectively. For the case of single pathline with exponential stress where analytical solutions exist, both criteria (Eqs. (101) & (102)) were used to study convergence. However, for rest of the cases, for which analytical solution were not available, only the criterion of Eq. (102) was used for convergence analysis. Results were assumed to be converged when $e_1 \leq 0.1$ or $e_2 \leq 0.1$, depending on which criterion is used.

2.5.2.2 Single pathline with exponential stress

C and α being constants, it is possible to analytically integrate Eq. (99) if the behavior of σ_s with time is known. The actual behavior of the representative stress along a pathline may be very complex in real blood contacting devices (which is a reason for using a discretized version instead). However, let us consider a simple case of a pathline on which σ_s is changing as a monotonic function of a normalized time,

$$\sigma_s = k(t^*)^p \qquad 0 \le t^* \le 1 \tag{103}$$

for increasing stress (Fig. 2-14a) and

$$\sigma_s = k[1 - (t^*)^p] \qquad 0 \le t^* \le 1 \tag{104}$$

for decreasing stress (Fig. 2.14b), where $p \ge 0$ and $t^* = t/T$. Note that $p = 0$ gives a constant stress for Eq. (103) and a trivial zero stress for Eq. (104).
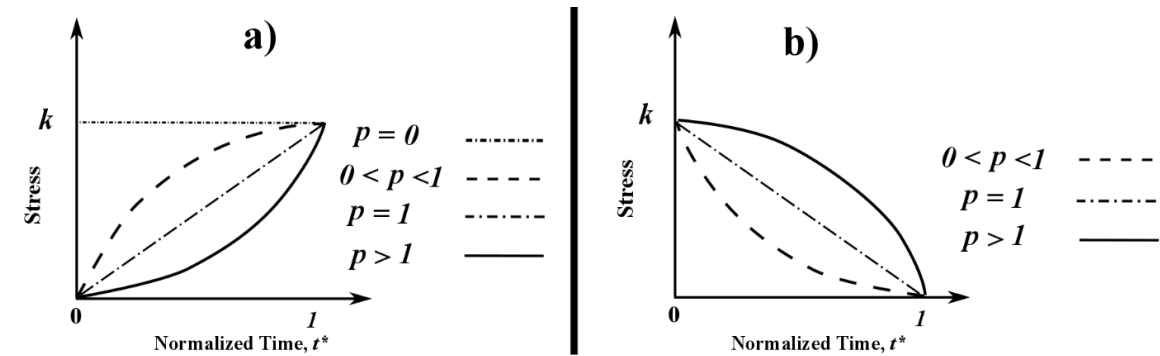
Fig. 2. 14 Behavior of the proposed scalar stress as a function of the normalized time in, a) an increasing and b) a decreasing type of stress.

For time beginning at $t = 0$, exposure time becomes $E = t$, and after the substitutions $E = Tt^*$ and $dt = Tdt^*$, the equation can be analytically integrated to yield

$$D = C\alpha k^\beta T^\alpha \int_0^1 (t^*)^{p\beta+\alpha-1} dt^* = \frac{C\alpha k^\beta T^\alpha}{p\beta + \alpha} \tag{105}$$

for the case of an increasing stress. And for the case of a decreasing stress, we have

$$D = C\alpha k^\beta T^\alpha \int_0^1 [1 - (t^*)^p]^\beta (t^*)^{\alpha-1} dt^*$$

$$= Ck^\beta T^\alpha \left[t^{*\alpha} \, {}_2F_1\left(-\beta, \frac{\alpha}{p}; \frac{\alpha+p}{p}; t^{*p}\right)\right]_0^1$$

(106)

where ${}_2F_1$ is the hypergeometric function. Calculating analytical result for integration in Eq. (106) is not straightforward, therefore MATLAB was used to calculate the numerical value of the integration in Eq. (106). The analytical results of Eq. (105) and (106) will be used to evaluate convergence of the discretized damage.

Now, let us consider the same pathline as before and discretize it in time into n equal temporal intervals, $\Delta t_i = T/n$. Now, E_i (which is equal to t_i in our case), which is the time from the beginning of the pathline to the ith discretization point can be written as Ti/n. Considering that $t_i^* = i/n$, the average stress during the ith interval for increasing and decreasing stress becomes $\sigma_{s,i} = kt_i^{*p} = k\left(\frac{i}{n}\right)^p$ and $\sigma_{s,i} = k[1 - (t^*)^p] = k[1 - (i/n)^p]$, respectively. (Note that the average value of the stress during each time step has been approximated by its value at the end of the corresponding interval.) By inserting these stress relationships, Eq. (106) can be rewritten as

$$D = C\alpha k^\beta T^\alpha \sum_{i=1}^n \left(\frac{i}{n}\right)^{p\beta+\alpha-1} \left(\frac{1}{n}\right)$$

(107)

for increasing stress and

$$D = C\alpha K^\beta T^\alpha \sum_{i=1}^n \left[1 - \left(\frac{i}{n}\right)^p\right]^\beta \left(\frac{i}{n}\right)^{\alpha-1} \left(\frac{1}{n}\right)$$

(108)

for decreasing stress.

Now, since the analytical solution exists for this case, the first question to be answered is how many discretization intervals, n, are necessary for Eqs. (107) and (108) to converge to Eqs. (105) or (106), respectively, depending on the value of p? Secondly, the convergence is examined based on the second criterion in Eq. (102). In other words, how many n are needed to converge Eqs. (107) and (108) using the criterion of Eq. (102). Then,

the results of convergence obtained based on Eq. (101) and Eq (102) are discussed and compared.

2.5.2.3 Inclined Couette flow

Dimensions of the two Couette flows are the same, with the top plane being stationary and the bottom plane moving at velocity of $U=5$ mm/s (Fig. 2.15). The contraction creates an accelerating flow, while the expansion causes a decelerating flow. The distance between the two planes varies as a function of longitudinal distance, x, as $d(x) = d_1 - \theta x$, where d_1 is the inlet gap and d_2 is the outlet gap, and θ is $4°$ for the gradual contraction and $-4°$ for the gradual expansion.
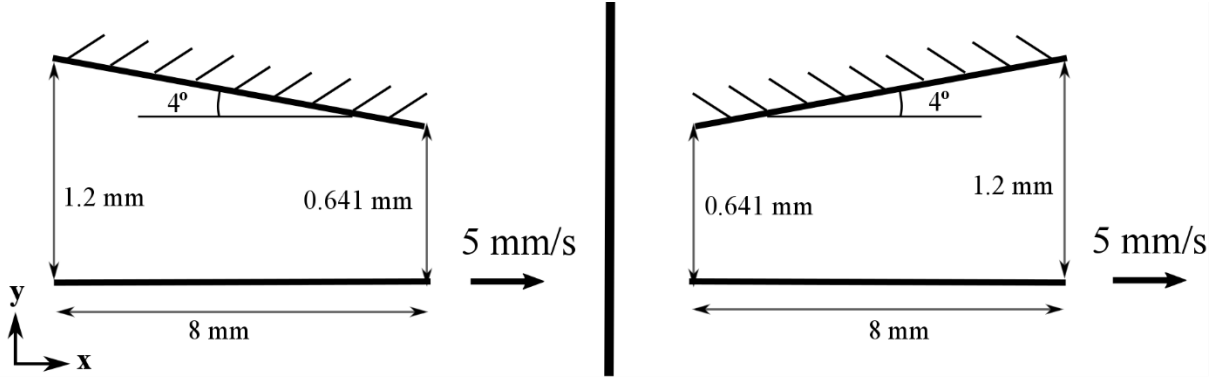
Fig. 2. 15 Laminar inclined Couette flow with gradual contraction (left) and gradual expansion (right).

For low Reynolds number, the velocities in the longitudinal (x) and transverse (y) directions are

$$V(x) = -\frac{4U\,y}{d_1 - \theta x} + \frac{3U\,y^2}{(d_1 - \theta x)^2} + \frac{6Ud^*\,y}{(d_1 - \theta x)^2} - \frac{6Ud^*\,y^2}{(d_1 - \theta x)^3} \qquad (109)$$

and

$$V(y) = \frac{2U\theta\,y^2}{(d_1 - \theta x)^2} - \frac{2U\theta\,y^3}{(d_1 - \theta x)^3} - \frac{6U\theta d^*\,y^2}{(d_1 - \theta x)^3} + \frac{6U\theta d^*\,y^3}{(d_1 - \theta x)^4} \qquad (110)$$

respectively, where $d^* = d_1 d_2/(d_1 + d_2)$. These velocity profiles at the exits of the contraction and expansion are shown in Figs. 2.16 and 2.17, respectively.
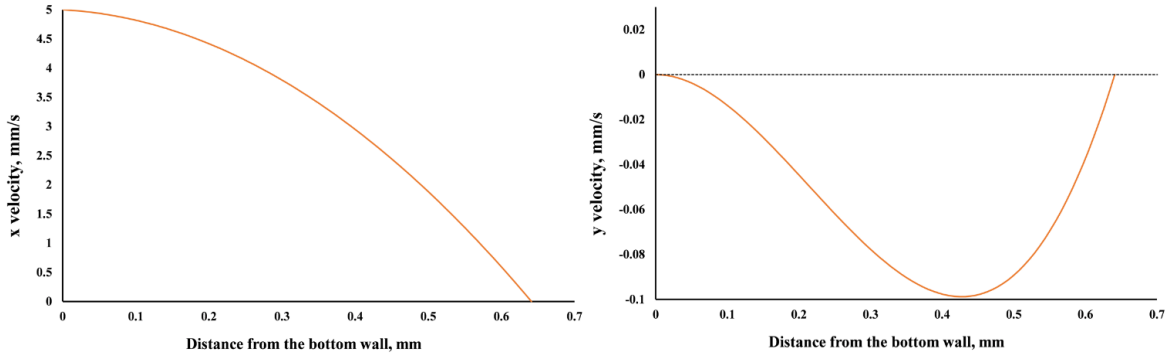
Fig. 2. 16 Velocity profile at the exit of the gradual contraction for longitudinal (left) and transverse (right) directions.
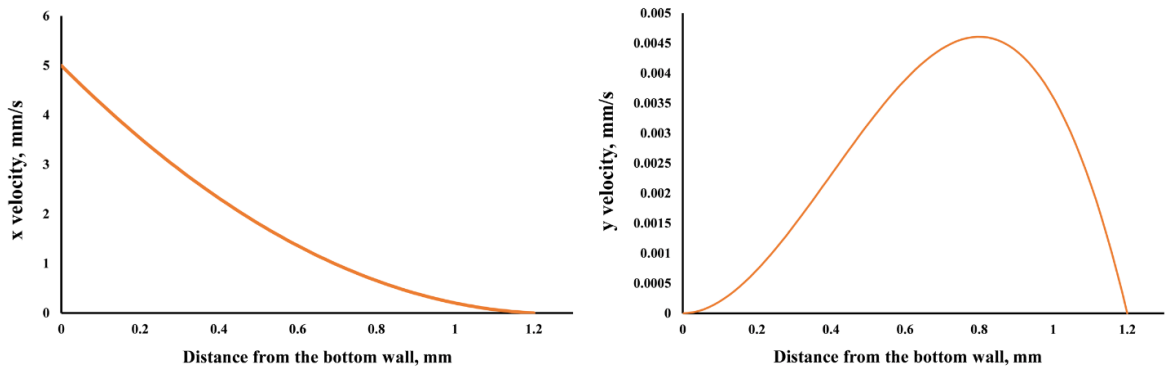
Fig. 2. 17 Velocity profile at the exit of the gradual expansion for longitudinal (left) and transverse (right) directions.

The fluid viscosity and density were taken as 3.5 cp (3.5 mPa.s) and 1056 kg/m^3 to simulate blood properties.

A MATLAB code was written to construct the steady-state stream functions for the two Couette geometries using the velocity profiles of Eqs. (105) and (106). Two sample pathlines, one close to the top plane and the other close to the bottom plane, were chosen for each Couette flow to study the convergence of the Lagrangian discretizations of the damage function. Additionally, the velocity-weighted average damage function was calculated for 50 sample pathlines to characterize the convergence of the damage function for the entire Couette domain.

100

2.5.2.4 Two-dimensional sudden radial expansion

Ansys Workbench v17 was used to generate the geometry, to mesh the domain and to simulate laminar flow in the radial sudden expansion (Fig. 2.18).
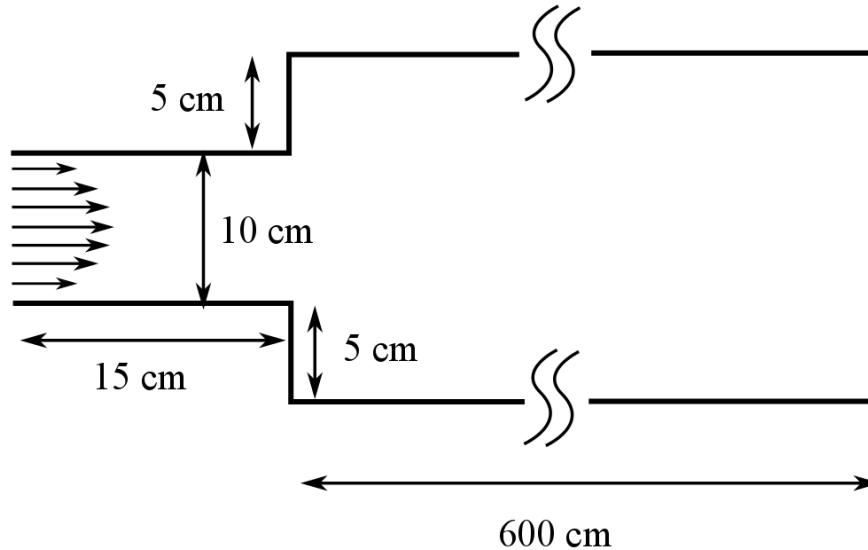
Fig. 2. 18 Schematic of the sudden expansion with a fully developed velocity profile at the inlet.

A fully-developed velocity profile with an average velocity equal to 1.33 mm/s was applied at the inlet. This condition corresponds to an inlet Reynolds number of 40. Then, 886,098 elements were used to mesh the flow domain, with very fine mesh at the sudden expansion area. Fluid density and viscosity were again selected as 1,056 kg/m^3 and 3.5 (mPa.s), respectively. The simulation convergence criteria were set as residuals of 10^{-10} for the continuity and momentum equations. A mesh independency study was performed to ensure sufficiency of the mesh density. Area-weighted average velocities at several sections across the flow domain were monitored for selection of the working mesh as well as for convergence of the velocities.

For verifying the CFD results, velocities for multiple planes at different axial distances were compared to the CFD results of Jithin et al. [209] and the experiments of Hawa and Rusak [24]. Velocity normalized by inlet average velocity vs. radial distance for a sample plane (1 m downstream of the sudden expansion) is shown in Fig. 2.19.
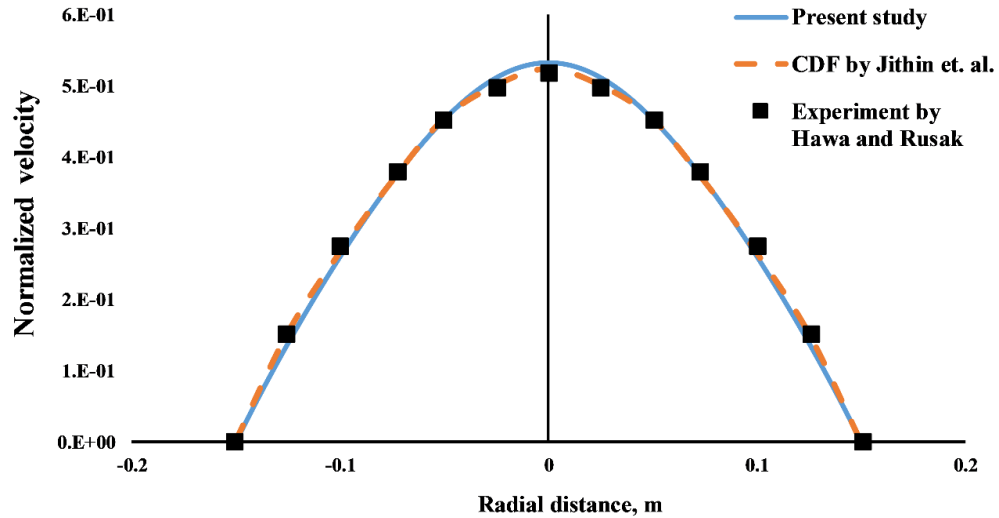
Fig. 2. 19 Profile of velocity normalized by the inlet average velocity vs. radial distance at 1 m downstream from the sudden expansion (CFD results by Jithin et al. [209] and experimental results by Hawa and Rusak [210]).

100 pathlines were generated that started from uniformly distributed points at the inlet. The velocities on the pathlines were smoothed using a 3-point moving average to limit numerical noise. Finally, the velocity histories from Ansys were exported to MATLAB for calculating the velocity-average damage function.

2.5.2.5 Three-dimensional FDA nozzle

The FDA benchmark nozzle is composed of a gradual contraction, followed by a sudden contraction (Fig. 2.20).
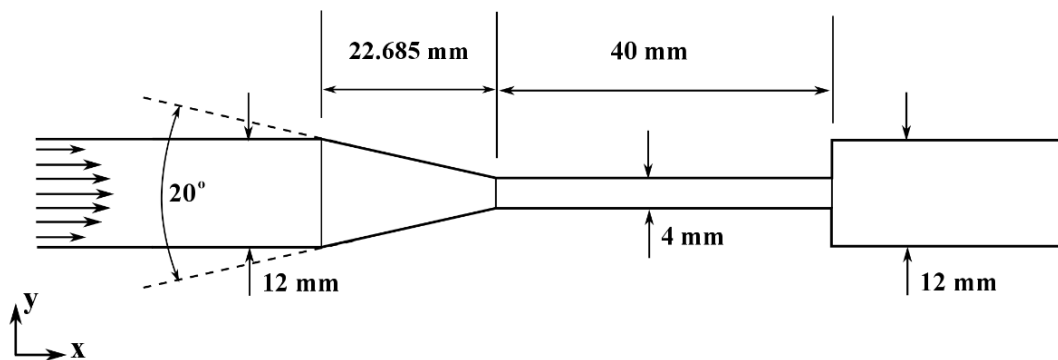
Fig. 2. 20 Schematic of the FDA nozzle with a fully developed velocity profile at the inlet.

Ansys Workbench v17 was used to generate the geometry, to mesh the domain and to simulate the flow, while MATLAB was used for post-processing of the CFD results. A

102

three-dimensional fully-developed velocity profile with an average velocity equal to 122 mm/s was applied to the inlet, which corresponds to a Reynolds number of 500 in the throat section. Fluid density and viscosity were selected as 1,700 kg/m^3 and 7.48 (mPa.s), respectively, to match the values used by Raben et al. [211] in their Particle Image Velocimetry (PIV) experiment. Area-average velocity was monitored at multiple sections for mesh independence as well as verification (Fig. 2.21). Based on the mesh independence study, a working mesh containing 851,419 elements was used to discretize the FDA nozzle domain.
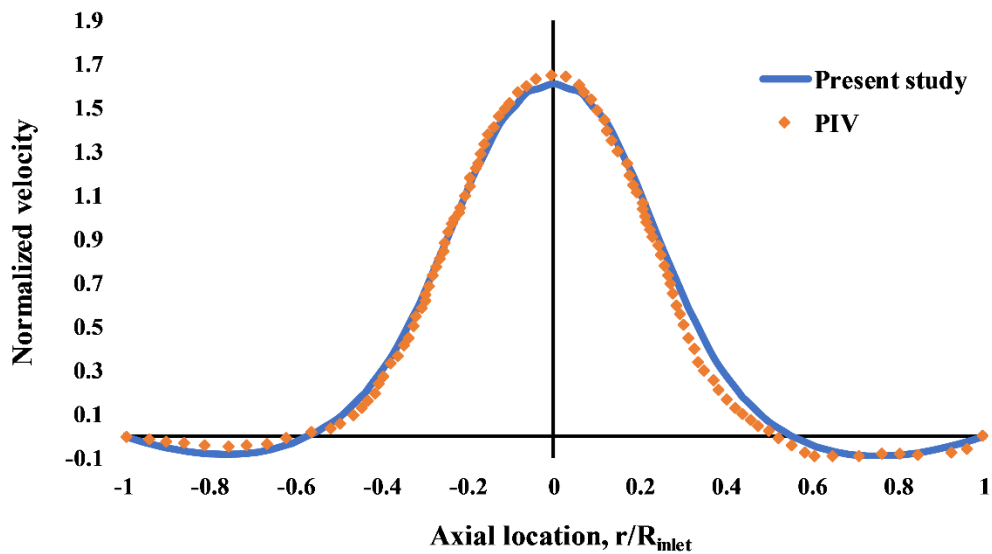
Fig. 2. 21 Profile of velocity normalized by the throat average velocity vs. radial distance at 20 mm downstream from the sudden expansion (PIV results by Raben et al. [211]).

500 pathlines were calculated that started from sample points uniformly distributed at the inlet. Again, the velocities from Ansys was smoothed by the 3-point moving average scheme to limit numerical noise. Then, the velocity-average damage function was calculated at the domain outlet.

2.5.3 Results

2.5.3.1 Exponential stress

First, convergence behavior of Lagrangian discretized power law is examined for the single pathline exponential stress case using convergence criterion e_1. For the exponential stress case, the number of time steps needed to converge the discretized power-

law model shows a completely different behavior for increasing stress as compared to the decreasing stress (Fig. 2.22a), which will be discussed afterwards.
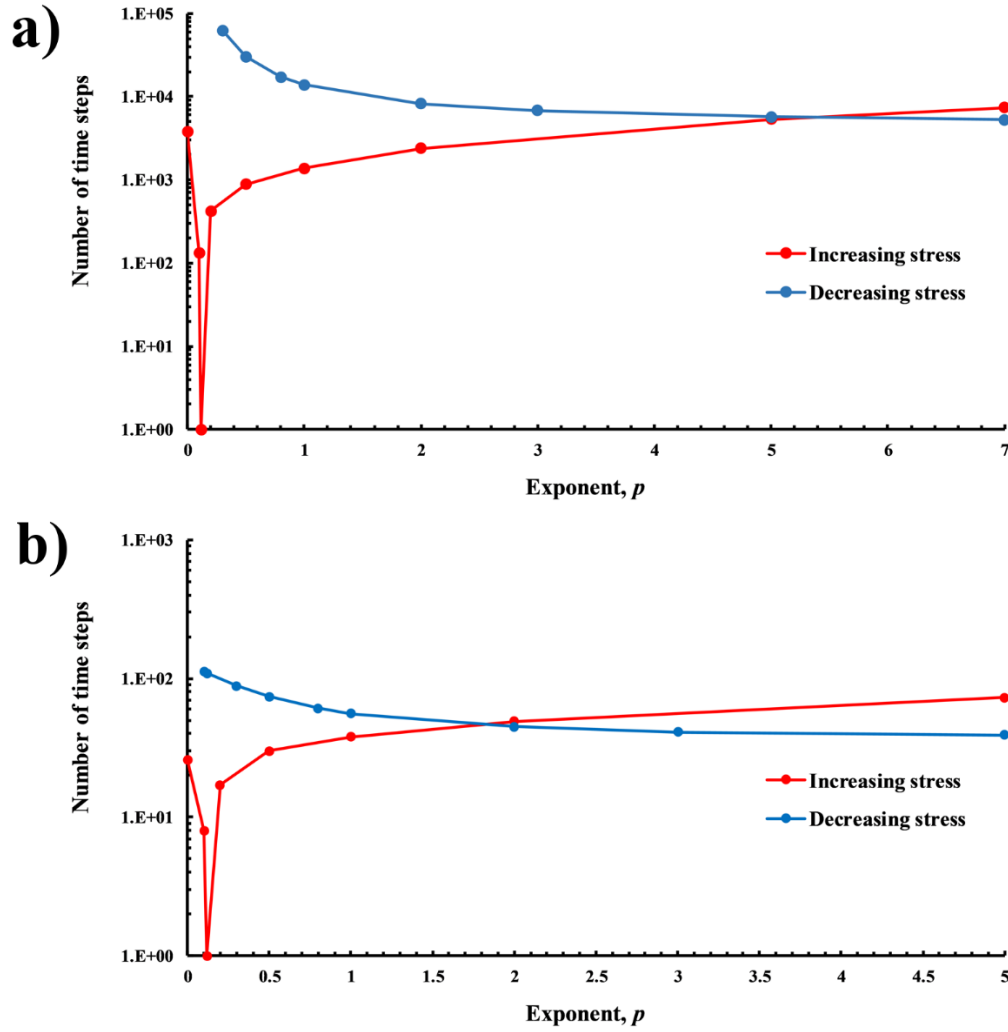
Fig. 2. 22 Required number of time steps vs. exponent for convergence of the discretized damage function (based on Heuser and Opitz [139] coefficients) for both increasing and decreasing type of the representative stress based on, a) e_1 and b) e_2.

For the increasing stress equation and $p = 0$, the stress is constant along the pathline and $\approx 3,800$ time steps are required to converge the damage function to within 0.1% of the analytical solution. Then, the number of required time steps decreases as p increases from zero to $p = \frac{1-\alpha}{\beta}$ (=0.118 for Heuser and Opitz [139] constants). For $p = \frac{1-\alpha}{\beta}$, only one time step is sufficient to obtain convergence for the Lagrangian discretized

damage function. For increasing p beyond $p = \frac{1-\alpha}{\beta}$, the number of required time steps increases monotonically, but at a decreasing rate. For $p < \frac{1-\alpha}{\beta}$, number of required time steps increases with decreasing p.

For decreasing stress (Eq. (104)), the number of required time steps decreases monotonically as p increases. As shown in Fig. 2.22a, the number of required time steps for increasing and decreasing stress are equivalent at around $p = 5$. Also implied from Fig. 2.22a, the number of time steps needed to analytically converge Eq. (104) (based on e_1) tends to increase dramatically as the exponent p becomes smaller than $\frac{1-\alpha}{\beta}$. For instance, the required n for $p = \frac{1-\alpha}{\beta}$ is more than 150,000.

The above results suggest that convergence may become an issue for flow regimes with regions of slowly decreasing stress or rapidly increasing stress. Achieving accurate estimates of the damage function based on Lagrangian discretization may become computationally expensive, and perhaps impossible, on such high-demand pathlines. As flow conditions become more complex, the possibility of having pathlines on which convergence is slow, or even impractical, becomes higher. This will be demonstrated by contrasting the relatively simple Couette flows to the more complex 2-D sudden expansion and 3-D FDA channel.

Now, convergence for the single pathline exponential stress case is investigated using the second criterion in Eq. (102), without taking into account the analytical solution. As depicted in Fig. 2.22b, the behavior of convergence for both decreasing and increasing stress is the same as when criterion Eq. (101) was used, but n is at least two orders of magnitude less. For example, for a decreasing stress, the required n is 15,000 when using the first criterion of Eq. (101), while n is 110 when using the second criterion of Eq. (102).

Although these results indicate that when using thesecond criterion (converging the discretized damage function based on previous number of time steps), the damage function is converged with smaller n compared to the case when using first criterion (converging the discretized damage function based on the analytical damage function), however, it does not mean that the damage function converged based on Eq. (102) is actually converging to

a correct damage value. For the real-life applications, an analytical solution is often not available for the damage function, therefore, the second criterion e_2 is usually used for convergence. For this reason it is instructive to evaluate whether convergence according to e_2 corresponds to convergence to the true analytical solution. The percent difference in damage function converged based on e_1 versus e_2 for different values of exponent p for both increasing and decreasing types of stress (Fig. 2.23) shows the same behavior as the results depicted in Fig. 2.22. Fig. 2.23 is in fact showing the percent error in the value of the damage function converged by criterion e_2.
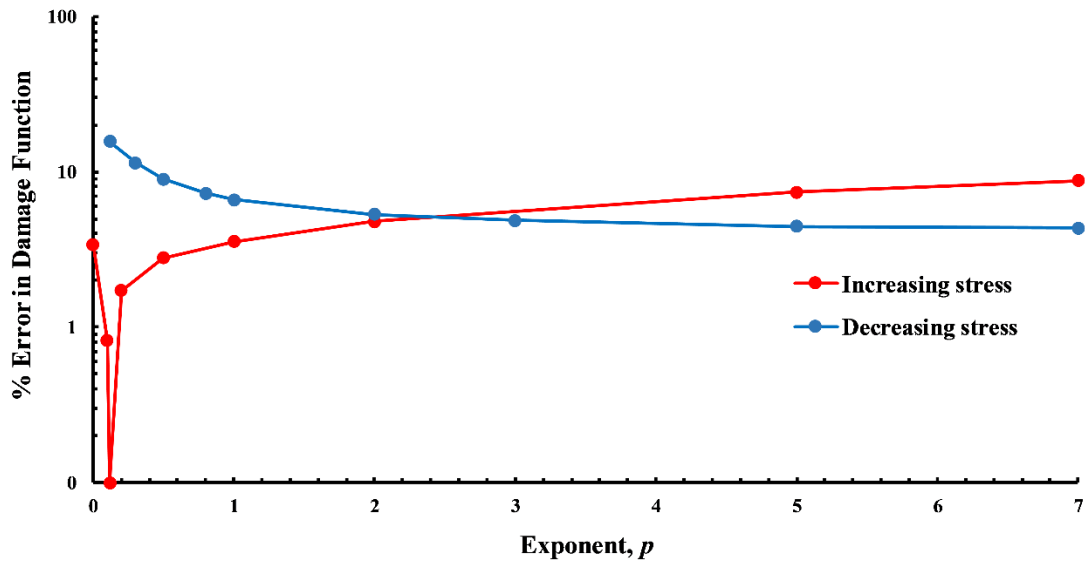
Fig. 2. 23 Percent difference in damage function vs. exponent for convergence of the discretized damage function based on e_1 vs. e_2 for both increasing and decreasing type of stress.

For decreasing stress, the error in the converged value of discretized damage function using criterion e_2 grows larger as p tends to zero, and almost plateaus as p becomes larger than 5. The results show that for the decreasing type of stress, there is always an error of at least 3% in the value of the damage function converged by e_2.

For increasing stress and $p = \frac{1-\alpha}{\beta}$, the damage function converged by e_1 is exactly the same as the value obtained by e_2. For $p > \frac{1-\alpha}{\beta}$, the error increases monotonically so that for $p = 10$, the error reaches a significant value of more than 10%. For a simple case of $p = 0$, which corresponds to a constant stress along a pathline, there is an error of 3.4%.

2.5.3.2 Inclined Couette flow

The two example pathlines for each Couette flow are shown in Fig. 2.24. The scalar stress is initially greater on the bottom pathline in the contraction, but the stress on the upper pathline increases exponentially to substantially exceed it at the exit (Fig. 2.25). For the expansion, the upper pathline initially exhibits higher stress, but decreases to less than the lower pathline a short distance into the channel. The greatest damage occurs on the upper pathline in both cases (Fig. 2.26).
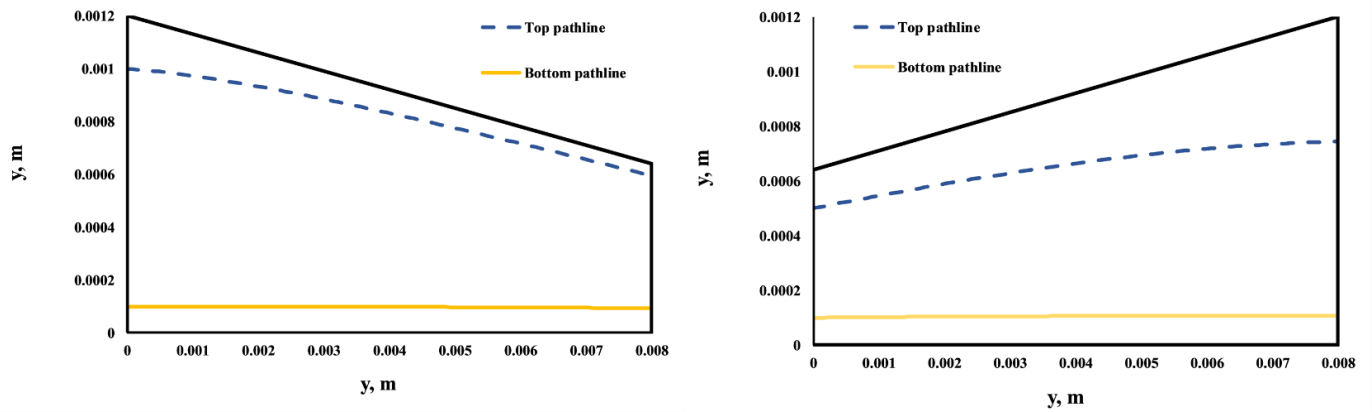
Fig. 2. 24 Example pathlines for gradual contraction (left) and gradual expansion (right).
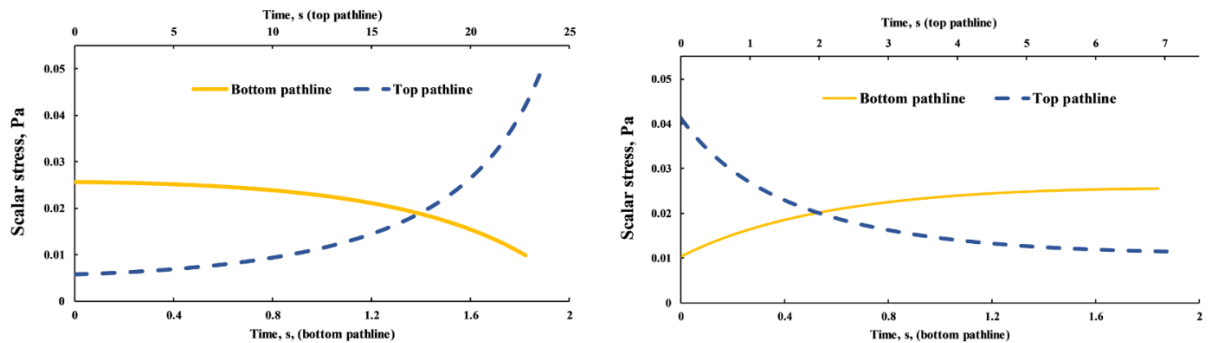
Fig. 2. 25 Scalar stress along the example pathlines for gradual contraction (left) and gradual expansion (right).
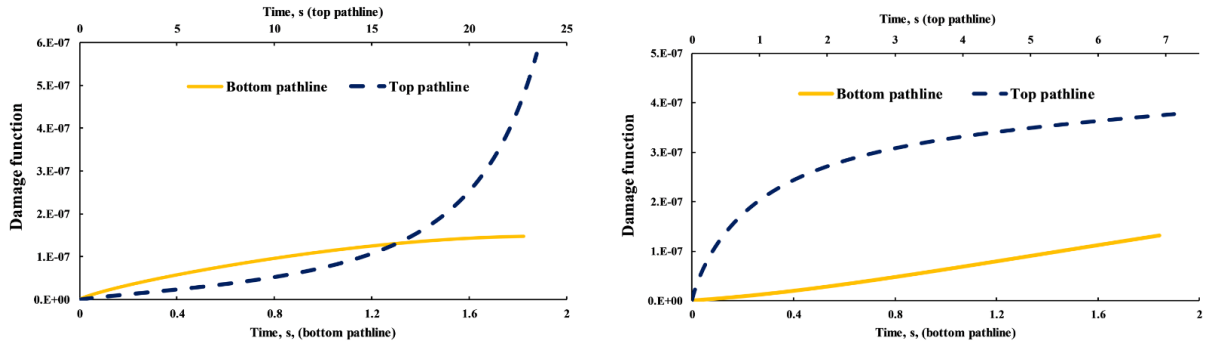
Fig. 2. 26 Cumulative damage function along the example pathlines for gradual contraction (left) and gradual expansion (right).

Convergence is shown in Fig. 2.27. In the contraction, the bottom pathline requires almost two times more time steps than the top one (Table 2.7). For the expansion, the top pathline needs three times more time steps than the bottom one. According to results in Fig. 2.22, a pathline with decreasing stress with upward concavity ($0<p<1$) requires the largest number of time steps. This is also verified by these results in the expansion and contraction. Based on Fig. 2.25, the top pathline in the expansion shows decreasing stress with upward concavity (it can be curve-fitted to an equation similar to Eq. (103) with $p=0.317$), which requires the largest number of time steps compared to the other three sample pathlines (Table 2.7). The next largest discretization is for the bottom pathline in the contraction (Table 2.7), which makes sense based on Fig. 2.22, as this pathline has decreasing stress (Eq. (103)) with $p=3.02$. The third largest number of time steps is for the top pathline in the contraction, which has increasing stress that can be curve fitted to Eq. 104 with $p=0.37$. The pathline requiring the least number of time steps is the bottom one in expansion, curve-fitted to Eq. 104 with $p=4.01$. (All four curves had good fits of at least $R^2=0.95$)
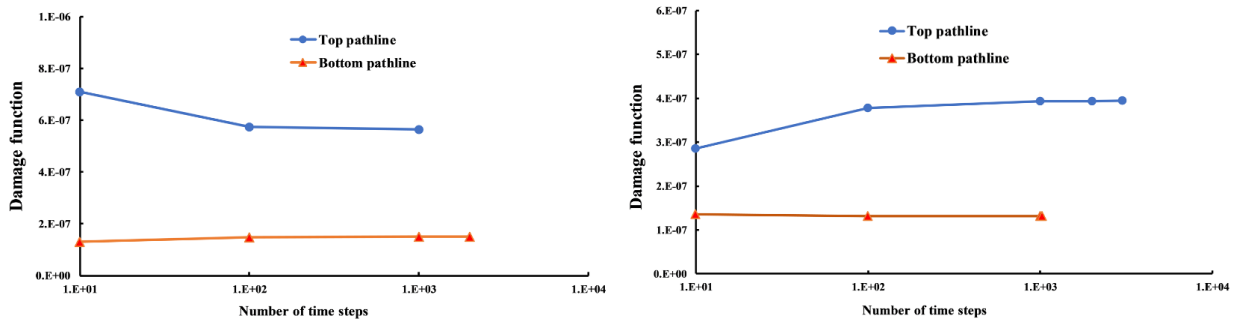
Fig. 2. 27 Damage function along the example pathlines with respect to the number of time steps for gradual contraction (left) and gradual expansion (right).

Table 2. 7 Number of time step discretization needed to converge the damage function for the four sample pathlines.

Flow channel	Number of time steps	
	Bottom pathline	Top pathline
Gradual contraction	2,032	1,112
Gradual expansion	988	3,244

From the results in Table 2.7 for single pathlines, it can be implied that the expansion geometry requires more discretizations to converge the total damage function (for the entire domain) compared to the contraction. To further examine this, sampling points were uniformly distributed at the inlet of each Couette flow to generate 50 pathlines, with all pathlines assigned the same number of time steps. To calculate the total damage function, a velocity-weighted average was calculated at the outlet. These calculations analyzed only convergence of longitudinal discretization (along the pathlines). Further refinement of transverse spatial resolution should be examined to fully evaluate convergence. The gradual contraction required 1,100 time steps to converge, while the gradual expansion needed 3,600 time steps (Fig. 2.28). As expected from the example pathlines (Table 2.7), the total damage function for the expansion required more steps to converge than that of the contraction.
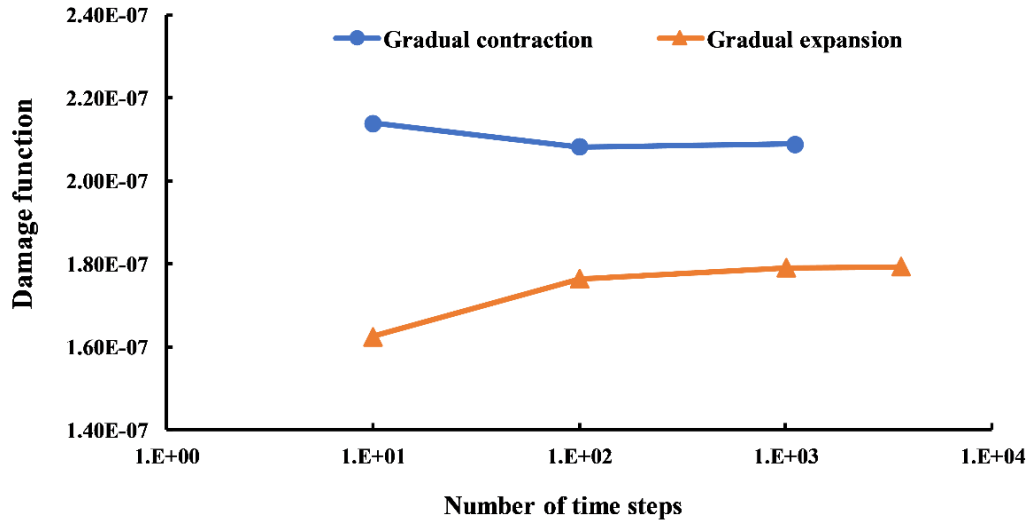
Fig. 2. 28 Damage function convergence based on 50 pathlines for gradual expansion and gradual contraction Couette flows.

2.5.3.3 Two-dimensional sudden expansion

A sample pathline and its corresponding scalar stress in the 2-D sudden expansion is depicted in Fig. 2.29. The result displays typical convergence behavior for 100 sample pathlines, and the percent error reached the convergence criterion of 0.1% after about 6,000 discretizations (Fig. 2.30).

110
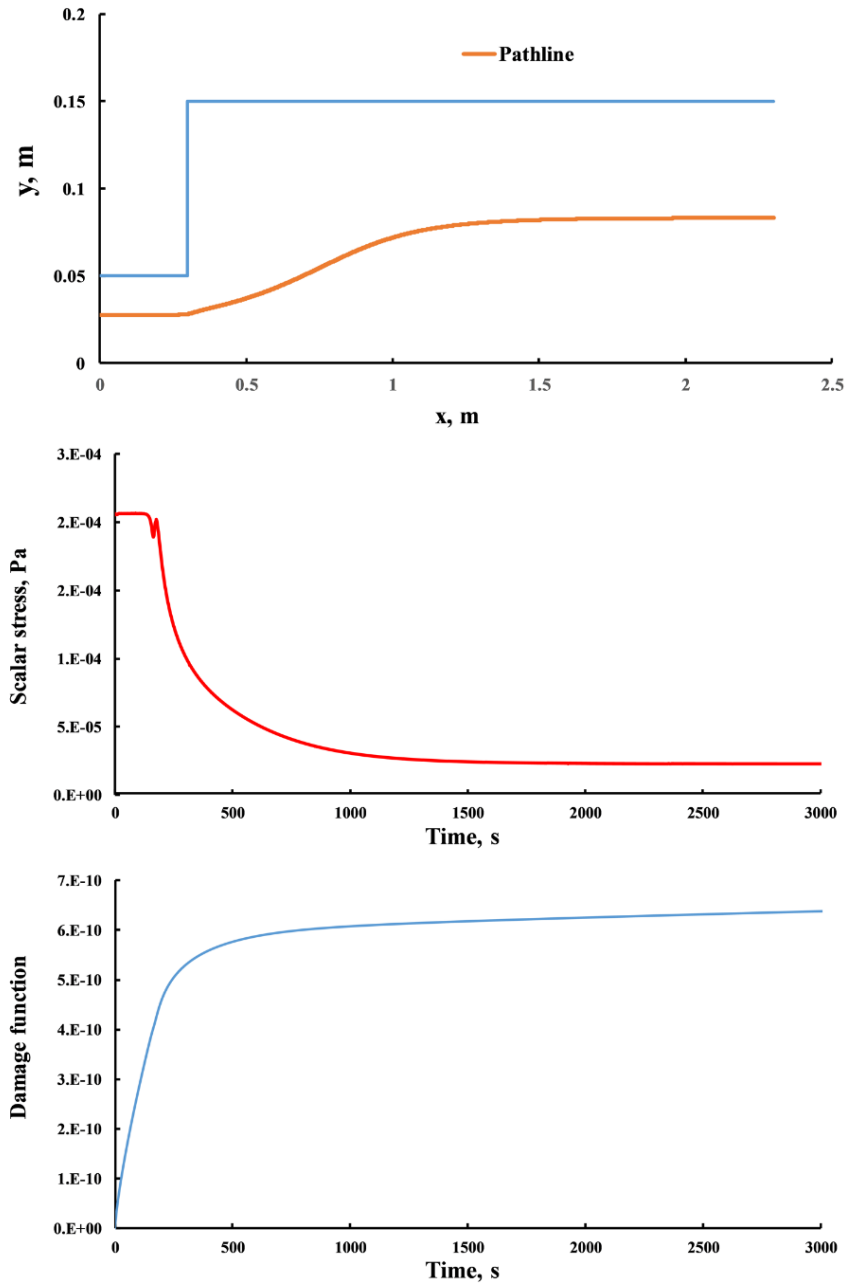
Fig. 2. 29 A sample pathline (upper), its corresponding scalar stress variation with time (middle) and damage function (lower) for the sudden expansion.

111
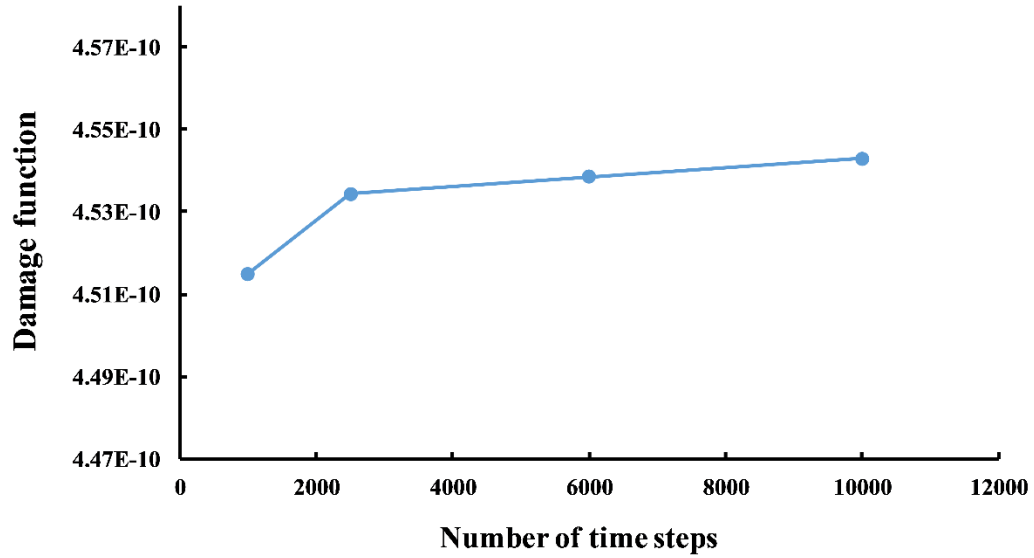
Fig. 2. 30 Damage function in the 2-D sudden expansion for different number of time steps.

2.5.3.4 3.1.3.   Three-dimensional FDA nozzle

An example pathline for the FDA nozzle and its corresponding scalar stress are shown in Fig. 2.31. Convergence of the velocity-weighted damage function for 500 uniformly-distributed pathlines is shown in Fig. 2.32. Results show that more than 15,000 discretizations are required.
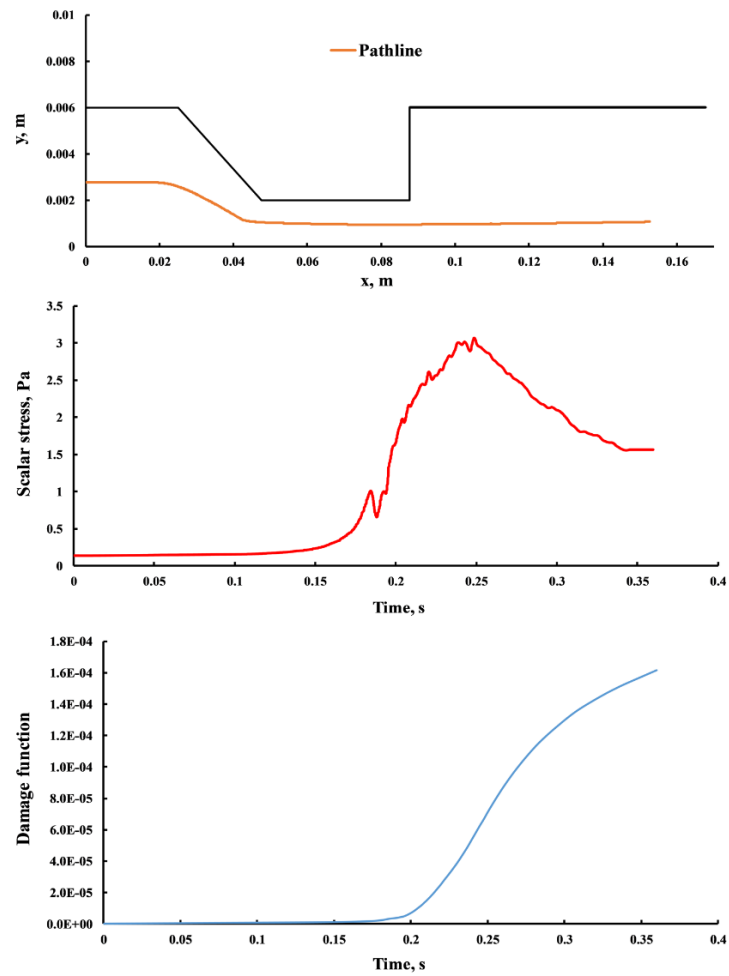
Fig. 2. 31 Example pathline (upper), its corresponding scalar stress variation with time (middle) and damage function (lower) for the FDA nozzle.
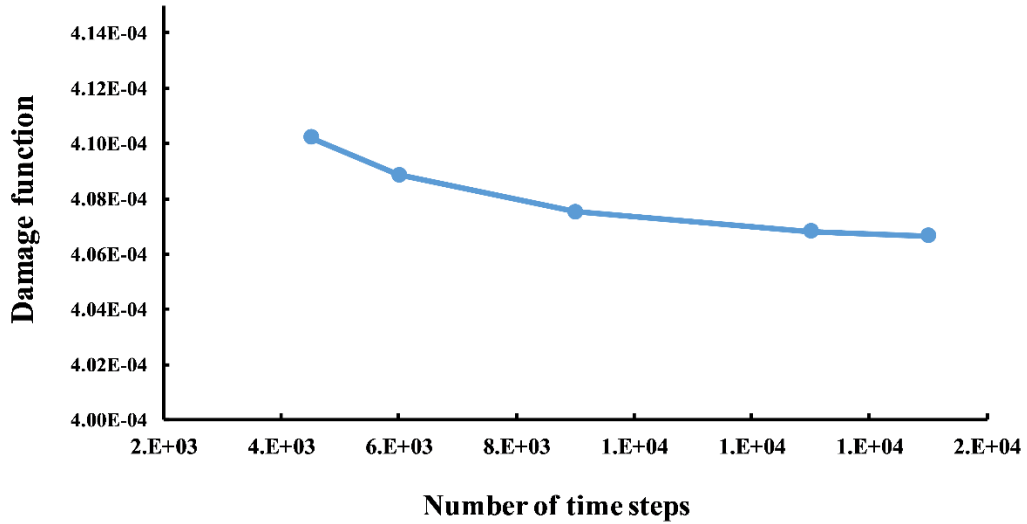
Fig. 2. 32 Damage function in the 3-D FDA nozzle for different number of time steps.

2.5.4 Discussion

From a CFD perspective, to apply the damage function to a flow domain, it needs to be discretized. The discretization can be either temporal along individual pathlines (Lagrangian) or spatial across the entire domain (Eulerian). As with any other numerical analysis, the common practice is to increase the number of discretization until the damage function is converged, i.e. the percent difference of damage function between the last and current discretization steps reaches an acceptable value, e.g. 0.1%.

In the Lagrangian temporal discretization, sufficient number of pathlines are generated at the inlet and followed to the outlet. Then, temporal discretization of the damage function is applied along each pathline. Finally, a velocity averaging of the damage function is carried out over all the pathlines at the outlet to calculate the total damage function across the entire domain. Depending on the behavior of the representative stress with time, the Lagrangian discretization may require a large number of discretizations to converge.

As a simplified case, we examined a condition where the representative stress of a particular pathline changes either as $\sigma_s = kt^{*p}$ or $\sigma_s = k(1 - t^{*p})$, for increasing and decreasing type of stress, respectively. For the case of increasing stress, the number of time steps required for convergence starts from around 3,800 for a constant stress case ($p = 0$)

114

and sharply drops to 1 for the case when $p = \frac{1-\alpha}{\beta}$. Then, n shows an increasing trend as p further increases.

However, for decreasing stress, the number of required time steps significantly increases as p tends to zero. This condition (i.e. p tending to zero for the decreasing stress case) corresponds to the condition when stress along a particular pathline drops sharply with upward concavity.

Based on the discussion above, it should be emphasized that the more complex geometry itself does not necessarily result in slower convergence rate or divergence of the damage function. In fact, more complex geometry causes more complex flow dynamics, which ultimately increases the likelihood of having pathlines with convergence issues.

This is also confirmed by the convergence results of damage function for several sample cases studied here. We started with simple 2-D geometry of inclined Couette flows, and continued with more complex 2-D sudden expansion and 3-D FDA nozzle cases. The convergence behavior is different even for the two Couette geometries with almost similar conditions, except one with gradual contraction and the other with gradual expansion. Taking 100 sample pathlines starting at the inlet, the 2-D sudden expansion requires at least 6,000 number of discretization to converge. Moreover, the 3-D FDA nozzle, although still a simple geometry compared to the actual blood contacting device but more complex than the Couette flows and 2-D sudden expansion, reached convergence after 15,000 time steps.

Only laminar flows were covered in the example cases in this study. However, following the same logic, chaotic nature of the turbulent flow that creates random complex structures increases the possibility of producing pathlines with problematic convergence behavior.

Another finding of the study is a possible error in the converged value of the damage function when using a convergence criterion based on the current and previous time steps (Eq. (102)). Generally, the common practice in CFD convergence procedure is to keep increasing the number of discretizations until the difference in the desired parameter obtained in current and previous time steps reaches a pre-determined value (Eq. (102) in this study). However, it is important to check whether the solution has actually

115

converged to a correct value. Fig. 2.23 shows that for an example case of single pathline experiencing a decreasing stress based on Eq. (104), there would always be an error of at least 3% between the actual value and the one obtained from convergence criterion in Eq. (102), for all the values of p. For the increasing stress, there is also some error for all the values of exponent p, except for $p = \frac{1-\alpha}{\beta}$ where the error is zero.

The number of sample pathlines in each of the geometry was selected arbitrarily in this study, since we are only concerned about convergence of Lagrangian discretization of the power-law model. For a complete study, it is highly important to choose enough sampling points with appropriate distribution at the geometries inlet to ensure all the important flow structures are captured by the pathlines. In actual cases, a convergence study must also be carried out for the number of pathlines. This also adds to complexity of the problem. Because increasing the number of pathline gain increases the likelihood of having pathlines with slow convergence rate or even divergent pathlines.

The main focus of this section is on the Lagrangian temporal discretization, however, the same discussion can be made for the Eulerian spatial discretization of the flow domain. In the Eulerian approach, the domain is spatially discretized into small volumetric elements. Then, the damage function is linearized (D_L) as

$$D_L = D^{1/\alpha} = C^{1/\alpha}\, \sigma^{\beta/\alpha} E \qquad\qquad (111)$$

Then, a source term (S) is defined, to be used in a standard transport equation, which is as follows:

$$S = \frac{d}{dt} D_L = \vec{v}\, \frac{\partial}{\partial \vec{x}} D_L = C^{1/\alpha}\, \sigma^{\beta/\alpha} \qquad\qquad (112)$$

where $\vec{v}$ is the velocity vector of each volumetric cell in the domain and $\vec{x}$ is the space coordinate. For further details about the derivation of above relation, please refer to section 2.6.

Finally, to get the overall hemolysis, volume integral is carried out over the entire domain as:

$$D = \left(\frac{1}{V} \int C^{1/\alpha} \, \sigma^{\beta/\alpha} \, dV\right)^{\alpha} \tag{113}$$

where V is the total volume of the flow domain. Here, the change in the representative stress with respect to space needs to be examined. If the stress changes in space as a general function as $\sigma = g(x, y, x)$ and the series $\frac{C^{1/\alpha}}{V} \sum_{i=1}^{n} g(x, y, z)^{\beta/\alpha} \Delta V$ becomes divergent or shows slow convergence rate, then the Eulerian spatial discretization also faces the same convergence issue discussed for the Lagrangian temporal discretization.

2.5.5 Conclusions

The power-law hemolysis prediction model (i.e., damage function) has been developed for pure laminar shear flow within limited range of shear stress and exposure time. However, it has been applied to much more complex flow, even in turbulent regime, due to simplicity and lack of another convenient model. With the advancement of computing technologies, a discretized form of damage function has been derived to predict the hemolysis (i.e., damage function) using the results from the CFD simulation. There is always some approximation error when discretizing a function, and discretized damage function is no exception. Therefore, it is always important to know how many discretization is needed for a discretized function to give an acceptable result (e.g. 0.1% error). In this article, we showed that for some particular pathlines with specific behavior with time/space, the damage function may never get converged, introducing a significant error into the predicted level of damage to the red cell. And for some other cases, the level of discretization may become so high that is simply beyond the current computational power.

2.6 On Eulerian discretization of the power-law model [5]

2.6.1 Introduction

Since the implementation of the first blood-contacting devices, mechanical blood damage, also known as mechanical hemolysis, has been a concern among researchers and manufacturers [213]. Non-physiologic fluid dynamical conditions in cardiovascular devices can cause either complete rupture of red cells or temporary pores in the cell membrane through which intracellular hemoglobin may escape.

Over the past half century, many attempts have been made to mathematically model mechanical blood damage, with the ultimate goal of creating a universally-accurate model to predict hemolysis across a full range of flow types. Early studies, which focused on fluid shear stress and exposure time to scale hemolysis, resulted in a class of empirical regression relations of the form of Eq. (35). For complex flows, it has been proposed that τ be replaced by a scalar stress [153]. However, problems have been recognized with this extension [148, 185]. There is also another class of more mechanistic hemolysis prediction models based on cell membrane strain [100, 170, 214]. With advances in computer technology, computational fluid dynamics (CFD) simulations have been extensively used in analysis of hemolysis [147, 188, 215, 216], including recent direct numerical simulations of flows containing deformable erythrocytes [144, 175]. Despite advancements in other models, the power-law model remains popular, perhaps in part because the limited data on hemolysis that is available in simple, controlled flows was originally fit to the power-law model.

This section investigates issues that arise with two modifications to the power-law model: 1) its transformation to an Eulerian control volume, and 2) the use of a linearized damage function. The power-law hemolysis function (Eq. (35)) is Lagrangian. The Lagrangian material derivative (following the fluid element) can be transformed to the substantial derivative (in a stationary fluid element). In their paper developing the Eulerian method for predicting hemolysis, Garon & Farinas [160] proposed a linearized damage function and gave a result for its transformation, but did not show the intermediate steps. Because the issue with transformation applies regardless of whether the damage function

---

[5] Most of the material in this section is adopted from our published work in Faghih and Sharp [212].

is linearized, the derivation will be outlined for both the original and linearized hemolysis prediction methods.

2.6.2 Methods

2.6.2.1 Transformation of the original hemolysis function

The transformation from material derivative to substantial derivative is given generally as

$$\frac{D}{Dt}(D) = \left(\frac{\partial}{\partial t} \bigg|_{\vec{x}=fixed} + \vec{v} \cdot \nabla|_{t=fixed} \right) D \tag{114}$$

where t is time. Note that duration of exposure to stress is not the same as time, $E \neq t$. Further, duration of exposure may be a function of both space and time, $E = E(\vec{x}, t)$. If the flow is steady, then both fluid stress and duration of stress are constant in time at a fixed point. However, the spatial derivative may include variations in both E and τ. Retaining the temporal derivative as a placeholder, Eq. (114) becomes

$$\frac{D}{Dt}(D) = \left[\frac{\partial D}{\partial t} + \vec{v} \cdot \left(\frac{\partial D}{\partial E} \frac{\partial E}{\partial \vec{x}} + \frac{\partial D}{\partial \tau} \frac{\partial \tau}{\partial \vec{x}} \right) \right] \frac{D}{Dt}(D) = \left(\frac{\partial}{\partial t} \bigg|_{\vec{x}=fixed} + \vec{v} \cdot \nabla|_{t=fixed} \right) D \tag{115}$$

The problem of decreasing τ causing a paradoxical reduction in hemolysis (negative derivative $\partial \tau / \partial \vec{x}$) has been identified by Grigioni et al. [151]. In the absence of a better approach, it was recommended that derivatives of τ be ignored. This is tantamount to shear stress being constant along streamlines, which was true in the Couette flow experiments that produced the power-law model. However, τ is not, in general, constant in more complex blood-contacting devices. Nonetheless, if the second part of the spatial derivative term is ignored, the spatial derivative can be simplified. Noting that $\partial D / \partial T$ is a scalar, the spatial derivative becomes

$$\vec{v} \cdot \frac{dD}{d\vec{x}} = \frac{\partial D}{\partial E} \vec{v} \cdot \frac{dE}{d\vec{x}} = \frac{\partial D}{\partial E} \left(u \frac{\partial E}{\partial x} + v \frac{\partial E}{\partial y} + w \frac{\partial E}{\partial z} \right) \tag{116}$$

in a Cartesian coordinate system with velocities u, v and w in the x, y and z directions, respectively.

Exposure time E is a Lagrangian quantity that is specific to particular streamlines. Exposure time is given by $S/\bar{V}_s$, where S is the length of the streamline and $\bar{V}_s$ is the mean velocity during time T along the streamline. Thus, the derivative of exposure time along the streamline is $\partial T/\partial s = 1/\bar{V}_s$, where s the streamwise direction. The derivatives along Cartesian coordinates become

$$\frac{dE}{d\vec{x}} = \frac{\partial E}{\partial s}\frac{\partial s}{\partial x_i} = \frac{n_i}{\bar{V}_s} \tag{117}$$

where $n_i = \partial s/\partial x_i$ is the direction cosine of the ith coordinate relative to the streamwise direction. Plugging the power-law damage function of Eq. (35) into Eq. (116), and using Eq. (117), the spatial part of the material derivative becomes

$$\vec{v}\cdot\frac{dD}{d\vec{x}} = C\alpha E^{\alpha-1}\tau^\beta\frac{V}{\bar{V}_s} \tag{118}$$

where V is local magnitude of velocity. Note that $\bar{V}_s$ is not the local velocity and may be a function of space and time, thus it complicates Eulerian analysis of complex flows.

To simplify for a uniaxial flow with constant velocities along each streamline, $\vec{v} = u\hat{\imath}$, where $\hat{\imath}$ is the unit vector in the direction of flow, and $\bar{V}_s = V = u$. The exposure time is x/u. Hemolysis only changes spatially and the spatial rate of change of hemolysis at a fixed point is

$$\frac{dD}{dx} = \frac{C\alpha E^{\alpha-1}\tau^\beta}{u} \tag{119}$$

For a streamline of length L, the hemolysis along the streamline can be found by integration

$$D = \int_0^L \frac{\partial D}{\partial x}dx = \frac{C\alpha\tau^\beta}{u}\int_0^L E^{\alpha-1}dx = \frac{C\alpha\tau^\beta}{u}\int_0^L \left(\frac{x}{u}\right)^{\alpha-1}dx = C\tau^\beta\left(\frac{L}{u}\right)^\alpha \tag{120}$$

Note that inserting the total duration of stress $E = L/u$ returns the original form of Eq. (35).

The average hemolysis for blood exiting the channel can be found by integrating the flux of damage over the exit cross section

$$\bar{D} = \frac{1}{\bar{u}A} \int uD dA \tag{121}$$

where $\bar{u}$ is the cross-sectional average velocity and A is the cross-sectional area.

2.6.2.2 Transformation of the linearized damage function

Garon & Farinas [160] presented an Eulerian method for calculating hemolysis in a flow field. They first modified the Lagrangian function to make it linear in duration of stress

$$D_I = D^{1/\alpha} = C^{1/\alpha} E \tau^{\beta/\alpha} \tag{122}$$

The Lagrangian-to-Eulerian transformation of Eq. (114) applied to this linearized function becomes

$$\frac{D}{Dt}(D_I) = \left(\left. \frac{\partial}{\partial t} \right|_{\vec{x}=fixed} + \vec{v} \cdot \nabla|_{t=fixed} \right) D_I \tag{123}$$

Inserting Eq. (122) into eq. (123) and using Eq. (117), the substantial derivative for steady flow becomes

$$\frac{D}{Dt}(D_I) = \left[\frac{\partial D_I}{\partial t} + \vec{v} \cdot \left(\frac{\partial D_I}{\partial T}\frac{dE}{d\vec{x}} + \frac{\partial D_I}{\partial \tau}\frac{\partial \tau}{\partial \vec{x}} \right) \right] = C^{\frac{1}{\alpha}} \left[0 + \vec{v} \cdot \left(\tau^{\frac{\beta}{\alpha}} \frac{n_i \hat{\iota}_i}{\bar{V}_s} + E\frac{\beta}{\alpha} \tau^{\frac{\beta}{\alpha}-1} \frac{\partial \tau}{\partial \vec{x}} \right) \right] \tag{124}$$

Again ignoring spatial variations in shear stress, the spatial derivative simplifies to

$$\vec{v} \cdot \frac{dD_I}{d\vec{x}} = C^{1/\alpha} \tau^{\beta/\alpha} \frac{V}{\bar{V}_s} \tag{125}$$

For uniaxial flow with constant velocities along streamlines ($V = \bar{V}_s$)

$$\vec{v} \cdot \frac{dD_I}{d\vec{x}} = C^{1/\alpha} \tau^{\beta/\alpha} \qquad (126)$$

Garon & Farinas [160] then define a source term in an Eulerian treatment of the steady flow field that is equivalent to the flux of linearized hemolysis in Eq. (126)

$$\sigma_s = \vec{v} \cdot \frac{dD_I}{d\vec{x}} = C^{1/\alpha} \tau^{\beta/\alpha} \qquad (127)$$

Issue 1 – Transformation limitations

The first issue with the Garon & Farinas [160] method is highlighted by the difference between Eqs. (127) and (125), which is that the difference between local velocity and the average velocity along the streamline that passes through the point is not included in Eq. (127). This means that Eq. (127) is only valid when these two velocities are the same, $V = \bar{V}_s$. Thus the conditions for which Eq. (127) is valid are the same as those for Eq. (126), *i.e.*, that the flow is uniaxial and that velocities are constant along streamlines.

Issue 2 – Exponents are not distributive across integrals

According to Garon & Farinas [160], the average hemolysis can be found by integrating the linearized Eulerian source term (Eq. 127) over the flow field and then readjusting the exponent to return the original damage function

$$\bar{D} = \left(\frac{1}{\bar{u}A} \int \sigma_s dV \right)^{\alpha} \qquad (128)$$

Note from Eq. (127) that integrating the source term over the volume is equivalent to integrating the flux of the linearized damage across the exit so long as the flow is steady and uniaxial flow with constant velocities along streamlines

$$\int \sigma_s dV = \int u \frac{\partial D_I}{\partial x} dx dA = \int u D_I dA \qquad (129)$$

Using Eqs. (121), (128) and (129), to equate hemolysis predicted by both methods

$$\frac{1}{\bar{u}A} \int uDdA = \bar{D} = \left(\frac{1}{\bar{u}A} \int uD_I dA\right)^\alpha \tag{130}$$

By inserting eq. (122) and rearranging

$$\frac{\int uDdA}{(\int uD^{1/\alpha}dA)^\alpha} = (\bar{u}A)^{1-\alpha} \tag{131}$$

Eq. (131) is satisfied if $\alpha = 1$ or if D is constant. However, $\alpha \neq 1$ for any of the power-law models, thus the second condition is the remaining possibility. From Eq. (35), D is constant when

$$E^\alpha \tau^\beta = constant \tag{132}$$

E and τ are both constant for steady Couette flow. Otherwise, although Eq. (132) has a number of potential solutions, it does not hold for common axisymmetric, pressure-driven flows. For instance for Poiseuille flow, shear at the centerline is always zero. Eq. (132) then shows that the Eulerian model only applies for stagnant Poiseuille flow, in which the predicted hemolysis is zero.

The root of the inconsistency is that exponents are not distributive across integrals, i.e., $\left(\int f^{1/\alpha} dx\right)^\alpha \neq \int fdx$, or as shown by Eq. (128), $\left(\int uD^{1/\alpha}dA\right)^\alpha \neq \int uDdA$, except for some rather limiting conditions.

2.6.3 Results

Comparison of original and linearized damage functions for an example flow

Let us consider two flow fields (Fig. 2.33) that expose the second issue. Both flows are steady and uniaxial with constant velocities along streamlines (the limitations of issue 1 are satisfied) and both have the same core velocity u_c. Both channels have the same half height h and length L (and, therefore, have the same flow rate). Both flow fields have shear only near the wall, with the core of the flow having constant velocity and, therefore, zero shear. For one flow field, the shear flow near the wall has velocity $u = \frac{y}{Fh}u_c$ and average velocity $u_c/2$, where u_c is the velocity of the core, F is the fraction of the half height that

each shear flow occupies (Fig. 2.33 left). The average velocity of the flow is $\bar{u}_1 = F\frac{u_c}{2} + (1-F)u_c = \left(1 - \frac{F}{2}\right)u_c$. This flow field is similar to that of flow at the entrance of a channel with stationary walls. The second flow field has a shear region of the same size and shear rate, but has velocity $u = \left(2 - \frac{y}{Fh}\right)u_c$ and average velocity $3u_c/2$ (Fig. 2.33 right). The shear flow occupies the same fraction F of the half height. The average velocity of the flow is $\bar{u}_2 = F\frac{3u_c}{2} + (1-F)u_c = \left(1 + \frac{F}{2}\right)u_c$. This flow field is similar to that of flow at the entrance of a channel with moving walls. For simplicity, it is assumed that the velocity profiles for both flows remain the same throughout the length of the channel. These velocity profiles can be generalized as $u = \left[1 + a\left(1 - \frac{y}{Fh}\right)\right]u_c$, where the shear layer has larger velocity than the core for $a > 0$ and lower velocity than the core for $a < 0$. The two cases in Fig. 2.33 correspond to $a = -1$ and $a = 1$, respectively. The average velocity is $\bar{u} = F\left(1 + \frac{a}{2}\right)u_c + (1-F)u_c = \left(1 + F\frac{a}{2}\right)u_c$. The velocity can thus also be written as

$$u = \left[1 + a\left(1 - \frac{y}{Fh}\right)\right]\frac{\bar{u}}{1 + \frac{Fa}{2}}\tag{133}$$
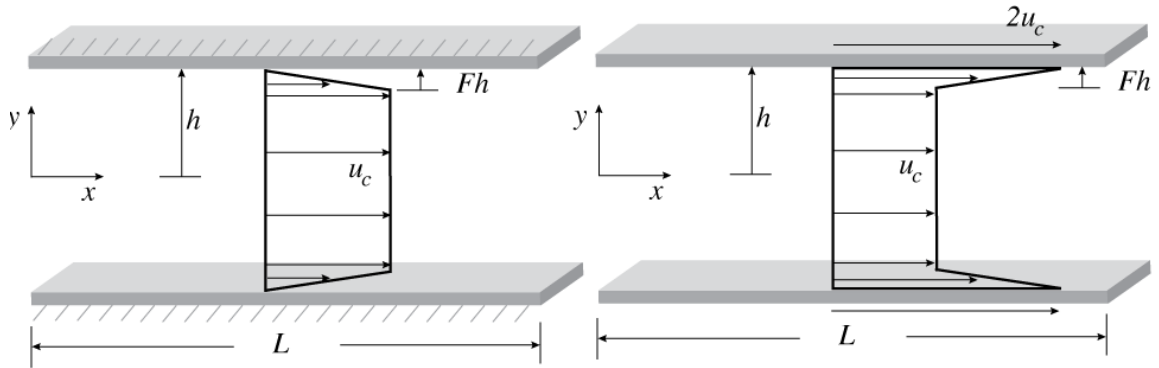
Fig. 2. 33 Two flows having the same core velocity and the same areas of equivalent shear, but one shear region has lower velocity (left) and the other has high velocity (right).

2.6.3.1 Original method

The current problem can be solved per unit breadth of the channel as

$$\overline{D} = \frac{1}{\overline{u}h} \int uD\,dy = \frac{1}{\overline{u}h} \int uC \left(\frac{L}{u}\right)^{\alpha} \tau^{\beta}\,dy = \frac{CL^{\alpha}\tau^{\beta}}{\overline{u}h} \int_{0}^{Fh} u^{1-\alpha}\,dy \tag{134}$$

(The integral need not extend to the center of the channel, because the shear is zero in the core.) Now inserting the velocity profile for the shear layer

$$\overline{D} = \frac{CL^{\alpha}\tau^{\beta}}{\overline{u}h} \int_{0}^{Fh} \left\{ \left[1 + a\left(1 - \frac{y}{Fh}\right)\right] \frac{\overline{u}}{1 + \frac{Fa}{2}} \right\}^{1-\alpha} dy$$

$$= \frac{CL^{\alpha}\tau^{\beta}}{\overline{u}h} \left(\frac{\overline{u}}{1 + \frac{Fa}{2}}\right)^{1-\alpha} \frac{\left(-\frac{Fh}{a}\right)}{2 - \alpha} \left\{ \left[1 + a\left(1 - \frac{y}{Fh}\right)\right]^{2-\alpha} \right\}_{0}^{Fh} \tag{135}$$

$$= \frac{CL^{\alpha}\tau^{\beta}}{\overline{u}^{\alpha}} \cdot \frac{\left(-\frac{F}{a}\right)}{(2 - \alpha)\left(1 + \frac{Fa}{2}\right)^{1-\alpha}} [1 - (1 + a)^{2-\alpha}]$$

For the first case with $a = -1$

$$\overline{D}_1 = \frac{CL^{\alpha}\tau^{\beta}\overline{u}_1^{-\alpha}(F)}{(2 - \alpha)\left(1 - \frac{F}{2}\right)^{1-\alpha}} \tag{136}$$

For the second case with $a = 1$

$$\overline{D}_1 = \frac{CL^{\alpha}\tau^{\beta}\overline{u}_1^{-\alpha}(F)}{(2 - \alpha)\left(1 - \frac{F}{2}\right)^{1-\alpha}} \tag{137}$$

The ratio of the two becomes

$$R = \frac{\overline{D}_2}{\overline{D}_1} = \frac{1 - \frac{F}{2}}{1 + \frac{F}{2}} [2^{2-\alpha} - 1] \tag{138}$$

For the typical power-law model, $\alpha \sim 1$. For the case of exactly $\alpha = 1$, R becomes $(1 - F/2)/(1 + F/2)$, which is the inverse of the ratio of the flow rates. The first case with lower velocity in the shear layer produces greater average hemolysis because the

exposure time is longer. However, for $\alpha < 1$, the ratio increases. For instance, for $\alpha = 0.765$ (the Heuser & Optiz [139] value), R becomes 1.354 times the inverse ratio of the flow rates. However, the first case still produces greater average hemolysis ($R < 1$) so long as $F > 0.3$. For $F < 0.3$, the flow with higher velocity in the shear area produces greater hemolysis at the exit of the channel, $R > 1$. Curiously, $R = 0$ in Eq. (135) for $\alpha = 2$, but this also causes a singularity in the predicted average hemolysis (Eq. (135)). Because $\alpha < 1$ for all known hemolysis models, this condition was not analyzed further.

2.6.3.2 Linearized method

For the linearized, Eulerian method, the Garon & Farinas [160] definition of the source term (Eq. (127)) is inserted into Eq. (128)

$$\bar{D} = \left(\frac{1}{\bar{u}A} \int \sigma_s dV \right)^{\alpha} = \left(\frac{1}{\bar{u}} C^{1/\alpha} \tau^{\beta/\alpha} FL \right)^{\alpha} = \bar{u}^{-\alpha} C\tau^{\beta} F^{\alpha} L^{\alpha} \tag{139}$$

which for the ratio of the two cases gives

$$R = \frac{\bar{D}_2}{\bar{D}_1} = \frac{\bar{u}_2^{-\alpha}}{\bar{u}_1^{-\alpha}} = \left(\frac{1 - \dfrac{F}{2}}{1 + \dfrac{F}{2}} \right)^{\alpha} \tag{140}$$

Comparing this ratio for the linearized method (Eq. (140)) to that for the original method (Eq. (138)), it is evident that the two are the same only for $\alpha = 1$. For $\alpha < 1$, characteristic of all known hemolysis models, the ratio is less than the inverse ratio of the flow rates regardless of F. Further, the ratio is always less than unity, $R < 1$. This behavior is distinctly different than for the original method.

2.6.3.3 Correcting the source term

The source term of Eq. (127) is, therefore, incorrect. Let us return to Eq. (128) for the linearized method and Eq. (121) for the original method to solve for a source term that matches the two hemolysis values. Equating Eqs. (121) and (128)

$$\left(\frac{1}{\bar{u}A} \int \sigma_s dV \right)^{\alpha} = \bar{D} = \frac{1}{\bar{u}A} \int uD dA \tag{141}$$

For fully-developed flow between flat plates with streamlines all of the same length L, the volume integral on the left-hand side and the area integral on the right-hand side can both be reduced to integrals on the y axis of the channel. For a channel of breadth b, Eq. (141) becomes

$$\left(\frac{1}{\bar{u}hb}\int \sigma_s Lbdy\right)^{\alpha} = \bar{D} = \frac{1}{\bar{u}hb}\int uDbdy \tag{142}$$

Differentiating to solve for σ

$$\sigma_s = (\bar{u}h)^{1-\frac{1}{\alpha}}C^{\frac{1}{\alpha}}\frac{\partial}{\partial y}\left[\left(\int \tau^{\beta}u^{1-\alpha}dy\right)^{\frac{1}{\alpha}}\right] \tag{143}$$

For the current problem, the shear inside the integral is a constant within the shear layer and zero in the core. Therefore, the source term is zero in the core, and in the shear layer is

$$\sigma_s = (\bar{u}h)^{1-\frac{1}{\alpha}}C^{\frac{1}{\alpha}}\tau^{\frac{\beta}{\alpha}}\frac{\partial}{\partial y}\left[\left(\int u^{1-\alpha}dy\right)^{\frac{1}{\alpha}}\right] \tag{144}$$

The integral of velocity, which was evaluated in Eq. (138), can be inserted

$$\sigma_s = \frac{\partial}{\partial y}\left[\frac{\bar{u}h}{L}(\bar{D})^{\frac{1}{\alpha}}\right]$$

$$= (\bar{u}h)^{1-\frac{1}{\alpha}}C^{\frac{1}{\alpha}}\tau^{\frac{\beta}{\alpha}}\left[\left(\frac{\bar{u}}{1+\frac{Fa}{2}}\right)^{1-\alpha}\frac{\left(-\frac{Fh}{a}\right)}{2-\alpha}\right]^{\frac{1}{\alpha}}\frac{\partial}{\partial y}\left(\left\{\left[1+a\left(1-\frac{y}{Fh}\right)\right]^{2-\alpha}+B'\right\}^{\frac{1}{\alpha}}\right) \tag{145}$$

where B' is the constant of integration.

Evaluating the derivative

$$\sigma_s = (\bar{u}h)^{1-\frac{1}{\alpha}} C^{\frac{1}{\alpha}} \tau^{\frac{\beta}{\alpha}} \left[\left(\frac{\bar{u}}{1 + \frac{Fa}{2}} \right)^{1-\alpha} \frac{\left(-\frac{Fh}{a} \right)^{\frac{1}{\alpha}}}{2 - \alpha} \left\{ \left[1 + a \left(1 - \frac{y}{Fh} \right) \right]^{2-\alpha} + B' \right\}^{\frac{1}{\alpha}-1} \frac{1}{\alpha} \left[1 \right.\right.$$
$$\left. + a \left(1 - \frac{y}{Fh} \right) \right]^{1-\alpha} (2 - \alpha) \left(-\frac{a}{Fh} \right) \tag{146}$$

B' is determined by the boundary condition that $\sigma_s = 0$ at $y = Fh$, which gives $B' = -1$. Plugging this value of B' back into Eq. (145), the source term becomes

$$\sigma_s = hC^{\frac{1}{\alpha}} \tau^{\frac{\beta}{\alpha}} \left(1 + \frac{Fa}{2} \right)^{\frac{\alpha-1}{\alpha}} (2 - \alpha)^{-\frac{1}{\alpha}} \left(-\frac{F}{a} \right)^{\frac{1}{\alpha}} \left\{ \left[1 + a \left(1 - \frac{y}{Fh} \right) \right]^{2-\alpha} - 1 \right\}^{\frac{1}{\alpha}-1} \frac{2-\alpha}{\alpha} \left[1 \right.$$
$$\left. + a \left(1 - \frac{y}{Fh} \right) \right]^{1-\alpha} \left(-\frac{a}{Fh} \right) \tag{147}$$

whereas from Garon & Farinas [160] (Eq. (127))

$$\sigma_s = C^{1/\alpha} \tau^{\beta/\alpha}$$

2.6.4 Discussion

A comparison of Eqs. (147) and (127) shows that even if the limitations of Issue 1 are satisfied, the proper source term for the linearized method depends on the flow field. Velocity profiles of the example flows of Fig. 2.33 were reducible to an analytical form that could be mathematically manipulated to solve for the valid source term (Eq. (147)). However, for more complex flows in complex geometries, such solutions may not be available.

Hariharan, et al. [217] found dependence of the ratio of predicted hemolysis between the original and linearized methods on the exponent of duration of exposure for fully-developed non-Newtonian pipe flow, which satisfies Issue 1. While they did not recognize the error in the Garon & Farinas [160] source term, this dependence confirms the inconsistency. The same ratio was calculated for Couette flow with converging channel walls. This flow does not satisfy Issue 1 because velocities are not constant along streamlines, but the same dependence was found.

At least five models for Lagrangian hemolysis rate have been derived from the power law [163]. Some of these are based on a linearized damage function and, therefore, suffer from problems related to Issues 1 and 2 identified here for the Eulerian approach.

It is worth mentioning the potential implications of turbulent flow. First, in contrast to the analysis performed here, turbulent flow is strictly unsteady. Therefore, truly Lagrangian pathlines become difficult to identify, and exposure time and stress history are potentially different for each red cell passing through an Eulerian fluid element. The typical approach has been to apply Reynolds averaging and to use a scalar stress that depends on Reynolds stresses or energy dissipation rate. While considerable uncertainty remains about how best to scale turbulent stresses, so long as the Reynolds average approximation is accepted, the results reported in this paper apply equally to laminar and turbulent flow, and the issues identified are independent of how the scalar stress is represented

2.6.5 Conclusions

Two issues have been identified with the linearized, Eulerian method of hemolysis prediction with the power-law model [160] and, in particular, the source term of Eq. (127). First, the transformation to a fixed control volume lacks dependence of duration of exposure on location. Therefore, the solution is valid only for uniaxial flow with constant velocities along streamlines. Second, the linearized model involves distribution of an exponent across an integral, which is valid only for very limited conditions. The simple source term of Eq. (127) is correct only for these limited conditions. The valid source term for more complex conditions, such as Eq. (147) for the example flows, depends on velocity fields that may not be easily reducible to analytical form, such as in blood pumps and other cardiovascular devices.

CHAPTER III: EXPERIMENTAL TESTS

3.1 Introduction

Developing a universal mechanistic model for blood damage prediction requires a thorough understanding of how red cell membrane behave in response to different flow conditions. Because it was thought that shear stress is the main factor in damaging red cells, it has received a considerable amount of attention in the literature.

Membrane deformation and different modes of red cell motion under different levels of shear rate has been well-established [81, 84, 96]. Furthermore, sufficient amount of literature exist on the amount of released hemoglobin based on the pure shear stress applied to the blood suspension [40].

On the contrary, it was not until recently that the possibility of extensional (sometimes also called elongational) type of flow in damaging red cells has received some attention [98, 148]. One of the rare studies on the deformation of the red cells in pure laminar extensional flow vs. pure laminar shear flow was done by Lee, et al. [101], using a hyperbolic microchannel and rabbit red cells. Although they only went up to 10 Pa, they found that the red cell membrane deforms more in extensional flow than it does in shear flow. Therefore, there is a great need to conduct more research in this area (i.e., red cell in extensional flow) and to go beyond the stress levels that Lee, et al. [101] studied in their experiment.

In the experimental part of my research, an experimental set-up was assembled to apply both extensional as well as shear stress to the red cells up to the stress level relevant to blood contacting devices, and also to compare how membrane deformation differs in extensional flow versus in shear flow.

3.2 Experimental set-up

A schematic of the experimental set-up is shown in Fig. 3.1. Details about each component of the experimental set-up are presented in the following sub-sections.
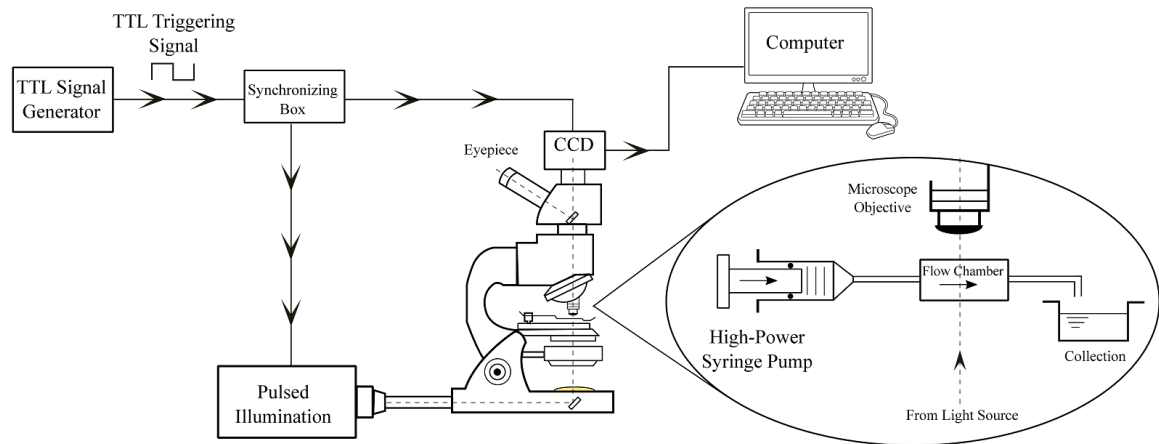
Fig. 3. 1 Schematic of the experimental set-up to capture images of the red cell flowing through microchannels.

3.2.1 Microchannel fabrication

All the microchannel parts were machined out of Poly(methyl methacrylate) (PMMA, also known as acrylic) sheets using an Othermill CNC machine (Othermill, Other Machine Company, Berkeley, USA, CA) in the Mechanical Engineering shop (Fig. 3.2) .
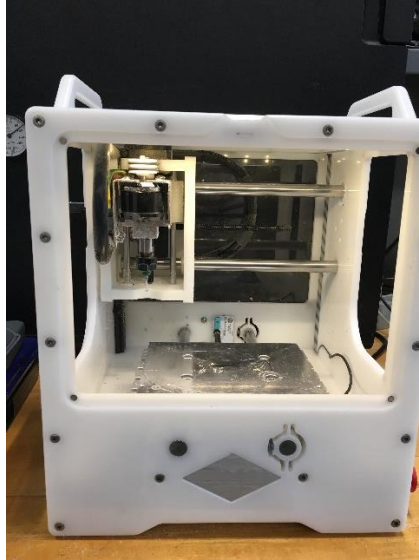
Fig. 3. 2 Othermill CNC machine used to machine the microchannel out of PMMA sheets.

The reason for choosing PMMA to channel fabrication is because it is inexpensive, abundant, ease to work with, has strong mechanical properties and most importantly it is highly transparent, allowing for optical access through the microchannel for digital imaging. The PMMA sheets were 1/32 inch (0.794±0.1 mm) thick and was purchased from McMaster-Carr Company (Elmhurst, USA). Brand-new general 2-flute carbide end mills of different diameters, available in Mechanical Engineering shop, were used to cut the flow channels.

A typical channel is composed of three PMMA sheets. The middle sheet is the one on which the channel geometry is machined. Then, there is the top sheet with inlet and outlet holes in it. And finally, there is a sheet, without any features, just to close the bottom of the channel. Also, two threaded PMMA blocks are used as the inlet and outlet connector into and out of the flow channel.
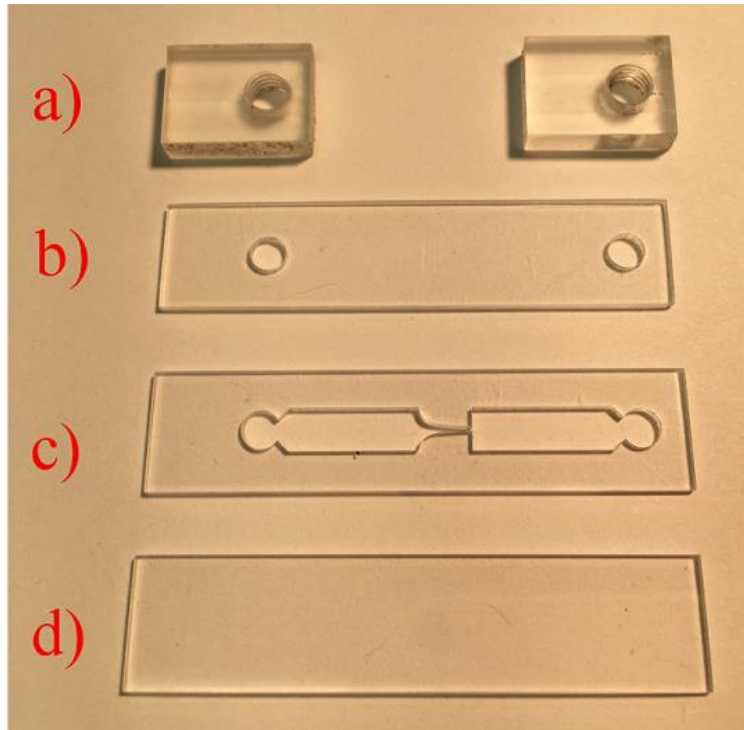
Fig. 3. 3 Parts of a typical microchannel, a) inlet and outlet blocks, b) top sheet with inlet and outlet holes, c) the middle sheet with microchannel geometry, and d) the bottom sheet to close the channel

3.2.1.1 Flow channel for pure extensional stress

A hyperbolic contraction was used in this study to apply a constant extensional strain rate to the red cells. As mentioned by James [218], a hyperbolic contraction is unique because it imposes a nominally constant extensional strain rate along its centerline [109, 110, 219].

A schematic of the channel used in this study is depicted in Fig. 3.4-a. The hyperbolic contraction starts with a width of 5 mm, which continues for 4 mm to reach a width of 0.35 mm at the end of the contraction, and finally is followed by an abrupt expansion with the same width as the beginning of the contraction. Also, depth of the channel (d) is the thickness of the PMMA sheet, i.e. 0.794±0.01 mm.
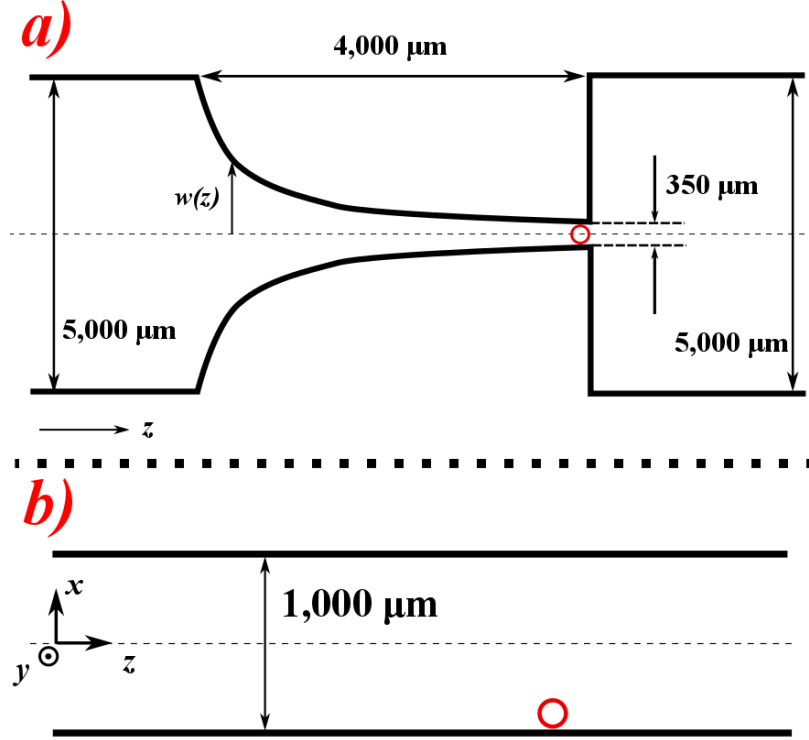
Fig. 3. 4 Schematic of a) the hyperbolic flow channel used in this study to exert extensional stress to the red cells and the b) rectangular channel for the pure shear flow experiments; red circle shows the field of view where the images were taken.

The width of the hyperbolic channel as a function z ($w(z)$) can be determined by the following equation

$$w(z) = \frac{L_c w_u w_d}{L_c w_d + z(w_u - w_d)} \tag{148}$$

where w_u and w_d are the upstream and downstream widths, respectively, and L_c is the length of the contracting region. The nominal extension rate ($\dot{\varepsilon}$) along the centerline of the hyperbolic channel can be calculated as

$$\dot{\varepsilon} = \frac{Q}{L_c d} \left(\frac{1}{w_d} - \frac{1}{w_u}\right) \tag{149}$$

where Q is the flow rate through the channel and d is the channel depth. For a fabricated example of the hyperbolic contraction channel with the fittings and inlet and outlet hoses, refer to Fig. 3.13.

Length of the upstream section of the channel (L_u) were designed to be long enough ($L_u > 30d$) for the flow to become fully developed and stable, before entering the contraction.

The field of view for taking images was the end of the contracting region, half-way deep inside the channel, to ensure that the pure extensional flow is acting on the cells.

3.2.1.2 Flow channel for pure shear flow

For shear flow, a simple flow channel with a rectangular cross section was fabricated, so that flow near the walls can be considered to be pure shear (Fig. 3.4-b). In this case, the depth of the channel is, again, the thickness of the PMMA sheet (0.794 mm) and the width of the channel is 1 mm.

The field of view for the pure shear case is the region near the bottom wall, and again half-way deep inside the channel (red circle in Fig. 3.4-b). Again, the length of the channel was chosen to be more than 60 times depth of the channel to ensure a fully developed and stable entrance flow.

The velocity profile for the rectangular channel is written as [220]

$$v_z(x,y) = \frac{48Q}{w_s d} \frac{\sum_{i=1,3,5,....}^{\infty} (-1)^{\frac{i-1}{2}} \cos(i\pi x/w_s)(1 - \frac{\cosh\left(\frac{i\pi y}{w_s}\right)}{\cosh\left(\frac{i\pi d}{2w_s}\right)})}{(1 - \frac{192w_s}{\pi^5 d} \sum_{i=1,3,5,...}^{\infty} \frac{\tanh(i\pi d/2w_s)}{i^5})} \tag{150}$$

where v_z is the streamwise velocity, Q is the total flow rate into the channel, w_s is the width if the channel (=1 mm in this case) and d is the depth of the channel (=0.8 mm in this case). For images acquired half-way deep inside the channel, $y=0$ in Eq. (147). Depending on the location of the red cell with respect to the wall (i.e. different x), Eq. (147) and its derivative can be used to calculate the velocity and shear rate at the corresponding point.

3.2.2 Bonding of the microchannel parts [6]

3.2.2.1 Introduction

One of the main challenges in PMMA microfabrication is sealing of the microdevice, i.e., bonding of different parts of the microdevice together in a way that eliminates leakage [222]. Bonding methods for microdevices are broadly categorized as direct and indirect [223]. Indirect bonding uses an additional intermediate layer, such as an adhesive, to bond PMMA to itself or to other types of plastics. In direct bonding, the bonded interface has the same chemical structure as the bulk of the PMMA and the resulting assembly is essentially one piece of PMMA. One advantage of direct bonding over indirect bonding is that, if done properly, optical clarity of the assembly is almost unaffected by bond interfaces, which is a beneficial factor for applications in which samples must be inspected/imaged by a microscope or other optical recording devices.

Examples of direct bonding includes thermal fusion, ultrasonic welding, and solvent bonding [224]. Solvent bonding, also known as solvent welding, is a poplar technique commonly used to join thermoplastic parts by allowing the polymer molecules at the bonding interface to be welded at room temperature (or sometimes in an oven) without leaving any permanent intermediate layer [225]. In this technique, a solvent is introduced on the bonding surfaces that locally dissolves the polymer, causing the molecules to crosslink across the interface. After the solvent evaporates, the result is a pure plastic-to-plastic bond that is nearly as strong as the base polymer. Solvent-based bonding offers several advantages, such as providing clean, durable near-permanent bonds, good sealing properties, homogenous distribution of mechanical loads, etc.

For solvent-based bonding to occur, the solvent molecules must overcome the van der Waals forces between the polymer molecules on each bonding surface, resulting in higher degrees of freedom for the polymer chains (Fig. 3.5). When the two solvent-softened surfaces are brought into contact, the polymer chains from the two surfaces entangle with each other. After the solvent starts evaporating, the entangled chains become more and

---

[6] Most of the material in this section is adopted from our published work in Faghih and Sharp [221]

more restricted, with the polymer motion ceasing when the solvent is completely evaporated.
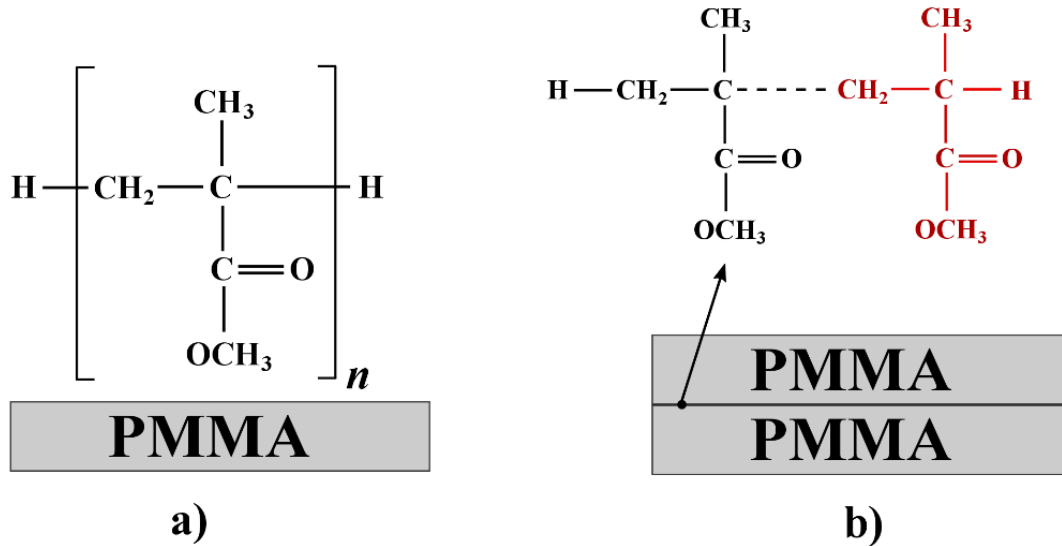
Fig. 3. 5 Chemical reaction during the solvent bonding of two PMMA samples, a) PMMA surface composition, b) cross-linked chains after the bonding

A simple indicator of material solubility is the Hildebrand solubility parameter [226], δ, which is based on the material's cohesive energy density, c, and is defined as:

$$\delta = \sqrt{c} = \sqrt{\frac{\Delta h_v - RT}{V_m}} \tag{151}$$

where Δh_v is the material's enthalpy of vaporization, R is the universal gas constant, T is the temperature, and V_m is the molar volume of the material. The unit used for Hildebrand solubility parameter is usually $J^{\frac{1}{2}} cm^{-\frac{3}{2}}$.

Based on the discussion above, two materials would be miscible if values of their solubility parameter are similar. Solubility parameters of some thermoplastic polymers and solvents are listed in Table 3.1, in increasing order [226].

Table 3. 1 Numerical values of the Hildebrand solubility parameter for selected thermoplastic polymers and solvents

Thermoplastic polymer	Abbreviation	$\delta \left[J^{\frac{1}{2}} \, cm^{-\frac{3}{2}} \right]$
Polytetrafluoroethylene	PTFE	12.6
Polypropylene	PP	16.3
Polyvinyl chloride	PVC	19.4
Polycarbonate	PC	19.4
Poly(methyl methacrylate)	PMMA	20.1
Polyethylene terephthalate	PET	21.8
Solvent	**Abbreviation**	$\delta \left[J^{\frac{1}{2}} \, cm^{-\frac{3}{2}} \right]$
Dichloromethane	DCM	19.8
Acetone	ACE	20.4
Isopropanol	IPA	23.4
Ethanol	ETOH	26.0
Methanol	MEOH	29.7
Water	H2O	47.7

The solubility parameter of the solvent selected for bonding microfluidic parts is usually selected such that it is not exactly the same as that of the polymer in order to avoid excessive solvent absorption, which can cause deformation in the polymer parts. On the other hand, a solvent with solubility parameter too different from that of the polymer may not cause enough freedom of the polymer molecules to entangle into each other, which could lead to a weak or failed bond. Sometimes, to provide better control of the exposure of the solvent to the polymer, solvent in vapor phase is used to soften the polymer molecules on the two bonding surfaces [227].

For applications in which strong bonding is required, thermoplastic parts can be forced together by pressure in an environment with elevated temperature. Clamping pressure and high temperature during the curing process has been shown to enhance polymer entanglement at the bonding surface [228-230]. However, excessive pressure and heating can cause deformation of the assembly and even melting of the polymer.

The effective solubility of solvents is adjustable by mixing different solvents. The Hildebrand solubility parameter of the mixture is estimated by a volume-weighted average of the solubilities of the individual solvents. For instance, a mixture of two parts dichloromethane and one part methanol has a Hildebrand solubility value of $23.1\ J^{\frac{1}{2}}\ cm^{-\frac{3}{2}}$ $(19.8 \times \frac{2}{3} + 29.7 \times \frac{1}{3})$ [231].

Many studies have used different solvent combinations and curing times, temperatures and pressures to bond PMMA microfluidic parts (Table 3.2).

Table 3. 2 Details of different solvent-bonding processes used for fabrication of PMMA microdevices

Author	Solvent	Curing temperature, °C	Curing time, min	Applied pressure, kPa	Bonding strength, MPa
Hsu and Chen [232]	Isopropanol	60	5	25	0.68
Lin, et al. [233]	20% 1,2-dichloroethane and 80% ethanol	Room temperature	5	100	3.80
Umbrecht, et al. [234]	Ethylene glycol dimethacrylate	85	5	Hydraulic press	3.5
Mona, et al. [229]	Ethanol	60	1.5	Small binder clips	3.00
Tran, et al. [235]	90% Ethanol	77	0.5	General clamps	6.2
Ng, et al. [236]	Isopropanol	80	30	267	0.8

Another important consideration when using high temperature to assist the solvent-bonding method is the glass transition of the thermoplastics. The glass transition temperature, T_g, is a temperature above which the thermoplastic becomes pliable. Therefore, setting the curing temperature too close to the glass transition temperature may cause deformation in the microdevice.

In this study, effects of four solvent combinations, two solvent states (liquid and vapor), three curing temperatures and two curing times on PMMA bonding were investigated. The results were compared in terms of bonding strength, leakage and optical clarity. The best solvent combination, solvent phase and curing temperature and time were identified.

3.2.2.2 Methods

Materials

      The PMMA samples used in this study were clear sheets with a thickness of 3.175 mm (0.125 inch) (McMaster-Carr Company, Elmhurst, USA). The samples were laser-cut to rectangular shape of 25mm×50mm (Fig. 3.6). The area of the bonding region was 25mm×25mm. The glass transition temperature of the PMMA sheets used in this study was 85 °C, according to manufacturer's manual.
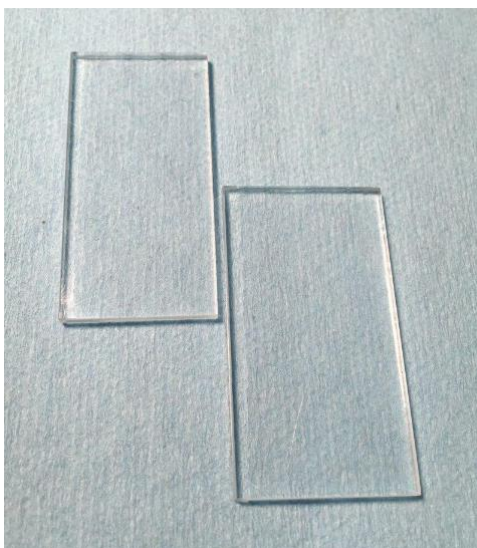
Fig. 3. 6 PMMA samples used in this study

      The solvents used in this study included isopropanol, ethanol, acetone and dichloromethane (Hydrox Laboratories Company, Elgin, IL, USA).

Solvent mixture preparation

      In this study, dichloromethane and acetone, with solubility parameters close to that of PMMA, were used as the main components of the solvent mixture (Table 3.3). Isopropanol and ethanol were added as secondary solvents to make the weighted solubility parameter of the mixture different from that of PMMA, in order to prevent excessive melting/deformation of the samples.

      In addition to the liquid solvent mixture in Table 3.3, vapors of pure dichloromethane and acetone were also tested to bond the PMMA samples.

Table 3. 3 Solvent mixtures used in this study for solvent-bonding of PMMA samples

Name of mixture	Primary solvent	% volume of primary solvent	Secondary solvent	% volume of secondary solvent	Mixture solubility value, $\left[J^{\frac{1}{2}} cm^{-\frac{3}{2}}\right]$
DCM+IPA	Dichloromethane	20	Isopropanol	80	22.68
DCM+ETOH	Dichloromethane	20	Ethanol	80	24.76
ACE+IPA	Acetone	20	Isopropanol	80	22.80
ACE+ETOH	Acetone	20	Ethanol	80	24.88

PMMA sample preparation

Laser-cutting (Boss LS-1630, Sanford, FL, USA) was used to manufacture the PMMA samples. To remove contaminations and debris from the sample surfaces, the samples were ultrasonically cleaned (Branson 8510 Ultrasonic Cleaner, Branson Ultrasonics, Danbury, CT, USA) using an aqueous 10% isopropanol solution for 5 minutes. The samples were then washed with deionized (DI) water. Finally, nitrogen gas was used to dry the samples.

Annealing the PMMA samples

Laser-cutting is one of the conventional methods to cut the PMMA parts, however, it produced stress concentrations on the edges of the samples that ultimately caused the samples to crack during solvent application or when applying the curing loads.

Therefore, the PMMA parts were annealed before bonding to release the internal stresses. In this study, a convection oven (Yamato DX 300, Japan) was used to anneal the PMMA samples. First, the samples were placed in an oven with temperature fixed at 70 °C for 3 hours. Then, the oven was turned off and allowed to gradually reach room temperature. Fig. 3.7 shows the significant effect of annealing on the PMMA bonding performance.
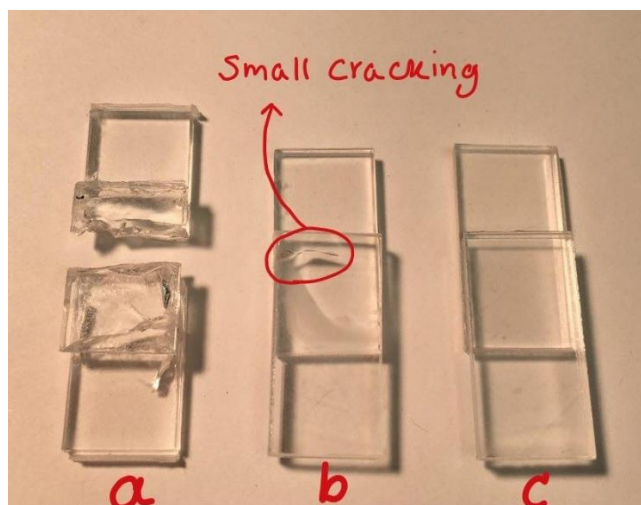
Fig. 3. 7 Effect of annealing on bonding performance of PMMA parts: a) samples bonded without annealing; b) samples annealed for one hour and then bonded; c) samples annealed for three hours and then bonded

Corona surface treatment

Corona treatment, also known as air plasma, is a surface modification method that uses a low temperature corona discharge plasma to activate surface energy. In order to investigate the effect of this surface treatment on bonding characteristics, some of the samples were treated with a corona device (Model BD-20, Electro-Technic Products Inc., Chicago, IL, USA) just before applying the solvent (Fig. 3.8).

Fig. 3. 8 Corona treatment on the PMMA samples just before adding the solvent to the samples

Vapor solvent bonding

A glass beaker that had a stopper with a horizontal nozzle was used to carry out the bonding for the case of vapor solvent. A hot plate (Thermolyne Cimarec 2, Thermo Fisher Scientific Company, Waltham, MA, USA) was used to boil the solvent inside the beaker.

Bonding procedure

0.2 ml of the solvent mixture was prepared for each side of the bonding surface. Then, the solvent mixture was evenly distributed to the bonding surfaces on each of the PMMA surfaces using a precision needle-tip applicator. The solvent mixture was allowed to sit for 10 seconds before bringing the two parts in contact with each other. After bringing the samples in contact, the bonding area was visually inspected for any trapped bubbles. In case of trapped bubbles, the samples were moved gently back and forth, while still pressed onto each other, until the bubbles were forced out of the bonding area. Finally, the samples were pressed together using clamps. To promote uniform clamping pressure across the bonding surfaces, two aluminum cauls with thickness of 20 mm were placed on both sides of the assembly (Fig. 3.9). The samples were placed inside a pre-heated oven set to the curing temperature. Three different curing temperatures, namely 50 °C, 60 °C and 70 °C and two different curing times, 2 and 5 minutes, were tested. Four identical samples were prepared for each bonding condition.

Applied pressure: 50kPa
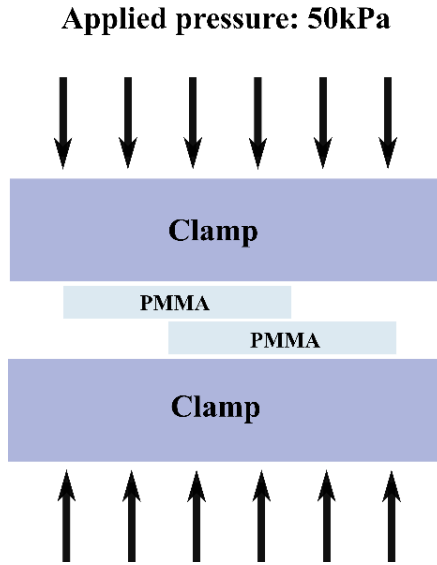
Fig. 3. 9 Application of load to the PMMA samples

The procedure was the same for the case of vapor bonding, except that instead of applying the liquid solvent to the PMMA parts, the samples were exposed to the solvent vapor for 5 seconds before being pressed together. Additionally, the samples bonded with the vaporized solvent were not placed in the oven, but rather were allowed to sit at room temperature for 15 min while polymer cross-linking occurred.

Optical clarity

Optical clarity of the bonding area on PMMA samples was measured before and after the bonding procedure using a visible light source and an optical power meter (840c, Newport Company, Irvine, CA, USA). Power transmittance ratio was used to quantify the optical clarity of the samples according to the following relation:

$$\emptyset = \frac{\emptyset_f}{\emptyset_i} \times 100 \tag{152}$$

where $\emptyset$ is the relative percent transmittance of the bonded area, $\emptyset_i$ is the power transmittance of the two PMMA samples simply lying on each other, and $\emptyset_f$ is the power transmittance of the bonded area after the full bonding procedure.

Tensile test

A standard lap-shear test, with the cross-head speed of 1 mm/min (MTI 2K tensile testing machine, Measurements Technology Incorporation, Roswell, GA, USA), was used to determine the bonding strength (Fig. 3.10).
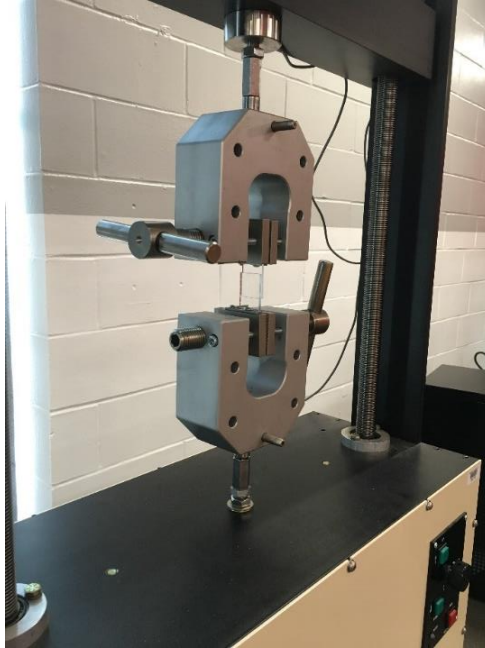
Fig. 3. 10 Lap-shear test used to determine the bonding strength

Leak and burst test

After the best bonding solvent combination and curing condition were determined, an example microchannel was fabricated to test whether the bonded parts would leak under high-pressure flow. A microchannel with a hyperbolic contraction (Fig. 3.12) was machined on a rectangular PMMA sheet (thickness 500 µm) using a bench-top micro-milling machine (Othermill, Other Machine Company, Berkeley, USA, CA, Fig. 3.11). Then, two other PMMA sheets (thickness 500 µm) were used to close the microchannel, with the top sheet having two holes for the inlet and outlet.

Fig. 3. 11 Machining the microchannel on a PMMA sheet
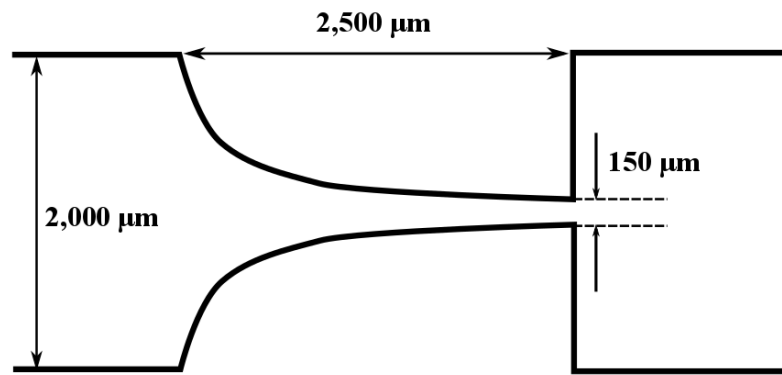
Fig. 3. 12 Schematic and dimensions of the hyperbolic microchannel

Also, two PMMA blocks with threaded holes were bonded to the inlet and outlet to accommodate tubing connections (Fig. 3.13). Two brass hose barb connectors were used to connect 0.16 mm internal diameter Tygon tubing into and out of the microchannel (Fig. 3.13).

The microchannel inlet was then connected to a fabricated syringe pump that pushed the water into the microchannel. The syringe pump provided a flow rate of 6.5 ml/s.

146

After 12 s of flow, the bonded surfaces were inspected for any signs of leakage. Food dye was added to the sample water to better inspect any possible leakage. Only the strongest solvent mixture and curing conditions, DCM+IPA, 70 ℃ and 5 min, were tested.
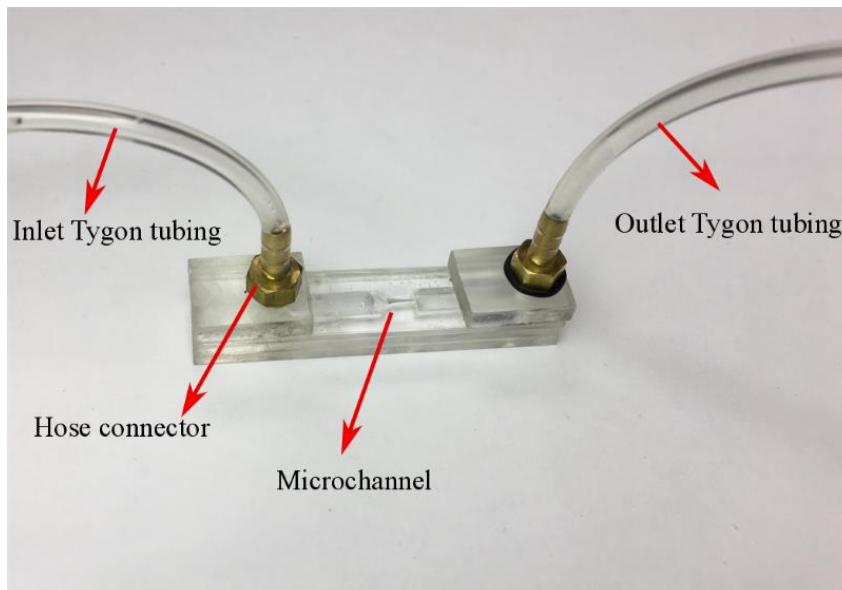
Fig. 3. 13 The assembled microchannel with its inlet connected to the syringe pump and its outlet to a collecting container (exposed to the atmosphere)

Finally, a simple burst test was used to determine the pressure at which the microchannel fails. For this test, the microchannel inlet was connected to a pressurized tank with a pressure regulator to adjust the air pressure entering the channel while the microchannel outlet was completely plugged. Then, the microchannel was placed inside a thick transparent cover to provide safety for the users (Fig. 3.14). Soap bubble was used to visually detect any air leakage from the inlet/outlet as well as other bonded areas of the microchannel while pressure entering the channel. The air pressure was gradually increased using the pressure regulator until the microchannel failed.
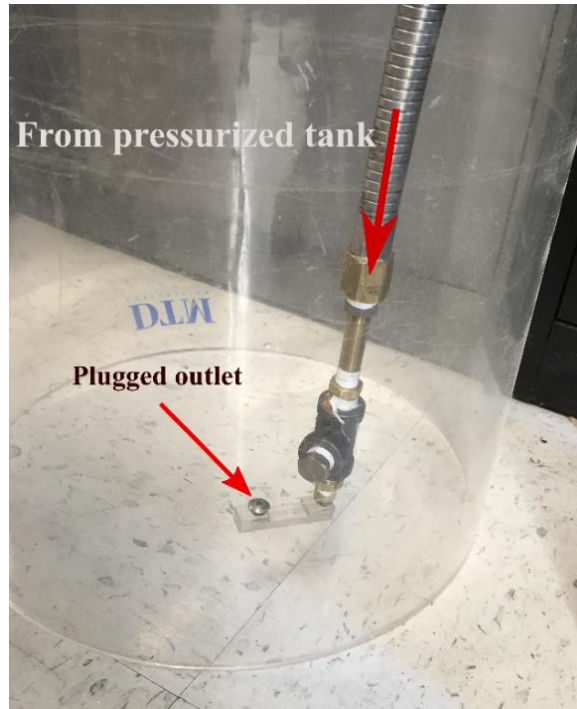
Fig. 3. 14 The microchannel placed inside a transparent cover for the burst test

Bonding coverage and channel quality

Bonding coverage is one of the important consideration when dealing with solvent-based bonding. Furthermore, a successful bonding procedure must cause the least amount of deformation on the channels and other important structures on the surfaces involved in bonding process. To check for these two features, a narrow square channel, with cross sectional area of 100 µm×100 µm and length of 5 cm, was machined on a PMMA sheet of thickness 500 µm. Then, another PMMA sheet (thickness 500 µm) was used to close the channel by using the solvent-based bonding method (DCM+IPA, 70 °C and 5 min). Afterwards, edges as well as the cross-section of the channel were inspected by an optical microscope to ensure that the solvent did not cause any significant deformation on the channel. The surfaces involved in the bonding were also examined both visually and by the microscope for bonding coverage.

Statistical analysis and uncertainty

Statistical analysis was carried out on all the results, for both optical clarity as well as bonding strength sections, using a general linear model in Minitab v18 Minitab INC., State College, PA, USA) with two-sided 95% confidence interval. Three factors (solvent,

temperature and curing time) and interactions among the factors were included in the model.

The accuracy of the optical power meter was ±2%. The accuracy of the load cell for the tensile tests was ±0.5%. The accuracy of linear measurements to determine cross sectional area of the bonding area was ±0.002%. The accuracy of the pressure gauge for the burst tests was ±0.1%. Total uncertainty included type A (repeated measures) and type B (instrument accuracy) uncertainties.

3.2.2.3 Results

Results for bonding strength and optical clarity of the samples are provided in this section. All differences among groups for both bonding strength and optical clarity were statistically significant ($p - value < 0.05$). Because all were significant, the p-values are not shown in the figures.

The maximum uncertainty for bonding strength and optical clarity were ±0.73% and ±2.12%, which occurred for ACE+IPA (50 °C and 2 min) and ACE+ETOH, respectively. Because the uncertainty for bonding strength is small compared to the differences observed, error bars are not shown to improve readability of the graphs.

Bonding strength

Mean strengths measured in the lap-shear tests increased with increasing temperature and curing time for all samples bonded with the liquid solvent (Fig. 3.15).
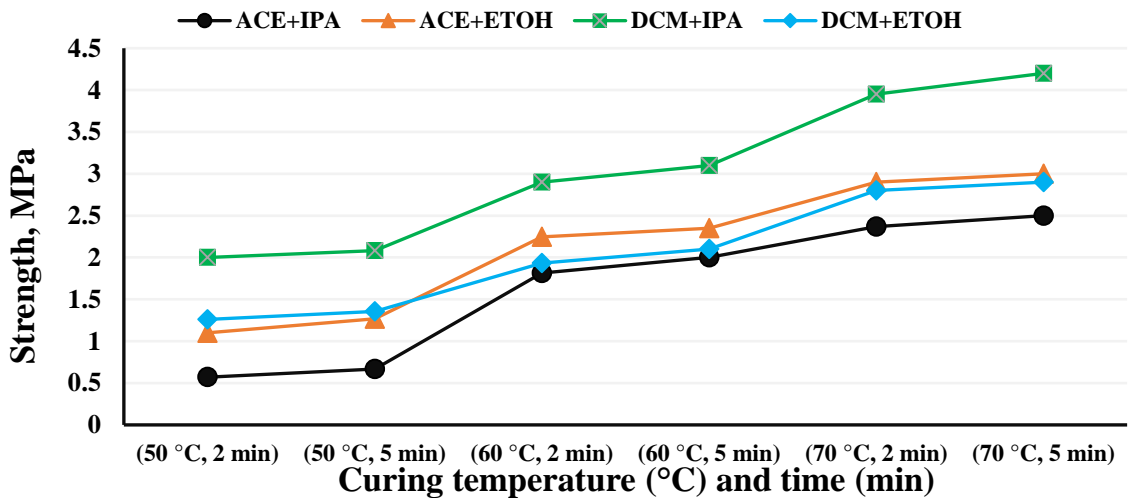
Fig. 3. 15 Bonding strength of the samples bonded with liquid solvent (ACE: acetone; IPA: isopropanol; ETOH: ethanol; DCM: dichloromethane) (refer to Table 3.3 for more)

Bonding strengths of the samples made with vaporized ACE and DCM (denoted by ACE_VAP and DCM_VAP, respectively) were higher than that of DCM+ETOH, but lower than that of DCM+IPA (liquid solvent) (refer to Table 3.3 for details about these abbreviations) at room temperature and curing time of 15 min (Fig. 3.16). DCM+ETOH and DCM+IPA were used for comparison because these combinations showed better bonding strength at lower temperatures (Fig. 3.15). The same clamping pressure, 50 kPa, was used for all the samples.
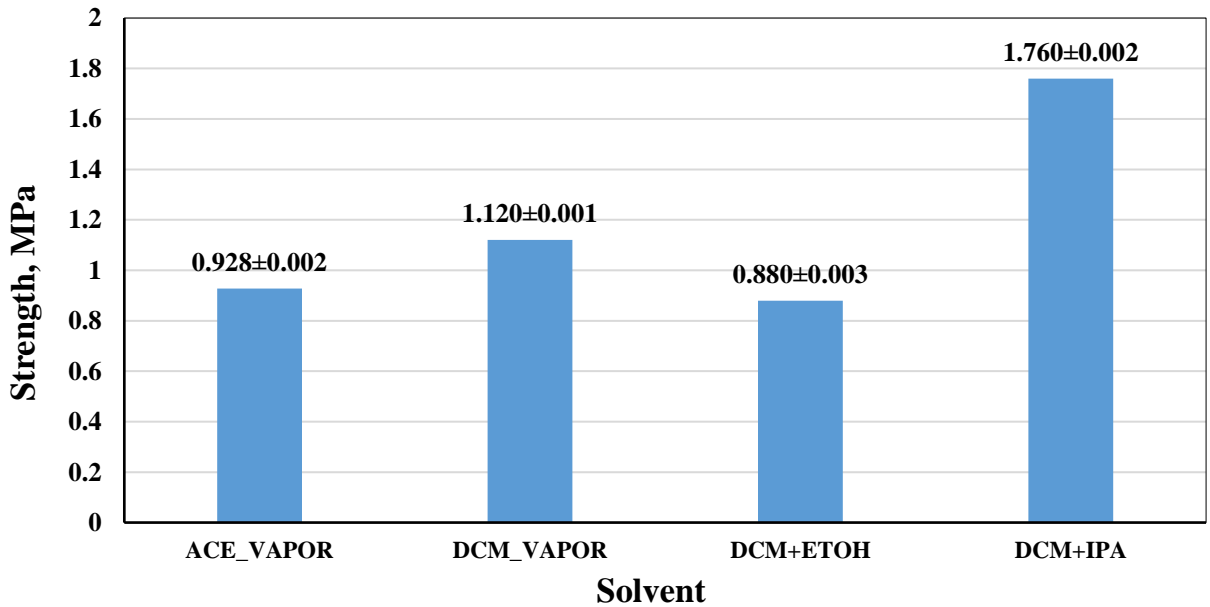
Fig. 3. 16 Comparison of bonding strength of samples made with liquid vs vapor solvents at room temperature and for curing time of 15 min

Effect of corona treatment on bonding strength

Corona surface treatment improved bonding strength for samples bonded with DCM+ETOH and DCM+IPA at room temperature (Fig. 3.17).
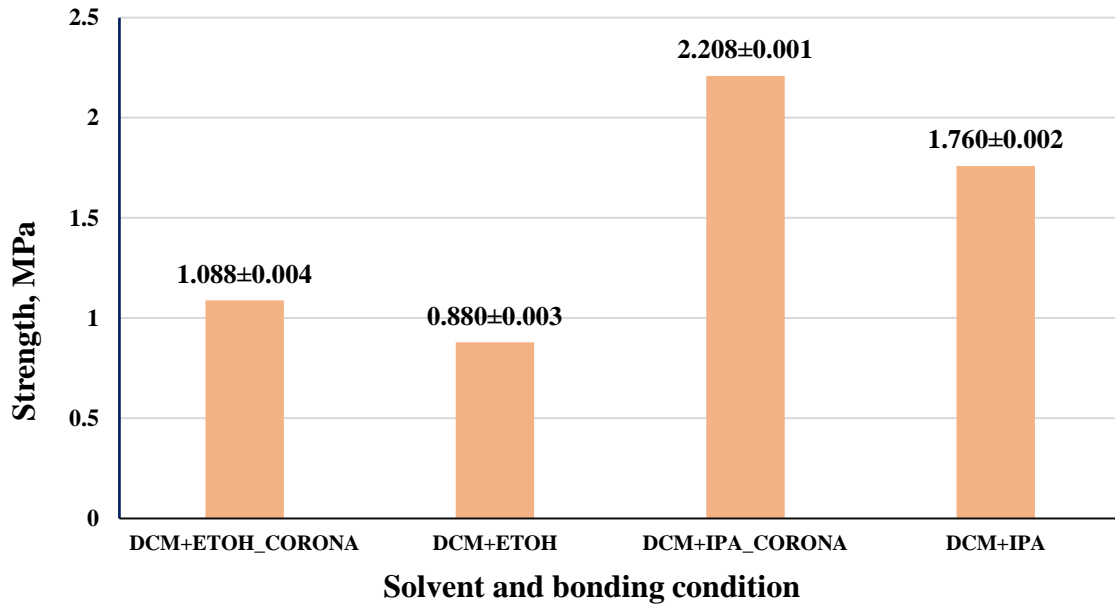
Fig. 3. 17 Effect of using Corona surface treatment on bonding strength at room temperature and for curing time of 15 min

To compare the effectiveness of the surface treatment to that of oven temperature and curing time, the same solvent mixture, DCM+IPA, was used to bond PMMA samples under four different conditions: first, untreated sample at room temperature and curing duration of 15 min; second, sample treated by corona surface modification bonded at room temperature and curing duration of 15 min; third, untreated sample at curing temperature of 50 °C for duration of 2 min; and fourth, untreated sample at curing temperature of 50 °C for duration of 5 min (Fig. 3.18). Corona treatment at room temperature was also more effective in increasing strength than was elevated temperature.
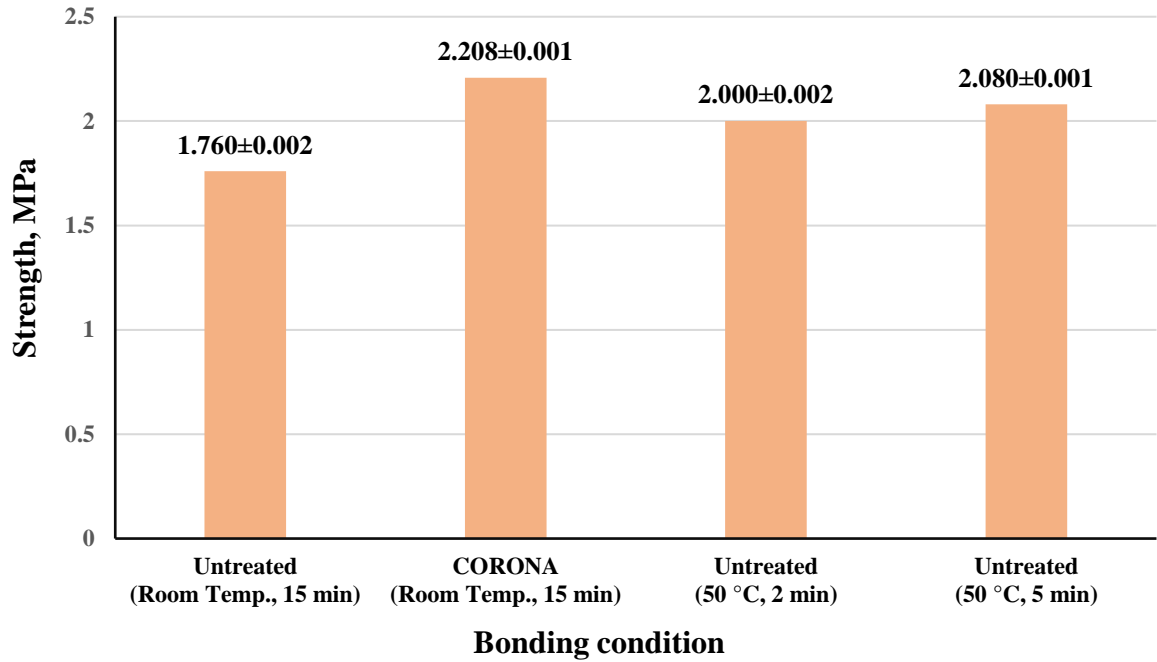
Fig. 3. 18 Effect of using Corona surface treatment vs. curing temperature and time on bonding strength of DCM+IPA

Optical clarity

Power transmittance ratios for samples for both liquid and vapor cases are shown in Fig. 3.19.
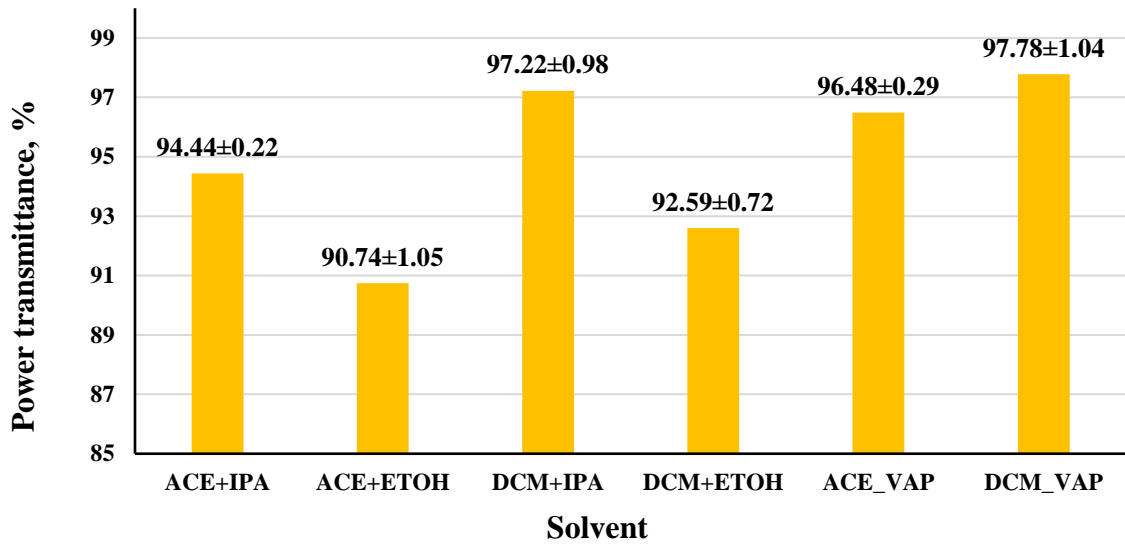
Fig. 3. 19 Power transmittance ratio for the samples bonded with liquid and vapor solvents

Effect of corona treatment on optical clarity

Power transmittance ratio was improved by corona surface treatment (Fig. 3.20). In this case, only DCM+ETOH and DCM+IPA solvents were compared.
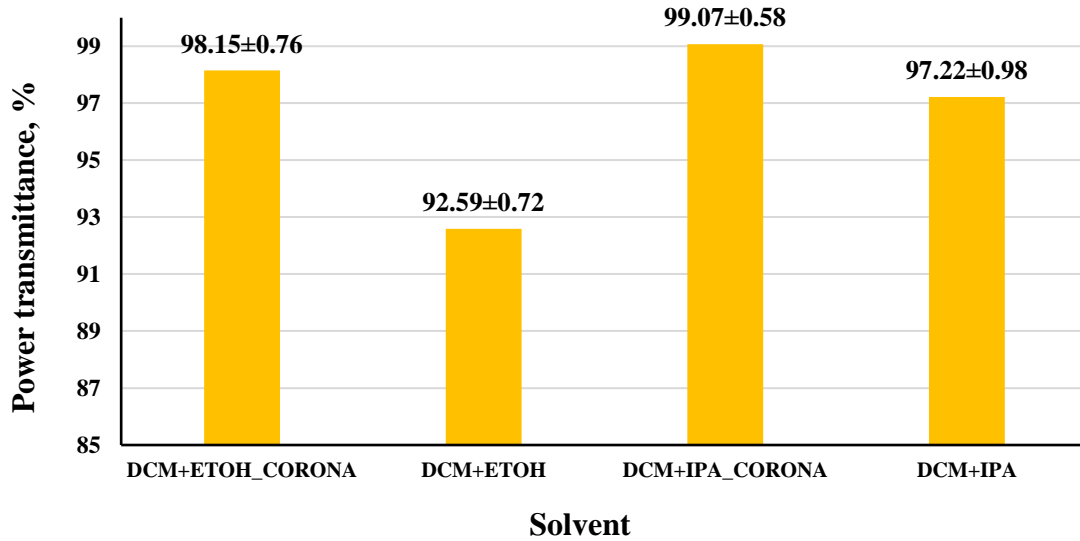
Fig. 3. 20 Power transmittance ratio for the samples with and without surface treatment

Leak and burst tests

For the best solvent mixture and curing conditions, DCM+IPA, 70 °C and 5 min, no leakage was evident between any bonded surfaces.

For the burst test, air pressure was successfully increased up to 370 psi, without any sign of air leakage from any part of the microchannel assembly, at which point the inlet PMMA block cracked.

Bonding coverage and channel quality

After the bonding was carried out, the channel was examined from the side view under an optical microscope to check for any sign of deformation. As shown in Fig. 3.21, the bonding process did not cause any significant deformation on the channel.
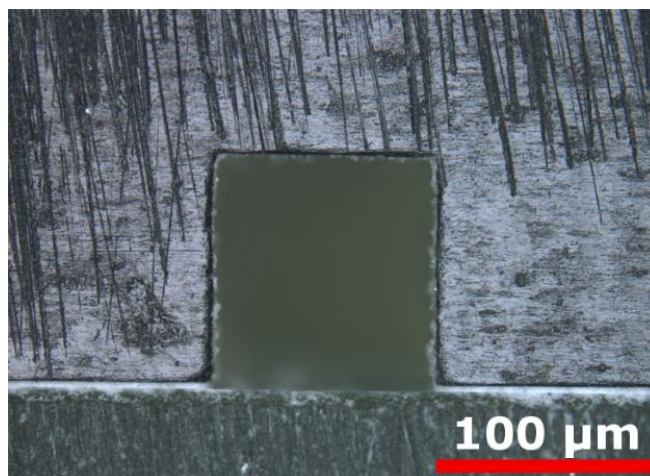
Fig. 3. 21 Side view of the square channel machined on a PMMA sheet and closed by another PMMA sheet using solvent-based bonding

Additionally, edges of the channels where the bonding were formed were carefully examined to ensure that the full bonding coverage is accomplished (Fig. 3.22).
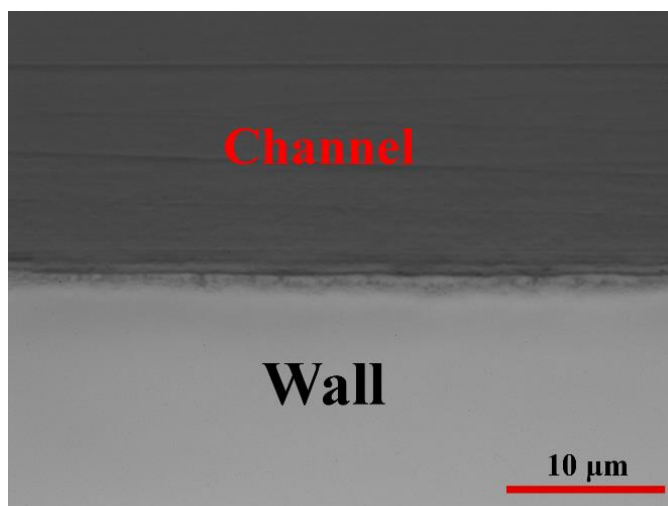
Fig. 3. 22 Top view of the square channel machined on a PMMA sheet and closed by another PMMA sheet using solvent-based bonding (40x magnification)

3.2.2.4 Discussion

It is apparent from the slopes of the different segments of curves in Fig. 3.15, that the effect of curing temperature is greater than that of curing time. According to Fig. 3.15, the strongest bond can be obtained by using DCM+IPA as the solvent mixture, and 70 °C and 5 min as the curing temperature and time, respectively.

Another finding evident from Fig. 3.15 is that the primary solvent tends to define the overall trend of variation of bonding strength with temperature and time. For instance, for solvent mixtures with primary solvent DCM, the behavior of the bonding strength with respect to time and temperature is similar, i.e., they have similar slope at the same segment of the curve. This is also valid for cases with primary solvent ACE.

As Fig. 3.16 demonstrates, both DCM and ACE vapors show stronger bond strength than that of liquid DCM+ETOH, but weaker than liquid DCM+IPA. Therefore, liquid DCM+IPA is the most promising solvent mixture for PMMA.

Corona discharge increased bond strength by 23.5% for the case of DCM+ETOH, while for DCM+IPA, improvement was 25.5% (Fig. 3.17).

For the DCM+IPA mixture, applying only the corona treatment improves the bonding strength more than does increasing curing temperature and time (Fig. 3.18).

DCM vapor had the least effect on optical clarity, followed by the liquid DCM+IPA mixture (Fig. 3.19). Corona treatment improved bond clarity with both DCM+ETOH and DCM+IPA (Fig. 3.20).

3.2.2.5 Conclusion

PMMA is one of the most common polymers used for fabricating microdevices mainly due to low cost and high availability. Bond quality, including bond strength and optical clarity, of the fabricated devices is of great importance. In this study, solvent-based bonding with different solvent mixtures, curing times and temperatures was used to determine the best solvent mixture.

A mixture of 20% dichloromethane and 80% isopropanol and curing time and temperature of 70 °C and 5 min, respectively, showed the highest bonding strength, 4.2 MPa, which was also used to bond the flow channels for the actual experimental tests. Dichloromethane vapor provided the best optical clarity on the bonded surfaces, but with greatly reduced strength. Additionally, it was shown that using corona surface treatment just before application of solvent improved both the bonding strength and the optical clarity.

3.2.3 Syringe pump

An in-house syringe pump was built in order to provide the required flow-rate into the flow channel to reach a stress level exceeding the values previously covered in the literature (Fig. 3.23).
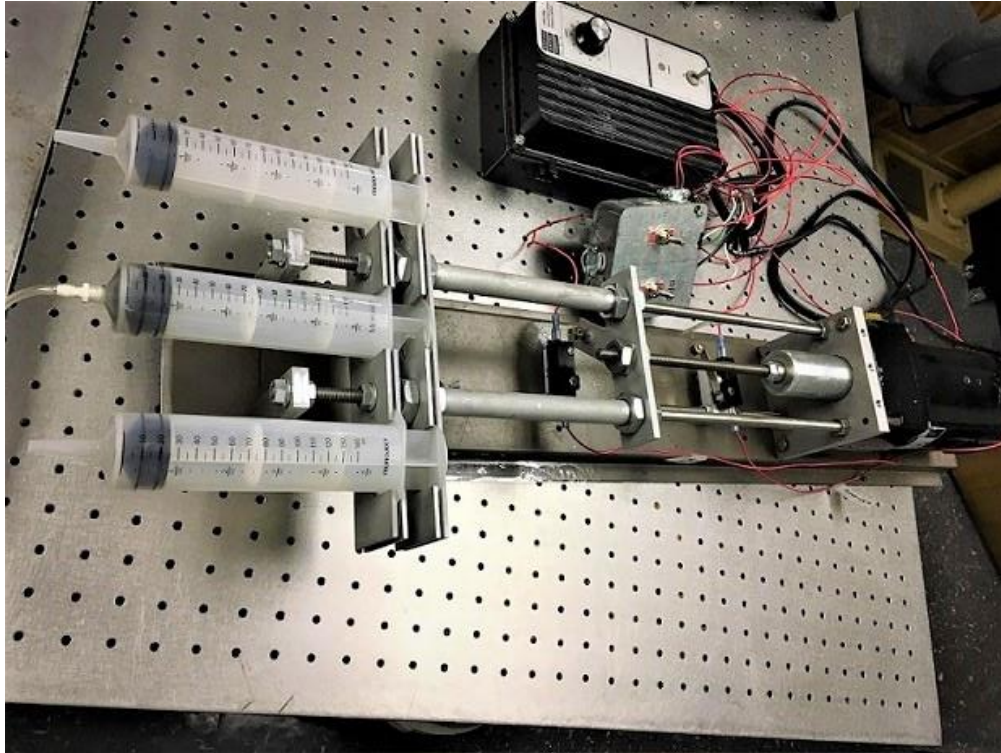
Fig. 3. 23 The in-house syringe pump used to provide the flow rate into the channel

The syringe pump utilizes a Bodine electric motor (Bodine Electric Company, Northfield, IL), with the characteristics listed in Table 3.4. The motor has a variable RPM setting, allowing us to push the working fluid into the flow channels with different flow rates. The syringe holder is capable of accommodating three 140 ml syringes.

Table 3. 4 Technical details of the motor driving the syringe pump

Volt (v) - DC	130	
Amp (A)	1.8	
HP	0.25	= 186.5 watt
Torque (lb.in)	25	
Max RPM	500	

A leadscrew of dimeter 3/8 inch with ACME threading and 16 Thread-per-Inch (TPI) was used to convert the rotating motion of the motor to a linear motion. Furthermore,

two general purpose limit switches (Fig. 3.24) and a corresponding wiring was incorporated into the syringe pump motor to stop the motion of the motor at end of its course, avoiding a collision and damage to the experimental set-up.

Fig. 3. 24 Limit switch used to stop the motion of the pump motor at the end of the course.

3.2.4 High-pressure syringe

Because of the high-pressure nature of our experiments, the common plastic syringe failed to withstand the working pressure. Therefore, a typical 140 ml Monoject plastic syringe was re-enforced for this purpose. First, the original plunger was discarded and a Delrin rod was used instead (Fig. 3.25 a). Delrin is a very strong thermoplastic which is also very easy to machine. A double O-ring system was also devised on the Delrin plunger to avoid leakage of the working fluid (Fig. 3.25 b).

Then, a PVC pipe was machined to be used as a cover on the syringe piston, without changing the cross-sectional area of the syringe piston (Fig. 3.25 c).
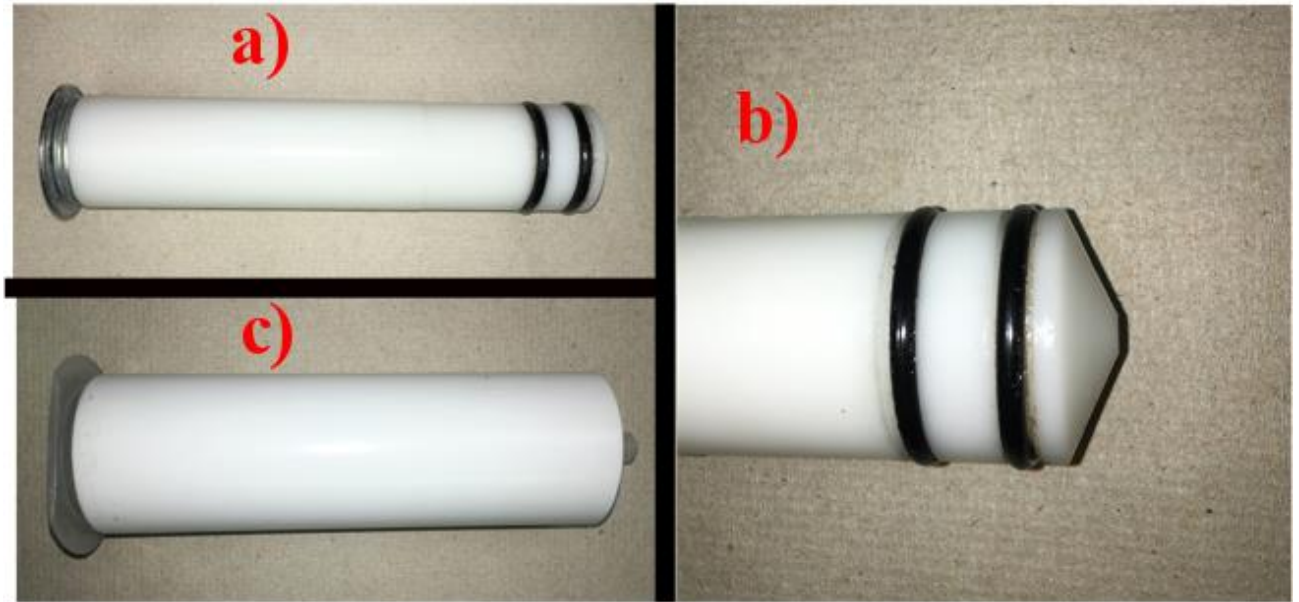
Fig. 3. 25 The syringe system designed and built to withstand the high-pressure application

3.2.5 Fittings and hose

All the fittings and the hose were purchased from the Grainger Company (Lake Forest, Il, US). A combination of a female Luer to Female Luer adaptor and a male Luer to 1/8 NPT male fitting was used to connect the syringe tip to a compression x FNPT female connector (1/4 inch tube size), to which the Nylon tubing (ID=11/64 in and OD=1/4 inch) was connected. Also, a compression x FNPT male connector (1/4 inch tube size) was used for the inlet and outlet of the flow channel.

3.2.6 Optical microscope

For the optical microscopy of the moving red cells through the flow channel, a Zeiss Imager D1 (Thornwood, NY, US) upright microscope was used.

3.2.6.1 Illumination type

Köhler illumination was used to illuminate the sample under the microscope. Köhler illumination is a type of specimen illumination used for both transmitted and reflected optical microscopy, which acts to generate an extremely even illumination of the sample and is the most common technique for sample illumination in modern scientific light microscopy.

3.2.6.2 Microscope objective

For our experimental tests, we needed to observe the sample deep through the flow channel (around 0.4 mm, which is half of the depth of the flow channel). Additionally, we had to compensate for the relatively thick cover slip (i.e. the top sheet of the flow channel, 0.8 mm). Therefore, a Nikon extra-long working distance microscope objective, CFI S Plan Fluor ELWD 40x, with a mechanical correction collar was used (Table 3.5).

Table 3. 5 Important details about the objective used for the experiments

Magnification	40X
Immersion	Air
Numerical aperture	0.6
Cover glass thickness	0-2 mm
Working distance	2.8-3.6 mm

We had to machine an adaptor, in order to use the Nikon objective on the Zeiss microscope.

3.2.7 Digital camera

A monochrome digital camera, QICAM Fast 1394 (QImaging Company, Canada), was used to record the images of the red cells passing through the flow channel. Important features of the camera are listed in Table 3.6.

Table 3. 6 Technical features of the digital camera used in this study

Resolution	1.4 million (1392 x 1040)
Frame rate at full resolution	10
Exposure tim	12μs to 17.9 min
Bit depth	12-bit digitization
Connectivity to PC	IEEE 1394 FireWire™
External triggering	Yes, TTL signal

Also, quantum efficiency of the camera is shown in Fig. 3.26. The best quantum efficiency for this camera is achieved at wavelengths 400-600 nm.
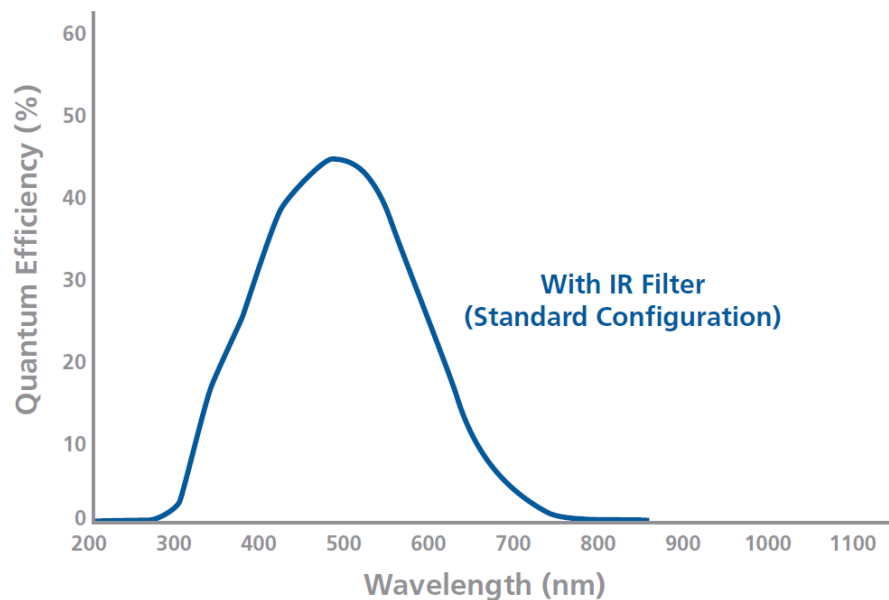
Fig. 3. 26 Quantum efficiency of the digital camera for different wavelength (Adopted from the device documentation)

3.2.7.1 Graphical user interface

The QCapture Pro image acquisition software was provided by the camera company, which enables the user the take full control over different features of the camera, including exposure time, binning, region of interest, external triggering, etc.

3.2.8 Pulsed light source

In order to freeze the fast motion of the red cell though the flow channel, a pulsed light source generator, Nanolite Driver 2000 (High-Speed Photo-Systeme, Germany), was used that can be triggered by an external TTL signal.

A Nanolite Nanosecond flash lamp, model KL-M (High-Speed Photo-Systeme, Germany), was connected to the pulsed light source generator unit, using a BNC cable. The duration of the spark for this type of flash lamp is 11 ns, while the discharged energy is 14 mJ, with the maximum flushing rate of 20 kHz.

Intensity of the spark from the flash lamp for different wavelength is shown in Fig. 3.27.

160
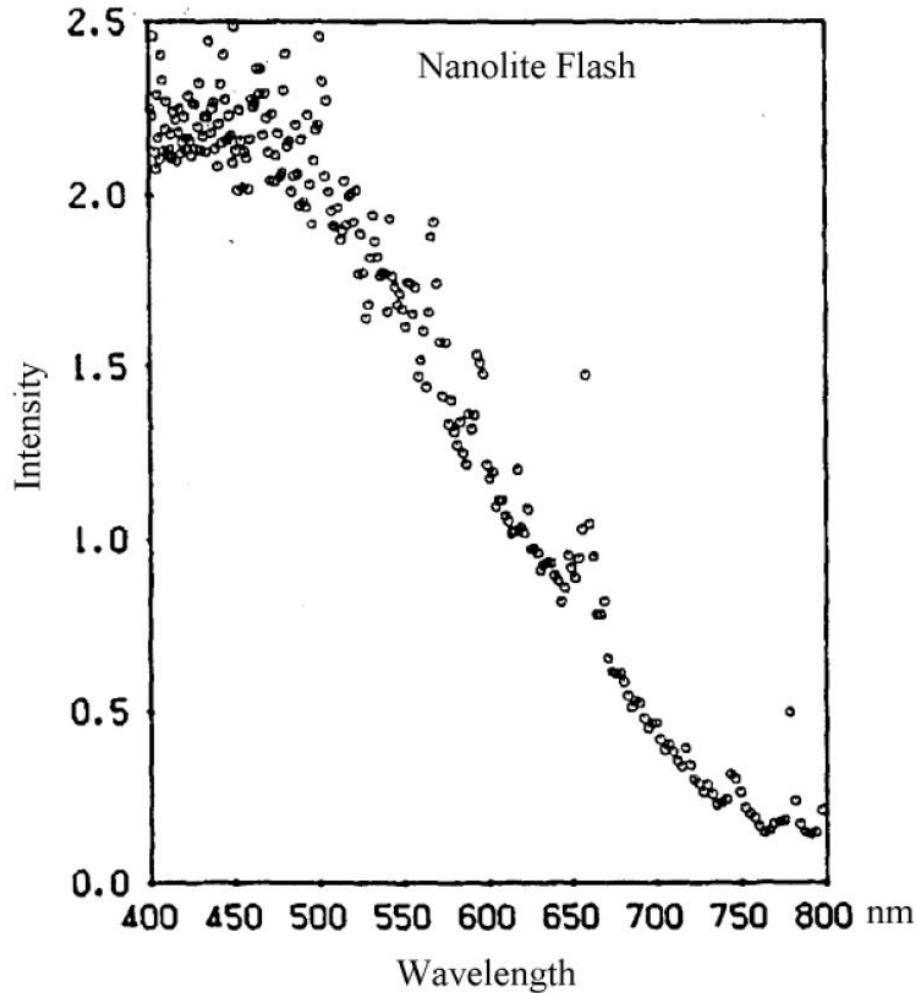
Fig. 3. 27 Intensity of the light from the flash lamp for different values of wavelength (adopted from the device documentation)

The maximum intensity is delivered at wavelength of 400-500 nm.

3.2.8.1 Laser

Laser can provide a brighter light with shorter duration, both of which help to capture better images. The reason why laser was not used in this study is that when using laser for this type of imaging, a destructive phenomenon occurs, which is called lase speckle. Laser speckle occurs because laser light is temporally coherent.

There are methods to reduce laser speckle, like passing the laser light through a multimode optical fiber to make it incoherent [237], but that would add more complexity and higher cost to the project (Fig. 3.28).
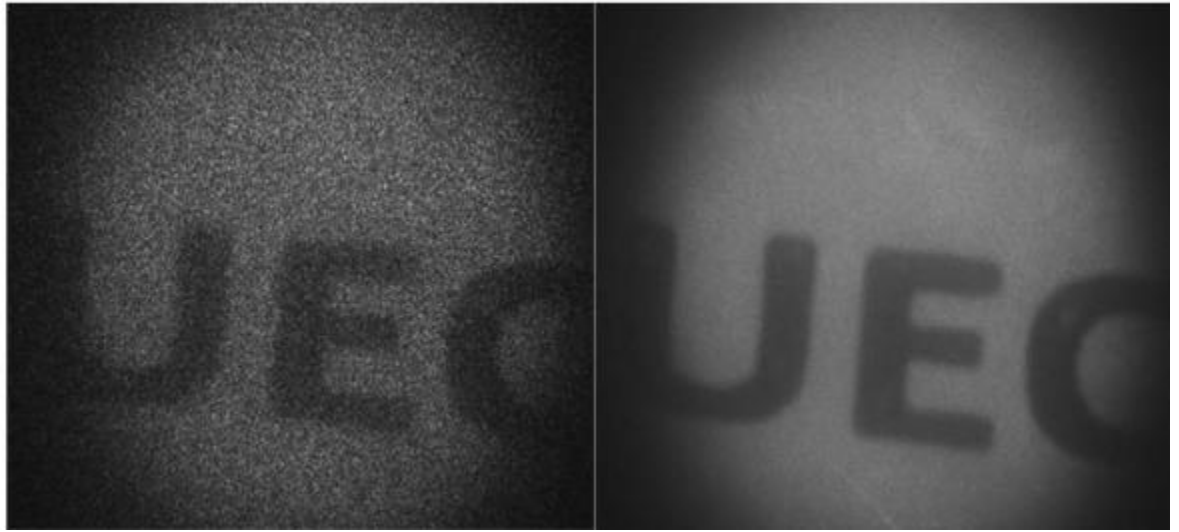
Fig. 3. 28 Image without laser speckle reduction (left) and imag with the speckle reduction (right) (adopted from [237])

3.2.9 Synchronization

When imaging a fast-moving object, it is very important to make sure that the pulsed light source hits the camera when the shutter is open. Therefore, it is important to know the response time of all the respective devices. In our case, the two devices whose response time should be taken into consideration for the synchronization purpose are the camera and the light source. Although the response time of both camera and the light source were reported in their documentation, the response time for the two devices were also manually measured using an oscilloscope. The response time of the camera shutter (the time it takes for the camera to open its shutter from when it receives the TTL triggering signal) and the light source (the time it takes for the light source to spark from when it receives the TTL triggering signal) were measured to be 15 μs and 2 μs, respectively.
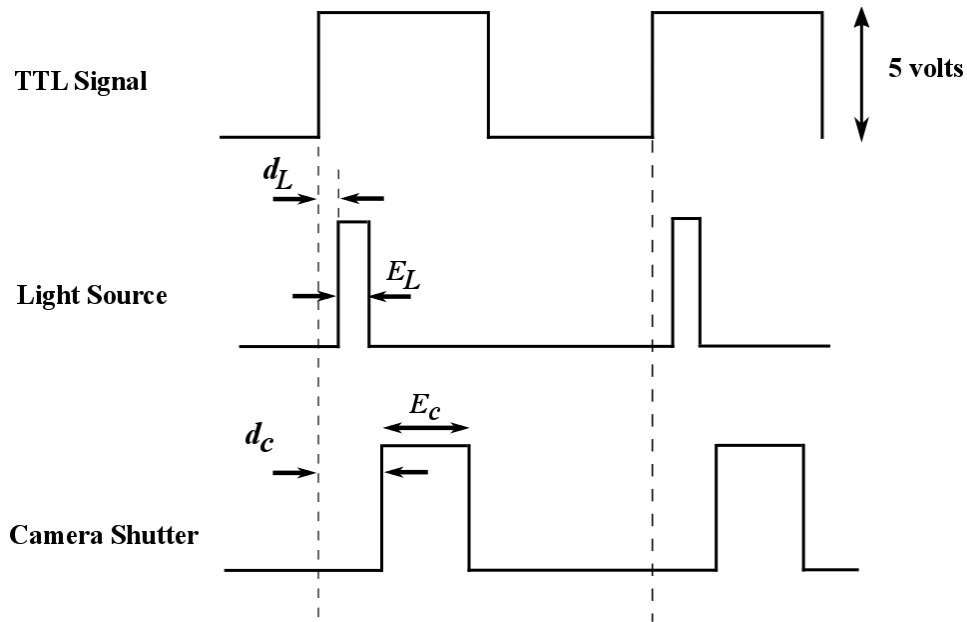
Fig. 3. 29 Schematic for timing of the TTL triggering signal, light source and camera shutter (unsynchronized case); d_L and d_c are the time response for the light source and camera, respectively and E_L and E_c are the duration of the light source and exposure time of the camera shutter

Fig. 3.29 shows an unsynchronized version of the timing for the TTL triggering signal, pulsed light source and camera shutter. In Fig. 3.29, $d_L = 2\ \mu s$, $d_c = 15\ \mu s$, $E_L = 2\ ns$ and E_c is the camera shutter exposure time, which can be set by the user. For, our case, exposure time is set to $E_c = 40\ \mu s$. Obviously, with no synchronization, the light source would spark and go out before the camera shutter begins opening, resulting in a completely dark image. Therefore, the two TTL signal with different phase is required to be sent to the light source and the camera to make sure the light source hits the camera in the middle of the camera exposure time.

Initially, this synchronization was done using a signal generator and a delay circuit (Fig. 3.30). Note that *R1* in Fig. (3.3.) is a rheostat which can be varied to change the delay between the two TTL signals.

The delay circuit worked just fine, but the same synchronization could also be done more easily with a LabView code without the need for external circuit and a bulky signal generator. Therefore, finally, a LabView code was written to conveniently synchronize the camera with the light source. However, Fig. 3.30 is presented here only for records and future reference.

163
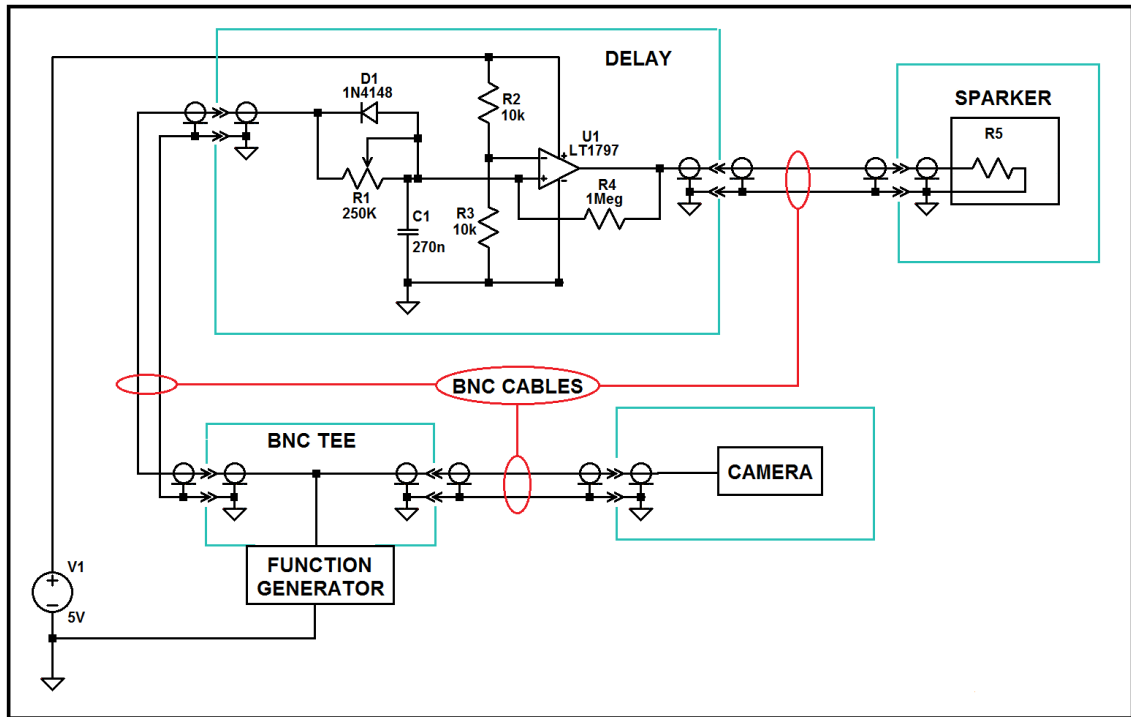
Fig. 3. 30 The delay circuit used to synchronize the camera with the light source

3.2.10 Blood samples

The human blood samples (Red Blood Cells, Adenine-Saline (AS-1) added, Leukocyte reduced) were provided from the American National Red Cross and the University of Louisville Hospital Blood Bank. The blood samples were already 28 days old when we received it. The experiments were done when the blood samples were 30 days old. The main experiments were done on two blood samples.

3.2.11 Working fluid

It is not possible to use the blood samples with the normal hematocrit for imaging purposes. It is because, the large number of red cells would block our view to capture images of red cells in the mid-plane of the flow channel. Therefore, 1 ml of human blood samples were diluted in 100 ml of 0.9% saline water. 0.9% saline water is commonly used to maintain a balance of osmotic pressure between the body's cells and the surrounding fluids. The saline solution was prepared by adding appropriate amount of sodium chloride

(Sodium Chloride certified for Biological Work, Fischer-Scientific Compony, Fair Lawn, NJ, US) to deionized water.

In order to do the experiments for higher level of stress, it was necessary to increase the viscosity of the working fluid (i.e. 0.9% saline water). Higher viscosities also enabled us to make sure the flow regime remained laminar. Dextran-500 (Fisher Scientific Inc., Hampton, NH) was used to increase the viscosity of suspending medium. Dextran have been previously shown to have no damaging effect on the red cells [238, 239]. Another important feature of Dextran is that it does not significantly deteriorate the optical clarity of the blood samples, which is highly desired in optical microscopy applications. Before adding the blood to the working fluid, the viscosity of the working fluid was measured by a cone and plate viscometer, model LVTCP42 (Brookfield, Stoughton, MA, US).

3.2.12 Uncertainty and statistical analysis

The accuracy of the viscometer measurement was ±0.1 cp. For each viscosity, a total of 10 measurements were done. Therefore, for the tests on the first blood sample, the total uncertainty (including Type A and Type B uncertainties) for the three viscosities used in the experimental testes were ±0.12 cp, ±0.11 cp and ±0.11 cp. Hence, the three values for the viscosities in AVERAGE±UNCERTAINTY format were 1.03±0.12 cp, 4.16±0.11 cp and 11.01±0.11. The values for the second blood samples were 1.04±0.14 cp, 4.2±0.12 cp and 11.04±0.11. Note that these three viscosities are conveniently denoted as 1 cp, 4.2 cp and 11 cp in the plots in the following sections.

Channel fabrication and channel measurement uncertainty was ±25 µm. The cell dimension and distance from the wall had a measurement uncertainty of ±0.1 µm.

All the statistical analyses were carried out on the results using Minitab v18 (Minitab INC., State College, PA, USA) with two-sided 95% confidence intervals. For the extensional flow case, one-way analysis of variance (ANOVA) was used to test sample-to-sample differences in aspect ratio at the same stress level. In the shear flow cases, analysis of covariance (ANCOVA) was used to test the difference between aspect ratios among two different viscosities within each blood sample. The same test was

used to examine the difference in aspect ratio for the three different viscosities within each blood sample.

3.2.13 Limitations

There was no limitation regarding the strength and leakage of the channel for the purpose of this study. The fabricated channel withstood a pressure of around 350 Pa without any leakage and rupture. However, there were limitations on image quality, motor power and duration of pulsed light. Since high pressure was necessary to achieve high flow rates, relatively thick cover plate (0.794 mm) were needed. The thicker cover plates necessitated a longer working distance objective lens. All of these limited on optical performance of the set-up and reduced image quality.

Some motion blur occurred in the images. The duration of the pulsed light for the spark lamp was 11 ns. For the 40X microscope objective, one camera pixel dimension (4.65 µm) of motion blur corresponds to a cell velocity of 4.65 µm/11 ns/40 = 10.6 m/s. For smaller velocities, subpixel blur occurs. For the velocity associated with each cell image, the motion blur was calculated and subtracted from the measured dimension of the cell. Motion blur correction was only applied to the streamwise, and not the transverse, direction.

The Abbe diffraction distance, which gives the smallest resolvable feature within an image, can be calculated by $L_{Abbe} = 0.53 \times \lambda/NA$, where λ is the light source wavelength and *NA* is the numerical aperture of the microscope objective. In our case, the peak wavelength is around 400 nm and the numerical aperture of the 40X objective is 0.75, resulting in $L_{Abbe} = 0.44$ µm. This is almost 20 times smaller than the typical size of a red cell ($\approx$ 8.8 µm). In addition, pixel oversampling can be calculated as $L_{Abbe} \times \frac{Magnification}{Camera\ pixel\ size} = 0.44\ \mu m \times \frac{40}{4.65\ \mu m} = 3.8$. Thus, the Abbe diffraction limit is 3.8 over-sampled, which means that pixelation did not limit the resolution of cell dimensions.

The proposed representative stress (Eq. (5)) is only taking into account two stress components from the fluid stress tensor. To come up with a universal hemolysis model, further experiments are needed to find the weight for other stress components.

Finally, the results here have been collected and analyzed for only two blood samples. While these two samples produced very similar values for C_n, more data from a larger number of samples would help confirm the results with higher confidence.

3.3 Experimental procedure

All the experiments were performed at room temperature (21 °C).

For extensional flow experiments, only the RBCs that were located within a central band with width of 20 μm in the middle of the channel were selected for measurement. For simplicity, the strain rate for cells within this band was characterized as that along the channel centerline, which is accurate to within ≈4%.

Three different medium viscosities were used for the hyperbolic contraction, namely 1 cp, 4.2 cp and 11 cp (note that 1 cp = 1 mPa.s). Only two viscosities (4.2 cp and 11 cp) were used for shear flow, because the cells in 1 cp fluid tumbled rather than tank-treaded even at the highest shear rate achievable by the pump.

For each experimental case, more than 50 images were taken. More than 30 cells with best image quality of cell boundaries were selected for the final measurement of each experimental run. ImageJ software was used to measure cell aspect ratio, i.e., the ratio of the cell major dimeter (a) to cell minor diameter (b) (example of aspect ratio measurement for extensional flow in Fig. 3.31 and for shear flow in Fig. 3.32).

For both extensional and shear flows, laminar flow was ensured by limiting the Reynolds number to no more than 2,000. After each run of the experiment, the samples were discarded to ensure that the cells were exposed to stress only once.
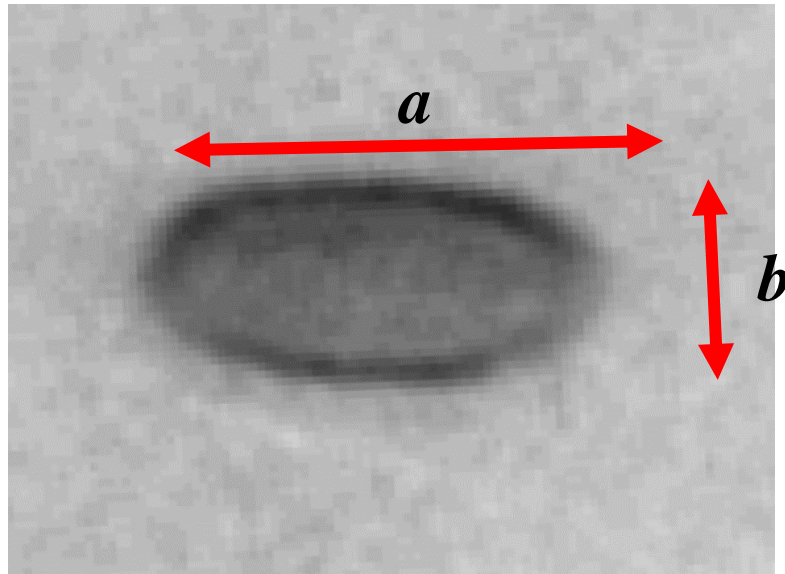
Fig. 3. 31 Measurement of aspect ratio for a red blood cell in extensional flow.
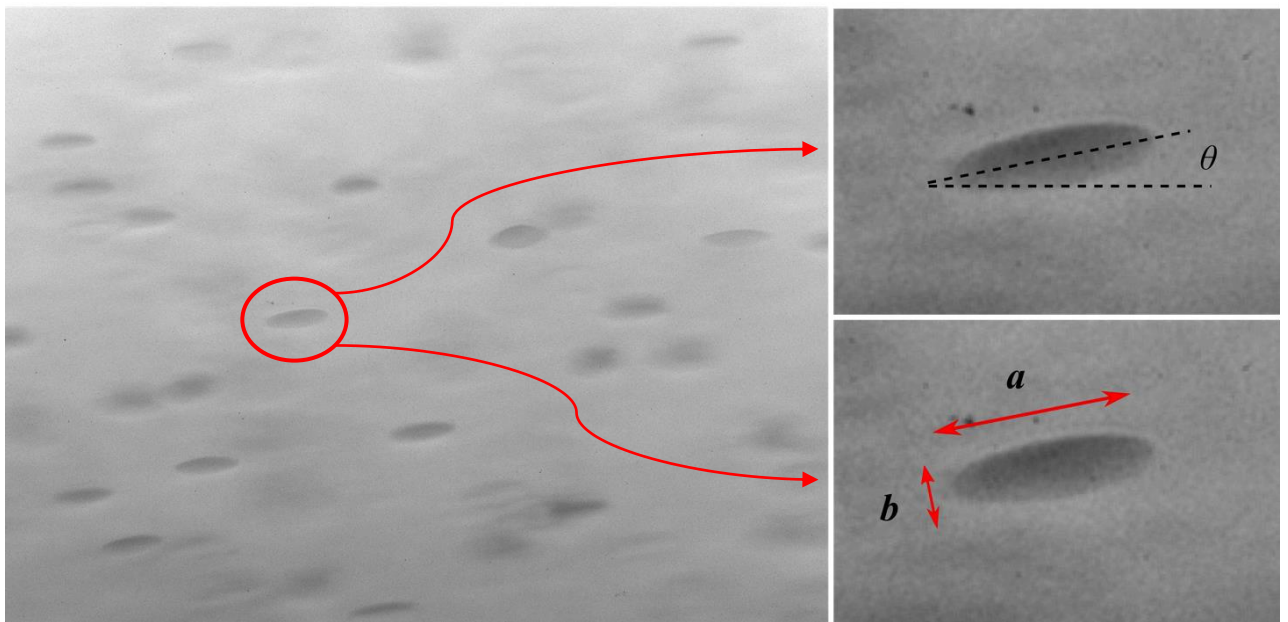
Fig. 3. 32 Measurement of RBC dimension and its tank-treading angle in the shear flow.

3.3.1 Representative stress

Previously, several types of representative stress have been introduced to be used in hemolysis prediction models, particularly the power-law model. Among them is the von-Mises-like scalar stress (σ_s), written as

168

$$\sigma_s = \sqrt{\frac{1}{3}\left(\sigma_{xx}{}^2 + \sigma_{yy}{}^2 + \sigma_{zz}{}^2\right) - \frac{1}{3}\left(\sigma_{xx}\sigma_{yy} + \sigma_{xx}\sigma_{zz} + \sigma_{yy}\sigma_{zz}\right) + \left(\tau_{xy}{}^2 + \tau_{xz}{}^2 + \tau_{yz}{}^2\right)}$$

where σ_{ii} is the extensional stress and, τ_{ij} is the shear stress. Another common representative stress is the dissipation-rate-equivalent stress (σ_e),

$$\sigma_e = \sqrt{\frac{1}{2}\left(\sigma_{xx}{}^2 + \sigma_{yy}{}^2 + \sigma_{zz}{}^2\right) + \left(\tau_{xy}{}^2 + \tau_{xz}{}^2 + \tau_{yz}{}^2\right)}$$

However, both of these hypothesized representative stresses lack validation across the range of flows that cells may encounter, with extensional flow being arguably the most important of the neglected cases.

In this study, a first attempt is made to develop a simplified representative stress that accommodates the contrasting responses of cells to shear stress versus extensional stress. Recognizing that the membranes of stretched cells in extensional flow and those of tank-treading cells in shear flow experience distinctly different tensions, the new representative stress applies an empirical weighting factor that scales the ratio of cell deformations by extensional versus shear flow

$$\sigma_n \\ = \sqrt{C_n^2\left[\sigma_{xx}{}^2 + \sigma_{yy}{}^2 + \sigma_{zz}{}^2 - \left(\sigma_{xx}\sigma_{yy} + \sigma_{xx}\sigma_{zz} + \sigma_{yy}\sigma_{zz}\right)\right] + \left(\tau_{xy}{}^2 + \tau_{xz}{}^2 + \tau_{yz}{}^2\right)}$$ (153)

where C_n is the empirical constant, which is obtained based on the experimental results in this study. The new representative stress has the same form as the von Mises stress (Eq. (66)), except that whereas the von Mises stress predicts that solid materials yield in pure shear for a shear stress that is $\sqrt{3}$ smaller than the extensional stress for pure extension, the new stress predicts that red cells fail in pure extensional flow for an extensional stress that is C_n times smaller than the shear stress for failure in pure shear flow.

In the experiments in this study, only two simple cases, pure shear in the xz plane in the shear channel (τ_{xz}) and extensional stress in z direction in the hyperbolic channel ($\sigma_{zz}, \sigma_{xx} = -\sigma_{zz}$), were tested. For these cases, the new representative stress is simplified as:

$$\sigma_n = \sqrt{(C_n \sigma_{zz})^2 + \tau_{xz}^2}$$

(154)

The objective was to find a value of C_n such that the representative stress accurately scales the cell aspect ratio for both pure shear and pure extension. To do this, first the experimental data points for the shear flow were curve-fitted by a log equation as

$$A_{shear} = c_1 \ln(\tau_{xz}) + c_2$$

(155)

where A_{shear} is the aspect ratio for experimental data points of shear flow and c_1 and c_2 are empirical constants from the curve-fitting. Then, a new set of extensional stresses adjusted by the factor C_n ($\sigma_{zz,a}$) were found by plugging the aspect ratio values measured for extensional flow into the curve-fitted equation for shear flow (Eq. (152)).

$$\sigma_{zz,a} = e^{\frac{(A_{extension} - c_2)}{c_1}}$$

(156)

Next, the root sum squared of the difference between the log of the newly obtained extensional stress and the log of the original extensional stress (ε) was minimized to calculate the constant value (C_n) needed to map the original extensional stress to the shear stress data points.

$$\sqrt{\sum_{i=1}^{n} \left(log(\sigma_{zz,a})_i - C_n \, log(\sigma_{zz})_i \right)^2} = \varepsilon$$

(157)

where i is the counter for experimental data points for the extensional stress.

3.4 Results

Results of the experiments on red blood cells flowing through both the hyperbolic contraction and the simple shear channel are presented in this section.

3.4.1 Extensional flow

Again, aspect ratio was chosen as a measure of cell deformation under different stress levels. Aspect ratio is the ratio of the cell major dimeter (*a*) to cell minor diameter

(*b*). However, note that aspect ratio can be related to deformation index (*DI*, Eq. (50)) by the relation: $a/b = \frac{1+DI}{1-DI}$.

The aspect ratio of human RBCs in pure laminar extensional stress increases as the fluid stress increases, with an asymptotic behavior at higher stresses (Fig. 3.33). Standard deviation values for the aspect ratio measurements are not included in the plots to increase readability. However, the same information along with the standard deviations are listed in Table 1.

Table 3. 7 Aspect ratio of the RBCs for the two blood samples in pure extensional flow.

Viscosity, cp	Stress, Pa	Aspect Ratio		Standard Deviation, ±	
		Sample 1	Sample 2	Sample 1	Sample 2
	2.70	2.17	2.06	0.091	0.118
1	4.42	2.63	2.44	0.131	0.087
	9.95	3.22	2.97	0.074	0.090
	11.89	3.36	3.25	0.087	0.073
	18.58	3.61	3.79	0.107	0.080
4.2	41.81	3.98	4.21	0.085	0.076
	83.62	4.14	4.38	0.126	0.038
	137.22	4.88	4.91	0.150	0.064
	30.42	3.81	3.93	0.092	0.086
	48.66	4.07	4.23	0.137	0.029
11	85.14	4.32	4.41	0.066	0.073
	152.02	4.95	4.91	0.109	0.048
	286.30	4.90	4.98	0.124	0.057
	359.10	5.11	5.04	0.082	0.103
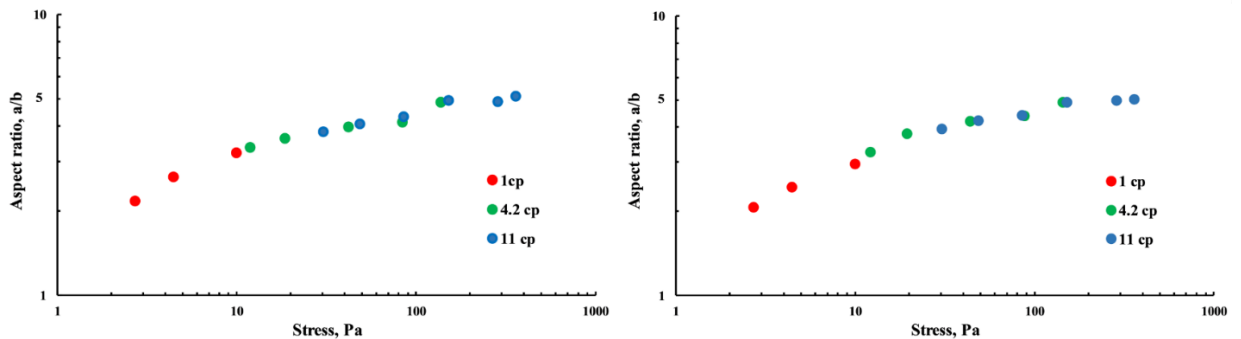
Fig. 3. 33 Measured aspect ratios in extensional flow for three different viscosities for sample 1 (left) and sample 2 (right)

Statistical analysis indicates that the difference between the aspect ratios in the two blood samples at the same stress value is not significant (*p>0.05*). Furthermore, within each blood sample, higher viscosity did not cause a significant difference in aspect ratio (*p>0.05*).

3.4.2 Shear flow

Aspect ratios for blood samples 1 and 2 in shear flow also exhibited similar trends (Fig. 3.34). Since good cell images occurred over a range of shear stresses associated with different distances from the wall, common shear stresses at which a standard deviation could be calculated were not obtained for shear flow.
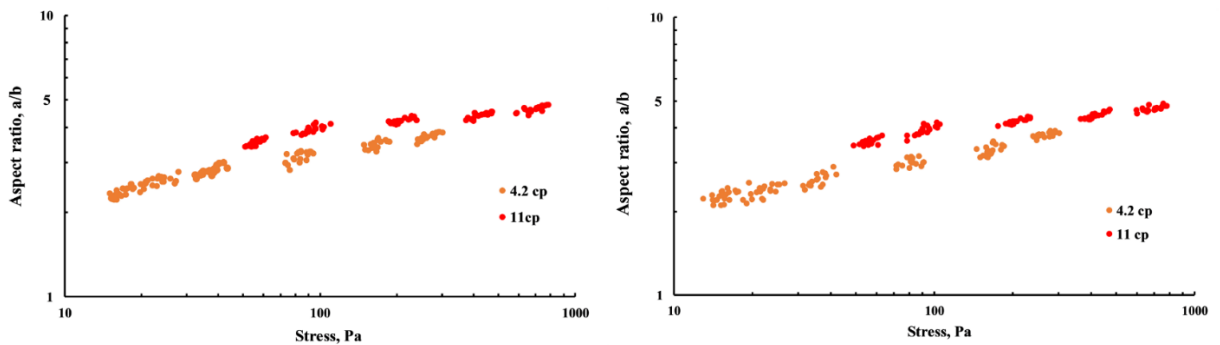
Fig. 3. 34 Aspect ratio of RBCs in shear channel at two different viscosities for the red blood cells in sample 1 (left) and sample 2 (right)

Within each blood sample, a significant difference was observed in aspect ratio between the two different medium viscosities (*p<0.05*). This result has also been observed in previous studies [240].

3.4.3 Representative stress

Statistical analysis within each blood sample indicated that there is a significant difference in the aspect ratio between shear stress and extensional stress (*p<0.05*). Therefore, a universal hemolysis prediction model should incorporate this difference. Assuming that hemolysis scales with the cell aspect ratio, the new scalar stress introduced in Eq. (151) weights the extensional stresses such that the same level of stress (shear or adjusted extension) gives the same cell deformation.

In another words, the goal is to re-scale the horizontal axis in Figs. 3.33 and 3.34 such that the data points for extensional stress lie on the same curve as the shear stress data points. To calculate the adjustment factor C_n, the data points for extensional stress for all viscosities were used. However, since the cell aspect ratio for shear flow depends on the suspending medium viscosity, only the data points for the suspending viscosity of 4.2 cp were used, because it is closest to that of normal whole blood.
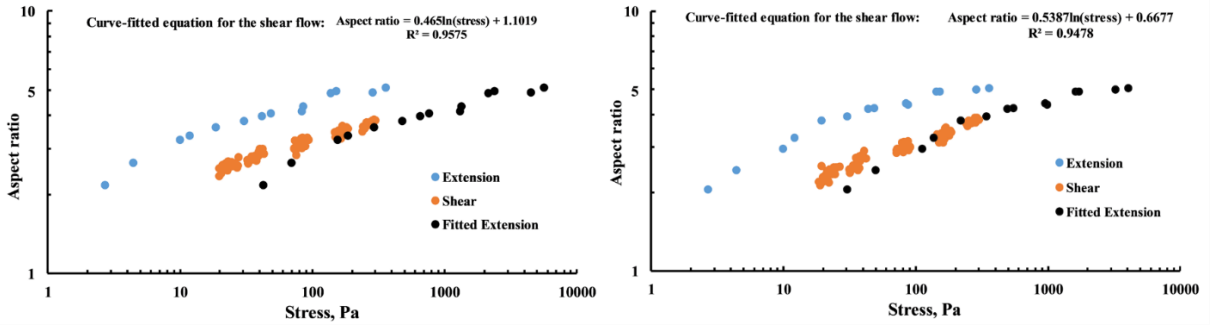
Fig. 3. 35 Re-scaling the extensional stress to fit the curve for shear stress, for blood sample 1 (left) and blood sample 2 (right)

The constant value C_n = 11.23 provided the best fit for the first sample and C_n = 11.26 for the second sample (Fig. 3.35).

3.5 Discussion

The value of C_n describes 11.23 - 11.26 greater cell deformation by extensional flow than by shear flow. The models of Chapter 2 (Fig. 2.12) show that laminar extensional flow causes 11.9 greater membrane tension than the RMS value for shear flow. While cell deformation and membrane tension can be expected to be nonlinear in other ranges of stress, these factors are quite similar.

Previously, there had only been one experimental study that compared aspect ratio of red cells in pure extensional flow versus pure shear flow [101]. The comparison was made for rabbit blood and only for stress levels up to 10 Pa. For the data of Lee, et al. [101], one can calculate the constant C_n as 9.70. Thus, these two studies are in substantial agreement that cells are deformed more by extensional stress than by shear stress by approximately an order of magnitude. Results in our study confirmed this trend for stress levels up to 300 Pa (Fig. 3.36). Note that the results of the current study shown in Fig. 3.36

are plotted for the first blood sample, but the second blood sample shows the same behavior. This suggests that extensional stress causes more hemolysis than shear stress. Therefore, a reliable representative stress must weigh extensional stress more than shear stress, i.e., by a factor C_n greater than one. This difference in cell deformation in shear versus in extension might be due to the fact that in extensional flow, the stress acts directly and continuously to pull the cell membrane apart, while in shear flow, the cell membrane rotates around the cytoplasm, thanks to the tank-treading motion, allowing for only a portion of the force to intermittently pull the membrane.
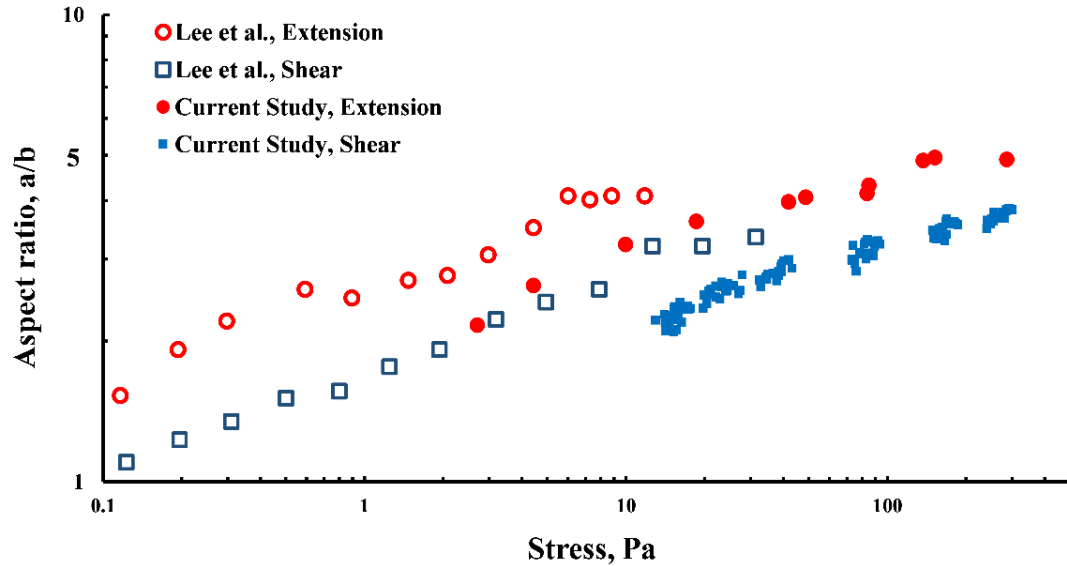
Fig. 3. 36 Results of cell deformation in shear and extensional flows in our study vs. Lee, et al. [101]

The results of RBC aspect ratio in shear flow (Fig. 3.34) indicate that higher external viscosity causes larger cell deformation. Pfafferott, et al. [240] also showed that for the same level of shear stress, RBCs are deformed more in a suspending medium of higher viscosity (Fig. 3.37).

174
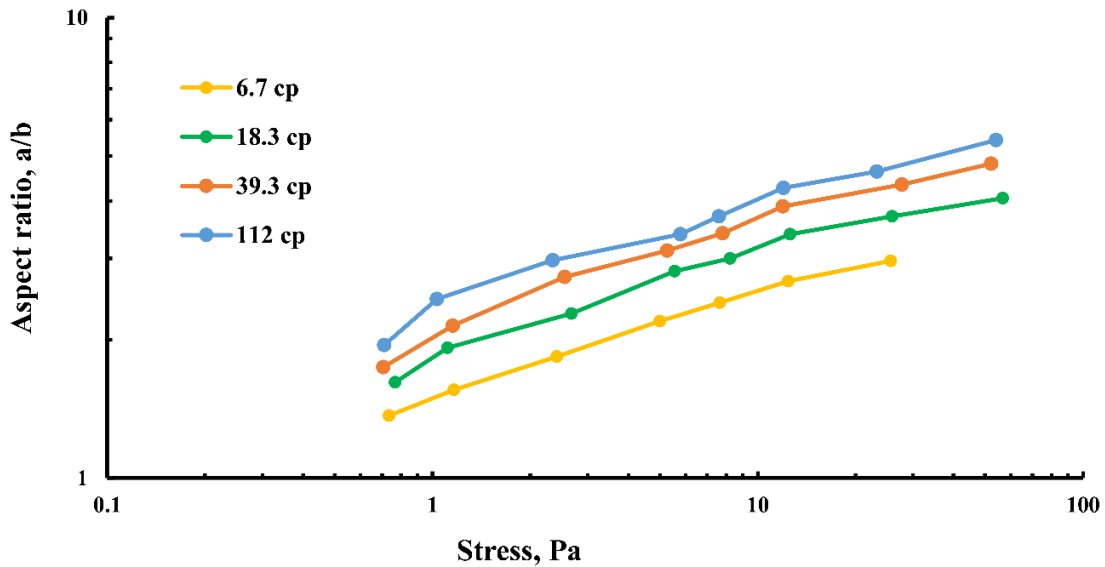
Fig. 3. 37 Aspect ratio of young RBCs vs. shear stress for different values of external viscosities, from [240]

Contrary to shear flow, higher external viscosity in extensional flow does not cause a significant increase in cell deformation. This finding is in general agreement with that of Lee, et al. [101] (Fig. 3.36). Nonetheless, there is a mismatch between the two results, in a sense that present results seems to be shifted to the right compared to those by Lee, et al. [101] (see also Fig. 3.38). The mismatch could be due to the difference in the species, as Lee, et al. [101] used rabbit blood, while human blood was used in the present study. Typical values for diameter and volume for rabbit RBCs are 6.1 µm, and 76 µm^3, while they are 7.3 µm, and 95 µm^3 for human RBCs [45]. Another possible reason for a mismatch might be that the suspending medium used by Lee, et al. [101] ($\sim$300 cp) was significantly higher than that used in the current study ($\sim$11 cp). While significant differences in deformation were not found for viscosity in the range $1 - 11$ cp, the effect of a much higher (93 - 890 cp) cannot be ruled out.

This difference in behavior of rabbit versus human red cells also suggests that inaccuracies can be expected when results from blood samples other than human are applied for human blood damage prediction. For example, the power-law equation based on data from Heuser and Opitz [139] for porcine blood has become popular for human blood damage prediction.

175
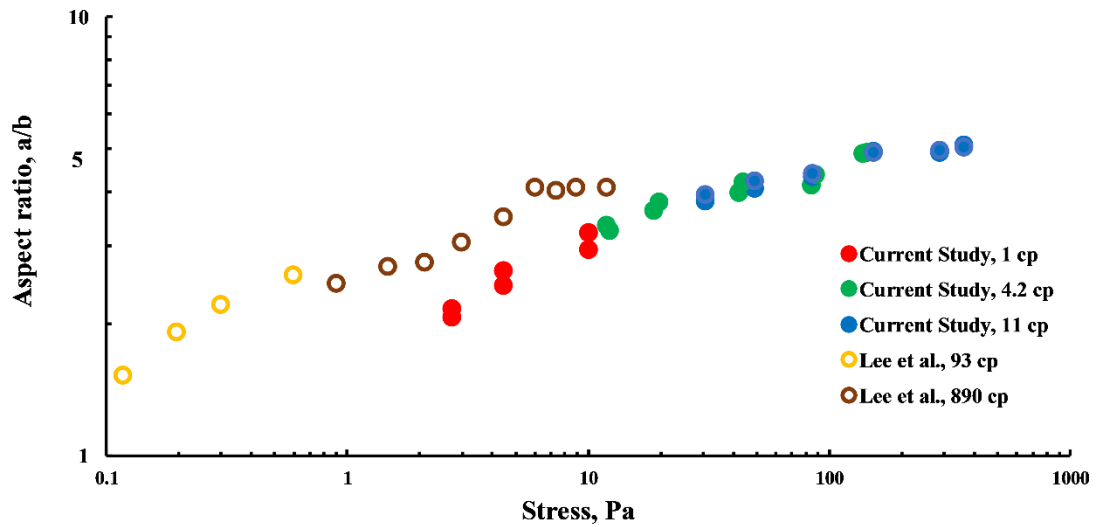
Fig. 3. 38 Aspect ratio of RBCs in pure extensional flow in our study (both samples) and in that of Lee, et al. [101]

3.6 Future work

Recognizing that deformation (in terms of aspect ratio) may be an imperfect scale for hemolysis, a significant next step would be to conduct experiments in pure extensional flow and measure the amount of hemoglobin release for a wide range of extensional stress. Such data would validate whether larger cell deformation in extensional flow correlates with greater hemoglobin release.

However, there is a technical challenge in measuring hemoglobin release in pure extensional flow. In contrast to pure shear, for which devices such as the cone and plate viscometer apply constant shear throughout the device, no device exists that applies constant extensional stress throughout the entire flow domain. An alternative would be to use the aspirator set-up of Sallam and Hwang [129] to sample pathlines with constant extensional stress, for instance, along the centerline of a hyperbolic contraction Their technique uses an injector placed at an upstream location to release cells in the middle of the channel. Then, an aspirator is used downstream of the contraction to collect the blood samples, for which hemoglobin content can be determined. This technique could also be used to study combinations of extensional and shear stresses by placing and collecting samples on other pathlines not in the center or the contraction

176

3.7 Conclusion

There has been a great deal of literature, both experimental as well as numerical, on behavior of red cells under pure shear flow [25, 81]. However, to develop a universal and accurate hemolysis model, it is equally important to understand the modes of motion and failure of red cell membranes under extensional flow. To the best of authors' knowledge, this study is the first to compare the deformation of human RBCs in pure extensional flow to that in shear flow for high stresses approaching the threshold for membrane failure. Results of the experiments showed that red cells are deformed significantly more in extensional flow than in shear flow, at the same stress level. Based on that, a new scalar stress was proposed such that extensional stress has a greater weight in causing cell deformation, compared to shear stress. This is in contrast to previous representative stresses, which weighed shear stress more than extensional stress.

REFERENCES

[1]   Faghih, M. M., and Sharp, M. K., 2019, "Modeling and prediction of flow-induced hemolysis: a review," Biomech Model Mechanobiol.

[2]   Sutera, S. P., 1977, "Flow-induced trauma to blood cells," Circ. Res., 41(1), pp. 2-8.

[3]   Lokhandwalla, M., and Sturtevant, B., 2001, "Mechanical haemolysis in shock wave lithotripsy (SWL): I. Analysis of cell deformation due to SWL flow-fields," Phys. Med. Biol., 46(2), pp. 413-437.

[4]   Offeman, R. D., and Williams, M. C., 1976, "Shear-induced hemolysis: effects of blood chemistry (including aging in storage) and shearing surfaces," Biomater. Med. Devices Artif. Organs, 4(1), pp. 49-79.

[5]   Girdhar, G., and Bluestein, D., 2008, "Biological effects of dynamic shear stress in cardiovascular pathologies and devices," Expert Rev. Med. Devices, 5(2), pp. 167-181.

[6]   Lippi, G., 2012, Hemolysis : an unresolved dispute in laboratory medicine, De Gruyter, Berlin.

[7]   Sayed, H. M., Dacie, J. V., Handley, D. A., Lewis, S. M., and Cleland, W. P., 1961, "Haemolytic anaemia of mechanical origin after open heart surgery," Thorax, 16(4), pp. 356-360.

[8]   Andersen, M. N., Gabrieli, E., and Zizzi, J. A., 1965, "Chronic hemolysis in patients with ball-valve prostheses," J. Thorac. Cardiovasc. Surg., 50(4), pp. 501-510.

[9]   Brodeur, M. T., Sutherland, D. W., Koler, R. D., Starr, A., Kimsey, J. A., and Griswold, H. E., 1965, "Red blood cell survival in patients with aortic valvular disease and ball-valve prostheses," Circulation, 32(4), pp. 570-581.

[10]   Rodgers, B. M., and Sabiston, D. C., 1969, "Hemolytic anemia following prosthetic valve replacement," Circulation, 39(5S1), pp. I-155-I-161.

[11]   Shivakumaraswamy, T., Mishra, P., Radhakrishnan, B., Khandekar, J., Agrawal, N., Patwardhan, A., and Khandeparkar, J., 2006, "Intravascular hemolysis in patients with

normally functioning mechanical heart valves in mitral position," Indian Journal of Thoracic and Cardiovascular Surgery, 22(4), pp. 215-218.

[12]   Shapira, Y., Vaturi, M., and Sagie, A., 2009, "Hemolysis associated with prosthetic heart valves: a review," Cardiol. Rev., 17(3), pp. 121-124.

[13]   AbouRjaili, G., Torbey, E., Alsaghir, T., Olkovski, Y., and Costantino, T., 2012, "Hemolytic anemia following mitral valve repair: A case presentation and literature review," Exp. Clin. Cardiol., 17(4), pp. 248-250.

[14]   Cardoso, C., Cachado, P., and Garcia, T., 2013, "Hemolytic anemia after mitral valve repair: a case report," BMC Res. Notes, 6, p. 165.

[15]   Cowger, J. A., Romano, M. A., Shah, P., Shah, N., Mehta, V., Haft, J. W., Aaronson, K. D., and Pagani, F. D., 2014, "Hemolysis: a harbinger of adverse outcome after left ventricular assist device implant," J. Heart Lung Transplant., 33(1), pp. 35-43.

[16]   Dewitz, T. S., Hung, T. C., Martin, R. R., and McIntire, L. V., 1977, "Mechanical trauma in leukocytes," J. Lab. Clin. Med., 90(4), pp. 728-736.

[17]   Fraser, K. H., Zhang, T., Taskin, M. E., Griffith, B. P., and Wu, Z. J., 2012, "A quantitative comparison of mechanical blood damage parameters in rotary ventricular assist devices: shear stress, exposure time and hemolysis index," J. Biomech. Eng., 134(8), p. 081002.

[18]   Waite, L., and Fine, J. M., 2007, Applied biofluid mechanics, McGraw-Hill, New York.

[19]   Fung, Y. C., 1993, Biomechanics : mechanical properties of living tissues, Springer-Verlag, New York.

[20]   R Skalak, N Ozkaya, a., and Skalak, T. C., 1989, "Biofluid Mechanics," Annu. Rev. Fluid Mech., 21(1), pp. 167-200.

[21]   Arwatz, G., and Smits, A. J., 2013, "A viscoelastic model of shear-induced hemolysis in laminar flow," Biorheology, 50(1-2), pp. 45-55.

[22]   Omar, H. R., Mirsaeidi, M., Socias, S., Sprenker, C., Caldeira, C., Camporesi, E. M., and Mangar, D., 2015, "Plasma free hemoglobin is an independent predictor of mortality among patients on extracorporeal membrane oxygenation support," PLoS One, 10(4), p. e0124034.

[23]   Sakota, D., Sakamoto, R., Sobajima, H., Yokoyama, N., Waguri, S., Ohuchi, K., and Takatani, S., 2008, "Mechanical damage of red blood cells by rotary blood pumps: selective destruction of aged red blood cells and subhemolytic trauma," Artif. Organs, 32(10), pp. 785-791.

[24]   Surgenor, D. M., and Bishop, C. W., 1974, The red blood cell, Academic Press, New York.

[25]   Fedosov, D. A., Caswell, B., and Karniadakis, G. E., 2010, "A multiscale red blood cell model with accurate mechanics, rheology, and dynamics," Biophys. J., 98(10), pp. 2215-2225.

[26]   Zhang, R., Zhang, C., Zhao, Q., and Li, D., 2013, "Spectrin: Structure, function and disease," Science China Life Sciences, 56(12), pp. 1076-1085.

[27]   Smith, J. E., 1987, "Erythrocyte membrane: structure, function, and pathophysiology," Vet. Pathol., 24(6), pp. 471-476.

[28]   Kodippili, G. C., Spector, J., Kang, G. E., Liu, H., Wickrema, A., Ritchie, K., and Low, P. S., 2010, "Analysis of the kinetics of band 3 diffusion in human erythroblasts during assembly of the erythrocyte membrane skeleton," Br. J. Haematol., 150(5), pp. 592-600.

[29]   Lux, S. E., and Palek, J., 1995, "Disorders of the red cell membrane.," Blood: Principles and Practice of Hematology, R. I. Handin., S. E. Lux., and T. P. Stossel, eds.Lippincott, Philadelphia, pp. 1701-1818.

[30]   Tse, W. T., and Lux, S. E., 1999, "Red blood cell membrane disorders," Br. J. Haematol., 104(1), pp. 2-13.

[31]   Burton, N. M., and Bruce, L. J., 2011, "Modelling the structure of the red cell membrane," Biochem. Cell Biol., 89(2), pp. 200-215.

[32]   Barns, S., Balanant, M. A., Sauret, E., Flower, R., Saha, S., and Gu, Y., 2017, "Investigation of red blood cell mechanical properties using AFM indentation and coarse-grained particle method," Biomedical engineering online, 16(1), p. 140.

[33]   Buys, A. V., Van Rooy, M.-J., Soma, P., Van Papendorp, D., Lipinski, B., and Pretorius, E., 2013, "Changes in red blood cell membrane structure in type 2 diabetes: a scanning electron and atomic force microscopy study," Cardiovasc. Diabetol., 12, pp. 25-25.

[34]   Boal, D., 2012, Mechanics of the cell, Cambridge University Press, Cambridge.

[35]   Akimov, S. A., Volynsky, P. E., Galimzyanov, T. R., Kuzmin, P. I., Pavlov, K. V., and Batishchev, O. V., 2017, "Pore formation in lipid membrane II: Energy landscape under external stress," Sci. Rep., 7(1), p. 12509.

[36]   Boal, D. H., Seifert, U., and Zilker, A., 1992, "Dual network model for red blood cell membranes," Phys. Rev. Lett., 69(23), pp. 3405-3408.

[37]   Boey, S. K., Boal, D. H., and Discher, D. E., 1998, "Simulations of the erythrocyte cytoskeleton at large deformation. I. Microscopic models," Biophys. J., 75(3), pp. 1573-1583.

[38]   Li, H., and Lykotrafitis, G., 2014, "Erythrocyte membrane model with explicit description of the lipid bilayer and the spectrin network," Biophys. J., 107(3), pp. 642-653.

[39]   Erickson, H. P., 2009, "Size and shape of protein molecules at the nanometer level determined by sedimentation, gel filtration, and electron microscopy," Biol. Proced. Online, 11, pp. 32-51.

[40]   Ding, J., Niu, S., Chen, Z., Zhang, T., Griffith, B. P., and Wu, Z. J., 2015, "Shear-induced hemolysis: species differences," Artif. Organs, 39(9), pp. 795-802.

[41]   Zhu, A., 2000, "Introduction to porcine red blood cells: Implications for xenotransfusion," Semin. Hematol., 37(2), pp. 143-149.

[42]   Adili, N., Melizi, M., Belabbas, H., and Achouri, A., 2014, "Preliminary study of the influence of red blood cells size on the determinism of the breed in cattle," Vet. Med. Int., 2014, p. 429495.

[43]   Baskurt, O. K., and Meiselman, H. J., 2013, "Comparative hemorheology," Clin. Hemorheol. Microcirc., 53(1-2), pp. 61-70.

[44]   Baskurt, O. K., 1996, "Deformability of red blood cells from different species studied by resistive pulse shape analysis technique," Biorheology, 33(2), pp. 169-179.

[45]   Namdee, K., Carrasco-Teja, M., Fish, M. B., Charoenphol, P., and Eniola-Adefeso, O., 2015, "Effect of Variation in hemorheology between human and animal blood on the binding efficacy of vascular-targeted carriers," Sci. Rep., 5, p. 11631.

[46]   Roland, L., Drillich, M., and Iwersen, M., 2014, "Hematology as a diagnostic tool in bovine medicine," J. Vet. Diagn. Invest., 26(5), pp. 592-598.

[47]   Houchin, D. N., Munn, J. I., and Parnell, B. L., 1958, "A Method for the Measurement of Red Cell Dimensions and Calculation of Mean Corpuscular Volume and Surface Area," Blood, 13(12), pp. 1185-1191.

[48]   Helms, C. C., Marvel, M., Zhao, W., Stahle, M., Vest, R., Kato, G. J., Lee, J. S., Christ, G., Gladwin, M. T., Hantgan, R. R., and Kim-Shapiro, D. B., 2013, "Mechanisms of hemolysis-associated platelet activation," J. Thromb. Haemost., 11(12), pp. 2148-2154.

[49]   Hellem, A. J., 1960, "The adhesiveness of human blood platelets in vitro," Scand. J. Clin. Lab. Invest., 12 Suppl, pp. 1-117.

[50]   Brown, C. H. I., Lemuth, R. F., Hellums, J. D., Leverett, L. B., and Alfrey, C. P., 1975, "Response of human platelets to shear stress," ASAIO J., 21(1), pp. 35-39.

[51]   Iuliano, L., Violi, F., Pedersen, J. Z., Pratico, D., Rotilio, G., and Balsano, F., 1992, "Free radical-mediated platelet activation by hemoglobin released from red blood cells," Arch. Biochem. Biophys., 299(2), pp. 220-224.

[52]   Sharp, M. K., and Mohammad, S. F., 1998, "Scaling of hemolysis in needles and catheters," Ann. Biomed. Eng., 26(5), pp. 788-797.

[53]   Da, Q., Teruya, M., Guchhait, P., Teruya, J., Olson, J. S., and Cruz, M. A., 2015, "Free hemoglobin increases von Willebrand factor-mediated platelet adhesion in vitro: implications for circulatory devices," Blood, 126(20), pp. 2338-2341.

[54]   Valladolid, C., Yee, A., and Cruz, M. A., 2018, "von Willebrand Factor, Free Hemoglobin and Thrombosis in ECMO," Frontiers in Medicine, 5(228).

[55]   Naito, K., Mizuguchi, K., and Nose, Y., 1994, "The need for standardizing the index of hemolysis," Artif. Organs, 18(1), pp. 7-10.

[56]   Ku, D. N., 1997, "Blood flow in arteries," Annu. Rev. Fluid Mech., 29(1), pp. 399-434.

[57]   Quinlan, N. J., 2014, "Mechanical loading of blood cells in turbulent flow," Computational Biomechanics for Medicine: Fundamental Science and Patient-specific Applications, B. Doyle, K. Miller, A. Wittek, and M. F. P. Nielsen, eds., Springer New York, New York, NY, pp. 1-13.

[58]   Çengel, Y. A., and Cimbala, J. M., 2006, Fluid mechanics : fundamentals and applications, McGraw-HillHigher Education, Boston.

[59]   Popov, E. P., Nagarajan, S., and Lu, Z. A., 1976, Mechanics of materials, Prentice-Hall, Englewood Cliffs, N.J.

[60]   Faghih, M. M., and Sharp, M. K., 2016, "Extending the power-law hemolysis model to complex flows," J. Biomech. Eng.

[61]   Bludszuweit, C., 1995, "Three-dimensional numerical prediction of stress loading of blood particles in a centrifugal pump," Artif. Organs, 19(7), pp. 590-596.

[62]   Alemu, Y., and Bluestein, D., 2007, "Flow-induced platelet activation and damage accumulation in a mechanical heart valve: numerical studies," Artif. Organs, 31(9), pp. 677-688.

[63]   Quinlan, N. J., and Dooley, P. N., 2007, "Models of flow-induced loading on blood cells in laminar and turbulent flow, with application to cardiovascular device flow," Ann. Biomed. Eng., 35(8), pp. 1347-1356.

[64]   Shakeri, M., Khodarahmi, I., and Sharp, M. K., 2012, "Preliminary imaging of red blood cells in turbulent flow," ASME 2012 Summer Bioengineering ConferencePuerto Rico, USA, pp. 887-888.

[65]   Baldwin, J. T., Deutsch, S., Petrie, H. L., and Tarbell, J. M., 1993, "Determination of principal Reynolds stresses in pulsatile flows after elliptical filtering of discrete velocity measurements," J. Biomech. Eng., 115(4A), pp. 396-403.

[66]   Maymir, J. C., Deutsch, S., Meyer, R. S., Geselowitz, D. B., and Tarbell, J. M., 1998, "Mean velocity and Reynolds stress measurements in the regurgitant jets of tilting disk heart valves in an artificial heart environment," Ann. Biomed. Eng., 26(1), pp. 146-156.

[67]   Nygaard, H., Giersiepen, M., Hasenkam, J. M., Westphal, D., Paulsen, P. K., and Reul, H., 1990, "Estimation of turbulent shear stresses in pulsatile flow immediately downstream of two artificial aortic valves in vitro," J. Biomech., 23(12), pp. 1231-1238.

[68]   Nyboe, C., Funder, J. A., Smerup, M. H., Nygaard, H., and Hasenkam, J. M., 2006, "Turbulent stress measurements downstream of three bileaflet heart valve designs in pigs," Eur. J. Cardiothorac. Surg., 29(6), pp. 1008-1013.

[69]   Baldwin, J. T., Deutsch, S., Geselowitz, D. B., and Tarbell, J. M., 1990, "Estimation of Reynolds stresses within the Penn State left ventricular assist device," ASAIO Trans., 36(3), pp. M274-278.

[70] Ge, L., Dasi, L. P., Sotiropoulos, F., and Yoganathan, A. P., 2008, "Characterization of hemodynamic forces induced by mechanical heart valves: Reynolds vs. viscous stresses," Ann. Biomed. Eng., 36(2), pp. 276-297.

[71] Barbaro, V., Grigioni, M., Daniele, C., D'Avenio, G., and Boccanera, G., 1997, "19 mm sized bileaflet valve prostheses' flow field investigated by bidimensional laser Doppler anemometry (part II: maximum turbulent shear stresses)," Int J Artif Organs, 20(11), pp. 629-636.

[72] Travis, B. R., Leo, H. L., Shah, P. A., Frakes, D. H., and Yoganathan, A. P., 2002, "An analysis of turbulent shear stresses in leakage flow through a bileaflet mechanical prostheses," J. Biomech. Eng., 124(2), pp. 155-165.

[73] Ishii, K., Hosoda, K., Nishida, M., Isoyama, T., Saito, I., Ariyoshi, K., Inoue, Y., Ono, T., Nakagawa, H., Sato, M., Hara, S., Lee, X., Wu, S. Y., Imachi, K., and Abe, Y., 2015, "Hydrodynamic characteristics of the helical flow pump," J. Artificial Organs, 18(3), pp. 206-212.

[74] Lu, P. C., Lai, H. C., and Liu, J. S., 2001, "A reevaluation and discussion on the threshold limit for hemolysis in a turbulent shear flow," J. Biomech., 34(10), pp. 1361-1364.

[75] Bluestein, M., and Mockros, L. F., 1969, "Hemolytic effects of energy dissipation in flowing blood," Med. Biol. Eng., 7(1), pp. 1-16.

[76] Morshed, K. N., Bark Jr, D., Forleo, M., and Dasi, L. P., 2014, "Theory to predict shear stress on cells in turbulent blood flow," PLoS One, 9(8), p. e105357.

[77] Pope, S. B., 2000, Turbulent flows, Cambridge University Press, Cambridge.

[78] Moulden, T. H., and Frost, W., 1977, Handbook of turbulence, Plenum Press, New York.

[79] Kolmogorov, A. N., 1991, "The local structure of turbulence in incompressible viscous fluid for very large Reynolds numbers," Proceedings: Mathematical and Physical Sciences, 434(1890), pp. 9-13.

[80] Tennekes, H., and Lumley, J. L., 1972, A first course in turbulence, MIT Press, Cambridge, Mass.

[81] Dupire, J., Socol, M., and Viallat, A., 2012, "Full dynamics of a red blood cell in shear flow," Proc. Natl. Acad. Sci. U. S. A., 109(51), pp. 20808-20813.

[82]   Viallat, A., and Abkarian, M., 2014, "Red blood cell: from its mechanics to its motion in shear flow," Int. J. Lab. Hematol., 36(3), pp. 237-243.

[83]   Abkarian, M., Faivre, M., and Viallat, A., 2007, "Swinging of red blood cells under shear flow," Phys. Rev. Lett., 98(18), p. 188302.

[84]   Kon, K., Maeda, N., and Shiga, T., 1987, "Erythrocyte deformation in shear flow: influences of internal viscosity, membrane stiffness, and hematocrit," Blood, 69(3), pp. 727-734.

[85]   Goldsmith, H. L., and Marlow, J., 1972, "Flow behaviour of erythrocytes. I. Rotation and deformation in dilute suspensions," Proceedings of the Royal Society of London B: Biological Sciences, 182(1068), pp. 351-384.

[86]   Keller, S. R., and Skalak, R., 1982, "Motion of a tank-treading ellipsoidal particle in a shear flow," J. Fluid Mech., 120, pp. 27-47.

[87]   Galdi, G. P., Rannacher, R., Robertson, A. M., and Turek, S., 2008, Hemodynamical flows modeling, analysis and simulation, Birkhäuser Verlag AG, Basel.

[88]   Becker, S. M., and Kuznetsov, A. V., 2015, "Heat transfer and fluid flow in biological processes."

[89]   Cardenas, N., Mohanty, S. K., Imaging, M., Analysis of Biomolecules, C., and Tissues, X., 2012, "Investigation of shape memory of red blood cells using optical tweezers and quantitative phase microscopy," Progr. Biomed. Opt. Imaging Proc. SPIE Progress in Biomedical Optics and Imaging - Proceedings of SPIE, 8225.

[90]   Yazdani, A., and Bagchi, P., 2012, "Three-dimensional numerical simulation of vesicle dynamics using a front-tracking method," Physical Review E, 85(5), p. 056308.

[91]   Abkarian, M., and Viallat, A., 2008, "Vesicles and red blood cells in shear flow," Soft Matter, 4(4), pp. 653-657.

[92]   Misbah, C., 2006, "Vacillating breathing and tumbling of vesicles under shear flow," Phys. Rev. Lett., 96(2), p. 028104.

[93]   Misbah, C., 2012, "Vesicles, capsules and red blood cells under flow," Journal of Physics: Conference Series, 392(1), p. 012005.

[94]   Shi, L., Pan, T. W., and Glowinski, R., 2012, "Deformation of a single red blood cell in bounded Poiseuille flows," Phys. Rev. E Stat. Nonlin. Soft Matter Phys., 85(1 Pt 2), p. 016307.

[95]   Coupier, G., Kaoui, B., Podgorski, T., and Misbah, C., 2008, "Noninertial lateral migration of vesicles in bounded Poiseuille flow," Phys. Fluids, 20(11), p. 111702.

[96]   Hiroshi, N., and Gerhard, G., 2005, "Vesicle dynamics in shear and capillary flows," Journal of Physics: Condensed Matter, 17(45), p. S3439.

[97]   Danker, G., Vlahovska, P. M., and Misbah, C., 2009, "Vesicles in Poiseuille flow," Phys. Rev. Lett., 102(14), p. 148102.

[98]   Down, L. A., Papavassiliou, D. V., and O'Rear, E. A., 2011, "Significance of extensional stresses to red blood cell lysis in a shearing flow," Ann. Biomed. Eng., 39(6), pp. 1632-1642.

[99]   Yaginuma, T., Oliveira, M. S. N., Lima, R., Ishikawa, T., and Yamaguchi, T., 2013, "Human red blood cell behavior under homogeneous extensional flow in a hyperbolic-shaped microchannel," Biomicrofluidics, 7(5).

[100]   Chen, Y., and Sharp, M. K., 2011, "A strain-based flow-induced hemolysis prediction model calibrated by in vitro erythrocyte deformation measurements," Artif. Organs, 35(2), pp. 145-156.

[101]   Lee, S. S., Yim, Y., Ahn, K. H., and Lee, S. J., 2009, "Extensional flow-based assessment of red blood cell deformability using hyperbolic converging microchannel," Biomed. Microdevices, 11(5), pp. 1021-1027.

[102]   Mcgraw, L. A., 1992, "Blood cell deformability in uniaxial extensional flow," Carnegie Mellon University.

[103]   Gossett, D. R., Tse, H. T. K., Lee, S. A., Ying, Y., Lindgren, A. G., Yang, O. O., Rao, J., Clark, A. T., and Di Carlo, D., 2012, "Hydrodynamic stretching of single cells for large population mechanical phenotyping," Proc. Natl. Acad. Sci. U. S. A., 109(20), pp. 7630-7635.

[104]   Rodrigues RO, F. V., Pinto E, Pinho D, Lima R., 2013, "Red blood cells deformability index assessment in a hyperbolic microchannel: the diamide and glutaraldehyde effect," WebmedCentral BIOMEDICAL ENGINEERING

[105]   Faustino, V., Pinho, D., Yaginuma, T., Calhelha, R. C., Kim, G. M., Arana, S., Ferreira, I. C. F. R., Oliveira, M. S. N., and Lima, R., 2014, "Flow of red blood cells suspensions through hyperbolic microcontractions," Visualization and Simulation of

Complex Flows in Biomedical Engineering, R. Lima, Y. Imai, T. Ishikawa, and N. M. S. Oliveira, eds., Springer Netherlands, Dordrecht, pp. 151-163.

[106]   Yaginuma, T., Pereira, A. I., Rodrigues, P. J., Lima, R., Oliveira, M. S. N., Ishikawa, T., and Yamaguchi, T., 2011, "Flow of red blood cells through a microfluidic extensional device: An image analysis assessment," Computational Vision and Medical Image Processing: VipIMAGE 2011, CRC Press, pp. 217-220.

[107]   Bae, Y. B., Jang, H. K., Shin, T. H., Phukan, G., Tran, T. T., Lee, G., Hwang, W. R., and Kim, J. M., 2015, "Microfluidic assessment of mechanical cell damage by extensional stress," Lab on a chip, 16(1), pp. 96-103.

[108]   Bento, D., Rodrigues, R., Faustino, V., Pinho, D., Fernandes, C., Pereira, A., Garcia, V., Miranda, J., and Lima, R., 2018, "Deformation of Red Blood Cells, Air Bubbles, and Droplets in Microfluidic Devices: Flow Visualizations and Measurements," Micromachines, 9(4), p. 151.

[109]   Oliveira, M., Alves, M. A., Pinho, F. T., and McKinley, G. H., 2007, "Viscous fluid flow through microfabricated hperbolic contractions," Exp. Fluids, 43(2-3), pp. 437-451.

[110]   Sousa, P. C., Pinho, F. T., Oliveira, M. S., and Alves, M. A., 2011, "Extensional flow of blood analog solutions in microfluidic devices," Biomicrofluidics, 5, p. 14108.

[111]   Sutera, S. P., and Mehrjardi, M. H., 1975, "Deformation and fragmentation of human red blood cells in turbulent shear flow," Biophys. J., 15(1), pp. 1-10.

[112]   Forstrom, R. J., 1969, "A new measure of erythrocyte membrane strength - the jet fragility test."

[113]   Williams, A. R., Hughes, D. E., and Nyborg, W. L., 1970, "Hemolysis near a transversely oscillating wire," Science, 169(3948), pp. 871-873.

[114]   Rooney, J. A., 1970, "Hemolysis near an ultrasonically pulsating gas bubble," Science, 169(3948), pp. 869-871.

[115]   Paul, R., Apel, J., Klaus, S., Schugner, F., Schwindke, P., and Reul, H., 2003, "Shear stress related blood damage in laminar couette flow," Artif. Organs, 27(6), pp. 517-529.

[116]   Leverett, L. B., Hellums, J. D., Alfrey, C. P., and Lynch, E. C., 1972, "Red blood cell damage by shear stress," Biophys. J., 12(3), pp. 257-273.

[117]   Laugel, J. F., and Beissinger, R. L., 1983, "Low stress shear-induced hemolysis in capillary flow," Trans. Am. Soc. Artif. Intern. Organs, 29, pp. 158-162.

[118]   Nakahara, T., and Yoshida, F., 1986, "Mechanical effects on rates of hemolysis," J. Biomed. Mater. Res., 20(3), pp. 363-374.

[119]   Polaschegg, H. D., 2009, "Red blood cell damage from extracorporeal circulation in hemodialysis," Seminars in dialysis, 22(5), pp. 524-531.

[120]   Nevaril, C. G., Lynch, E. C., Alfrey, C. P., Jr., and Hellums, J. D., 1968, "Erythrocyte damage and destruction induced by shearing stress," J. Lab. Clin. Med., 71(5), pp. 784-790.

[121]   Lee, S., KH, A., SJ, L., Sun K Goedhart, P. T., and Hardeman, M. R., 2004, "Shear induced damage of red blood cells monitored by the decrease of their deformability," Korea-Australia Rheology Journal, 16(3), pp. 141-146.

[122]   Kameneva, M. V., Burgreen, G. W., Kono, K., Repko, B., Antaki, J. F., and Umezu, M., 2004, "Effects of turbulent stresses upon mechanical hemolysis: experimental and computational analysis," ASAIO J., 50(5), pp. 418-423.

[123]   Zhao, R., Antaki, J. F., Naik, T., Bachman, T. N., Kameneva, M. V., and Wu, Z. J., 2006, "Microscopic investigation of erythrocyte deformation dynamics," Biorheology, 43(6), pp. 747-765.

[124]   Boehning, F., Mejia, T., Schmitz-Rode, T., and Steinseifer, U., 2014, "Hemolysis in a laminar flow-through Couette shearing device: an experimental study," Artif. Organs, 38(9), pp. 761-765.

[125]   Ozturk, M., O'Rear, E., and Papavassiliou, D., 2016, "Reynolds Stresses and Hemolysis in Turbulent Flow Examined by Threshold Analysis," Fluids, 1(4), p. 42.

[126]   Evans, E. A., Waugh, R., and Melnik, L., 1976, "Elastic area compressibility modulus of red cell membrane," Biophys. J., 16(6), pp. 585-595.

[127]   Keshaviah, P. R., 1976, "Hemolysis in the accelerated flow region of an abrupt contraction."

[128]   Stein, P. D., and Sabbah, H. N., 1976, "Turbulent blood flow in the ascending aorta of humans with normal and diseased aortic valves," Circ. Res., 39(1), pp. 58-65.

[129]   Sallam, A. M., and Hwang, N. H., 1984, "Human red blood cell hemolysis in a turbulent shear flow: contribution of Reynolds shear stresses," Biorheology, 21(6), pp. 783-797.

[130]   Tamagawa, M., Akamatsu, T., and Saitoh, K., 1996, "Prediction of hemolysis in turbulent shear orifice flow," Artif. Organs, 20(6), pp. 553-559.

[131]   Grigioni, M., Daniele, C., D'Avenio, G., and Barbaro, V., 1999, "A discussion on the threshold limit for hemolysis related to Reynolds shear stress," J. Biomech., 32(10), pp. 1107-1112.

[132]   Barbaro, V., Grigioni, M., Daniele, C., D'Avenio, G., and Boccanera, G., 1997, "19 mm sized bileaflet valve prostheses' flow field investigated by bidimensional laser Doppler anemometry (part I: velocity profiles)," Int J Artif Organs, 20(11), pp. 622-628.

[133]   Yen, J. H., Chen, S. F., Chern, M. K., and Lu, P. C., 2014, "The effect of turbulent viscous shear stress on red blood cell hemolysis," Journal of artificial organs : the official journal of the Japanese Society for Artificial Organs, 17(2), pp. 178-185.

[134]   Jhun, C. S., Stauffer, M. A., Reibson, J. D., Yeager, E. E., Newswanger, R. K., Taylor, J. O., Manning, K. B., Weiss, W. J., and Rosenberg, G., 2018, "Determination of Reynolds Shear Stress Level for Hemolysis," ASAIO J., 64(1), pp. 63-69.

[135]   Lee, H., Tatsumi, E., and Taenaka, Y., 2009, "Experimental study on the Reynolds and viscous shear stress of bileaflet mechanical heart valves in a pneumatic ventricular assist device," ASAIO J., 55(4), pp. 348-354.

[136]   Jones, S. A., 1995, "A relationship between Reynolds stresses and viscous dissipation: implications to red cell damage," Ann. Biomed. Eng., 23(1), pp. 21-28.

[137]   Hund, S. J., Antaki, J. F., and Massoudi, M., 2010, "On the representation of turbulent stresses for computing blood damage," International journal of engineering science, 48(11), pp. 1325-1331.

[138]   Blackshear, P. L. J., Dorman, F. D., Steinbach, J. H., Maybach, E. J., Singh, A., and Collingham, R. E., 1966, "Shear, wall interaction and hemolysis," ASAIO J., 12(1), pp. 113-120.

[139]   Heuser, G., and Opitz, R., 1980, "A couette viscometer for short time shearing of blood," Biorheology, 17(1-2), pp. 17-24.

[140] Giersiepen, M., Wurzinger, L. J., Opitz, R., and Reul, H., 1990, "Estimation of shear stress-related blood damage in heart valve prostheses--in vitro comparison of 25 aortic valves," Int J Artif Organs, 13(5), pp. 300-306.

[141] Richardson, E., 1975, "Applications of a theoretical model for haemolysis in shear flow," Biorheology, 12(1), pp. 27-37.

[142] Ezzeldin, H. M., de Tullio, M. D., Vanella, M., Solares, S. D., and Balaras, E., 2015, "A strain-based model for mechanical hemolysis based on a coarse-grained red blood cell model," Ann. Biomed. Eng., 43(6), pp. 1398-1409.

[143] Koleva, I., and Rehage, H., 2012, "Deformation and orientation dynamics of polysiloxane microcapsules in linear shear flow," Soft Matter, 8(13), pp. 3681-3693.

[144] Vitale, F., Nam, J., Turchetti, L., Behr, M., Raphael, R., Annesini, M. C., and Pasquali, M., 2014, "A multiscale, biophysical model of flow-induced red blood cell damage," AICHE J., 60(4), pp. 1509-1516.

[145] Yu, H., Engel, S., Janiga, G., and Thevenin, D., 2017, "A Review of Hemolysis Prediction Models for Computational Fluid Dynamics," Artif. Organs, 41(7), pp. 603-621.

[146] Zhang, Tao, Taskin, M. E., Fang, H.-B., Pampori, A., Jarvik, R., Griffith, B. P., and Wu, Z. J., 2011, "Study of flow-induced hemolysis using novel couette-type blood-shearing devices," Artif. Organs, 35(12), pp. 1180-1186.

[147] Song, X., Throckmorton, A. L., Wood, H. G., Antaki, J. F., and Olsen, D. B., 2003, "Computational fluid dynamics prediction of blood damage in a centrifugal pump," Artif. Organs, 27(10), pp. 938-941.

[148] Faghih, M. M., and Sharp, M. K., 2018, "Characterization of erythrocyte membrane tension for hemolysis prediction in complex flows," Biomech Model Mechanobiol.

[149] Giersiepen, M., Krause, U., Knott, E., Reul, H., and Rau, G., 1989, "Velocity and shear stress distribution downstream of mechanical heart valves in pulsatile flow," Int J Artif Organs, 12(4), pp. 261-269.

[150] Nygaard, H., Giersiepen, M., Hasenkam, J. M., Reul, H., Paulsen, P. K., Rovsing, P. E., and Westphal, D., 1992, "Two-dimensional color-mapping of turbulent shear stress distribution downstream of two aortic bioprosthetic valves in vitro," J. Biomech., 25(4), pp. 429-440.

[151] Grigioni, M., Daniele, C., Morbiducci, U., D'Avenio, G., Di Benedetto, G., and Barbaro, V., 2004, "The power-law mathematical model for blood damage prediction: analytical developments and physical inconsistencies," Artif. Organs, 28(5), pp. 467-475.

[152] Grigioni, M., Morbiducci, U., D'Avenio, G., Benedetto, G. D., and Gaudio, C. D., 2005, "A novel formulation for blood trauma prediction by a modified power-law mathematical model," Biomech Model Mechanobiol, 4(4), pp. 249-260.

[153] Bludszuweit, C., 1995, "Model for a general mechanical blood damage prediction," Artif. Organs, 19(7), pp. 583-589.

[154] Zimmer, R., Steegers, A., Paul, R., Affeld, K., and Reul, H., 2000, "Velocities, shear stresses and blood damage potential of the leakage jets of the Medtronic Parallel bileaflet valve," Int J Artif Organs, 23(1), pp. 41-48.

[155] Yeleswarapu, K. K., Antaki, J. F., Kameneva, M. V., and Rajagopal, K. R., 1995, "A mathematical model for shear-induced hemolysis," Artif. Organs, 19(7), pp. 576-582.

[156] Mitoh, A., Yano, T., Sekine, K., Mitamura, Y., Okamoto, E., Kim, D. W., Yozu, R., and Kawada, S., 2003, "Computational fluid dynamics analysis of an intra-cardiac axial flow pump," Artif. Organs, 27(1), pp. 34-40.

[157] Yano, T., Sekine, K., Mitoh, A., Mitamura, Y., Okamoto, E., Kim, D. W., Nishimura, I., Murabayashi, S., and Yozu, R., 2003, "An estimation method of hemolysis within an axial flow blood pump by computational fluid dynamics analysis," Artif. Organs, 27(10), pp. 920-925.

[158] Wu, J., Antaki, J. F., Snyder, T. A., Wagner, W. R., Borovetz, H. S., and Paden, B. E., 2005, "Design optimization of blood shearing instrument by computational fluid dynamics," Artif. Organs, 29(6), pp. 482-489.

[159] Goubergrits, L., 2006, "Numerical modeling of blood damage: current status, challenges and future prospects," Expert Rev. Med. Devices, 3(5), pp. 527-531.

[160] Garon, A., and Farinas, M. I., 2004, "Fast three-dimensional numerical hemolysis approximation," Artif. Organs, 28(11), pp. 1016-1025.

[161] Farinas, M. I., Garon, A., Lacasse, D., and N'Dri, D., 2006, "Asymptotically consistent numerical approximation of hemolysis," J. Biomech. Eng., 128(5), pp. 688-696.

[162] Zhang, Juntao, Gellman, B., Koert, A., Dasse, K. A., Gilbert, R. J., Griffith, B. P., and Wu, Z. J., 2006, "Computational and experimental evaluation of the fluid dynamics and hemocompatibility of the CentriMag blood pump," Artif. Organs, 30(3), pp. 168-177.

[163] Taskin, M. E., Fraser, K. H., Zhang, T., Wu, C., Griffith, B. P., and Wu, Z. J., 2012, "Evaluation of Eulerian and Lagrangian models for hemolysis estimation," ASAIO J., 58(4), pp. 363-372.

[164] Pauli, L., Nam, J., Pasquali, M., and Behr, M., 2013, "Transient stress-based and strain-based hemolysis estimation in a simplified blood pump," International journal for numerical methods in biomedical engineering, 29(10), pp. 1148-1160.

[165] Burton, A. C., 1972, Physiology and biophysics of the circulation; an introductory text, Year Book Medical Publishers, Chicago.

[166] Rand, R. P., and Burton, A. C., 1964, "Mechanical properties of the red cell membrane: I. membrane stiffness and intracellular pressure," Biophys. J., 4(2), pp. 115-135.

[167] Morris, D. R., and Williams, A. R., 1979, "The effects of suspending medium viscosity on erythrocyte deformation and haemolysis in vitro," Biochim. Biophys. Acta, 550(2), pp. 288-296.

[168] Rand, R. P., 1964, "Mechanical properties of the red cell membrane: II. viscoelastic breakdown of the membrane," Biophys. J., 4(4), pp. 303-316.

[169] Richardson, E., 1974, "Deformation and haemolysis of red cells in shear flow," Proceedings of the Royal Society of London A: Mathematical, Physical and Engineering Sciences, 338(1613), pp. 129-153.

[170] Arora, D., Behr, M., and Pasquali, M., 2004, "A tensor-based measure for estimating blood damage," Artif. Organs, 28(11), pp. 1002-1015.

[171] Barthès-Biesel, D., and Rallison, J. M., 1981, "The time-dependent deformation of a capsule freely suspended in a linear shear flow," J. Fluid Mech., 113, pp. 251-267.

[172] Maffettone, P. L., and Minale, M., 1998, "Equation of change for ellipsoidal drops in viscous flow," Journal of Non-Newtonian Fluid Mechanics, 78(2–3), pp. 227-241.

[173] Chen, Y., Kent, T. L., and Sharp, M. K., 2013, "Testing of models of flow-induced hemolysis in blood flow through hypodermic needles," Artif. Organs, 37(3), pp. 256-266.

[174]   Discher, D. E., Boal, D. H., and Boey, S. K., 1998, "Simulations of the erythrocyte cytoskeleton at large deformation. II. Micropipette aspiration," Biophys. J., 75(3), pp. 1584-1597.

[175]   Sohrabi, S., and Liu, Y., 2016, "A cellular model of shear-induced hemolysis," Artif. Organs, pp. n/a-n/a.

[176]   Poorkhalil, A., Amoabediny, G., Tabesh, H., Behbahani, M., and Mottaghy, K., 2016, "A new approach for semiempirical modeling of mechanical blood trauma," Int J Artif Organs, 39(4), pp. 171-177.

[177]   Fedosov, D. A., Peltomäki, M., and Gompper, G., 2014, "Deformation and dynamics of red blood cells in flow through cylindrical microchannels," Soft Matter, 10(24), pp. 4258-4267.

[178]   Omori, T., Ishikawa, T., Barthès-Biesel, D., Salsac, A. V., Imai, Y., and Yamaguchi, T., 2012, "Tension of red blood cell membrane in simple shear flow," Physical Review E, 86(5), p. 056321.

[179]   Tran-Son-Tay, R., Sutera, S. P., Zahalak, G. I., and Rao, P. R., 1987, "Membrane stress and internal pressure in a red blood cell freely suspended in a shear flow," Biophys. J., 51(6), pp. 915-924.

[180]   Liu, J. S., Lu, P. C., and Chu, S. H., 2000, "Turbulence characteristics downstream of bileaflet aortic valve prostheses," J. Biomech. Eng., 122(2), pp. 118-124.

[181]   Dooley, P. N., and Quinlan, N. J., 2009, "Effect of eddy length scale on mechanical loading of blood cells in turbulent flow," Ann. Biomed. Eng., 37(12), pp. 2449-2458.

[182]   Hochmuth, R. M., and Waugh, R. E., 1987, "Erythrocyte membrane elasticity and viscosity," Annu. Rev. Physiol., 49(1), pp. 209-219.

[183]   Antiga, L., and Steinman, D. A., 2009, "Rethinking turbulence in blood," Biorheology, 46(2), pp. 77-81.

[184]   Ozturk, M., O'Rear, E. A., and Papavassiliou, D. V., 2015, "Hemolysis related to turbulent eddy size distributions using comparisons of experiments to computations," Artif. Organs, 39(12), pp. E227-239.

[185]   Faghih, M. M., and Keith Sharp, M., 2016, "Extending the Power-Law Hemolysis Model to Complex Flows," J. Biomech. Eng., 138(12).

[186] Bludszuweit, C., 1994, "A theoretical approach to the prediction of haemolysis in centrifugal blood pumps," Doctoral Thesis, University of Strathclyde.

[187] Apel, J., Paul, R., Klaus, S., Siess, T., and Reul, H., 2001, "Assessment of hemolysis related quantities in a microaxial blood pump by computational fluid dynamics," Artif. Organs, 25(5), pp. 341-347.

[188] Arvand, A., Hormes, M., and Reul, H., 2005, "A validated computational fluid dynamics model to estimate hemolysis in a rotary blood pump," Artif. Organs, 29(7), pp. 531-540.

[189] Chua, L. P., Song, G., Lim, T. M., and Zhou, T., 2006, "Numerical analysis of the inner flow field of a biocentrifugal blood pump," Artif. Organs, 30(6), pp. 467-477.

[190] de Tullio, M. D., Nam, J., Pascazio, G., Balaras, E., and Verzicco, R., 2012, "Computational prediction of mechanical hemolysis in aortic valved prostheses," Eur J Mech B-Fluid, 35, pp. 47-53.

[191] Segalova, P. A., Venkateswara Rao, K. T., Zarins, C. K., and Taylor, C. A., 2012, "Computational modeling of shear-based hemolysis caused by renal obstruction," J. Biomech. Eng., 134(2), p. 021003.

[192] Throckmorton, A. L., Wood, H. G., Day, S. W., Song, X., Click, P. C., Allaire, P. E., and Olsen, D. B., 2003, "Design of a continuous flow centrifugal pediatric ventricular assist device," Int J Artif Organs, 26(11), pp. 1015-1031.

[193] Dongdong, X., Chunzhang, Z., Xiwen, Z., and Jing, B., 2006, "Computational fluid dynamics modeling and hemolysis analysis of axial blood pumps with various impeller structures," Prog Nat Sci, 16(9), pp. 993-997.

[194] Kennington, J. R., Frankel, S. H., Chen, J., Koenig, S. C., Sobieski, M. A., Giridharan, G. A., and Rodefeld, M. D., 2011, "Design optimization and performance studies of an adult scale viscous impeller pump for powered fontan in an idealized total cavopulmonary connection," Cardiovasc. Eng. Technol., 2(4), pp. 237-243.

[195] Soares, J. S., Sheriff, J., and Bluestein, D., 2013, "A novel mathematical model of activation and sensitization of platelets subjected to dynamic stress histories," Biomech Model Mechanobiol, 12(6), pp. 1127-1141.

[196] De Wachter, D., and Verdonck, P., 2002, "Numerical calculation of hemolysis levels in peripheral hemodialysis cannulas," Artif. Organs, 26(7), pp. 576-582.

[197]   Untaroiu, A., Throckmorton, A. L., Patel, S. M., Wood, H. G., Allaire, P. E., and Olsen, D. B., 2005, "Numerical and experimental analysis of an axial flow left ventricular assist device: the influence of the diffuser on overall pump performance," Artif. Organs, 29(7), pp. 581-591.

[198]   Giridharan, G. A., Koenig, S. C., Kennington, J., Sobieski, M. A., Chen, J., Frankel, S. H., and Rodefeld, M. D., 2013, "Performance evaluation of a pediatric viscous impeller pump for Fontan cavopulmonary assist," J. Thorac. Cardiovasc. Surg., 145(1), pp. 249-257.

[199]   Nakamura, M., Bessho, S., and Wada, S., 2014, "Analysis of red blood cell deformation under fast shear flow for better estimation of hemolysis," Int J Numer Method Biomed Eng, 30(1), pp. 42-54.

[200]   Chiu, W. C., Girdhar, G., Xenos, M., Alemu, Y., Soares, J. S., Einav, S., Slepian, M., and Bluestein, D., 2014, "Thromboresistance comparison of the HeartMate II Ventricular Assist Device with the device thrombogenicity emulation-optimized HeartAssist 5 VAD," J. Biomech. Eng., 136(2), pp. 0210141-0210149.

[201]   Shadden, S. C., and Arzani, A., 2015, "Lagrangian postprocessing of computational hemodynamics," Ann. Biomed. Eng., 43(1), pp. 41-58.

[202]   Marom, G., and Bluestein, D., 2016, "Lagrangian methods for blood damage estimation in cardiovascular devices - How numerical implementation affects the results," Expert Rev. Med. Devices, 13(2), pp. 113-122.

[203]   Cokelet, G. R., and Meiselman, H. J., 1968, "Rheological comparison of hemoglobin solutions and erythrocyte suspensions," Science, 162(3850), pp. 275-277.

[204]   Hochmuth, R. M., Buxbaum, K. L., and Evans, E. A., 1980, "Temperature dependence of the viscoelastic recovery of red cell membrane," Biophys. J., 29(1), pp. 177-182.

[205]   Kelemen, C., Chien, S., and Artmann, G. M., 2001, "Temperature transition of human hemoglobin at body temperature: effects of calcium," Biophys. J., 80(6), pp. 2622-2630.

[206]   Faghih, M. M., and Sharp, M. K., 2018, "Evaluation of Energy Dissipation Rate as a Predictor of Mechanical Blood Damage," Artif. Organs(Accepted Author Manuscript).

[207] Ståhl Wernersson, E., and Trägårdh, C., 2000, "Measurements and analysis of high-intensity turbulent characteristics in a turbine-agitated tank," Exp. Fluids, 28(6), pp. 532-545.

[208] Schobeiri, M. T., 2014, Fluid mechanics for engineers: A graduate textbook, Springer Berlin, Berlin.

[209] Jithin, M., Mishra, A., De, A., and Das, M. K., 2016, "Numerical study of bifurcating flow through sudden expansions: effect of divergence and geometric asymmetry," International Journal of Advances in Engineering Sciences and Applied Mathematics, 8(4), pp. 259-273.

[210] Hawa, T., and Rusak, Z., 2001, "The dynamics of a laminar flow in a symmetric channel with a sudden expansion," J. Fluid Mech., 436, pp. 283-320.

[211] Raben, J. S., Hariharan, P., Robinson, R., Malinauskas, R., and Vlachos, P. P., 2016, "Time-Resolved Particle Image Velocimetry Measurements with Wall Shear Stress and Uncertainty Quantification for the FDA Nozzle Model," Cardiovasc. Eng. Technol., 7(1), pp. 7-22.

[212] Faghih, M. M., and Sharp, M. K., 2019, "On Eulerian versus Lagrangian models of mechanical blood damage and the linearized damage function," J. Artificial Organs, p. Accepted.

[213] DeCesare, W., Rath, C., and Hufnagel, C., 1965, "Hemolytic Anemia of Mechanical Origin with Aortic-Valve Prosthesis," New Engl. J. Med., 272(20), pp. 1045-1050.

[214] Svetina, S., Kokot, G., Kebe, T. S., Zeks, B., and Waugh, R. E., 2015, "A novel strain energy relationship for red blood cell membrane skeleton based on spectrin stiffness and its application to micropipette deformation," Biomech Model Mechanobiol.

[215] Fraser, K. H., Taskin, M. E., Griffith, B. P., and Wu, Z. J., 2011, "The use of computational fluid dynamics in the development of ventricular assist devices," Med. Eng. Phys., 33(3), pp. 263-280.

[216] Behbahani, M., Behr, M., Hormes, M., Steinseifer, U., Arora, D., Coronado, O., and Pasquali, M., 2009, "A review of computational fluid dynamics analysis of blood pumps," European Journal of Applied Mathematics, 20(4), pp. 363-397.

[217]   Hariharan, P., D'Souza, G., Horner, M., Malinauskas, R. A., and Myers, M. R., 2015, "Verification benchmarks to assess the implementation of computational fluid dynamics based hemolysis prediction models," J. Biomech. Eng., 137(9).

[218]   James, D. F., 1991, "Flow in a converging channel at moderate reynolds numbers," AIChE J. AIChE Journal, 37(1), pp. 59-64.

[219]   Sousa, P. C., Pinho, I. S., Pinho, F. T., Oliveira, M. S. N., and Alves, M. A., 2011, "Flow of a blood analogue solution through microfabricated hyperbolic contractions," Computational Vision and Medical Image Processing: Recent Trends, S. J. M. R. Tavares, and N. R. M. Jorge, eds., Springer Netherlands, Dordrecht, pp. 265-279.

[220]   White, F. M., 1991, Viscous fluid flow, McGraw-Hill, New York.

[221]   Faghih, M. M., and Sharp, M. K., 2018, "Solvent-based bonding of PMMAPMMA for microfluidic applications," Microsyst Technol Microsystem Technologies.

[222]   Temiz, Y., Lovchik, R. D., Kaigala, G. V., and Delamarche, E., 2015, "Lab-on-a-chip devices: How to close and plug the lab?," Microelectronic Engineering, 132, pp. 156-175.

[223]   Tsao, C.-W., and DeVoe, D. L., 2009, "Bonding of thermoplastic polymer microfluidics," Microfluid Nanofluid Microfluidics and Nanofluidics, 6(1), pp. 1-16.

[224]   Troughton, M. J., 2008, Handbook of plastics joining : a practical guide, William Andrew Inc., Norwich, NY.

[225]   Muccio, E. A., 1995, Plastic part technology, ASM International, [S.l.].

[226]   Gedde, U. W., 2001, "Polymer physics."

[227]   Akhil, A. V., Raj, D. D. D., Raj, M. K., Bhat, S. R., Akshay, V., Bhowmik, S., Ramanathan, S., and Ahmed, S., 2016, "Vaporized solvent bonding of polymethyl methacrylate," Journal of Adhesion Science and Technology, 30(8), pp. 826-841.

[228]   Bamshad, A., Nikfarjam, A., and Khaleghi, H., 2016, "A new simple and fast thermally-solvent assisted method to bond PMMA-PMMA in micro-fluidics devices," J Micromech Microengineering Journal of Micromechanics and Microengineering, 26(6).

[229]   Mona, R., Sumanpreet, C., Dan, S., and Parameswaran, M., 2010, "Microwave-induced, thermally assisted solvent bonding for low-cost PMMA microfluidic devices," Journal of Micromechanics and Microengineering, 20(1), p. 015026.

[230] Wan, A. M. D., Moore, T. A., Young, E. W. K., Moore, T. A., and Young, E. W. K., 2017, "Solvent bonding for fabrication of PMMA and COP microfluidic devices," J. Visualized Exp. Journal of Visualized Experiments, 2017(119).

[231] Burke, J., 1984, "Solubility parameters : theory and application," Book and paper group annual., pp. 13-58.

[232] Hsu, Y. C., and Chen, T. Y., 2007, "Applying Taguchi methods for solvent-assisted PMMA bonding technique for static and dynamic micro-TAS devices," Biomed. Microdevices, 9(4), pp. 513-522.

[233] Lin, C.-H., Chao, C.-H., and Lan, C.-W., 2007, "Low azeotropic solvent for bonding of PMMA microfluidic devices," Sensors Actuators B: Chem., 121(2), pp. 698-705.

[234] Umbrecht, F., Müller, D., Gattiker, F., Boutry, C. M., Neuenschwander, J., Sennhauser, U., and Hierold, C., 2009, "Solvent assisted bonding of polymethylmethacrylate: Characterization using the response surface methodology," Sensors and Actuators A: Physical, 156(1), pp. 121-128.

[235] Tran, H. H., Wu, W., and Lee, N. Y., 2013, "Ethanol and UV-assisted instantaneous bonding of PMMA assemblies and tuning in bonding reversibility," Sensors Actuators B: Chem., 181, pp. 955-962.

[236] Ng, S. P., Wiria, F. E., and Tay, N. B., 2016, "Low Distortion Solvent Bonding of Microfluidic Chips," Procedia Engineering, 141, pp. 130-137.

[237] Mehta, D. S., Naik, D. N., Singh, R. K., and Takeda, M., 2012, "Laser speckle reduction by multimode optical fiber bundle with combined temporal, spatial, and angular diversity," Appl. Opt., 51(12), pp. 1894-1904.

[238] Fischer, T. M., 2007, "Tank-tread frequency of the red cell membrane: dependence on the viscosity of the suspending medium," Biophys. J., 93(7), pp. 2553-2561.

[239] Fischer, T. M., Stohr-Lissen, M., and Schmid-Schonbein, H., 1978, "The red cell as a fluid droplet: tank tread-like motion of the human erythrocyte membrane in shear flow," Science, 202(4370), pp. 894-896.

[240] Pfafferott, C., Nash, G. B., and Meiselman, H. J., 1985, "Red blood cell deformation in shear flow. Effects of internal and external phase viscosity and of in vivo aging," Biophys. J., 47(5), pp. 695-704.

APPENDIX A

The constants in the equations T_φ and T_α are calculated as

$$T_1{}^\alpha = \Delta P \frac{c^2}{2}\left(\frac{b}{a} - \frac{a}{b}\right) + \frac{c^2}{2}\left[\left(\frac{8\eta_0 A'}{abc} - S_0\right)\frac{b}{a} - \left(\frac{8\eta_0 B'}{abc} - S_0\right)\frac{a}{b}\right] \tag{A-1}$$

$$T_2{}^\alpha = c^2 L' \tag{A-2}$$

$$T_3{}^\alpha = \frac{ab}{2}\left(\Delta P + \frac{8\eta_o C'}{abc} - S_0\right) \tag{A-3}$$

$$T^\varphi = \Delta P\left(\frac{ab}{2c^2} + \frac{1}{2}\left(\frac{b}{a} + \frac{a}{b} - \frac{2ab}{c^2}\right) + \frac{1}{2}\left[\left(\frac{8\eta_0 A'}{abc} - S_0\right)\frac{b}{a} + \left(\frac{8\eta_0 B'}{abc} - S_0\right)\frac{a}{b} - \left(\frac{8\eta_0 C'}{abc} - S_0\right)\frac{2ab}{c^2}\right] + \frac{ab}{2c^2}\left(\frac{8\eta_o C'}{abc} - S_0\right) \tag{A-4}$$

where

$$\Delta P = p_i - P_\infty \tag{A-5}$$

$$S_0 = 4\eta_o(\alpha_o A' + \beta_o B' + \gamma_o C') \tag{A-6}$$

$$A' = \left(\alpha_0{}'' + \frac{\beta_0{}''}{2}\right)\dot\gamma \, sin2\theta \, / \, [6(\alpha_0{}''\beta_0{}'' + \beta_0{}''\gamma_0{}'' + \gamma_0{}''\alpha_0{}'')] \tag{A-7}$$

$$B' = -\left(\beta_0{}'' + \frac{\alpha_0{}''}{2}\right)\dot\gamma \, sin2\theta \, / \, [6(\alpha_0{}''\beta_0{}'' + \beta_0{}''\gamma_0{}'' + \gamma_0{}''\alpha_0{}'')] \tag{A-8}$$

$$C' = -(\alpha_0{}'' - \beta_0{}'')\dot\gamma \, sin2\theta \, / \, [12(\alpha_0{}''\beta_0{}'' + \beta_0{}''\gamma_0{}'' + \gamma_0{}''\alpha_0{}'')] \tag{A-9}$$

$$\alpha_0 = \frac{2[F(v,q) - E(v,q)]}{(a^2 - c^2)\sqrt{a^2 - b^2}} \tag{A-10}$$

$$\beta_0 = \frac{-2E(v,q)}{(c^2 - b^2)\sqrt{a^2 - b^2}} + \frac{2}{(c^2 - b^2)}\sqrt{\frac{\lambda + c^2}{(\lambda + b^2)(\lambda + a^2)}} \tag{A-11}$$

$$\gamma_0 = \frac{2E(v,q)\sqrt{a^2 - b^2}}{(c^2 - b^2)(a^2 - c^2)} - \frac{2F(v,q)}{(a^2 - c^2)\sqrt{a^2 - b^2}} - \frac{2}{(c^2 - b^2)}\sqrt{\frac{\lambda + b^2}{(\lambda + c^2)(\lambda + a^2)}} \tag{A-12}$$

$$\gamma_0' = \frac{(\beta_0 - \alpha_0)}{(a^2 - b^2)} \tag{A-13}$$

$$\alpha_0'' = \frac{b^2\beta_0 - c^2\gamma_0}{(b^2 - c^2)} \tag{A-14158}$$

$$\beta_0'' = \frac{c^2\gamma_0 - a^2\alpha_0}{(c^2 - a^2)} \tag{A-15}$$

$$\gamma_0'' = \frac{a^2\alpha_0 - b^2\beta_0}{(a^2 - b^2)} \tag{A-16}$$

$$F(v,q) = \int_0^v \frac{dm}{\sqrt{1 - q^2 \sin^2 m}} \tag{A-17}$$

$$E(v,q) = \int_0^v \sqrt{1 - q^2 \sin^2 m}\, dm \tag{A-18}$$

$$v = arc\sin\sqrt{\frac{(a^2 - b^2)}{(a^2 - \lambda)}} \tag{A-19}$$

$$q = \sqrt{\frac{(a^2 - c^2)}{(a^2 - b^2)}} \tag{A-20}$$

$$L' = \frac{8\eta_0 H'}{abc} - E' \tag{A-21}$$

$$E' = \eta_i f_t\left(\frac{a}{b} - \frac{b}{a}\right) \tag{A-22}$$

$$H' = \frac{\alpha_0[\frac{1}{2}\dot{\gamma}\cos 2\theta - f_t(a^2 - b^2)/2ab] - b^2\gamma_0'[-\frac{1}{2}\dot{\gamma} + f_t(a^2 + b^2)/2ab]}{2\gamma_0'(a^2\alpha_0 + b^2\beta_0)} \tag{A-23}$$

where f_t is the tank treading frequency, θ is the cell inclination and $\dot{\gamma}$ is the shear rate. For points on the ellipsoid surface, $\lambda = 0$.

CURRICULUM VITAE

Mohammad Mohaghegh Faghih

Biofluid Mechanics Lab. at University of Louisville
332 Eastern Parkway, Louisville, KY, 40208
(502)-296-0668 **-** m0moha12@louisville.edu

Education

2015-2019, PhD, Mechanical Engineering, University of Louisville
2009-2011, MSc, Biomedical Engineering, Iran University of Science and Technology
2005-2009, BSc, Mechanical Engineering, Iran University of Science and Technology

Journal Publication

- In preparation: Experimental study on Deformation of Human Red Blood Cell in Extensional Flow through a Hyperbolic Contraction.

- In preparation: On the Discretization of the Power Law Hemolysis Model.

- Faghih MM, Sharp MK (2019) Modeling and prediction of flow-induced hemolysis: a review. Biomech Model Mechanobiol.
- Faghih, M. M., and Sharp, M. K., 2019, "On Eulerian versus Lagrangian Models of Mechanical Blood Damage and the Linearized Damage Function," Artif. Organs.
- Faghih, M. M., and Sharp, M. K., 2018, "Evaluation of Energy Dissipation Rate as a Predictor of Mechanical Blood Damage," Artif. Organs.

- Faghih, M. M., and Sharp, M. K., 2018, "Solvent-based bonding of PMMA–PMMA for microfluidic applications," Microsystem Technologies.

- Faghih, M. M., & Sharp, M. K. (2018). "Is bulk flow plausible in perivascular, paravascular and paravenous channels?", Fluids and Barriers of the CNS, 15, 17. http://doi.org/10.1186/s12987-018-0103-8.
- M M Faghih, Sharp MK (2018). "Characterization of erythrocyte membrane tension for hemolysis prediction in complex flows". Biomech Model Mechanobiol doi:10.1007/s10237-017-0995-2
- Faghih, M. M., & Keith, S. M. (December 01, 2016). Extending the Power-Law Hemolysis Model to Complex Flows. Journal of Biomechanical Engineering, 138, 12, 124504.

- Attar, M.M., Haghpanahi, M., Amanpour, S., Faghih, M.M., "Analysis of Bioheat Transfer Equation for Hyperthermia Cancer Treatment.", J Mech Sci Technol (2014) 28: 763.

Conference

- 2018 8th World Congress of Biomechanics: Faghih, MM., Keith Sharp M, "Plausibility of lymph-like flow through the brain via periarterial and paraarterial spaces".

- 2017 Summer Biomechanics, Bioengineering and Biotransport Conference: Faghih, MM., Keith Sharp M, "Applying the Scalar Stress Concept in the Power-Law Hemolysis Model".

- 2017 Summer Biomechanics, Bioengineering and Biotransport Conference: Faghih, MM., Keith Sharp M, "Limitations of The Scalar Stress for Predicting Hemolysis in Complex Flows".

- 2017 Louisville local ASME conference: Faghih, MM, "Blood Damage in Blood-Contacting Devices".

- 2017 4th International CSF Hydrodynamics Symposium: Faghih, MM, Keith Sharp M, "Flow of Amyloid-β along Basement Membranes in Perivascular Space of Cerebral Arteries".

Teaching experience

- Teaching assistant for Fluid Mechanics Lab., Spring 2019, University of Louisville
- Teaching assistant for Fluid Mechanics II, Fall 2018, University of Louisville
- Lecturer for Thermodynamics I, Summer 2018, University of Louisville
- Teaching assistant for Fluid Mechanics I, Spring 2017, University of Louisville
- Teaching assistant for Thermodynamics I, Spring 2017, University of Louisville
- Teaching assistant Fluid Mechanics Lab., Fall 2017, University of Louisville

Research Skills

- Computational Fluid Dynamics.
- Lattice Boltzmann Method (Beginner).
- Optical microscopy.
- Micro-CNC.
- Fabrication of micro-devices (solvent-based bonding).
- Particle Image Velocimetry (intermediate).
- Intermediate knowledge about other flow visualization techniques.

- Data acquisition using LabView (Beginner).

Research interest

- Blood flow mechanics
- Cardiovascular modelling
- Cerebrospinal flow analysis

Work experience

- Design and implementation of the small to medium-sized HVAC systems, 2 years.

Awards and Accomplishments

- Recipient of University of Louisville Graduate Fellowship.
- Our paper "Extending the Power-Law Hemolysis Model to Complex Flows" published as JBME 138:124504 was selected as the top ten papers by the JBME Editors' Choice papers for 2016.
- Ranked third in student presentation competition in local ASME conference event.
- Selected to receive the 2017 University of Louisville Graduate Research Funding.

Software

- Ansys Workbench
- MATLAB
- Solidworks
- ImageJ
- Office
- Hourly Analysis Program HVAC System Design Software

Certificates

- Bloodborne Pathogens Training, University of Louisville, 2018, issued by BioRAFT.
- Introduction and calibration of medical equipment, Iranian Academic Center for Education, Culture and Research, 2010.

Other Activities

- Worked with high-school students as part of their lab shadowing.

Professional Membership

- Kentucky Academy of Science